Imperial College London

Computerized Analysis of Magnetic Resonance Images to Study Cerebral Anatomy in Developing Neonates

Hui Xue

A dissertation submitted in partial fulfillment
of the requirements for the degree of
Doctor of Philosophy
of the
Imperial College London

March 2008
Robert Steiner MR Unit, Imaging sciences Department
Visual Information Processing, Department of Computing
Imperial College London

Abstract

The study of cerebral anatomy in developing neonates is of great importance for the understanding of brain development during the early period of life. This dissertation therefore focuses on three challenges in the modelling of cerebral anatomy in neonates during brain development. The methods that have been developed all use Magnetic Resonance Images (MRI) as source data.

To facilitate study of vascular development in the neonatal period, a set of image analysis algorithms are developed to automatically extract and model cerebral vessel trees. The whole process consists of cerebral vessel tracking from automatically placed seed points, vessel tree generation, and vasculature registration and matching. These algorithms have been tested on clinical Time-of-Flight (TOF) MR angiographic datasets.

To facilitate study of the neonatal cortex a complete cerebral cortex segmentation and reconstruction pipeline has been developed. Segmentation of the neonatal cortex is not effectively done by existing algorithms designed for the adult brain because the contrast between grey and white matter is reversed. This causes pixels containing tissue mixtures to be incorrectly labelled by conventional methods. The neonatal cortical segmentation method that has been developed is based on a novel expectation-maximization (EM) method with explicit correction for mislabelled partial volume voxels. Based on the resulting cortical segmentation, an implicit surface evolution technique is adopted for the reconstruction of the cortex in

neonates. The performance of the method is investigated by performing a detailed landmark study.

To facilitate study of cortical development, a cortical surface registration algorithm for aligning the cortical surface is developed. The method first inflates extracted cortical surfaces and then performs a non-rigid surface registration using free-form deformations (FFDs) to remove residual alignment. Validation experiments using data labelled by an expert observer demonstrate that the method can capture local changes and follow the growth of specific sulcus.

Acknowledgements

My parents, Shaoping and Zhenghua, deserve the most credits for giving me great encouragement and support over my whole life.

Finally, this dissertation is dedicated to my loving wife, Haiyan. It is your patience, understanding and love that really drive me to achieve the goal.

Contents

List of Figures

List of Tables

List of Abbreviations

AAM	Active Appearance Model
ACA	Anterior Cerebral Artery
AFCM	Adaptive Fuzzy C-Means
ASM	Active Shape Model
ASP	Anatomic Segmentation using Proximities
BET	Brain Extraction Tool
BFGS	Broyden-Fletcher-Goldfarb-Shanno
BSE	Brain Surface Extractor
CE-MRA	Contrast Enhanced MRA
CNR	Contrast-to-Noise Ratio
CSF	Cerebro-Spinal Fluid
CTA	Computerized Tomography Angiography
DM	Distance Metric
DOF	Degree Of Freedom
DSC	Dice Similarity Coefficient
EM	Expectation-Maximization
ENO	Essentially Non-Oscillatory scheme
EPI	Echo Planar Imaging

FFD	Free-Form Deformation
FN	False Negative
FP	False Positive
GA	Gestational Age
Gd-DTPA	Gadolinium-Diethylene-Triamine Pentaacetic Acid
GM	Grey Matter
GVF	Gradient Vector Flow
HJ-PDE	Hamilton-Jacobi Partial Differential Equations
ICI	Intrinsic Curvature Index
ICM	Iterated Conditional Modes
ICP	Iterative Closest Point
IXI	Information eXtraction from Images
k-NN	k-Nearest Neighbor
MAP	Maximum A Posterior
MCA	Middle Cerebral Artery
MIP	Maximum Intensity Projection
MLN	Mean Curvature L_2 Norm
MLPV	Mislabeled Partial Volume Voxel
MP-RAGE	Magnetization Prepared RApid Gradient Echo
MRI	Magnetic Resonance Imaging
MRA	Magnetic Resonance Angiography
MRD	Mean Residual Displacement
MRF	Markov Random Field

NVL	Normalized Vasculature Length
N3	Nonparametric Nonuniform intensity Normalization
PCA	Posterior Cerebral Artery
PC-MRA	Phase Contrast MRA
PD	Proton Density
PDF	Probability Density Function
RF	Radio Frequency
ROI	Region-Of-Interest
SENSE	SENSitivity Encoding
SNR	Signal-to-Noise Ratio
SPM2	Statistical Parametric Mapping v.2
SRE	Surface Reconstruction Errors
TCA	Topological Constraint Algorithm
TOF-MRA	Time Of Flight MRA
TP	True Positive
TVD-RK	Total Variation Diminishing Runge-Kutta Integration Scheme
T1w-MRI	T1 weighted-MRI
T2w-MRI	T2 weighted-MRI
WM	White Matter
ZBS	Z-Buffer Segmentation

List of Publications

Articles in Journals

Hui Xue, Latha Srinivasan, Shuzhou Jiang, Mary Rutherford, A. David Edwards, Daniel Rueckert and Joseph V. Hajnal. Automatic segmentation and reconstruction of the cortex from neonatal MRI. *NeuroImage* 38(3), 461 – 477, 2007.

Shuzhou Jiang, **Hui Xue**, Alan Glover, Mary Rutherford, Jo V Hajnal. MRI of moving subjects using multi – slice Snapshot images with Volume Reconstruction (SVR): application to fetal, neonatal and adult brain studies. *IEEE Transactions on Medical Imaging* 26(7), 967 – 980, 2007.

Articles in Conference Proceedings

Hui Xue, Jens Guehring, Latha Srinivasan, Sven Zuehlsdorff, Kinda Saddi, Christophe Chefdhotel, Jo Hajnal and Daniel Rueckert. Evaluation of Rigid and Non-Rigid Motion Compensation of Cardiac Perfusion MRI. Submitted to *The 11th International Conference on Medical Image Computing and Computer Assisted Intervention (MICCAI 2008)*.

Hui Xue, Latha Srinivasan, Shuzhou Jiang, Mary Rutherford, Anthony D. Edwards, Daniel Rueckert and Jo Hajnal. Longitudinal Cortical Registration for Developing Neonates. *The 10th International Conference on Medical Image Computing and Computer Assisted Intervention (MICCAI 2007)*. 127 – 135, Oct 29 – Nov 2, 2007, Brisbane, Australia.

Shuzhou Jiang, **Hui Xue**, Serena Counsell, Mustafa Anjari, Joanna Allsop, Mary Rutherford, Daniel Rueckert, Joseph Hajnal. In–utero Three Dimension High Resolution Fetal Brain Diffusion Tensor Imaging. *The 10th International Conference on Medical Image Computing and Computer Assisted Intervention (MICCAI 2007).* 17 – 25, Oct 29 – Nov 2, 2007, Brisbane, Australia.

Hui Xue, Latha Srinivasan, Shuzhou Jiang, Mary Rutherford, Anthony D. Edwards, Daniel Rueckert and Jo Hajnal. Automatic Cortical Segmentation in the Developing Brain. *The 20th International Conference of Information Processing in Medical Imaging (IPMI 2007).* 257 – 269, July 2 – 6, 2007, Kerkrade, The Netherlands.

Hui Xue, Christina Malamateniou, Joanna Allsop, Latha Srinivasan, Jo V Hajnal, Daniel Rueckert. Automatic Extraction and Matching of Neonatal Cerebral Vasculature. *IEEE 2006 International Symposium on Biomedical Imaging.* April 6 – 9, 2006, Arlington, Virginia.

Shuzhou Jiang, **Hui Xue**, Alan Glover, Mary Rutherford, Jo V Hajnal. A Novel Approach to Accurate 3D High Resolution and High SNR Fetal Brain Imaging. *IEEE 2006 International Symposium on Biomedical Imaging.* April 6 – 9, Arlington, Virginia.

Hui Xue, Christina Malamateniou, Serena Counsell, Mary Ruthford, Daniel Rueckert, Jo V Hajnal. Extraction and Registration of Neonatal Cerebral Vasculature for Preterm and Term Infants. Proceedings of *the 9*[th] *Annual Conference on Medical Image Understanding and Analysis (MIUA 2005).* 19 – 20 July, Bristol, UK.

Abstracts in Conferences

Hui Xue, Jens Guehring, Jo Hajnal, Daniel Rueckert, Sven Zuehlsdorff, Kinda Saddi, Christophe Chefdhotel. Evaluation of Rigid and Non-Rigid Motion

Compensation of Cardiac Perfusion MRI. *The Annual Meeting of ISMRM 2008. May 3 – 9, Toronto, Canada* (**Oral presentation**).

Hui Xue, Latha Srinivasan, Shuzhou Jiang, Serena J. Counsell, Mary A. Rutherford, David Edwards, Daniel Rueckert, Jo Hajnal. Automatic Cortical Segmentation for Developing Neonates with the Correction of Mislabeled Partial Volumes (MLPVs). *The Joint Annual Meeting ISMRM – ESMRMB*. May 19 – 25, 2007, Berlin, Germany (**Oral presentation**).

Hui Xue, Shuzhou Jiang, Latha Srinivasan, Serena J. Counsell, Mary A. Rutherford, David Edwards, Daniel Rueckert, Jo Hajnal. Cortical Surface Reconstructions for Developing Neonates. *The Joint Annual Meeting ISMRM – ESMRMB*. May 19 – 25, 2007, Berlin, Germany.

Hui Xue, Shaihan J. Malik, Stephan Schmitz, Declan Oregan, Daniel Rueckert, Jo Hajnal. Automatic Peripheral Vessel Tracking in 3D Contrast – Enhanced MR Angiography. *The Joint Annual Meeting ISMRM – ESMRMB*. May 19 – 25, 2007, Berlin, Germany.

James Myers, **Hui Xue**, Adam Waldman, Daniel Rueckert, Jo Hajnal. Decline in Extent Macroscopic Cerebral Vasculature with Age Quantified Using Computerized Automatic Vessel Tracking. *The Joint Annual Meeting ISMRM – ESMRMB*. May 19 – 25, 2007, Berlin, Germany.

Latha Srinivasan, **Hui Xue**, Serena J. Counsell, Joanna M. Allsop, Julie Fitzpatrick, A David Edwards, Mary A. Rutherford, Daniel Rueckert, Joesph V. Hajnal. Cortical Curvature and Allometric Scaling of Cerebral Cortex in Preterm Infants. *The Joint Annual Meeting ISMRM – ESMRMB*. May 19 – 25, 2007, Berlin, Germany.

Shuzhou Jiang, Serena J. Counsell, **Hui Xue**, Joanna M. Allsop, Mary A. Rutherford, Daniel Rueckert, Joseph V. Hajnal. In – Utero 3D High Resolution

Fetal Brain Diffusion Tensor Imaging. *The Joint Annual Meeting ISMRM – ESMRMB*. May 19 – 25, 2007, Berlin, Germany (**Oral presentation**).

Shuzhou Jiang, **Hui Xue**, Mary A. Rutherford, Adam Waldman, Kate McLeish, Derek Hill, Daniel Rueckert, Joseph V. Hajnal. Brain MRI of Moving Subjects: Snapshot Images with Volume Reconstruction (SVR) Extended to Multi – Shot Sequences and Applied to Neonates and Adults. *The Joint Annual Meeting ISMRM – ESMRMB*. May 19 – 25, 2007, Berlin, Germany.

Hui Xue, Christina Malamateniou, Joanna M. Allsop, Latha Srinivasan, Daniel Rueckert, Jo V Hajnal. Automatic Extraction and Matching of Neonatal Cerebral Vasculature from MRA – TOF Images. *The Annual Meeting of ISMRM 2006*. May 6 – 12, Seattle, Washington, USA.

Hui Xue, Christina Malamateniou, Serena Counsell, Mary Ruthford, Daniel Rueckert, Jo V Hajnal. Indirect registration of neonatal cerebral vasculature across time – points. *The 22th Annual Conference of the European Society for Magnetic Resonance in Medicine and Biology (ESMRMB 2005)*. 19 – 20 July, 2005, Basel, Swiss.

Chapter 1

Introduction

1.1 Motivation

The study of cerebral anatomy in developing neonates is of great importance for the understanding of the microscopic and macroscopic brain development during the early period of life and can help identify variant neurological lesions in immature brains. (Shah et al., 2005; Marlow et al., 2005; Inder et al., 2005; Wilson et al., 2006; Kostovic and Judas, 2006; Boardman et al., 2006; Kapellou et al., 2006; Srinivasan et al., 2007; Counsell et al., 2007; Adamsbaum, 2007). With advanced magnetic resonance imaging (MRI) techniques, especially using 3T MRI scanners and rapid imaging techniques (Huppi et al., 1998; Inder and Huppi, 2000; Huppi and Inder, 2001; Counsell et al., 2003; Neil and Inder, 2004; Rutherford et al., 2005; O'Shea et al., 2005; Rutherford et al., 2006; Rousseau et al., 2006; Jiang et al., 2007; Boardman and Dyet, 2007), detailed images of the developing brain anatomy in neonates can be reliably acquired using the MR anatomical imaging sequences, e.g. T1 weighted (T1w) or T2 weighted (T2w). Although these advances lead to highly improved images of the cerebral anatomy, the morphometric analysis of the three-dimensional (3D) brain images is still difficult due to the lack of automated image processing tools. The goal of this dissertation is the development of automatic image processing tools for the analysis of these images.

The manual delineation of the human brain anatomy from high-resolution 3D MR images requires expert knowledge and is a tedious and very time-consuming task.

This is especially true for population studies. For example, the systematic study of cortical morphometric abnormality caused by preterm birth requires the manually segmentation and labeling of the cerebral cortex from MR images for tens of preterm neonates at different gestational ages, which can take months for an experienced neonatologist. Additionally, the manual delineation is influenced by the variability of the human operator, which limits its reliability and reproducibility.

Ideally, an accurate and robust algorithm could automate this task, therefore reducing the workload of clinical scientists and simultaneously minimizing intra- and inter-operator variability. The main goal of the research in this dissertation is to develop and validate the computerized segmentation and modeling algorithms to reconstruct the cerebral anatomy across different neonates and across different ages. Specifically, three aims are addressed: The first goal is to develop an algorithm to extract and model the cerebral vasculature in neonates. This is motivated by the difficulties in characterizing 3D vasculature accurately from 2D projections or cross-sectional images which are currently used in radiological practice. The second goal is to develop an effective segmentation and reconstruction algorithm for developing cortex in neonates. The analysis of cortical morphometry has attracted significant interest in the neuroscience community in order to explore the structure and function of the human brain. However, there remain significant challenges in extending this to the developing cortex during the early phase of life. The final goal is to develop cortical mapping/registration methods which are based on the successful reconstruction of neonatal cortical surfaces, as the effective cortical registration will favor the comparison of developing cortical structures across different time-points and different subjects.

To maximize the acceptance of developed image analysis algorithms by clinicians and neonatologists, the accuracy, robustness and reliability of proposed techniques are emphasized. This leads to a requirement that the proposed image-processing methods can be applied reliably by clinician scientists and fulfill the requirements

of effective neuroscience studies. As a result, considerable amount of effort has been spent to validate the developed techniques in several ways.

1.2   Contribution and overview

This dissertation focuses on a couple of tasks in the modeling of cerebral anatomy in neonates during brain development: extraction of cerebral vasculatures, automatic segmentation and reconstruction of cortical surfaces and comparison of developing cortical structures. The main contributions are:

- A complete image analysis pipeline to extract and model cerebral vessel trees in neonatal MRI. The whole process consists of cerebral vessel tracking from automatically placed seed points, vessel tree generation, and vasculature registration and matching. These algorithms have been tested on clinical Time-of-Flight (TOF) MR angiographic datasets with regards to robustness to noise, segmentation completeness and precision. The algorithms have also been applied to adult vascular analysis and in a study of normal volunteers where a statistically significant age related decline in detected extent of arterial tree is shown.

- A cerebral cortex segmentation algorithm for neonatal MRI. The segmentation of neonatal cortex is much more challenging than the segmentation of cortex in adults. The main reason is the inverted intensity contrast between grey matter (GM) and white matter (WM) that occurs when myelination is incomplete. This causes the misclassification of voxels, especially in voxels affected by partial volume effects, e.g. at the interface between GM and cerebrospinal fluid (CSF). A fully automatic cortical segmentation approach based on the expectation-maximization (EM) is proposed: Mislabeled voxels are detected using a knowledge-based approach and corrected by adjusting the local priors. Our results show that

the proposed algorithm corrects errors in the segmentation of both GM and WM compared to the classic EM algorithm.

- A complete cortical reconstruction workflow for neonatal MRI. Although many approaches have been proposed for the cortical reconstruction in adults, to the best of our knowledge, none of them have been applied to neonates ranging from very premature to term equivalent age. This is partly due to the difficulties encountered in segmenting neonatal brain MRI. Based on the cortical segmentation developed for neonates, an implicit surface evolution technique is adapted for the reconstruction of the cortex in neonates. The performance of the method is investigated by performing a detailed landmark study. The results show that all three cortical surfaces (inner, central and outer) are reliably reconstructed with sub-voxel accuracy. The proposed cortical segmentation-reconstruction pipeline is applied to a large number of neonatal MR brain images for developing neonates (99 preterm infants with GA from 27 to 49 weeks).

- A cortical surface registration algorithm for aligning the cortical surface in longitudinal MRI. In the first step, two cortical surfaces are adaptively smoothed until their folding complexity is similar. In the second stage any residual misalignment of the cortex is corrected by performing a non-rigid surface registration using free-form deformations (FFDs). This method is able to obtain the direct correspondence of cortical surface features, which differs from previously published strategies in which cortical feature correspondence is obtained using an intermediate coordinate system, e.g. a plane or a sphere. The experiments demonstrate the ability to capture local changes and follow the growth of specific sulcus across gestational ages (GAs).

The dissertation is organized as follows: After this introductory chapter in which the motivations and the problems for this work are described, Chapter 2 presents

the image analysis pipeline to extract and model cerebral vessel trees for developing neonates. Chapter 3 reviews the current state-of-the-art in cortical segmentation and reconstruction for adults, which forms the context for the following studies of neonatal cortex reconstruction in Chapter 4 and 5. Specifically, a cortex segmentation algorithm for neonatal MRI is presented in Chapter 4. Based on this method a reconstruction technique for the neonatal cortex is introduced in Chapter 5. A cortical surface registration algorithm is also presented in this chapter. The final chapter summarizes the work in this thesis and presents the conclusions. Potential future work in this area is also discussed here.

Chapter 2

Extraction and Matching Cerebral Vasculature for Developing Neonates from MR Angiography Images

2.1 Introduction

Neonatal brain development proceeds rapidly in the 3rd trimester of pregnancy and is accompanied by fast growth of the cerebral vascular system. Imaging the neonatal cerebral vasculature is important for the identification of congenital cerebrovascular abnormalities and the investigation of anatomical and physiological characteristics not only during normal development but also in diseases such as perinatal stoke and neonatal encephalopathy.

Both Magnetic Resonance Angiography (MRA) and ultrasound have been used for imaging of the neonatal cerebral vasculature. Although ultrasound has been the most widely used method for imaging the brain and vasculature of neonates (d'Orey et al., 1999; Robel-Tillig et al., 1999; Robel-Tillig et al., 2000; Seydel, 2001; Pezzati et al., 2002), it lacks spatial resolution and is limited by the narrow imaging window due to the ossification of the fontanelles which is more problematic for the more mature infants. As a result, some vessels, e.g. the posterior cerebral arteries, are particularly difficult to insonate. In contrast to this, MRA can provide better spatial resolution and signal-to-noise ratio (SNR). MRA

can resolve fine anatomical details and allows the non-invasive study of the cerebral vascular architecture without the requirement of contrast injection. More importantly, recent technique advances in MRA have led to markedly improved image quality from MRA in neonates (Malamateniou et al., 2005; Malamateniou et al., 2006). This opens new possibilities for clinical research to study systematic differences in the vasculature of neonates and to follow growth and development in individual subjects. The rapid evolution of neonatal cerebral vasculatures (Tarby and Volpe, 1982; Husain et al., 2000; Okahara et al., 2002; Anstrom et al., 2002; Reith and Shamdeen, 2003) and non-invasive nature of MRA suggests that serial studies could yield valuable information about both normal and abnormal vessel development. Current radiological practice generally relies on comparisons using 2D maximum intensity projections (MIP) of 3D Time of Flight-MRA (TOF -MRA) images as well as direct visual inspection of the source images themselves. The 2D projections cannot provide quantitative morphological information about the 3D vasculature and inspection of the images does not facilitate thorough comparisons on where significant change has occurred (An example of 2D MIP can be seen in Figure 2.10). The development of 3D vessel analysis methods may enable the effective analysis and improved quantification of developing cerebral vasculature. The analysis of the vasculature in longitudinal studies requires accurate, automatic vascular segmentation and vessel tree composition, as well as the ability to determine detailed branch-by-branch correspondences over time. We have developed such tools and tested them on a cohort of neonatal subjects.

Because blood vessel extraction from medical image data is a prerequisite for several clinical applications, it has been intensively studied during the past 15 years. Existing methods can broadly be divided into two categories: skeleton and non-skeleton approaches. Skeleton based methods (Aylward et al., 1996; Frangi et al., 1999; Niessen et al., 1999; Wink et al., 2000; Frangi et al., 2001; Aylward and Bullitt, 2002) explicitly extract vessel centerlines and represent results as discrete sets of points or parametric curves in 3D space. For example, Wink et al. (2000) proposes a fast vessel delineation technique and tests its performance on different

imaging modalities such as computerized tomography angiography (CTA), phase contrast (PC) MRA and contrast enhanced (CE) MRA. This method begins from a user supplied starting point. The next candidate point is estimated by making small steps towards a defined end point. The potential perpendicular vessel lumen plane is defined by a predetermined maximal vessel diameter. As the candidate point may not be the vessel centre, its position is optimized by maximizing a center likelihood measure defined from the local intensity gradient information. The tracking process stops if the end point is reached or no vessel centre can be found. This method is fast as only local information is used in vessel tracking; however, no vessel scale is considered to tune the algorithm parameters to fit both large and small vessels. On the other hand, Frangi et al. (1999, 2001) proposes a model based approach using the deformable contour technique. In this scheme, the vessel centerline is approximated by a B-spline curve. The deformation process is based on moving the control points of B-spline toward voxel points which have a high likelihood and lie along the central vessel axis. The required external force is defined from a vesselness filter (Frangi et al., 1998). This filter reaches its maximum at the symmetric centre of the vessel and explicitly takes into account information of vessel scale (its radius). Thus it is sensitive to vessels with a selected characteristic size. After the vessel centerline is extracted, another deformable model is used to find the vessel wall, where the initialization is achieved using a simple isosurface method. This vessel extraction method has been tested to model the carotid from TOF-MRA images. One drawback of this approach is the initial centerline provided as the starting point for the deformable B-spline curve has to be sufficiently close to the vessel centre, which makes it difficult to extract complex vasculatures for which it is difficult to provide a good initialization. Aylward et al. (1996) and Aylward and Bullitt (2002) propose another algorithm to track the vessel centerline. This method is based on the observation that vessel centerline often corresponds to the intensity ridge in the 3D TOF-MRA images. The vessel tracking starts from the seed point near the vessel centre and moves towards a local ridge point by minimizing a ridgeness function. As supplying the seed points is much easier than initializing a centerline, this

method, compared to Frangi et al. (1999), is more suitable for detection of complex vasculatures. We therefore adopted this approach and developed it further to model the neonatal cerebral vasculature by automating the extraction process.

Non-skeleton based methods label all voxels belonging to the vasculature on a voxel-by-voxel basis. An extra skeletonization step is usually needed if vessel centerlines are required. A typical non-skeleton based method is the expectation-maximization (EM) based algorithm, proposed in Wilson and Nobel (1997, 1999). In this scheme, the probability of observing intensities in TOF-MRA image is modeled by a mixture Gaussian model. The mixture model consists of two classes: arteries and background. An iterative EM algorithm is used to estimate the mean, variance and weights of the mixture model. Based on the estimated EM parameters, the lower threshold of vessel intensity is determined. All voxels with higher intensity values are classified as vessel points. This method is straightforward to use and has the potential to work on many bright-blood angiography images. However, as the contrast-to-noise ratio (CNR) can be lower for smaller vessels due to the slow blood flow in TOF-MRA, a single Gaussian distribution may not be sufficient to approximate the real intensity distribution of all vessels across different spatial scales.

Masutani et al. (1995) proposes another non-skeleton based method employing four fundamental operators of mathematical morphology: dilation, erosion, opening and closing. In this approach, a series of morphological operations are preformed to achieve a single connected vasculature component. This method relies on the good CNR between vessels and background tissues, which may not be true for small vessels.

There are other non-skeleton based methods, including the image moment-based segmentation (Luo et al., 1993), scale-space fuzzy connectedness techniques (Saha et al., 2000), geodesic active contours (Lorigo et al., 1999; Lorigo et al., 2000), and multi-scale vasculature modeling (Krissian et al., 1998; Krissian et al., 2000). The

comprehensive review of algorithms for vasculature extraction can be found in Suri et al. (2002a), Suri et al. (2002b), and Kirbas and Quek (2004).

After vessel segments are extracted from MRA images, they need to be linked to form a tree which is the natural representation of human vasculature. Little attention has so far been paid to vessel tree formation, with most works focusing on vasculature segmentation and modeling. However, the accurate symbolic vessel tree representation is a key requirement for further vasculature analysis. In this chapter, we transformed the extracted vessel branches into a tree which is then matched to other trees to achieve both topological and geometrical correspondence. Such vasculature matching is distinct from vasculature registration. The latter aims to recover voxel-by-voxel correspondence, which means that any point in a given vessel branch in one image is mapped to its corresponding point in another image. However in neonates, voxel-by-voxel mapping is often impossible because of vasculature changes caused by brain development, so we have developed a vessel matching scheme to determine topological correspondence between different branches. Establishing branch-by-branch correspondence exploits the observation that in the developing brain the vasculature topology usually remains unchanged except for the addition of newly developing peripheral branches.

There are relatively few other vessel tree matching methods in the literature. Some authors have applied graph matching methods (Tschirren et al., 2002; Tschirren et al., 2005) or subtree isomorphism (Pisupati et al., 1996) to object recognition and scene interpretation. Tree structures, however, are topologically different from graphs in that the former are oriented and any two nodes are connected with a unique path, which implies that tree matching algorithms are potentially simpler than graph matching. To the best of our knowledge, the only work on vessel tree matching was proposed by Arnaud et al. (2005). They presented a tree matching algorithm for intra-patient hepatic vasculature. The method calculates a matching measure using a linear combination of vessel radius, length and angle between two branches. Although good results were reported in CT hepatic images, the need to

estimate vessel radius is a potential impediment when using MRA data, since limited image resolution can make it difficult to precisely measure the radius of small vessels.

In this chapter, we adopt a ridge detection based vessel extraction algorithm (Aylward et al., 1996; Aylward and Bullitt, 2002) to detect centerlines throughout cerebral vasculatures. We improve the original algorithm in several ways: First, we develop a seed generation algorithm to automate the extraction process and achieve the extraction of complete cerebral vasculature. To improve the efficiency of the vessel extraction seeds are only generated near vessels. Secondly, we develop an algorithm for the automatic tree composition from segmented vessel branches which ensures correct parent-child relationships. This serves as input for the tree matching that establishes branch-by-branch correspondences and so allows the pattern of vessel development in individual infants to be assessed and quantified. Finally, we demonstrate the utility of proposed methods in providing quantitative 3D information and capturing neonatal vasculature development.

The rest of this chapter is organized as follows: In section 2.2, we present the vessel extraction methods including the ridge detection, seed generation and optimal scale estimation. In section 2.3, we develop the algorithm to automatically match the cerebral vasculatures. Results and evaluation of applying both algorithms to clinical neonatal MRA-TOF images are presented in section 2.4. Also, in this section the proposed technique is further used to model the vessels from contrast-enhance MRA and adults TOF-MRA datasets, which further proves its applicability. Finally, section 2.5 discusses the results and section 2.6 provides some conclusions.

2.2 Cerebral vasculatures extraction

The goal is to recover the 3D structure of blood vessels from MRA-TOF images. Because the fastest blood flow normally exists along the vessel centerline, voxels in this region are brightest. Using this knowledge as a-priori information, a vessel segment in MRA-TOF images can be approximated as a tubular object with highest intensity along its centerline. This high intensity centerline is also called an "intensity ridge".

2.2.1 Intensity ridge

Given a continuous image function $L(\vec{x})$, if the intensity value is considered as the height from zero, ridge points are those points where the image has a local maximum in the direction of the principal curvature of $L(\vec{x})$. Stated otherwise, ridge points are distinguished by the local extrema of principle curvatures. This definition of ridge is a so-called "height ridge". There are several other definitions of ridges in the literature (Haralick, 1983; Griffin and Colchester, 1995), but the height ridge definition is frequently used in image analysis because it is an intuitive property of digital images and relatively straightforward to compute. More details

(a)   (b)
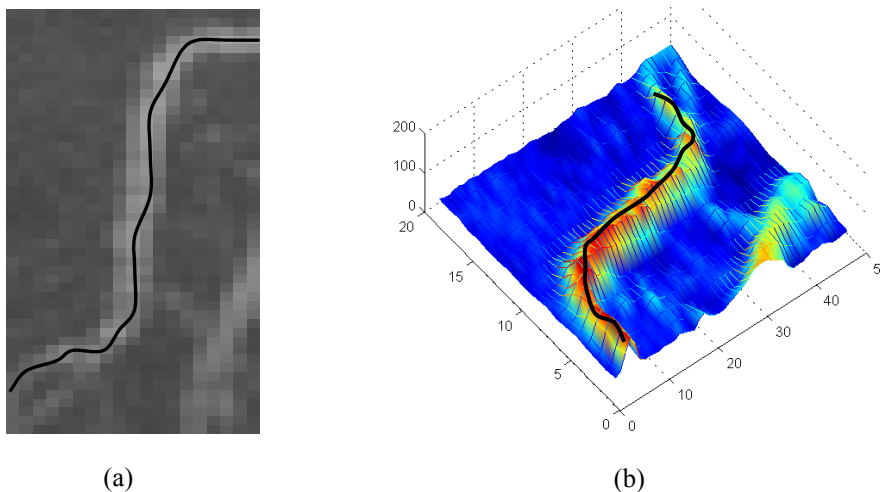
Figure 2.1. An intuitive example of an intensity ridge for a 2D image. The centerline of a single vessel corresponds to the ridge line in the 2D intensity space.

about height ridges and their computation can be found in Eberly (1996). As an example, Figure 2.1 shows an intuitive example of an intensity ridge in a 2D image. The centerline of a single vessel corresponds to the ridge line in the 2D intensity space.

If we assume the continuous image function $L(\vec{x})$, $\vec{x} = (x, y, z)$ and its second order derivatives exist within an image area, the Hessian matrix for the 3D image at any point $\vec{x}$ is defined as:

$$H = \begin{bmatrix} \dfrac{\partial^2 L}{\partial x^2} & \dfrac{\partial^2 L}{\partial x \partial y} & \dfrac{\partial^2 L}{\partial x \partial z} \\ \dfrac{\partial^2 L}{\partial x \partial y} & \dfrac{\partial^2 L}{\partial y^2} & \dfrac{\partial^2 L}{\partial y \partial z} \\ \dfrac{\partial^2 L}{\partial x \partial z} & \dfrac{\partial^2 L}{\partial y \partial z} & \dfrac{\partial^2 L}{\partial z^2} \end{bmatrix} \qquad (2.1)$$

Let $|\lambda_1| > |\lambda_2| > |\lambda_3|$ denote the eigenvalues of the Hessian matrix and $\vec{v}_1$, $\vec{v}_2$ and $\vec{v}_3$ are the corresponding eigenvectors. Because the principal curvature directions are given by $\vec{v}_1$ and $\vec{v}_2$, the zero-crossing points of the image gradient in the principal curvature directions correspond to:

$$\vec{v}_1 \cdot \nabla L = 0 \qquad (2.2)$$

$$v_2 \cdot \nabla L = 0$$

Because ridge points are the points with maximal local intensities (for bright vessels), the corresponding eigenvalues λ_1 and λ_2 should be negative:

$$\lambda_1 < 0 \qquad (2.3)$$

$$\lambda_2 < 0$$

Points that satisfy (2.2) and (2.3) are defined as ridge points in the 3D intensity space (Eberly, 1996).

2.2.2 Interactive vessel detection by ridge traversal

Ridge transversal as a method for extracting vessel centre lines has been originally presented in Aylward et al. (1996, 2002). The method starts from a user-supplied seed point near the vessel centre and a scale factor σ. The scale factor σ is crucial for effective vessel extraction. The scale factor defines the width of a Gaussian kernel used to blur the image to suppress noise. The blurring of the image before the ridge detection also overcomes the problem of MR signal loss. For the TOF-MRA imaging sequence, fast blood flow in some big vessels (e.g. carotid arteries) may cause MR signal loss due to intra-voxel dephasing (Haacke et al., 1999). In this case voxels near the centerline will appear dark in the image while after the Gaussian blurring, the correct intensity profile can be recovered (Figure 2.2). The Gaussian blurring here acts as a enhancement filter and creates the maximal responses at the vessel centerline. After the image is blurred, we use the cubic B-spline as the interpolator to compute subvoxel intensity values and the Hessian matrix $\boldsymbol{H}$.

(a) Before blurring

(b) After blurring
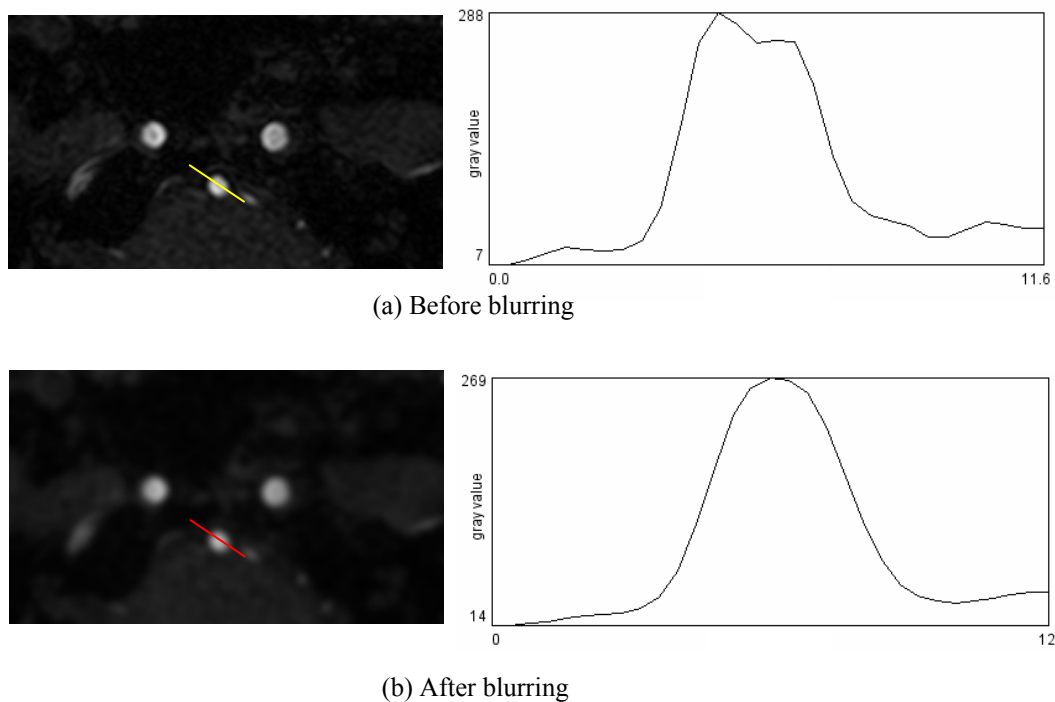
Figure 2.2. (a) Due to signal loss in the carotid artery caused by fast blood flow, the intensity profile does not reach a peak at the vessel center. (b) By blurring the image using a Gaussian kernel, the correct intensity profile is recovered, which is very important for accurate vessel extraction.

The user-supplied seed is moved to the centerline by minimizing a ridgeness function J (equation 2.4). A Quasi-Newton minimization method (the Broyden-Fletcher-Goldfarb-Shanno (BFGS) method) was used (Press et al., 1992). By viewing a 3D image as a 3D intensity surface in 4D, J is minimal on the 1D height ridge points of the 3D surface (Aylward et al., 1996; Aylward and Bullitt, 2002), as shown in Figure 2.3:

$$J(\vec{x}) = (\vec{v}_1 \cdot \nabla L)^2 + (\vec{v}_2 \cdot \nabla L)^2 \approx 0 \qquad\qquad (2.4)$$
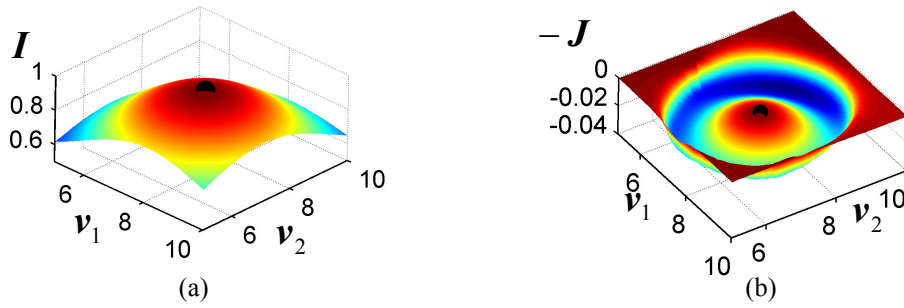
Figure 2.3. (a) The intensity profile of a vascular cross-section is shown. (b) The valley point of ridgeness function, J corresponds to the vessel center point. They are marked as black dots.

For an ideal bright tubular structure in a 3D image, the eigenvalues satisfy $\lambda_1 \leq \lambda_2 < 0 \approx \lambda_3$. The eigenvector $\vec{v}_3$ can be used to approximate the tangent direction and to define the local vessel orientation. Thus, the next ridge point $\vec{x}_i$ is found by stepping in the direction $\vec{v}_3$ with a small traversal step size t from the previous ridge point $\vec{x}_{i-1}$ (Figure 2.4). Then, if $J(\vec{x}_i) > Tol$, the Quasi-Newton optimization is reapplied to move $\vec{x}_i$ to the ridge.
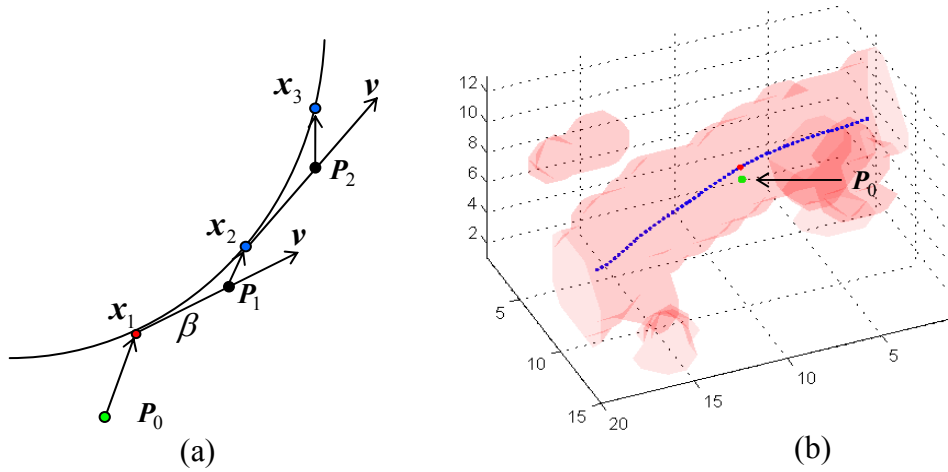
Figure 2.4. Diagram of ridge traversal. (a) The seed p_0 (green dot) is moved to the first ridge point x_1 by the minimization process. By stepping in the direction of local tubular v with a small step size β and minimizing the cost function again, next ridge point x_2 can be found. By repeating this process, a whole vessel can be extracted, as shown in (b).

2.2.3 Seed generation

Due to image noise and limited image resolution, more than one seed is normally required to extract an entire vessel branch. The number of seeds required depends on the image quality and the vessel size. If the SNR in the images is low or vascular abnormalities are included, hundreds of seeds may be required to extract the whole vasculature. The extraction process using manual seed identification will quickly become tedious. Also, the extraction results may be influenced by the variability in manual seed placement which limits reliability and reproducibility. Thus, we have developed a strategy to automatically localize seeds to extract whole vessel trees. This minimizes user interaction and reduces the work load for clinicians.

The key requirement for the seed points is that they must be located within the vessel lumen so that the minimization of the ridgeness localizes the vessel centre. Thus, we need to generate a set of 3D points belonging to vessels. For this we use a

(a)   (b)
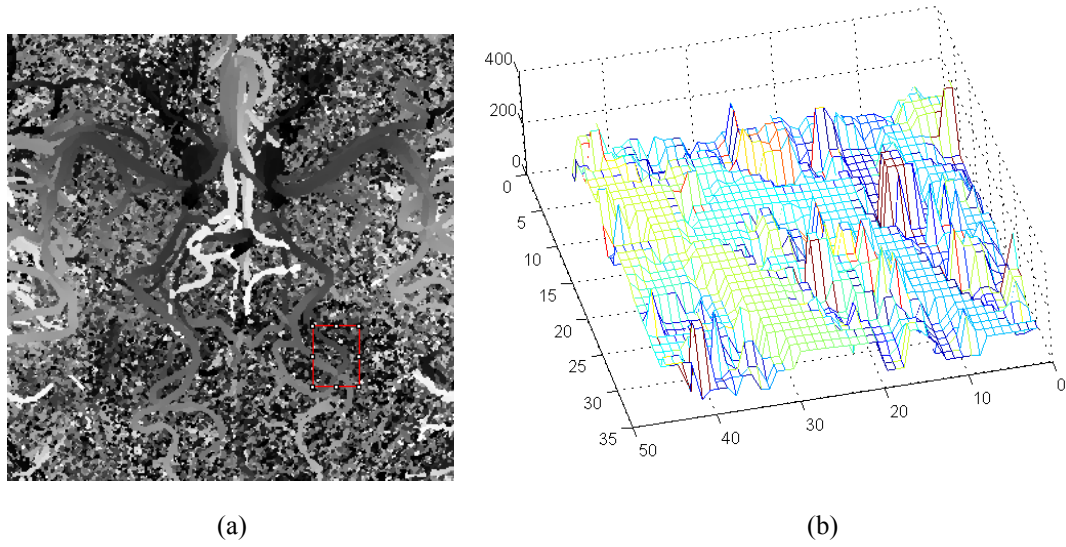
Figure 2.5. (a) A Z-buffer image records the depth for every pixel in a MIP. Vessels appear as
regions of very slow variation in the Z-buffer while the background exhibits rapid and large
variation. This fact is indicated in (b) by focusing on the data within the red box.

method based on the Z-buffer Segmentation (ZBS) algorithm (Parker et al., 2007).
The Z-buffer records the depth in the 3D image for every pixel in the MIP of that
image. The Z-buffer is a computerized data visualization method and is generated
by projecting the 3D dataset into a visualization plane where the projection value
for every voxel is taken as the maximum intensity value along the ray traced from
the viewpoint to the plane of projection). As shown in Figure 2.5, vessels appear as
regions of very slow variation in the Z-buffer while the background exhibits rapid
and large variation. This characteristic is used to differentiate vessels from
background by defining a roughness χ to quantify the local Z-buffer variation rate
for each point in the MIP. The roughness is defined as follows:

$$\chi(i) = \min_{j}\left(\sum_{k}\left(z_{ijk} - p_{ijk}\right)^{2} \right) \qquad (2.5)$$

where z_{ijk} is the depth value at the kth pixel in the jth direction from the ith point in
the Z-buffer. p_{ijk} is the predicted value of z_{ijk} obtained by linear regression on
depth values along the jth direction from the ith point. A total of four directions
($j = 1\cdots4$ for horizontal, vertical and two diagonal) are used. Because vessels
appear as oriented lines, p_{ijk} along one direction should approximate z_{ijk} well and

the corresponding roughness is small, while for non-vessel pixels all four approximations result in large residuals due to the inconsistency of the Z-buffer. All pixels with χ smaller than a preset threshold κ (empirically set to be 1.5 in all experiments) are selected and serve as 3D seeds for vessel extraction.

To detect all possible vessels, MIPs in three orthogonal directions are used. This has proved to be very robust in our experiments, producing seeds covering all main vessels. However, thousands of seeds are normally produced, so we decimate these randomly, and use only 5%-10%, which is sufficient to extract the whole vasculature. As it is possible to obtain multiple seed points for a vessel segment, those seeds flowing into ridge points that have already been detected were ignored.

2.2.4 Optimal scale selection

Given the importance of proper scale factors discussed above, to complete the seed generation process, each seed should be given a correct scale factor which approximates the local vessel diameter. In the context of vessel enhancement, many authors proposed local vessel size estimators based on the linear scale space theory and scale selection (Lorenz et al., 1997; Manniesing and Niessen, 2005). The multi-scale characteristic and linear scale selection originally proposed by Lindeberg (Lindeberg, 1998) ensures that different vessel diameters are treated equally, without favoring certain vessel diameters.

We have used Frangi's multi-scale vessel enhancement filter (Frangi et al., 1998) as an estimator of the vessel diameters although other filters (Chapman and Parker, 2005) may also work in this case. Frangi's vessel enhancement filter assumes tubular vessels in 3D. Using the Hessian matrix of image intensity and following the same notation as before, we have $|\lambda_1| > |\lambda_2| > |\lambda_3|$ and corresponding eigen-vectors are $\vec{v}_1$, $\vec{v}_2$ and $\vec{v}_3$. As vessels are bright tubular structures in a dark background, the local vessel direction is given by $\vec{v}_3$ and vessel voxels satisfy

$|\lambda_3| \approx 0$ and $|\lambda_3| << |\lambda_1| \approx |\lambda_2|$. The pattern of eigenvalues is used to differentiate vessel structures from the background.

The formulation of Frangi's vessel filter at the scale σ is as follows:

$$v(\sigma) = \begin{cases} 0 & \text{if } \lambda_1 > 0 \text{ or} \\ \left(1 - \exp\left(-\dfrac{A^2}{2\alpha^2}\right)\right) \exp\left(-\dfrac{B^2}{2\beta^2}\right)\left(1 - \exp\left(-\dfrac{S^2}{2\gamma^2}\right)\right) \end{cases}$$

(2.6)

where

$$A = \frac{|\lambda_2|}{|\lambda_1|}$$

$$B = \frac{|\lambda_3|}{\sqrt{|\lambda_2 \lambda_1|}}$$

$$S = \sqrt{\lambda_1^2 + \lambda_2^2 + \lambda_3^2}$$

A differentiates between plate and line like structures while B accounts for blobs like structures. S is defined as the second order structureness which separates vessels from background noise.

The filter response is computed at different scales. The maximal response will be obtained when the scale δ approximates the vessel size:

$$\delta_{optimal} = \max_{\sigma \in [\sigma_{min}, \sigma_{max}]} (v(\sigma))$$

(2.7)

The optimal scale is computed for all 3D seeds.

Seeds can be further refined by performing the ridgeness minimization process: Those seed points for which no ridge point can be found are abandoned for vessel extraction. This both decreases segmentation noise and increases efficiency of vessel segmentation.

2.2.5 Vessel tree composition
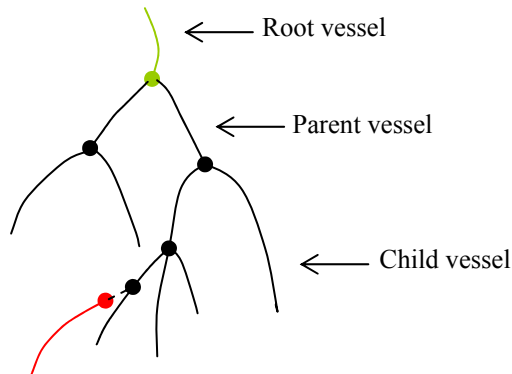
Figure 2.6. An unattached vessel must be allocated and attached to a proper parent vessel during the tree construction process.

The ridge detection method generates a set of disconnected vessel segments from which we can compose connected vessel trees using a modified minimum spanning tree algorithm (Bullitt et al., 2001). This method requires the user to define one segment as a root node and then the algorithm automatically calculates the spatial distance between all unattached vessel segments and the current tree. The vessel segment with the minimal distance is attached to its parent to extend the vessel tree and the process is repeated to build a complete tree with defined parent-child relationships for all connected vessel segments. This process is illustrated in Figure 2.6. When adding a new branch, the parent-child pair can have one of four possible configurations (Figure 2.7).   Note the "X" connection (Figure 2.7(d)) is not permitted as it is inconsistent with the directed flow characteristics of human cerebral vasculature. The tree composition process continues until there are no unconnected segments left or the minimal spatial distance is too much larger than a threshold (normally 3~5 times of a voxel size). Due to the image noise and imperfections in vessel extraction, the errors can be found in the obtained tree structures. At this moment, we still rely on human operator to check all results and interactively correct all mistakes. As the final step of this tree composition, every branch from the root to the leaf node is allocated a unique ID.
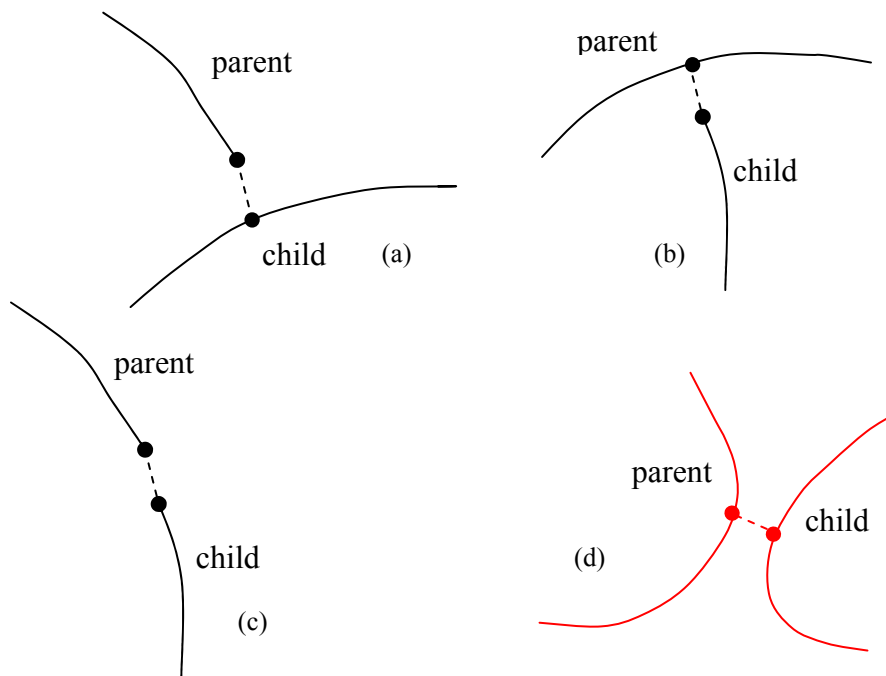
Figure 2.7. Four possible configurations of parent-child pairs when adding a new branch into the vessel tree. Note the "**X**" connection (d) is not permitted as it is impossible for human cerebral vasculature.

2.3   Vasculature matching

The output of the previous step is a cerebral vasculature tree, in which each branch is automatically assigned a label by which it can be identified. These annotated trees may in themselves be useful for characterizing vascular architecture in individuals at a given time point. However, to compare across time some form of vessel matching is helpful. The vessel matching algorithm proposed in this section finds branch-by-branch correspondences for follow-up studies of the same infant.

We exploit average spatial distance between two vessel branches as a measure for determining branch-by-branch correspondences. This is based on the observation that if two vessel trees are geometrically registered, corresponding branches are spatially close while uncorresponding branches often sprawl out at different

orientations. Therefore, two vessel trees can be matched by first placing them in an appropriate geometrical correspondence and then computing a cost function measuring the average spatial distance between pairs of vessel branches. The matching process starts from the roots of the two trees and finally stops when leaf branches are reached. It is clearly possible that, due to imperfect vessel extraction or changes in vasculature as a result of brain development, two or more branches in one tree need to be merged to match a branch in another tree due to the new-born vessels. Also, some vessel segments may not have a corresponding match. The output of this process records all pairs of corresponding branches and can include cases where segments are merged. Figure 2.8 givens an example of vasculature tree matching. These two middle cerebral artery trees are reconstructed from two TOF-MRA images consecutively acquired for the same infant.

| Tree A | 0 | 1 | 2 | 8 | 3 | 4 | 6 | 5 | 20 | 19 | … |
| Tree B | 0 | 2 | 1 | 10 | 4 | 3 | 5 | 6 | 7 | 8 | … |
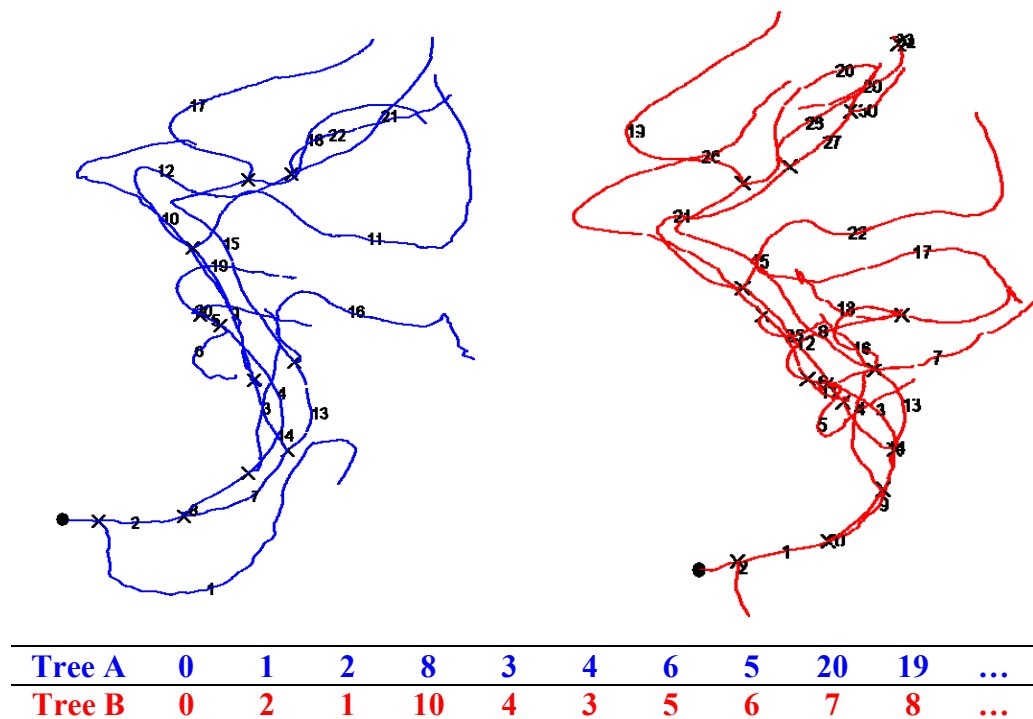
Figure 2.8. An example of vasculature tree matching. The vessel tree matching, unlike registration, aims to recover the semantic correspondences between two vasculatures. The branch-to-branch correspondence can be represented by a matching form.

2.3.1 Vasculature registration

In contrast to intensity-based registration of anatomical images, precise vasculature registration includes extra challenges resulting from low visibility of small vessels and non-overlap of sparse vascular structures. In fact precise registration may not be always possible due to changes in the vasculature over time. We therefore seek only to remove any global affine differences between the two vessel trees in order to bring them into approximate alignment. Provided robust alignment could be achieved, this approach was found to be sufficient to initialize vessel tree matching.

We tested four different registration strategies. (a) Direct MRA-MRA image registration performed by maximizing the mutual information between source image pairs. (b) Extracted vessel trees registered using the iterative closest point (ICP) algorithm (Besl and Mckay, 1992) which is a popular method to register 3D point sets. (c) An improved ICP algorithm with ε -reciprocal correspondence applied to provide robustness for outliers (Pajdla and Gool, 1995). The details of ε -reciprocal correspondence are given in the next section. (d) An indirect registration strategy that combined anatomical information from T2 images routinely acquired in addition to the MRA data. Each MRA image is first registered to its T2 image by a rigid transformation T_r. The two T2 images are then aligned by a multi-level extension of a free-form non-rigid registration algorithm (Rueckert et al., 1999) which deforms an object by manipulating an underlying mesh of control points and using cubic B-spline to interpolate intermediate locations.

2.3.2 Cerebral vasculature matching

The inputs to the vessel matching are two approximately registered vessel trees where each branch is labeled by a unique ID. The aim of vessel matching is to recover branch correspondence between two trees. The method starts from root nodes which are assumed to be matched by definition. In each iteration, subtrees of the current node are extracted. The subtree depth is determined by the maximal

possible length of matched paths, as multiple branches in one tree may correspond to one branch in the other tree. Note that due to possible neonatal vascular development and extraction imperfections, two or three branches in tree A may need to be merged and matched to one branch in tree B. Thus, a search depth P is defined as the extracted subtree depth. Once two subtrees are extracted from the current node, a spatial distance function S is computed for all possible matching pairs which should include all one-to-one matches and merged matches. Those matching pairs with minimal cost values are selected as correct matches. Once the correct match at the current level is obtained, the roots of subtrees for the next level are set to be leaf branches of current matching pairs. This process runs iteratively from root to leaf and stops when extracted subtrees only include leaf branches.

The spatial distance function S is defined as follows for two vessel segments $\Gamma_1(t_1)$ and $\Gamma_2(t_2)$:

$$S(t_1) = \frac{1}{L_1} \int_0^{L_1} \|\Gamma_1(t_1) - \Gamma_2(t_2)\|^2 dt_1$$

$$t_2 = nearest\_Point\_in\_\Gamma_2\_for\_t_1$$

$$S(t_2) = \frac{1}{L_2} \int_0^{L_2} \|\Gamma_2(t_2) - \Gamma_1(t_1)\|^2 dt_2$$

$$t_1 = nearest\_Point\_in\_\Gamma_1\_for\_t_2$$

$$S(t_1, t_2) = S(t_2, t_1) = \frac{1}{2}(S(t_1) + S(t_2)) \qquad (2.8)$$

where t_1 and t_2 are the arc length parameterization of the two vessels and S is the averaged 3D spatial distance between two segments. L_1 and L_2 denote vessel lengths in mm.

Any residual misalignment between corresponding branches can be further reduced if subtrees extracted during the matching process are further registered. Our experiments show that the residual mismatches decreased when this piece-wise subtree registration is integrated into the matching process.

(a)   (b)   (c)

(d)   Iterations
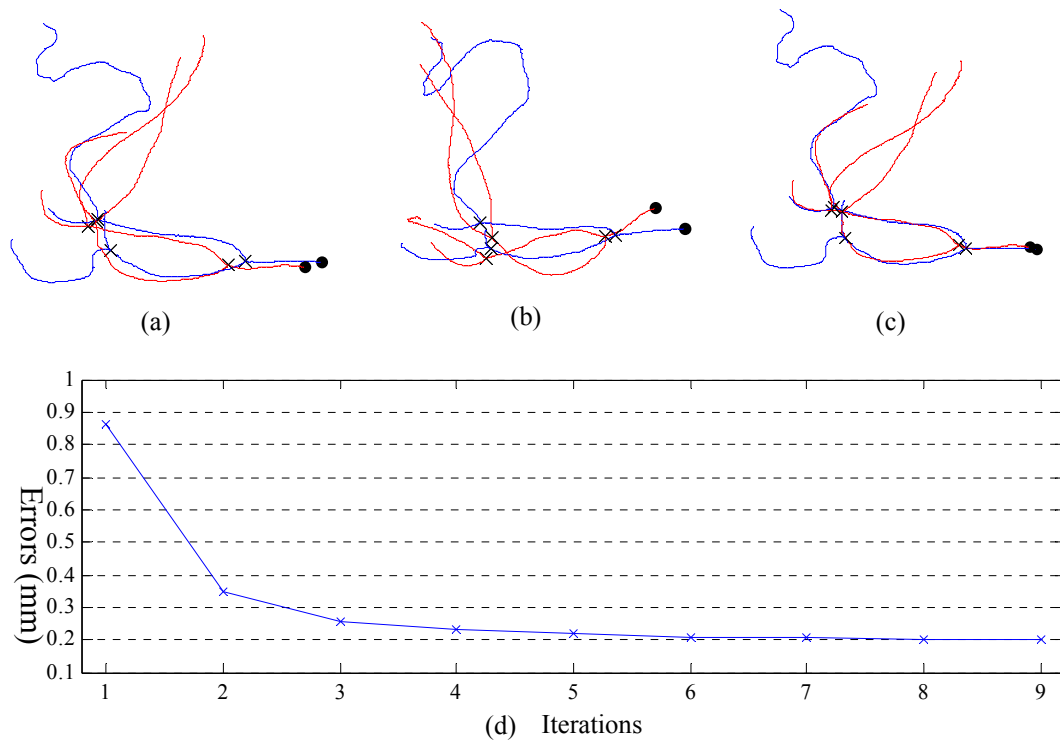
Figure 2.9. An example of subtree registration: (a) Two subtrees are extracted and rendered in their original position found from global registration; (b) The ICP algorithm converges to an incorrect result when the partial trees are matched; (c) By eliminating the mismatched point pairs, the two subtrees are successfully registered; (d) The consistently decreasing cost of improved ICP algorithm is plotted.

The ICP algorithm can be used to register subtrees. However, this method tends to converge to an incorrect result if mismatched point pairs dominate the closest point selection, which frequently occurred in our experiments. The reasons for this are: a) subtrees often include unmatched branches or newly formed segments which do not have correspondences in the other vessel tree, e.g. Figure 2.9(a); b) vessel trees are very sparse, which degrades the convexity of cost function and induces difficulties for local optimization methods such as the ICP algorithm; c) Subtree registration is more vulnerable to mismatched points than whole vasculature registration because there are fewer corresponding point pairs. To improve the registration, we need to identify mismatched point pairs and only count correct ones. As a solution, a robust extension of ICP algorithm (Pajdla and Gool, 1995) was used for registering subtrees. This method exploits the ε-reciprocal

correspondence: given a point $\vec{p} \in P$ and the closest point $\vec{m} \in M$, $\vec{m}$ is back-projected onto P by finding the closest point $\vec{p_0} \in P$. If $\|\vec{p} - \vec{p}_0\| > \varepsilon$, the pair $(\vec{p}, \vec{m})$ is rejected. Because mismatched point pairs are gradually eliminated from the cost function, the algorithm is more robust. Figure 2.4 gives an example to show the performance of the improved ICP algorithm which is very robust in our experiments.

To further deal with the effects of vasculature development and extraction errors, two matching criteria need to be added:

- Peripheral vessels experience the most significant development and geometrical changes in the neonatal brain, matched leaf branches in two vessel trees may only have partial correspondence. Accordingly, only overlapped parts in two leaf branches are used to compute the spatial distance cost.

- Inconsistencies (e.g. when two branches in one tree are matched to the same segment in another tree) may be detected from the matching results. Whenever this happens, there are matching errors in the previous level. In this case, the previously selected optimal solutions are replaced by the next best solutions. This feedback mechanism corrects mismatching and improves robustness.

2.4 Results and evaluation

We have applied the presented algorithms to extraction and matching of the cerebral vasculature using the MRA-TOF images. The accuracy and reliability of these algorithms were assessed and the matching results compared to the ground-truth determined by manual matching all vascular trees.

All images were acquired on a 3T MR imaging system (Philips Intera) using a 6 element sensitivity encoding (SENSE) array head coil. Imaging parameters were optimized for neonatal cerebral vasculature for better contrast and visibility of peripheral vessels (Malamateniou et al., 2005; Malamateniou et al., 2006): TR 18ms, TE 3.5ms, flip angle 16 degrees, slice thickness 0.61 mm, FOV 160 mm and 100 slices with scan matrix 288×288. All TOF images were interpolated to isotropic voxels (0.4mm^3) using cubic spline interpolation and a centre region including vessels was selected for analysis.

The proposed technique was implemented and tested on 51 subjects (18 preterm and 33 term-born neonates, mean gestational age at birth 36.2 ± 5.4 weeks). As an example, an image is shown in Figure 2.10. All scans were performed with the same imaging parameters. All infants were sedated or imaged during natural sleep.

(a)   (b)
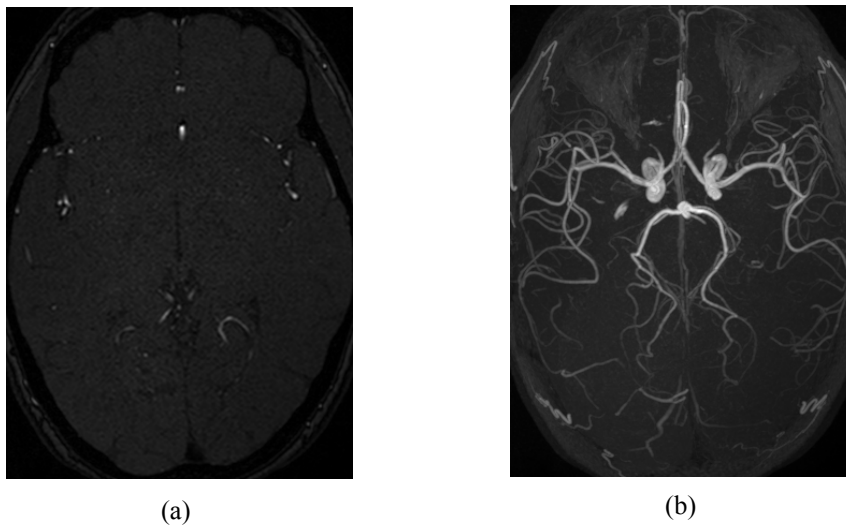
Figure 2.10. MRA-TOF images: (a) a slice from the 3D image volume and (b) transversal MIP of this TOF image.

2.4.1   Seed generation and vasculature extraction

Because effective seed generation is essential for exhaustive vascular segmentation, we evaluated the performance of the proposed seed generation method on MRA-

TOF images with different noise levels. Noise was added to a selected MRA image which presents the typical and reasonable image quality. Specifically, four variants of images were generated by adding Gaussian noise with standard deviation δ of 10, 20, 30 and 40 to data with a mean vessel intensity 145.0 ± 70.8 and mean signal from suppressed background 58.7 ± 7.2. Although the original image has good quality, the visibility of small vessels clearly decreases with the degradation of image quality. The $\delta = 20$ data represents a case of low-quality image while $\delta = 40$ data challenges the method, as the corresponding contrast-to-noise ratio (CNR) drops by about 6 fold to 2.2 (the CNR is computed as $(average\_vessel\_intensity - backgroud\_intensity)/noise\_level$).

Figure 2.11 shows the MIP of the original image and its 3D rendering with seeds (blue dots). Only seeds within the cerebral artery trees are shown. Seeds detected from peripheral arteries and veins which are not connected to the main cerebral vasculature network have been discarded. All five test images were processed with the same parameters (although relaxing some thresholds for low SNR images may improve results). The seeds are shown on the MIPs for all images in Figure 2.12. Due to the large number of seeds detected, only 20% randomly selected have been rendered. A multi-scale selection process was used to compute the optimal scales for the seeds generated from the images. The results are shown in Figure 2.13 and the corresponding extracted vessels are shown in Figure 2.14 as the transverse MIPs.

(a)   (b)
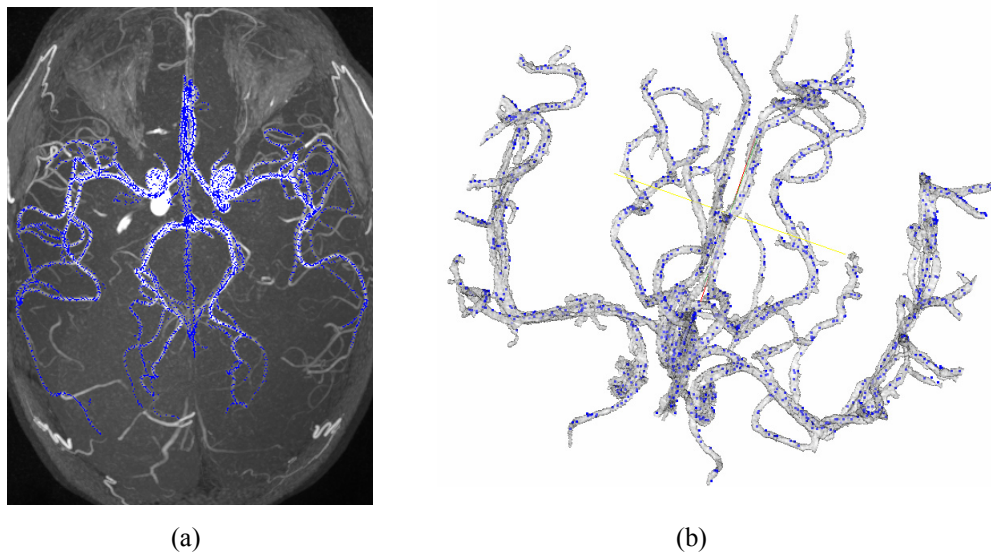
Figure 2.11. (a) MIP of original MRA-TOF image with seeds overlapped. (b) Its 3D rendering showing the cerebral vasculature. The generated seeds spread over the whole cerebral vascular trees which is important for robust extraction.

There are four remarks that can be found from these results. First, the seed generation method is able to produce seeds spreading over the cerebral vasculature for a wide range of vessel radii and in the presence of variable levels of noise. Second, the optimal scale computed for each seed by maximizing the multi-scale response function gives plausible indication of the vessel sizes, with generally decreasing values from proximal to distal branches (colour coding progressing from red to blue in Figure 2.13), proportional to the vessel scale. Although the optimal scale itself can not be treated as a precise estimate of the vessel radius, the extraction results in Figure 2.14 show that it is sufficient for the ridge detection. Third, after random selection there are enough seeds for whole vasculature extraction. In the example in Figure 2.13, 6000 seeds were randomly chosen from about 30,000 seeds originally generated and 4459 are finally used for vessel extraction, as those seed points from which no ridge point can be found are abandoned. Fourth, extraction results are found to be correct, with visible vessels extracted to form quite complete vascular trees. We quantify completeness as the ratio of the length of vessel trees segmented automatically and manually at each noise level. The mean is $93.2\% \pm 2.1\%$ for all five extractions (the original image and four noisy ones).

To test the precision and consistency of vessel extraction, the longest branch in the left middle cerebral artery tree (LMCA) is extracted from the four noisy images (Figure 2.14(a-d)) and the original image (Figure 2.14(e)). The precision may be quantified by the averaged spatial distance, C, between the branch extracted from a noisy image and from the original image:

$$C = \frac{1}{N} \sum_{i=1}^{N} |\boldsymbol{p}_i - nearest\_point(\boldsymbol{p}_i, Tree')| \qquad (2.9)$$

Here $\boldsymbol{p}_i \in Tree$ is a vessel point in one extracted vessel tree. $nearest\_point(\boldsymbol{p}_i, Tree')$ is the nearest vessel point of $\boldsymbol{p}_i$ in another tree. If two extractions for the same branch are highly consistent, the distance measure C should be close to zero. For these experiments the average distance between all extractions from noisy images and the original image are 0.25 ± 0.11mm. Given the reconstructed voxel size of this image is 0.4mm^3, this result shows that subvoxel precision can be achieved.

Based on the extracted vessel segments, a vessel tree can be defined. Four main cerebral artery trees are generated. During the automated vessel tree composition a distance threshold of 1mm was used. Occasionally, the tree composition can cause parent-child connection errors if two vessels are very close to each other. They are manually identified and corrected. The final patient-specific 3D vessel tree is shown in Figure 2.14(f) where the four main cerebral artery trees (anterior/posterior, left-middle/right-middle arteries) are differently colored.

The explicit parent-child relationship can be recovered from the extracted vasculatures. The vessel tree composition method proposed in section 2.2.5 is applied to both left and right middle cerebral arteries of the vessel tree shown in Figure 2.14(f). The tree structures recovered are illustrated in Figure 2.15, where every vessel branch is detected with a unique ID number allocated. Therefore, for every branch node in the tree, its parent and children can be directly assessed.

We applied the propose technique to all neonatal TOF-MRA datasets. For all datasets three orthogonal MIPs were displayed with the extracted vessels overlaid on the MIP rendering. In general extracted vessel centerlines are accurately centered on the vessels and the segmentations obtained were complete and the vessel tips were extracted. Figure 2.16 shows the vasculature extraction results for developing neonates with different gestational ages. The process for each subject takes approximately 15min on a PC with one Pentium 4-3.0GHz processor and 1GB memory.

(a) $\delta = 10$ (b) $\delta = 20$

(c) $\delta = 30$ (d) $\delta = 40$
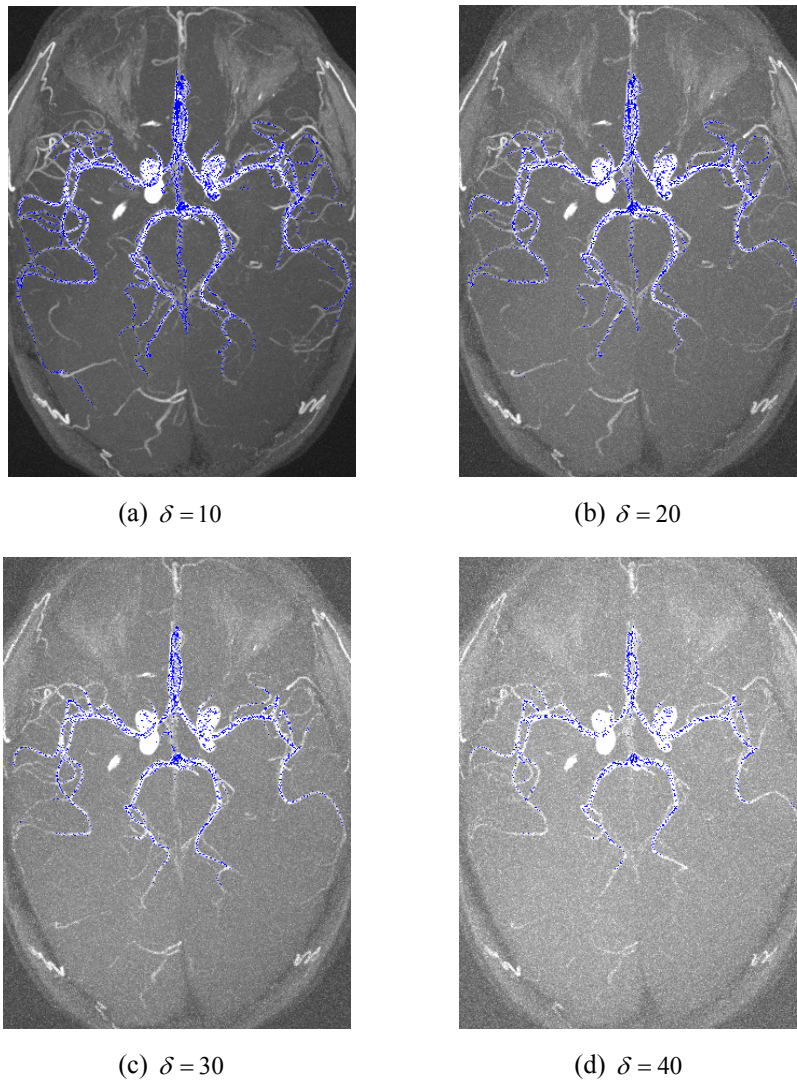
Figure 2.12. Seeds are overlapped on the MIPs for $\delta = 10$, 20, 30 and 40. More noise degrades the visibility of distal vessels, which causes the detectable seeds also to decrease. However, the algorithm allocated seed to the visible cerebral vasculature for all values of δ tested.
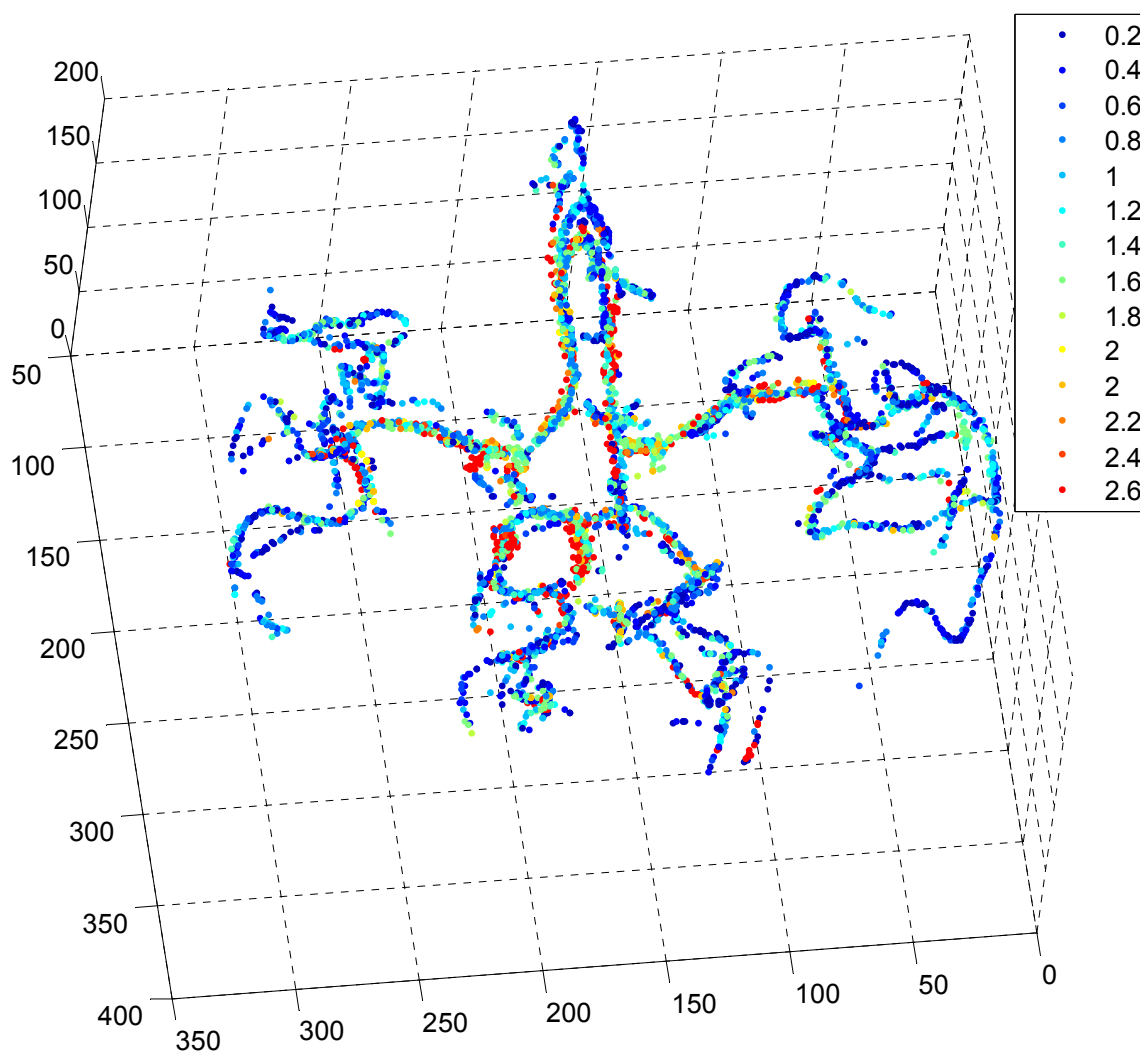
Figure 2.13. Results of multi-scale seed selection. By maximizing a vesselness function, each seed is
allocated an optimal scale (mm). In this example seeds are colour coded by detected vessel size from
0.2mm to 2.6mm which covers the possible radius range of neonatal cerebral vessels. Although the
minimal detectable radii of vessels are limited by the imaging system, the results show computed scales
for distal vessels are small (colored in blue) while the carotid artery has larger scale (colored in red).

(a) $\delta = 10$ (b) $\delta = 20$ (c) $\delta = 30$

(d) $\delta = 40$ (e) original image   (f) four artery trees
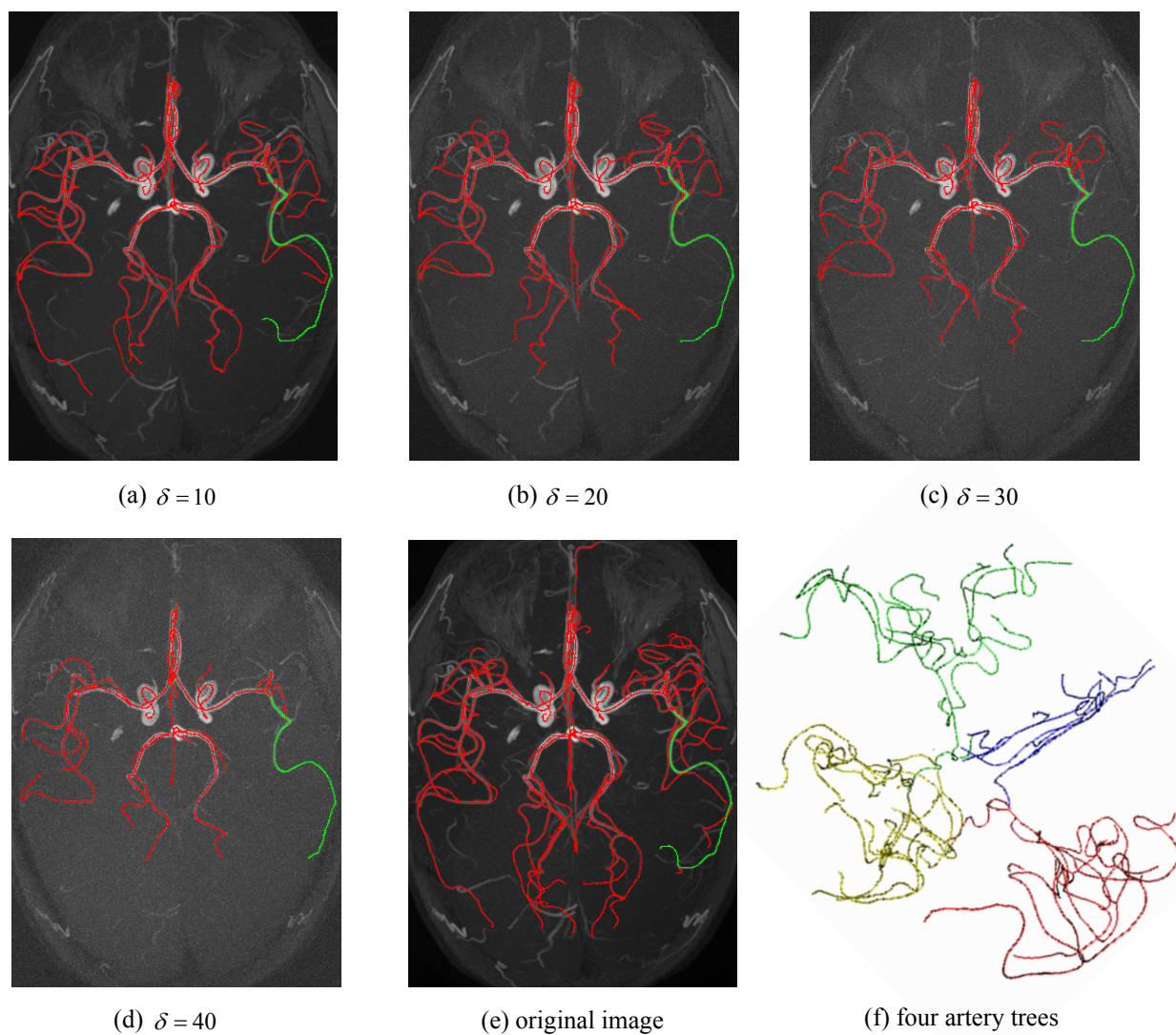
Figure 2.14. (a-e) Vessel extraction with different noise levels. In all cases, the algorithm robustly extracted most visible cerebral vessel branches. (f) Four artery trees are composed from extracted vessel segments. These trees define a patient-specific model of cerebral vasculature.
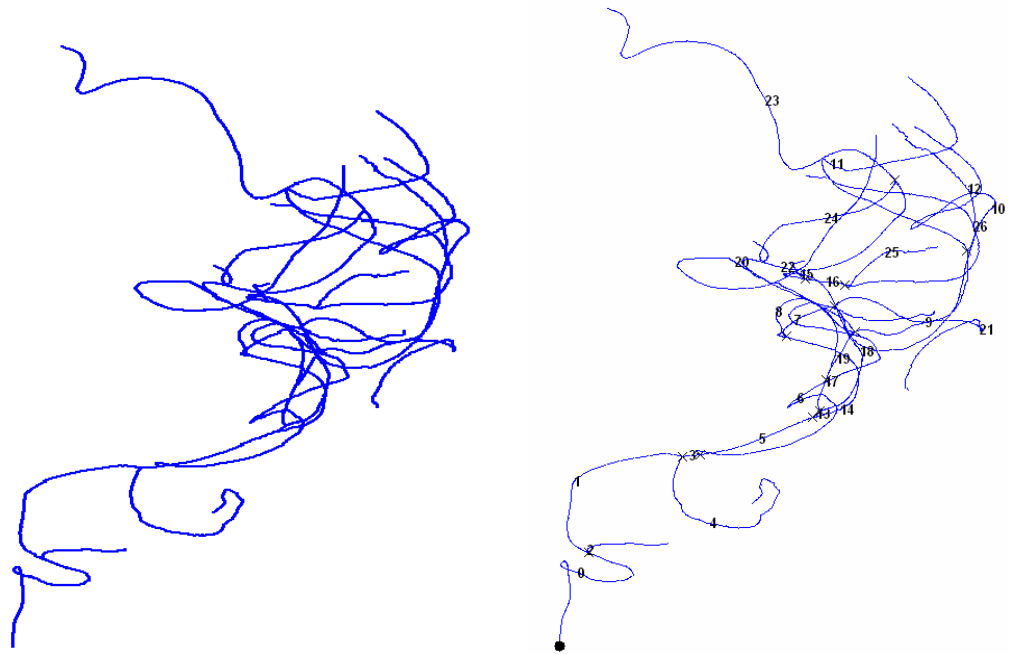
(a) Left MCA
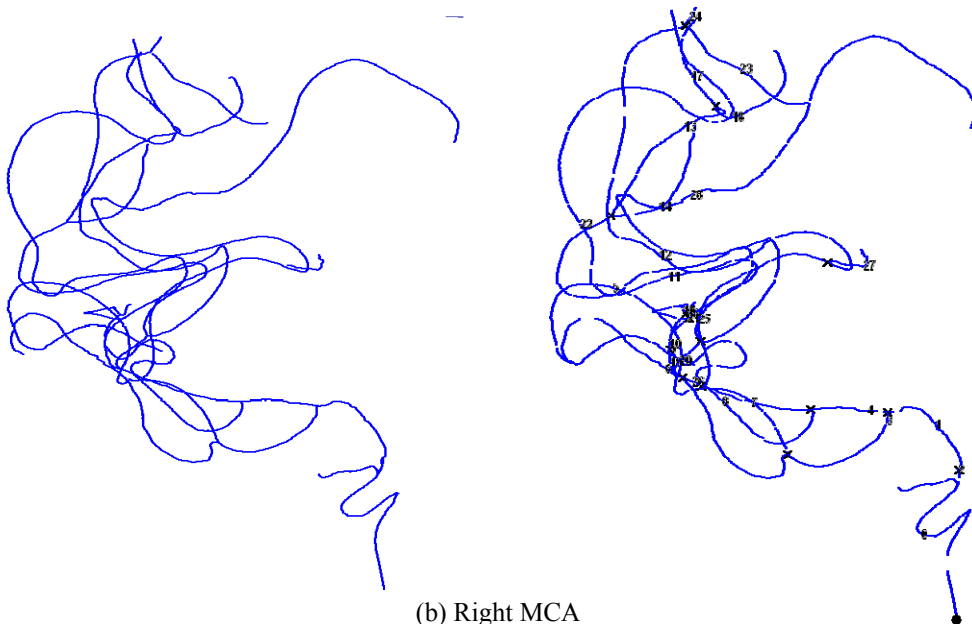
(b) Right MCA
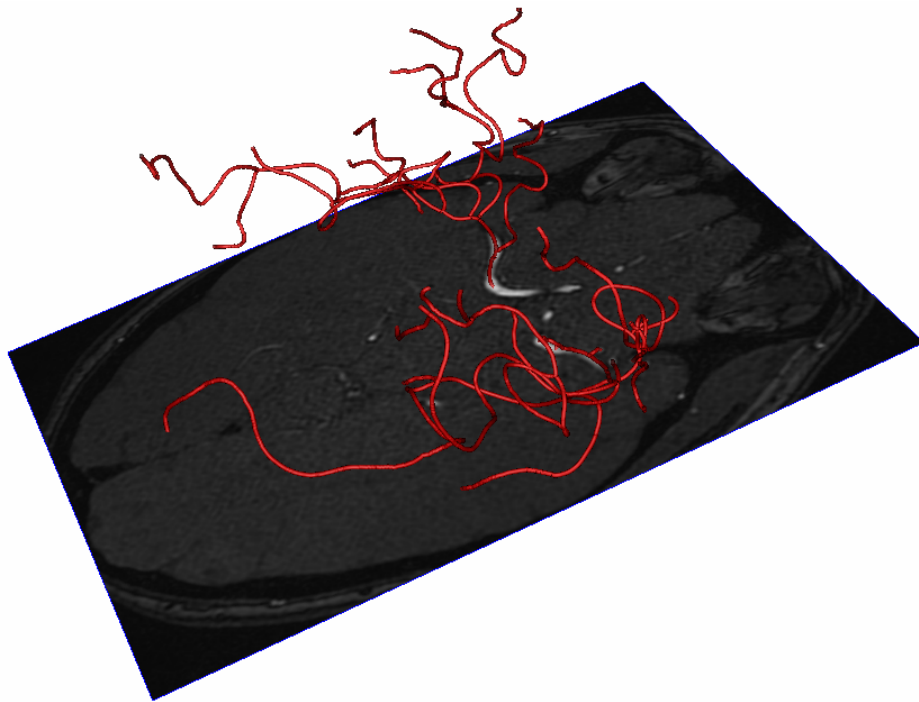
(c) 3D rendering of both arterial trees

Figure 2.15. Vessel tree composition. (a) Left middle cerebral artery tree; (b) Right middle cerebral artery tree; (c) A 3D rendering of both vessel trees with the TOF-MRA image.

GA: 29.86 weeks

GA: 34.29 weeks

GA: 39.86 weeks
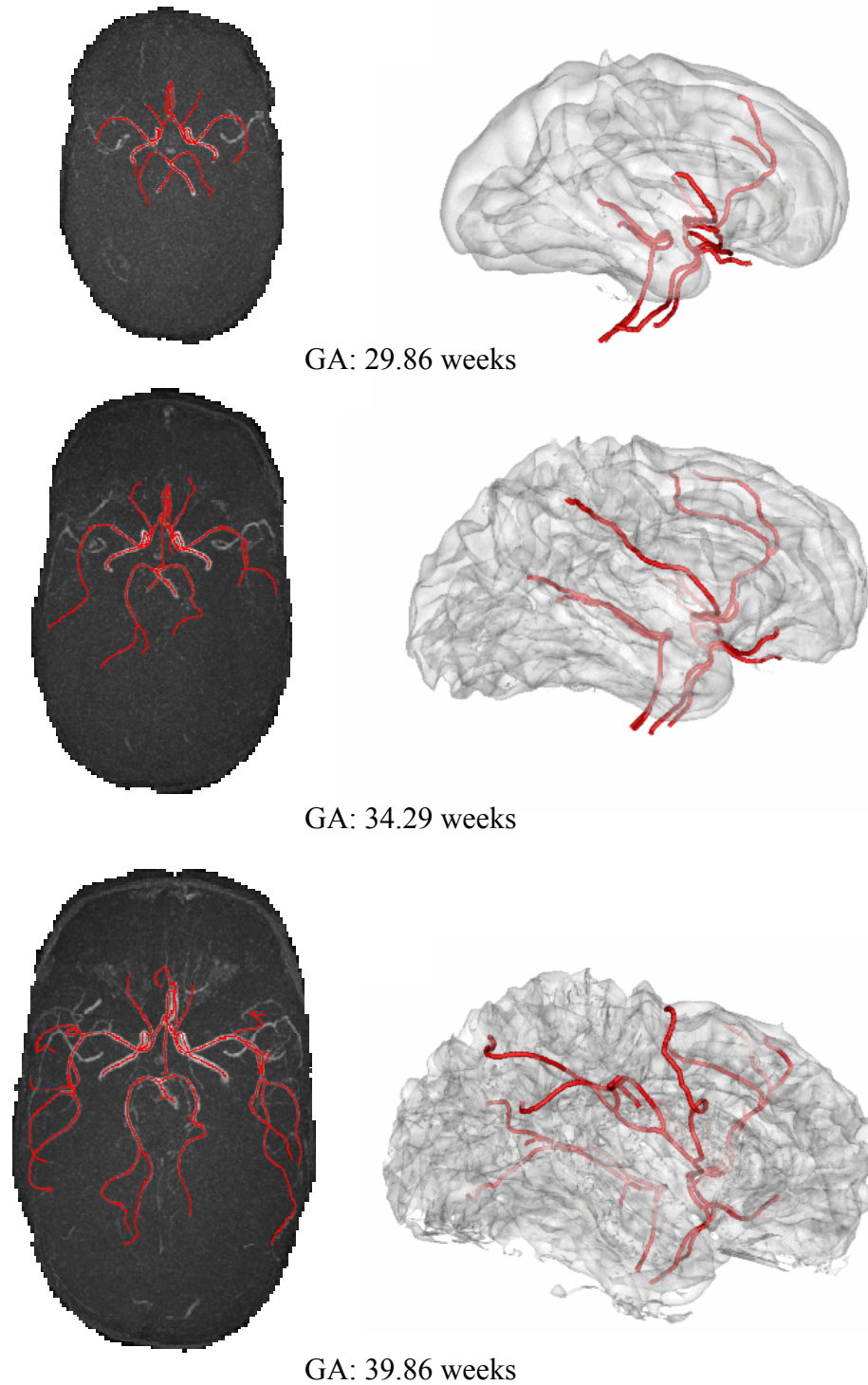
Figure 2.16. Vasculature extraction results for developing neonates with different gestational ages. Note that in the MIP images there are also disconnected vessels that a located caudal to the cerebral arteries– these are not part of the extracted trees

2.4.2   Vessel tortuosity measurement

Based on the generated vessel trees, a quantification of the vessel morphology can be performed. To illustrate the applicability of proposed algorithm we demonstrate how the algorithm can be used to assess middle cerebral artery (MCA) tortuosity.

A previous clinical study of term born and preterm infants imaged at term equivalent age showed that there is decreased tortuosity in the middle cerebral arteries of the preterm infants at term compared to the term born infants (Malamateniou et al., 2006). Here the tortuosity was manually measured using a distance metric (DM) which is defined as the ratio between the length along the vessel path and the distance between the start and end point of the selected vessel segment (Bullitt et al., 2003a; Bullitt et al., 2003b; Bullitt et al., 2004; Bullitt et al., 2005a; Bullitt et al., 2005b). In Malamateniou et al. (2006a), a group of 24 neonates, including 12 term born infants (GA: 40.3 ± 1.0 weeks) and 12 preterm infants (GA: 29.5 ± 2.5 weeks) was studied and 3D MRA-TOF images were acquired for all subjects. The starting point used was the origin of the MCA at the internal carotids and the end point was the first MCA trunk bifurcation point. Although the vessels exist in 3D space all measurements were taken from transversal MIPs. The tortuosity in both the left and right MCAs was found to be significantly decreased for preterm infants (1.17 ± 0.05 and 1.16 ± 0.05) compared to term infants (1.45 ± 0.08 and 1.48 ± 0.16).

With the 3D structure reconstructed for cerebral vasculatures, we can perform a quantitative test in real 3D space. To compare with the previous study we computed the DM for a group of 5 preterm infants (GA: 29.4 ± 2.8) and 5 term ones (GA: 39.8 ± 1.5) for the MCA segments between the same landmarks, as shown in Figure 2.17. The left and right MCA for preterm infants have mean tortuosity of 1.06 ± 0.06 and 1.03 ± 0.03, respectively; for term born, these values are 1.36 ± 0.23 and 1.29 ± 0.14. The mean differences of DM values between term

and preterm infants for left and right MCA are 0.28 (95% CI: 0.07 − 0.69) and 0.18 (95% CI: 0.08 − 0.69) respectively. In a summary, the computerized vessel tortuosity measurement is shown to agree with the previous clinical study, which demonstrates the applicability of the proposed vessel extraction method and its potential for clinical applications.
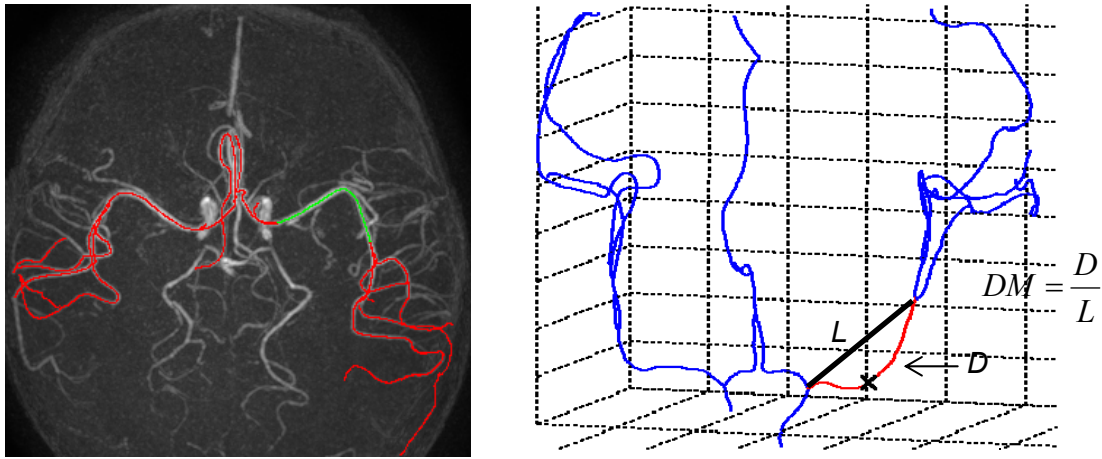
Figure 2.17.   An illustration of MCA tortuosity measurement. The distance metric (DM) is defined as the sum of distances between adjacent 3D points along the actual vessel path divided by the length of the straight path between the first and last 3D points – since the vessel centreline has been parameterised in 3D this whole process is fully automatic.

2.4.3   Vessel matching

We applied the proposed vessel matching algorithm to a group of 4 preterm neonates that were each scanned twice at different ages (first scan: ages 6-50 days, mean 22.8 days; second scan: ages 41-90 days, mean 70.3 days). The left and right middle cerebral artery trees were extracted for all subjects and used for vessel matching. Successful vessel extraction was carried out for all 4 subjects and 8 pairs of artery trees were correctly composed. The parent-child connection errors (total 6 locations for the eight trees) in the generated vessel trees were manually corrected.

All vessel trees were first registered using each of the four approaches previously described (direct registration of source TOF-MRA data, indirect registration using

T2 weighted images and two variants of registration of the composed vessel trees themselves) to remove global spatial displacements. To evaluate the performance of different registration strategies, corresponding bifurcation points are manually selected for all tree pairs and their mean residual displacements (MRD) after registration used as a statistic for assessing registration. MRD is defined as:

$$MRD = \frac{1}{N}\sum_{i=1}^{N}\left|\boldsymbol{p}_i - corresponding(\boldsymbol{p}_i)\right| \qquad (2.10)$$

where $\boldsymbol{p}_i$ is a branch bifurcation point in one tree and its corresponding point in another tree is $corresponding(\boldsymbol{p}_i)$.
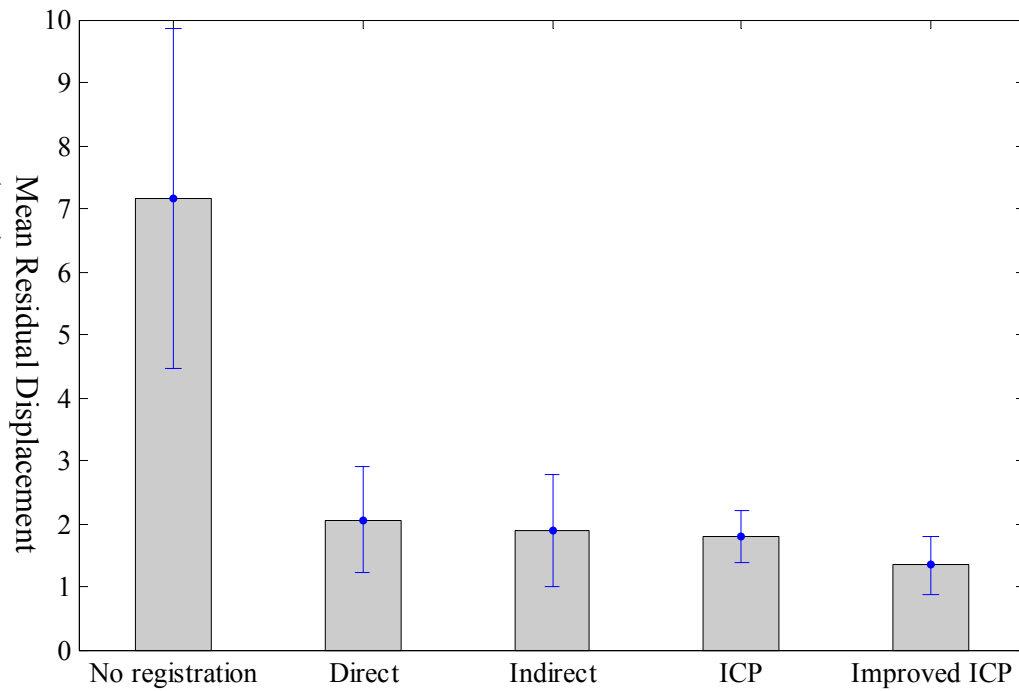
Figure 2.18. Summary of vessel tree registration results. Four registration strategies are used to register 8 pairs of vessel trees and the mean residual displacements are shown here.

Figure 2.18 summarizes the registration results. All four registration methods (section 2.3.1) decreased residual displacements compared to the case where no registration is performed, indicating that the tree pairs were being brought into improved alignment. An illustration of vascular registration is given in Figure 2.19.

Here (a) and (b) shows an example of extracted middle cerebral artery trees overlaid on original MIPs. The performance of vasculature registration is shown in (c) and (d). Three methods (direct, indirect and ICP) gave comparable residual displacements while the improved ICP method gave the lowest value (MRD: 1.34mm). This is expected as the improved ICP method eliminates most mismatched point pairs from the optimization.

Clearly, the positive contribution of the subtree registration is determined by its robustness. If the subtree registration is incorrect, the tree matching will lead to higher errors. The proposed subtree registration method was tested on a total of 68 subtree pairs extracted from the 8 pairs of vasculature trees. After these subtrees were registered, the branch-to-branch correspondence is established by performing the proposed tree matching method. If the matching results agree with the ground-truth which is manually established by the author, the registration is defined to be successful. Table 2.1 reports the numbers of failures with different combinations of global/subtree registration strategies. The improved ICP algorithm clearly increases the success rate of subtree registration. Moreover, despite the performance fluctuation of different global registration strategies, the results of subtree registration are similar for the improved ICP algorithm. In our experiments, the different global vasculature registration techniques had little influence on matching results. This can be explained by the fact that all registration methods are able to roughly align vessel trees and provide sufficiently good initial estimates for the subtree registration to reach an optimal minimum. It is the subtree registration which offsets the fluctuations in initial registration and provides robustness for vessel matching.

The results of vessel matching for all 8 pairs of artery trees are summarized in Table 2.2. The improved ICP algorithm is exploited here for the subtree registration. In this case subtree registration does have a positive effect, reducing the number of incorrectly matched branches. In the case of vessel pair 8, the subtree registration reduced the number of errors from 8 out of 11 to 2 out of 11

branches. A total of 146 vessel segments are matched with correct results in 95.2% of cases. In general the errors that still remained after use of subtree registration occurred at the tip vessels. This may be because the self correcting feedback based on the consistency of the next subtree is not available for leaf branches. The robustness of the results for the main arterial branches suggests that the proposed matching algorithm is capable of establishing reliable branch-by-branch correspondence for neonatal follow-up studies.

2.4.4   Other applications

Although the focus of this chapter is the modeling of the vasculature in developing neonates, the proposed method can also be used in other applications. In this section, we report the experimental results for two vasculature modeling applications.

2.4.4.1 Decline in macroscopic cerebral vasculature with age

It is well-known that human brain size decrease with advance into middle and old age and that this process is accelerated by some dementias and structural MRI has proved to be a sensitive method for detecting this loss in volume (Fox and Schott, 2004). Also, although vascular disease increases in the aging brain this is generally detected on anatomical MRI rather than direct observation of the vasculature through MR angiography (MRA). While it is well known that both perfusion and blood velocity in major arteries decline with old age (Farkas and Luiten, 2001), the general pattern of macroscopic cerebral vascular change with age has not, to our knowledge, been a subject of previous study. In section 2.2, we have developed an automated computerized technique to extract information about the centre lines of vessels detected by time of flight MRA (TOF-MRA). In this section this methodology is applied to study the length of arteries detected in TOF-MRA in 40 subjects aged from 21-70 years to explore the impact of age on the extent of the detected vessels.
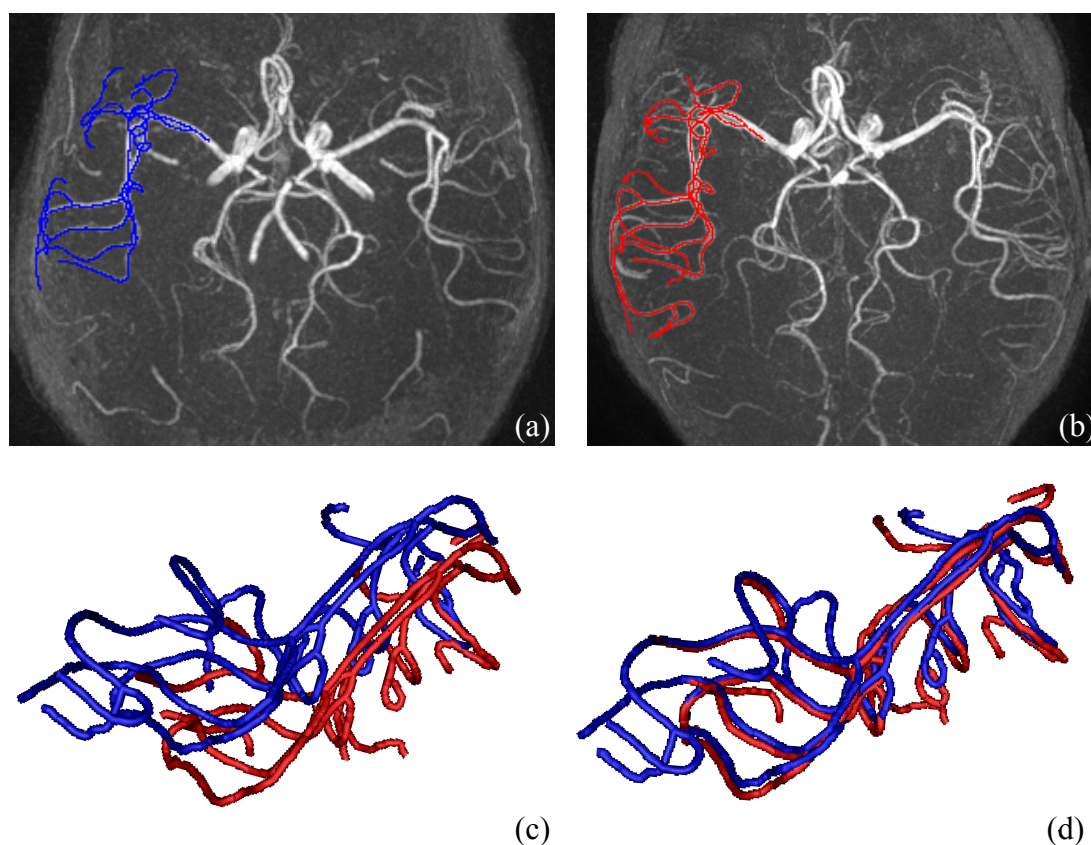
Figure 2.19. (a) and (b) show two left middle cerebral artery trees are extracted and overlapped on the MIPs. Vessel trees are visualized in (c) and (d) with a constant radius of 0.2mm. This infant was scanned at the age of 7 days and 63 days. (c) Before registration, significant misalignment can be observed for the two composed vessel trees. (d) The vascular registration using the improved ICP algorithm effectively decreases the misalignment between the two vessel trees, which is necessary for correct branch matching. Local misalignment can be further reduced after the subtree registration.

Table 2.1
Summary of subtree registration results reporting branch matching errors for different combinations of global and subtree registration strategies. Table entries are total errors for all vessel trees.

Global registration / Subtree registration	Direct TOF registration	Indirect registration	ICP	Improved ICP
No subtree registration	14	15	21	22
Original ICP	14	13	17	17
Improved ICP	10	8	8	8

Table 2.2
Summary of vessel matching results on 8 pairs of artery trees (the numbers before and after the slash shows the amount of mismatches and total manually established matches)

Vessel trees pairs	1	2	3	4	5	6	7	8
No subtree registration	2/23	1/23	1/30	5/25	1/12	1/13	1/9	8/11
With subtree registration	0/23	1/23	1/30	2/25	0/12	0/13	1/9	2/11

All TOF-MRA datasets were acquired as part of the Information eXtraction from Images (IXI) cohort of normal adult subjects (www.ixi.org.uk). The IXI database contains brain MR images from 550 normal subjects between the age of 20 and 80 years. The brain MR images acquired include standard anatomical T1 weighted volumes (Magnetization Prepared RApid Gradient Echo, MP-RAGE) and dual echo (proton density and T2 weighted) fast spin echo images acquired with overlapping slices to produce a densely sampled "pseudo-volume". In addition diffusion tensor MR and the TOF-MRA images were also acquired for each subject. All TOF-MRA images we used here were acquired in a 3T Philips Intera system (Best, Holland) with a standard 6 channel head array coil. The MR sequence parameters were as follows: multi-slab 3D TOF field echo sequence: TR 16.62 /TE 5.75ms, FOV 240mm, matrix $512 \times 512 \times 100$, flip angle 15°, voxel size $0.47 \times 0.47 \times 0.8\text{mm}^3$.

TOF-MRA images of 20 males and 20 females were randomly selected from the whole data cohort and processed to extract whole cerebral vasculatures. The mean age for males is 39.5±12.4 (24 to 60 yrs) and 43.1±16.6 (21 to 70yrs) for females. All images were first interpolated to isotropic voxels (0.47mm^3) using cubic B-spline before any image processing. The vessel tracking method was then applied to extract the whole cerebral vasculature for every subject. The extracted vessel center-lines were then manually checked and if necessary more seeds were provided manually to ensure that any remaining unsegmented peripheral vessels were included. The tolerance for minimizing J was 1.0e-4 and κ is 1.5 for all subjects.

The total extracted vessel length was then calculated in mm. Brain volumes for all subjects were also measured from the T2w images acquired in the same scan session as the TOF datasets. A dimensionless normalized vasculature length (NVL) was computed for each subject by dividing the total length of vessels by a characteristic brain length taken as the cube root of brain volume.

Figure 2.20 shows a representative example of an extracted vessel tree. Visual inspection confirmed that the extracted vasculatures are precisely centered on the vessels and are virtually complete including tip branches. Figure 2.21 shows the measured normalized vasculature length (NVL) versus age for all subjects. There is a clear decline in NVL with age in both men and women and this was found to be consistent with a linear trend (correlation coefficient $r = 0.5111$, $p = 0.0008$). Linear trend lines were fitted independently for each gender and these both show consistent slopes of -0.13 with the same offset projected back to zero of ~37.8. This slope represents a decline in NVL of ~0.3% per year and was not consistent with zero change (95% CI: -0.20 to -0.06).
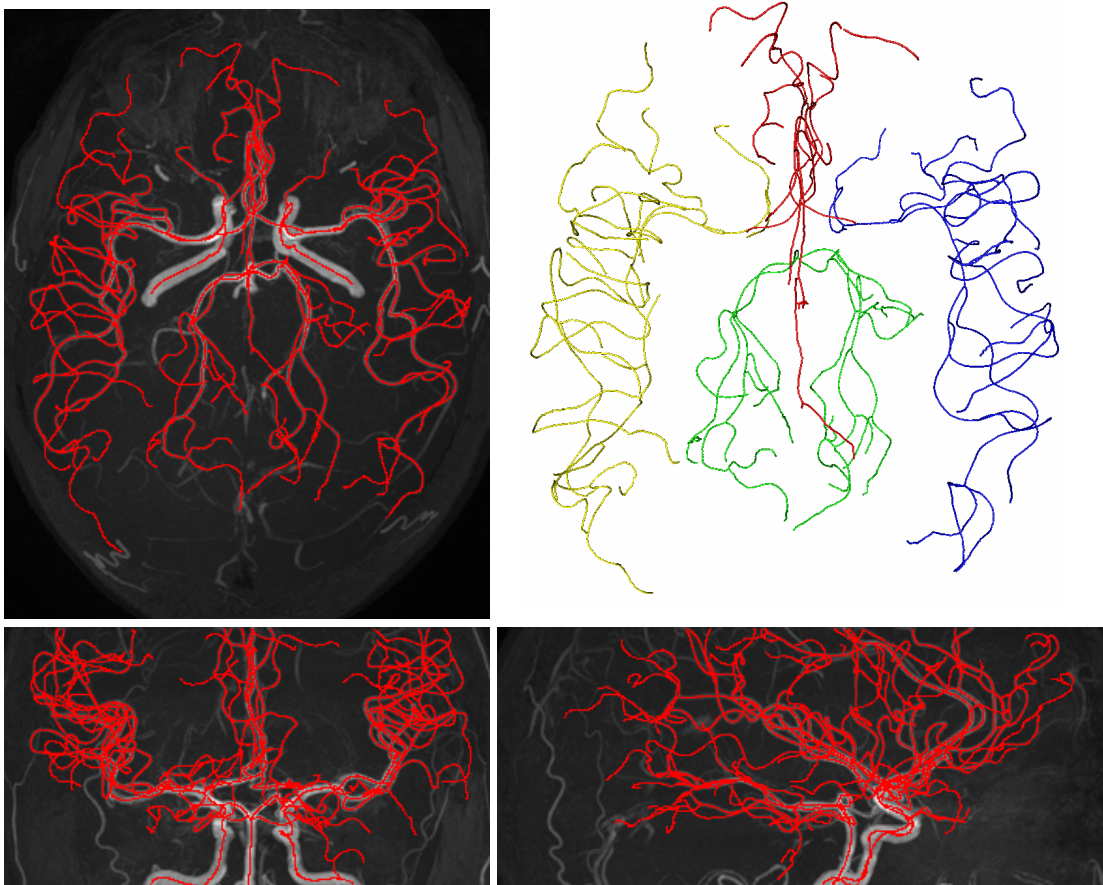
Figure 2.20. An example of extracted cerebral vasculature. A female aged at 47 years was scanned to acquire the 3D TOF-MRA image. Note that there are peripheral vessels in the MIP images that are not part of the cerebral arterial tree and therefore excluded from the segmentation..

This study shows a linear decline in detected vessel extent with age during the whole of adult life. A parallel pattern of decline occurs in brain volumes, with an initial rate of 0-0.2%/yr from 30-50yrs increasing to 0.3-0.5% /yr by age 70-80yrs (Fox and Schott, 2004). Although we normalized to brain volume, our segmentation was not designed to be precise enough to be sensitive to this rate of normal tissue loss. In considering this result it is important to be aware that TOF-MRA is a velocity dependent method and that the NVL represents only the extent of those vessels that could be detected in the images. There may be several reasons why the detected vessel length could decline. These include reductions in vessel diameter of the distal branches so that they are no longer adequately resolved in the images and/or reductions in flow rates that lead to a progressive loss of visibility of vessels in older subjects. Thus although the results are unequivocal, their significance and origin remains to be further investigated.
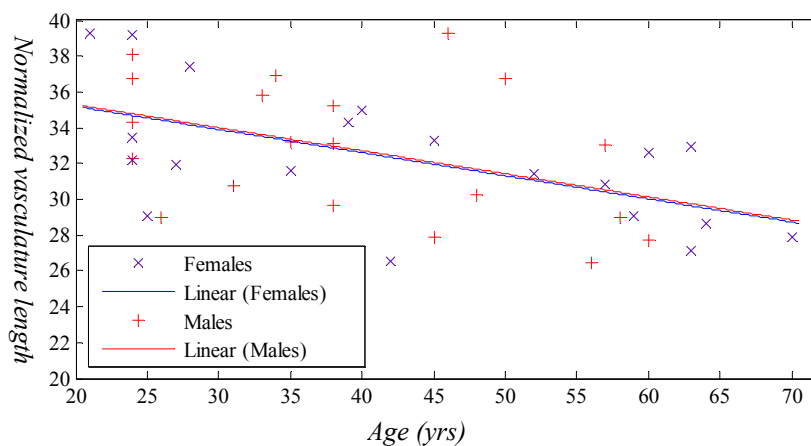
Figure 2.21. The measured normalized vasculature length (NVL) versus age for all subjects.

2.4.4.2 Vessel extraction and stenosis quantification for Contrast-Enhanced MR Angiography (CE-MRA)

Three dimensional Contrast-Enhanced MR Angiography (3D CE-MRA) has become a clinically accepted technique for vascular imaging. With the injection of

T1 shortening contrast agent, such as gadolinium-diethylene-triamine penta-acetic acid (Gd-DTPA), CE-MRA can provide 3D angiograms of excellent contrast and minimal flow-related artifacts. With new imaging sequences and parallel imaging techniques, it has been successfully used in imaging renal, pulmonary and peripheral vessels (Reith and Shamdeen, 2003; Bullitt et al., 2003a; Bullitt et al., 2005b). However, although state-of-art clinical scanners can routinely generate high-quality 3D CE-MRA images analysis and clinical diagnosis generally relies on MIP processing as in other types of MRA. Clearly, 3D vessel image analysis methods could play a role in many clinical applications, such as stenosis quantification, vascular morphology comparison and identification of blood supply in surgery planning.

The proposed vasculature modeling framework has been adapted to automatically extract vessels from the 3D CE-MRA datasets. Automatic tracking starts from the seed generation process that works on MIPs of the CE-MRA data. A multi-scale seed selection step is used to estimate the vessel radius for each seed. All selected seeds are then used for 3D ridge detection algorithm to track the whole vessel tree.

In order to estimate vessel stenosis precisely in CE-MRA images an improved vessel radius estimator is required. Some approaches based on edge detectors have been presented for the diameter estimation of coronary from high resolution DSA images (Reith and Shamdeen, 2003; Shechter et al., 2003; Shechter et al., 2006). Although very precise, these methods mainly work in 2D and are not easily extended to handle tortuous 3D vessels. Other methods exploit multi-scale criteria (Aylward et al., 1996). These multi-scale methods usually assume a circular cross-section whose radius is proportional to an optimal scale. This value is estimated by optimizing a vesselness response. Although these methods can work in 3D, they tend to over-estimate the radius of vessels near the bifurcation points as well as when two vessels are very close. Also, due to the variable morphology of vasculature, the vessel shape in the cross-sectional plane may deviate from a circle, which causes large errors in model-based methods (see Figure 2.22(a-b)).

The method we have developed is based on the detection of local gradient maxima. The vessel centerline is first smoothed using an approximating spline and orthogonal cross-sectional images are generated using B-spline interpolation. From the vessel centre points in these planes, a number of rays are cast. The rays are terminated if the vessel border is reached. We use the existence of a local gradient maximum to identify the vessel border. To make the gradient computation robust, the image is smoothed at the scale δ and image gradients are evaluated using B-spline. A total of N rays are generated each with corresponding border points $P_i, i = 1 \ldots N$, the equivalent radius r is then computed from the area A of vessel lumen approximated by the polygon $P_1 P_2 \cdots P_N$: $r = \sqrt{A/\pi}$.

This simple gradient-based vessel border detector will still cause over-estimation near the bifurcation points where the assumption that vessels are circular does not hold. As shown in Figure 2.22(a-b), the detected vessel border for a bifurcation point degrades and the radius is over-estimated. Because these incorrect border points present as abrupt deviation from overall shape, they can be detected and smoothed out by a low-order polynomial approximation. A low-order polynomial (order 1 or 2) is fitted to the N successive border points and the residual is denoted by E:

$$E(j) = \frac{1}{N} \sum_{i=1}^{N} \left(Py_{i+j} - Zy_i \left(P_{1+j}, P_{2+j}, \cdots, P_{N+j} \right) \right)^2 \qquad (2.11)$$

(a)   (b)

(c)   (d)
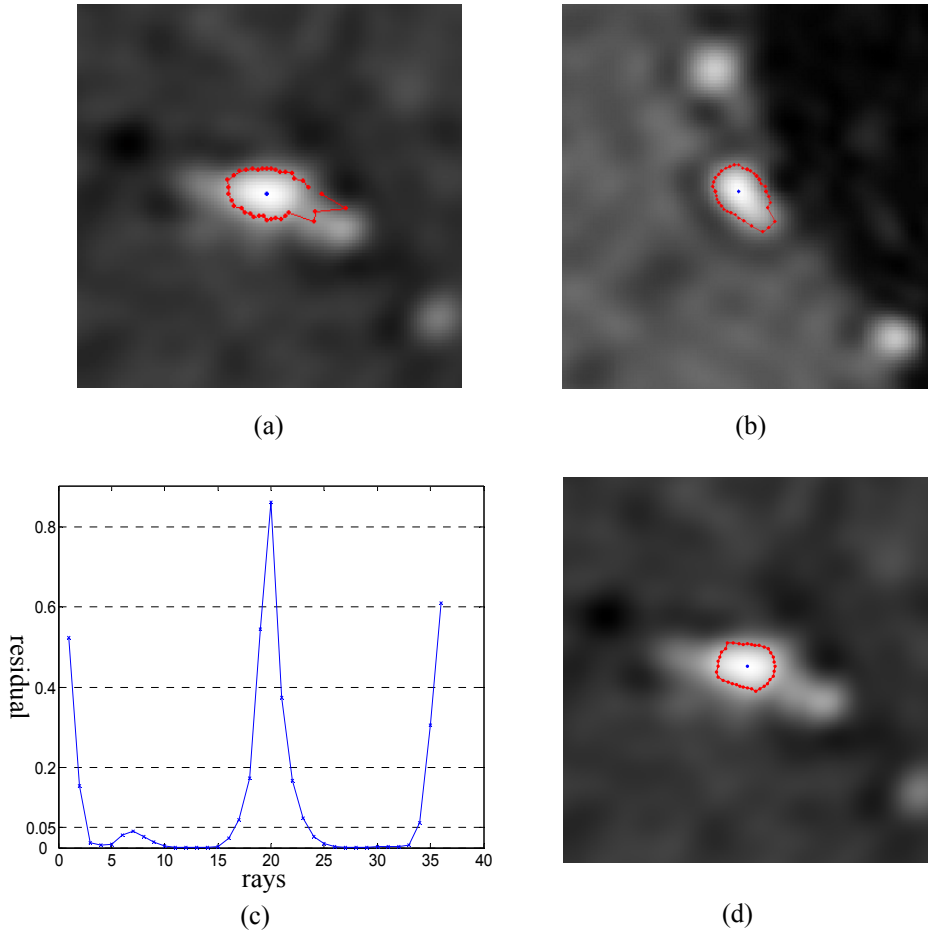
Figure 2.22. Radius estimation based on the detection of gradient maximum and low-order polynomial approximation. (a: a bifurcation point) and (b: two adjacent vessels) show two examples where the vessel shapes deviate from a circle. The simple gradient-based detection results in over-estimation of radius. (c) shows the residual E of the vessel border in (a). A threshold 0.05 is used to identify the outlier. (d) presents the vessel borders in (a) after outliers are successfully removed.

where $\boldsymbol{P}_{i+j} = \left(Px_{i+j}, Py_{i+j} \right)$ denotes the $(i+j)^{st}$ border point. Zy_i is the low-order polynomial approximation value for the i^{st} point. The approximation is performed on the N successive border points $\boldsymbol{P}_{1+j}, \boldsymbol{P}_{2+j}, \cdots, \boldsymbol{P}_{N+j}$. The residual E is computed for every border point and those points with their residual larger than a threshold are replaced by the linear interpolation of adjacent low residual points. Figure 2.22(c) shows the residual curve for the bifurcation point and Figure 2.22(d) presents the vessel border after outliers are successfully removed. The residual threshold here is empirically selected as 0.05. With the border correction of low-

order polynomial approximation, the over-estimation near the bifurcation point is clearly suppressed. Furthermore, it is shown that similar improvement can be obtained when two vessels are adjacent.

The method has been tested on 4 data sets. All images were acquired at a 3T MR imaging system (Philips Intera) using a 6 element sense torso coil. A Gadopentetic acid (Gd-DTPA) contrast agent (Magnevist, Schering, Berlin, Germany) administered at 4ml/sec has been applied in all cases. The following imaging parameters were used: TR 4.1ms, TE 1.2ms, flip angle 18 degrees, scan matrix $256 \times 215 \times 55$, voxel size $1.0 \times 1.0 \times 1.0 mm^3$. The first-pass image is subtracted from off-peak data to generate vessel image. If significant motion is observed between the two acquisitions, image registration may be used to align the data sets before the subtraction. However in our experiments, we found that all data sets are largely free from motion artifacts.

(a) (b)
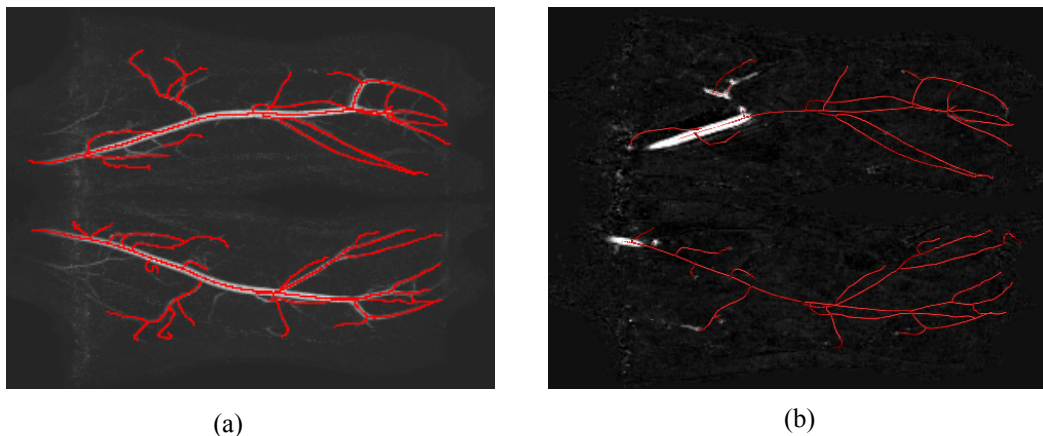
Figure 2.23. (a) Extracted vessels are overlapped on the MIP. Overall segmentation is quite exhaustive as even tip vessels are included in the results. (b) A 3D rendering of vessel tree.

The typical performance of the proposed method is indicated in Figure 2.23. For quantitative validation, we quantified the segmentation completeness (ability to extract all visible vessel branches), and consistency (spatial distance error between different extractions) of the proposed algorithm. The radius estimation method is further evaluated on both patients with stenosis and normal volunteers.

Table 2.3
Quantitative results of peripheral vessel tree tracking.

	Case1	**Case2**	**Case3**	**Case4**
Completeness C **(%)**	94.0	91.4	91.8	95.6
Distance D **(mm)**	0.55 ± 1.31	0.41 ± 1.00	0.34 ± 0.62	0.28 ± 0.55

The completeness of segmentation denotes the ability to extract all visible vessel branches from the image. An automatic algorithm with high completeness is able to robustly segment vessels with different scales and cope with the fluctuation of noise level and local contrast. We quantify the completeness by computing a statistic $C = LA/LM$. LA is the total length of vessel tree automatically extracted. LM is the total length of the manual segmentation of the same image. All visible vessels belonging to the peripheral vessel tree are segmented. The completeness statistic is reported in Table 2.3 for all subjects. The mean completeness is $93.2 \pm 1.96\%$. In all tests, our method is able to segment all main vessels and most distal branches, which is consistent with the initial visual inspection.

The precision and consistency of vessel extraction is also quantified by the averaged spatial distance between the branches from noisy image and original image (equation 2.9). The distance measures are computed between all manual segmented trees and the automatic results and quantitative results are reported in Table 2.3. The mean distance is 0.396 ± 0.118 mm and its upper bound is 0.552 mm. Given the image resolution of this image is 1.0 mm^3, this result shows that reproducibility is to within one voxel.

A further test for the radius estimation is performed. Both a healthy volunteer and a patient with bilateral popliteal artery stenosis are scanned. The results of vessel extraction and radius estimation are reported in Figure 2.24. For both subjects, the estimated radii indicate the expected gradual variation from root to tip. The overall tendency agrees with the visual inspection of MIPs. However, due to the limited

spatial resolution of our CE-MRA datasets, the vessel radii still show discernible fluctuation. Smoothing is usually required to suppress the fluctuation and compute the mean radius to quantify stenosis. The mean relative stenosis is quantified by the ratio $\dfrac{normal\_radius - narrowd\_radius}{normal\_radius}$ which is 8.3% and 13.0% for the left and right popliteal arteries in the patient (see arrows in Figure 2.24a).
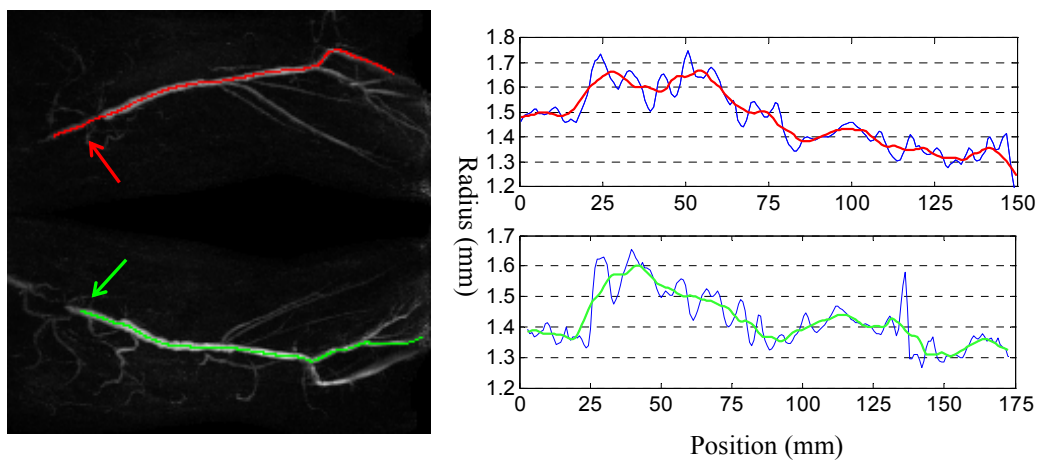
(a) Patient with bilateral popliteal artery stenosis
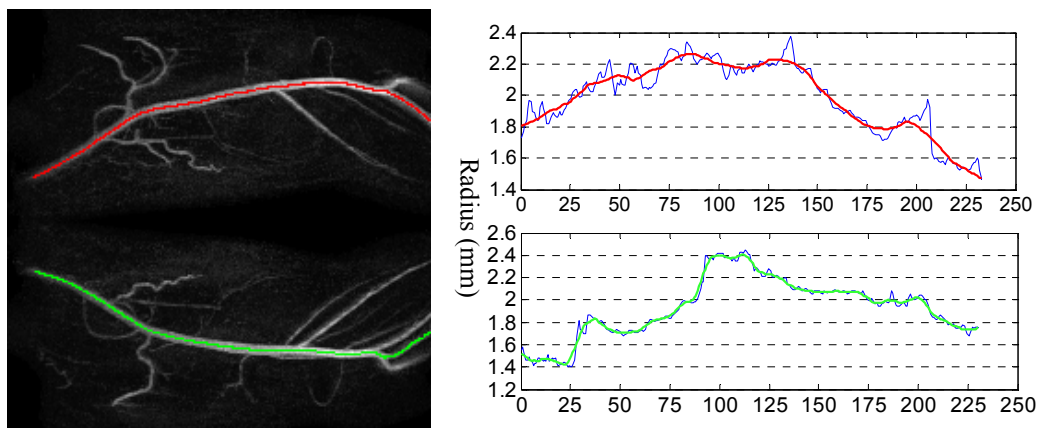
(b) Healthy volunteer

Figure 2.24. A patient with bilateral popliteal artery stenosis and a healthy volunteer were scanned, their bilateral popliteal arteries were extracted and the vessel radius as a function of position determined. (a) Patient: in the stenosed regions (arrows) the estimated radii can be used to quantify degree of stenosis. (b) The radius variation from the healthy volunteer agrees with the visual inspection of MIP.

2.5 Discussion

In this chapter we have presented a methodology for automatically extracting and matching the cerebral vasculature from MRA-TOF images. The extraction step consists of automatic seed generation, optimal scale estimation and a ridge traversal algorithm. Even when the SNR is low the method is able to provide seed points across the whole vessel tree allowing the extraction of most visible vessels. The consistency of the vessel extraction in the presence of noise was demonstrated by computing the averaged spatial distance between the same branches extracted from a data set as random noise was progressively added. The extractions remained consistent within sub-voxel precision. The completely automatic extraction algorithm has been tested on a group of 51 neonates and in all cases relatively complete segmentation was achieved.

A tree matching algorithm is proposed for use in serial studies of neonates, to allow vasculatures to be compared in the presence of growth and development. The tree matching algorithm is able to recover branch-by-branch correspondences and so can highlight newly-developed vessel segments. A prerequisite step for vessel matching is the approximate alignment of the vasculatures. Four vasculature registration strategies were tested for this purpose. All methods were equally effective as pre-processing steps, although the improved ICP algorithm achieved the best overall spatial correspondence as judged by mean spatial distance between vessel points. The most accurate tree matching results were achieved with sub-tree registration and an iterative approach that recursively corrected vessel correspondences as each level was tested. This produced virtually error free results, with the few remaining incorrect assignments occurring at leaf branches.

Several aspects of the proposed methods should be noted: The use of more seed points improves completeness of vessel extraction, since increased seed density

increases the chance of obtaining complete vasculatures. However, this will degrade the processing speed. A good compromise should simultaneously provide completeness of the vessel tree as well as efficiency. Although we can remove seeds far from vessel centerlines, there are still some redundancies. The current random selection strategy is unbiased, but may not guarantee optimal efficiency.

Although the indirect registration combining non-rigid registration to align brain anatomy is not superior in our experiments, it may be helpful if the time difference between two scans becomes larger, because more new branches emerge and the deformation of existing branches will become larger.

The present work has focused on serial studies in which the vascular topology of existing vessel trees remains essentially unaltered. Inter-subject comparisons are another area of great interest and pose extra challenges because of topological difference between vascular trees. Non-rigid registration will be required and is likely to be successful for aligning the main cerebral arteries, but complete vasculature correspondences may not be possible by image registration because of topological differences between vessel trees in different subjects. In fact the definition of corresponding branches between subjects is ambiguous and it is not clear what a proper definition should be. On a coarse scale vessel trees can be matched by dividing them into separate arterial trees, e.g. Anterior Cerebral Artery (ACA) and Posterior Cerebral Artery (PCA), but on a fine scale the correspondence is likely to be ambiguous.

2.6 Conclusion

In conclusion, automated and reliable methods for extraction of cerebral arteries from MRA-TOF images and for construction of arterial trees with all branches labeled according to their connectivity have been developed. These have been tested on images of neonates, but still have wide applicability to cerebral

angiography in general. A vessel matching algorithm for comparing cerebral vasculatures in single subjects across time has been developed and shown to be both accurate and robust when compared to the ground truth specified by manual labeling of vessels. These methods are now being applied to the study of neonates to explore the effect of prematurity.

Chapter 3

Review of Cortex Reconstruction and Registration

Effective cerebral cortical analysis plays an important role in many neuroscience studies. The accurate reconstruction of the cortical surface has a number of applications in neuroimaging, including visual inspection of cortical folding patterns, cortical morphometry and functional brain mapping across different subjects and populations (Carman et al., 1995; Thompson et al., 1998; Fischl et al., 1999a; Van et al., 2001b; Rettmann et al., 2006; Gilmore et al., 2007). Also, the automated cortical reconstruction enables the extraction of quantitative information about the cortical surface such as volume (Kim et al., 2000), surface area (Magnotta et al., 1999; Kapellou et al., 2006), thickness (Smith et al., 1982; Fischl and Dale, 2000; Kruggel et al., 2003; Yezzi, Jr. and Prince, 2003; Martinussen et al., 2005; Shaw et al., 2006; Han et al., 2006), sulcal depth (Manceaux-Demiau et al., 1998; Barkovich et al., 2002; Kochunov et al., 2005; Fornito et al., 2007) and curvature (Batchelor et al., 2002).

Anatomical magnetic resonance (MR) imaging techniques, e.g. T1 weighted (T1w) and T2 weighted (T2w) imaging sequences, which are nowadays routinely used in the clinical setting, can reliably provide high-resolution images of the human brain with good white matter (WM) and gray matter (GM) contrast and sufficient signal-to-noise ratio (SNR), as shown in Figure 3.1 which presents examples of T2w images for neonates at 27 and 40 weeks gestational age (GA) and T1w images for a child at 1 year old and an adult. These images demonstrated the potential for

(a) T2w, 27 weeks   (b) T2w, 40 weeks

(c) T1w, 1 year   (d) T1w, 30 years
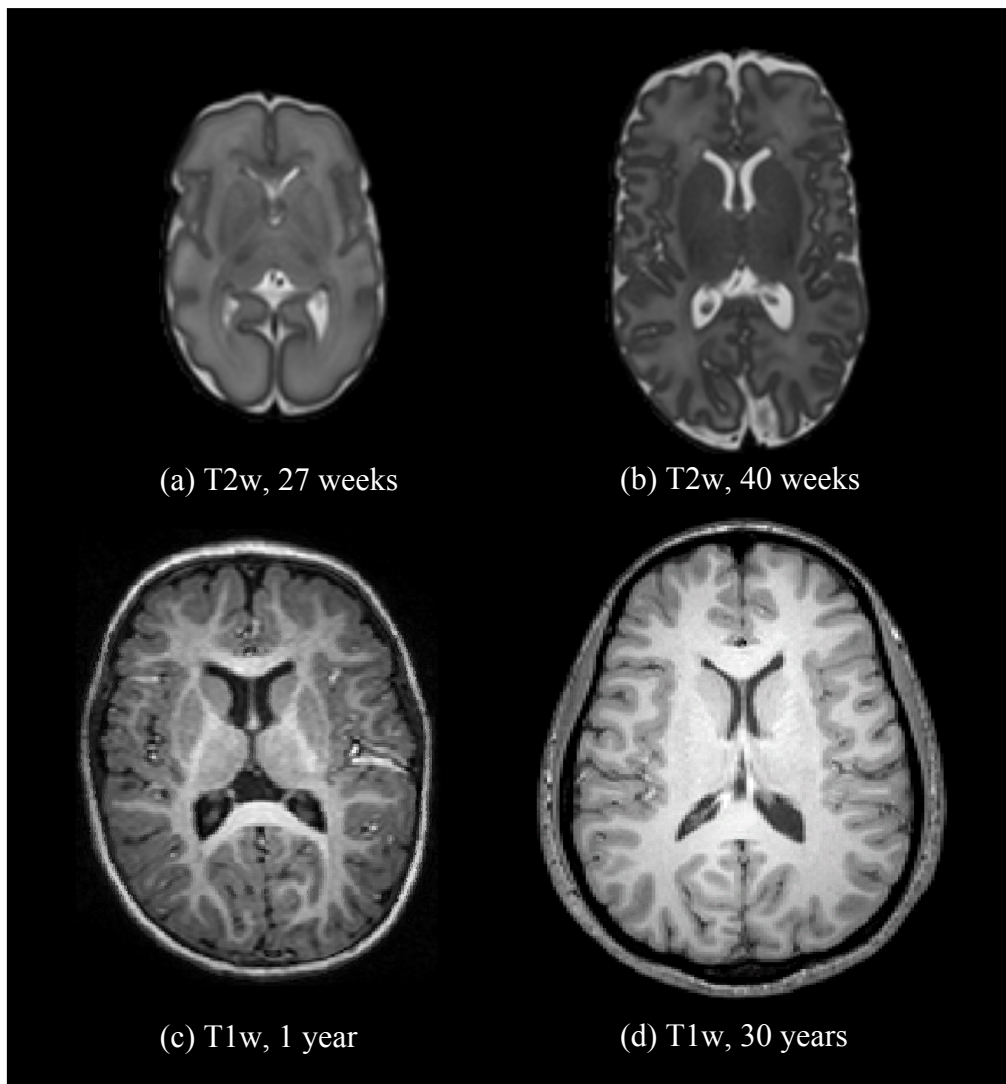
Figure 3.1. Examples of MR cerebral anatomy images with different ages.

developing algorithms used for the reconstruction of the cortical surface at different ages.

More importantly, automatic tools are necessary for cortical morphometry. As pointed out in Dale et al. (1999), many measures of cortical morphometry, e.g. cortical thickness, main curvature and local orientation of specific sulcus, require an explicit geometrical representation of the cortical surfaces. Measuring these attributes directly from 2D image slices is either error-prone or not possible.

The accurate and detailed manual delineation of cortical gray matter from high-resolution MR anatomical images is very labour-intensive and suffers from low level of inter-operator reproducibility. Even more problematic is the precise localization of central cortical surfaces because of the lack of clear anatomical clues. Another motivation for automated cortical surface reconstruction is the human brain mapping which aims to normalize the cortical functional or morphometric data into a standardized 3D space. Computing an explicit cortical representation is a crucial first step for this brain mapping process. Cortical normalization or registration procedures can then be applied to build standardized cortical maps.
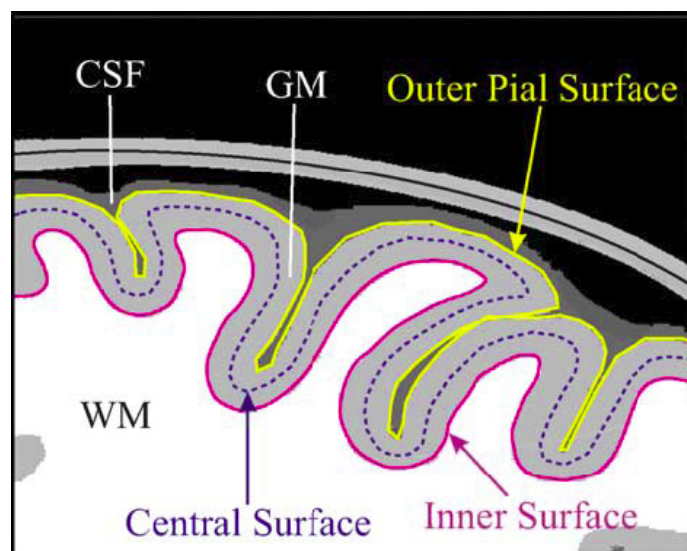
Figure 3.2. A drawing taken from (Han et al., 2004c) to illustrate the basic cerebral cortical anatomy and the definition of three cortical surfaces.

The cortex by itself is a thin layer of gray matter with the average thickness between 1 and 5 mm (von Economo, 1929; Zilles, 1990; Griffin, 1994; Edwards et al., 2001; Beatty, 2001; Martinussen et al., 2005). Figure 3.2 taken from Han et al. (2004) shows a schematic diagram of the outer, central and inner cortical surfaces bounded by the cerebrospinal fluid (CSF) and WM. The boundary between the CSF and cortical GM forms the outer surface (also called the pial surface). The boundary between the GM and WM is defined as the inner cortical surface. The
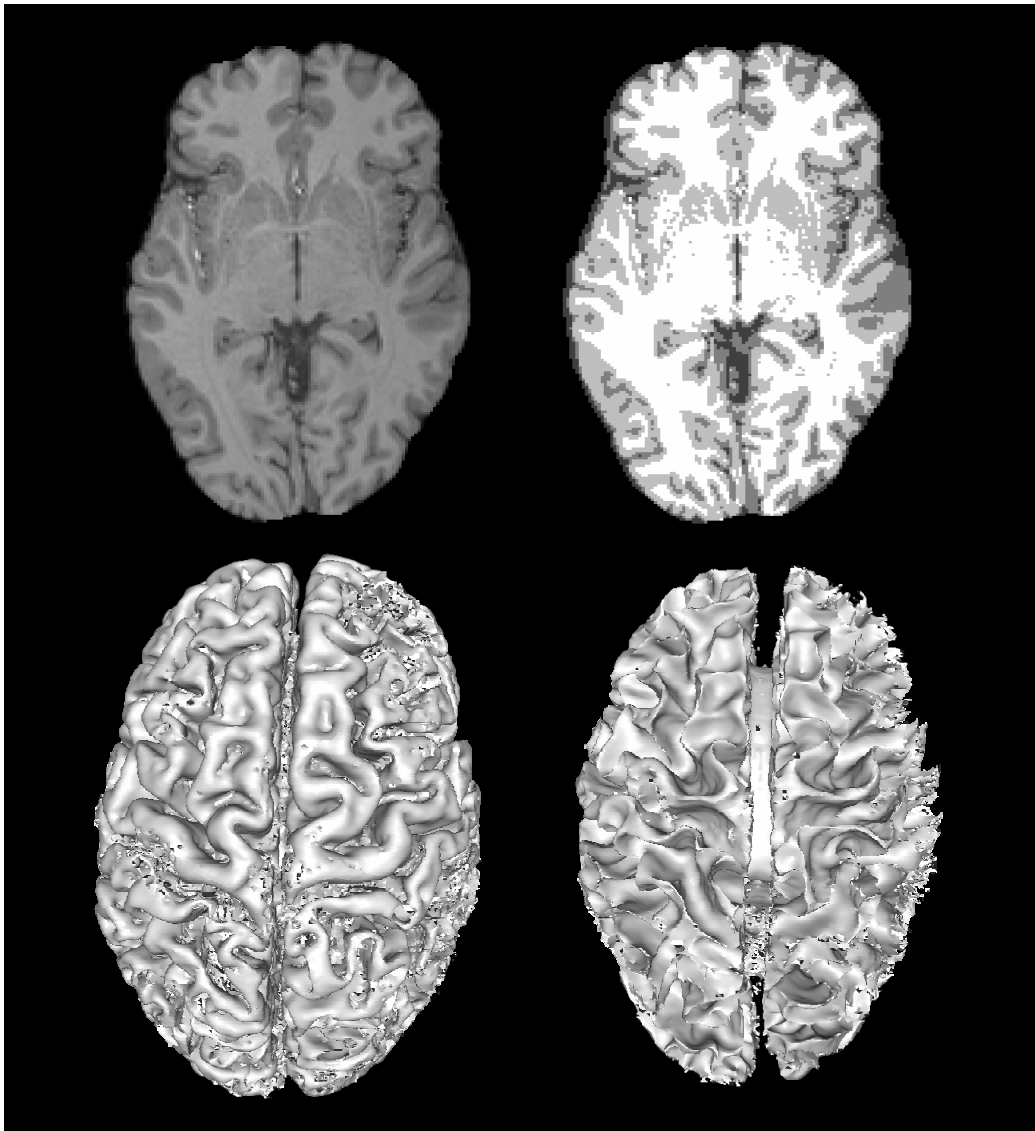
Figure 3.3 An adult T1w image with its segmentation. The renderings of outer and inner cortical surfaces show visible imperfections caused by the image noise.

central cortical surface is geometrically defined as the equidistant surface between the inner and outer surfaces.

Automatic cortical reconstruction from MR images is a challenging task. First of all, because the cerebral cortex is highly folded in the 3D space, discrete surface representations such as polygonal meshes require a large number of triangles to generate a detailed approximation of cortical surfaces with sufficient precision,

which places a significant computational burden on memory requirements and processing time, compared to less complex anatomical structures like the thalamus or the ventricles. The complex cortical shape and its inter-subject variability also prevent the effective use of approaches based on statistical shape modelling, e.g. active shape models or active appearance models (often referred as ASM and AAM, (Cootes and Taylor, 1992; Cootes et al., 2001; Cootes and Taylor, 2004)).

A common problem undermining the cortex reconstruction is the image noise which often causes errors in the segmentation of cortical GM. These errors can be visible as holes and handles on the 3D rendering of segmented cortical GM (see Figure 3.3).

Another important issue that complicates the cortical surface segmentation and reconstruction is the MR intensity inhomogeneity. This phenomenon is usually characterized as a slow intensity variation within the same tissue class over the spatial domain of the image. Figure 3.5 shows a T1w slice with the MR intensity inhomogeneity highlighted by presenting the bias field estimated. The intensity inhomogeneity is caused by a combination of poor radio frequency (RF) coil uniformity, static field deviation, eddy currents and variations in the interaction between the patient and the RF system. Although the studies have shown that image intensity variation of up to 30% may not influence the visual interpretation of image content (Meyer et al., 1995; Guillemaud and Brady, 1997), it can pose serious problems for automated segmentation algorithms, in particular for cortical GM segmentation.

The precision of the reconstructed cortical surfaces is further limited by the so-called partial volume effect. Partial volume effect is caused by the mixing of different tissues in a single voxel. As the image resolution is finite and limited in MR brain images, this effect always appears at tissue boundaries. As an example, partial volume effects are particularly intrusive in sulci where CSF is present. In this case the gray matter of sulcus banks can be very close and the little CSF within

the sulcus often shows different intensity compared to its typical level due to the partial volume effect. This effect is more problematic for neonatal MR because the brains of infants are considerably smaller. More seriously, the consequences of mixing tissues within a voxel are very different for neonatal MRI than normal adults, as the neonatal WM is not fully myelinated and the GM-WM contrast is inverted compared to adults. In the next chapter, we will present a detailed analysis of cerebral tissue contrast in neonatal MR images and propose an automatic cortex segmentation that functions in the presence of these inverted tissue contrast properties.

This chapter aims to present a comprehensive review of published methodology work for cortical segmentation and reconstruction of adult MRI, which will form the context for following neonatal cortex studies. It is worth mentioning that, to the best of our knowledge, none of these published methods have been applied to successfully reconstructing cortical surface models from neonatal MRI. This is partly due to the difficulties to segment the cortical gray matter from neonatal MRI. For example, although the T1w imaging of adults can reliably generate images with sufficient WM/GM contrast, it is not the best contrast for neonates (Rutherford, 2002). On the other hand, although none of these techniques has proven its applicability for neonatal applications, in the next two chapters we will show the basic reconstruction workflow summarized from adult methods is valuable and does motivate our studies for neonates.

This chapter is organized as follows: Section 3.1 describes a cortex reconstruction workflow summarizing the basic procedure. Existing image pre-processing methods for cortex reconstruction are reviewed in section 3.2, including brain extraction and bias correction. Cortex segmentation and corresponding surface reconstruction techniques are discussed in section 3.3. In the last section, cortical surface registration techniques are reviewed.

3.1 Cortex reconstruction pipeline

Given the significant interests in automated cortex reconstruction, a number of different approaches have been published in the literature. The majority of them consist of a sequence of image processing steps.

Raw MR images

Brain extraction/skull stripping

Pre-processing

Bias correction

Brain segmentation

Cortical reconstruction
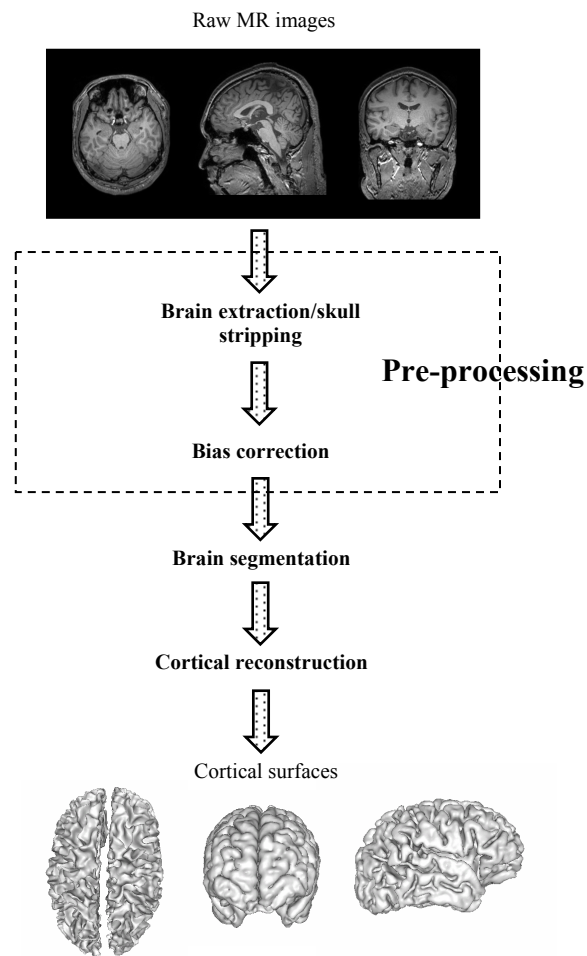
Cortical surfaces

Figure 3.4. A flow diagram to show the general cortical reconstruction workflow.

Figure 3.4 presents a cortex reconstruction pipeline which can be found in most methods published in the literature. The first step of cortical surface construction is the so-called 'skull-stripping' of the original MR images. The purpose of this step is to remove the extra-cerebral tissues, including skull and scalp and other non-brain tissues. The cerebellum and brain stem are often removed in this step as

| Authors | Methodology | | | | Outer/central/inner surface | Validation |
| | Image pre-processing | | Brain segmentation | Surface reconstruction | | |
	Skull stripping	Bias correction				
Xu et al., 1999	Semiautomatic, remove the cerebellum and brain stem	Adaptive fuzzy C-means(AFCM), robust to intensity inhomogeneity		Parametric deformable surface, median filtering for topology correction, gradient vector flow forces	Only central cortex	6 T1 volumes, landmarks on 5 main sulci/gyri, mean errors 1-2mm
Joshi et al., 1999	—	—	Match the local histogram to manual segmentation, EM algorithm	Isosurface algorithm, manual editing to remove imperfections	Inner surface	Mainly used for macaque cryosectional images
Dale et al., 1999	Normalized into the Talairach coordinate, deform a tessellated ellipsoidal template into the shape of the inner surface	Normalize the WM peaks for multiple 2D slices, a cubic spline is used to approximate the bias filed	First simple thresholding, then statistical filtering to find ambiguous voxels, Find the plane of least intensity variance	Parametric deformable surface, initialized by the isosurface of WM segmentation, explicitly detect and prohibit self-intersection	Inner and outer surface	Visual inspection, reproducibility test, FreeSurfer software
Zeng et al., 1999 Goldenberg et al., 2002	no skull stripping is required	A simple fix map determined manually by sampling tissue types throughout the image domain	The segmentation is achieved as a result of surface propagation	Coupled surface propagation using level-set equation with the range constraint on cortex thickness, narrow-band implementation	Inner and outer	MNI simulated brain images, 20 real T1w images, cortical gray matter, overlap ratio 0.657
MacDonald et al., 2000; Kim et al., 2005	Label propagation	The N3 algorithm	A neural network-based classification algorithm; later replaced by a k-nearest neighbor classifier	Parametric deformable model, dual surface propagation, CSF skeletonization	Inner and outer	150 T1w images, one-to-one surface mapping, cortex thickness measurement
Shattuck et al., 2002	Brain surface extractor (BSE)	Estimation of local tissue intensity variation, tri-cubic BSpline to interpolate the bias filed	Simple gibbs prior, Bayes estimator, iterated conditional modes algorithm to maximize the posterior	Simple isosurface generation, no smoothing constraints	Inner surface	Stand-alone interactive tool
Han et al., 2004; Tosun et al., 2006	Semiautomatic, remove the cerebellum and brain stem, identify the central vertical plane	An extended version of AFCM by adding a regularizer to smooth the membership functions, more tolerated to image noise		Level-set based surface reconstruction, GM enhancement, pressure forces, nested surface evolution	Outer/central/inner surfaces	~300 T1 volumes, 60 landmarks for central sulcus, average error 0.51mm; 420 landmarks for inner and outer surfaces, average error 0.46mm
Xu and Thompson et al., 2007	—			Adaptive particle system, gradient vector flow field, inward pressure force, Voronoi diagram, time-consuming	Inner and outer surface	21 T1 datasets, mean errors 0.96 to 0.99mm for outer surface, 1.24 to 1.29mm for inner surface

Table 3.1 A summary of cortical reconstruction methods.

they are not part of the cortical anatomy. Afterwards the MR intensity inhomogeneity needs to be corrected. A segmentation step is next used to identify cortical gray matter within the brain volume. The most common approach of brain segmentation is based on tissue classification and aims to assign every voxel within the brain to a tissue class. The topic of brain segmentation for adult MR images has been extensively studied during the past decade and many approaches have been developed and carefully validated. After the segmentation step a separate step is required for surface reconstruction. This step converts the binary cortical volume generated by the brain segmentation into an explicit geometrical representation (a triangle mesh is often used), including multiple lobes (frontal, occipital, temporal and parietal), gyri and sulci. An accurate representation should be consistent with the true 3D geometry of sulci and gyri and show no bias of reconstruction errors for either cortical lobe.

To give an overall explanation, Table 3.1 summarizes different cortical reconstruction approaches by dividing the whole procedure into image pre-processing, segmentation and surface recovery. The following sections will describe every step in detail.

3.2   Image pre-processing

Effective image pre-processing often eases the reconstruction of cerebral cortex. Generally there are two tasks in the pre-processing step: skull stripping and bias correction. These two terms are also referred to as brain extraction and inhomogeneity correction. For the brain extraction, the removal of bone, fat, skin (basically the skull and scalp) and deep gray matter will simplify the process to model the cerebral cortical surface by reducing the number of tissue classes involved in the cortical segmentation. The aim of bias correction is to correct the MR inhomogeneity which can deteriorate the cortical segmentation by causing tissue intensities deviating from their typical levels.

3.2.1. Brain extraction

Both interactive and fully automated brain extraction approaches have been presented and integrated into the cortex reconstruction workflow. Specifically, a semiautomatic brain extraction is proposed in Xu et al. (1999) using a software package developed by Davatzikos and Miller (Goldszal et al., 1998). This image-processing system was originally designed to perform qualitative and quantitative volumetric analysis of brain images by interactively drawing the region-of-interest (ROI). The removal of extracranial tissues is accomplished by a sequential application of morphological operators, thresholding, seeding, region growing, and manual editing (Xu et al., 1999; Tosun et al., 2006). Generally, a 3-D morphological erosion operator is first used to detach the brain tissue from the surrounding dura. The more detailed manual delineation of brain tissues is then achieved using a 3D region growing method. The binary mask obtained can be smoothed with mathematical morphology operators. A set of manual editing tools are provided to edit out the cerebellum and brain stem, to extract the sagittal sinus, and to remove portions of the dura left. The averaging processing time is 5 to 10 minutes, which significantly increases the workload for clinicians, compared to a fully automated solution. However, the approach is more robust to images of low quality as well as to a large variety of brain shapes. Also, the semiautomatic approach will work on MR images with different contrast patterns such as proton-density (PD) and T2w images. The same software is also used in Han et al. (2004) and Tosun et al. (2006), where they added more interaction to identify the mid sagittal plane.

Compared to the interactive methods, the fully automated brain extraction attracts more interests as it is easy to use. Dale et al. (1999) presents a skull stripping method based on the deformable template. In this scheme, all MR brain images are first normalized into a standardized coordinate system using the automated Talairach registration procedure developed by the Montreal Neurological Institute (Talairach and Tournoux, 1988; Collins and Neelin, 1994). A tessellated ellipsoidal

template is then deformed into the shape of inner surface of the skull. The internal force constraining the smoothness is based on the mean curvature of the deformed ellipsoid. The image based external force is designed to gradually diminish if the template is deformed into the CSF which has low intensity values in T1w images. The authors simply fixed the intensity threshold for CSF to be 40, which clearly limits its applicability for different image acquisition parameters.

Another automated brain extraction method is based on label propagation using image registration. It is proposed in MacDonald et al. (2000) and its further extended version in Kim et al. (2005), where the T1w MR images are automatically registered to a template in the standardized Talairach space (Talairach and Tournoux, 1988; Evans et al., 1992; Collins and Neelin, 1994). During the registration cross-correlation is used as image similarity measure and each image is transformed to match the shape of the template brain using an affine transformation. A 3D stereotaxic brain mask which is manually established on the template brain is used to remove all extracranial voxels.

Shattuck and Leahy (2002) develops a cortical reconstruction and visualization system called BrainSuite. The skull-stripping here is achieved using the popular Brain Surface Extractor (BSE) algorithm originally presented in Sandor and Leahy (1997). This method starts by applying an anisotropic diffusion filter (Gerig et al., 1992) to smooth the continuous image areas while preserving the tissue boundaries. This edge-preserving filter favors the edge detector by suppressing the image noise. The classic Marr Hildreth edge detector (Marr and Hildreth, 1980) is used to produce a binary edge image which is then used to define the brain mask. As the brain is not guaranteed to be completely separated from the skull in the binary edge image, a sequence of morphological operators are used to break any remaining attachments. Finally, a morphological closing operation is used to fill small holes. The obtained brain mask is used to exclude the extracranial voxels from cerebral tissues.

Some authors present the reconstruction workflows where no explicit brain extraction is required. For example, Zeng et al. (1999) proposes a coupled-surfaces propagation technique to reconstruct the inner and outer cortical surfaces simultaneously. The surface deformation starts from 3D seed points within the WM and stops at the WM-GM and GM-CSF boundary. Thus, no skull stripping is required in this framework. Another reconstruction procedure requiring less image pre-processing is presented in Joshi et al. (1999). In this approach the inner cortices of macaques are reconstructed from the cyrosection images. The brains of macaques have been detached from the skull and dura before any image acquisition, so no brain extraction is needed.

Besides those used in the cortex reconstruction more skull stripping methods have been developed. Specifically, in the early stage of brain image analysis, manual brain extraction is used to exclude the extracranial tissues. Depending on the level of detail required to delineate the brain surface and the interactive software used, this process can take between 15min to 2 hours (Goldszal et al., 1998; Xu et al., 1999; Fischl et al., 1999a; MacDonald et al., 2000; Richard, 2000; Yoon et al., 2001). The first attempt to automate the differentiation of brain/non-brain tissues is based on thresholding and morphological operators: Hohne and Hanson (1992) proposed a method based on thresholding the brain image to exclude very bright parts, e.g. eyeballs and scalp and dark parts, e.g. skull and air, as tissues with medium intensities mostly correspond to the brain. A more sophisticated thresholding strategy is presented in Lemieux et al. (1999). In this method, a number of morphology steps are applied and user input is provided to supervise the brain extraction. The thin connection between brain mask and non-brain parts is removed manually. Generally, these thresholding-based approaches are error-prone and difficult to achieve the high degree of automation. The selection of low and high thresholds has a strong influence on final output. Tuning the method to fit different imaging sequences is very challenging.

More automation comes from approaches based on deformable models. Cox R. (1999) and Ward (1999) propose a pre-segmentation based on a Gaussian mixture model on every 2D slice. The obtained binary mask is smoothed by fitting a deformable surface model. The idea of using a deformable model to perform brain extraction is further extended in Smith (2002). They proposed a popular brain extraction method called Brain Extraction Tool (BET). BET first finds the lower and upper intensity values for the image. As these thresholds are used to differentiate the brain from the air, they can be easily selected. The centroid of the binary head image is then recorded and the rough size of the head is estimated. A triangular tessellation of a sphere is initialized at the centroid with its radius set to half of the estimated head radius. The smoothness of the brain mask is achieved by only allowing vertices to move along the direction which will make the mask more like a sphere. Unlike the definition of external force in Dale et al. (1999), the threshold for low intensity CSF and skull is not fixed, but determined locally by sampling the intensities along the normal direction of every vertex. The BET algorithm has been tested on 45 MR images taken from 15 different scanners from 6 different manufacturers. Four different MR sequences (T1w, T2w, PD and echo planar imaging (EPI)) are involved. The automatic extraction results are compared with the manually established ground-truth, which suggests that the average performance of BET is superior to Brain Surface Extractor and the thresholding-morphology method proposed in Cox R. (1999). However, although BET is widely accepted by the research community and reasonably accurate in routine uses, Boesen K. et al. (2004) reported a comparison study between BET and brain label propagation using image registration provided by Statistical Parametric Mapping v.2 (SPM2) (Ashburner and Friston, 2000). The percentage for misclassified tissues for BET is 4.6% while it is only 2.5% for registration based approaches. The registration based brain extraction however requires a proper brain template with accurate manual labelling while approaches like BET and BSE do not require any pre-segmentation or templates.

3.2.2. Inhomogeneity correction

The majority of inhomogeneity correction methods used in the cortex reconstruction is based on explicitly estimating and eliminating the local variation of image intensity. As the first example in this category, Dale et al. (1999) employs a simple intensity inhomogeneity correction strategy to normalize the intensity levels for the high-resolution T1w MR images. It is based on the assumption that for every axial 2D slice, the tissue class with the highest intensity level is the WM. This method only employs slices in the central brain region and computes a histogram for each slice. The resulting histograms are smoothed with a Gaussian kernel to suppress the influences of image noise. The mean WM intensity level for every 2D slice is identified using a peak-finding algorithm. The WM voxels from all 2D slices are selected as control points for inhomogeneity correction if their intensity levels are within the top 15% of all voxels in the image. The histogram peaks for every 2D slices are adjusted to a mean value and the gain coefficient for every control point is computed. To decide the gain coefficients for all other voxels, a voronoi diagram is built. The gain coefficient for a voxel is assigned as the value of the nearest control point. The procedure is typically iterated 5-10 times. This inhomogeneity correction method simply assumes constant WM intensity levels throughout the brain volume and does not consider the intra-tissue class intensity variation at all. However this variation is much more noticeable in neonatal brains because of the mix of myelinated and unmyelinated white matter.

Another ad-hoc bias correction protocol is proposed in Zeng et al. (1999). This method requires significant user interaction. Specifically, the tissue intensities are manually measured throughout the image domain for both GM and WM. Their mean values are computed and used to compute the average inhomogeneity. This approach can be very time-consuming to estimate a detailed bias field.
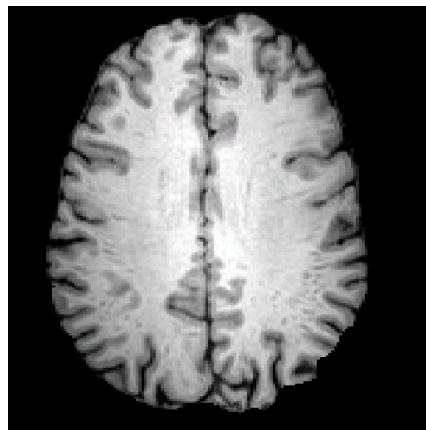
(a)
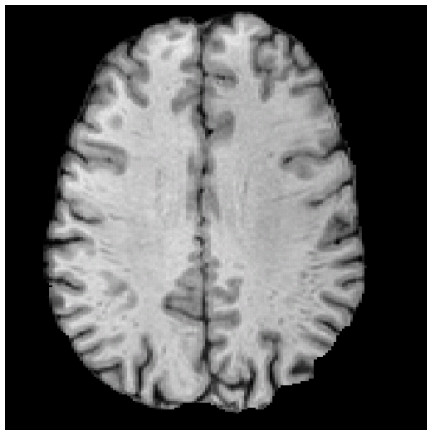
(b)
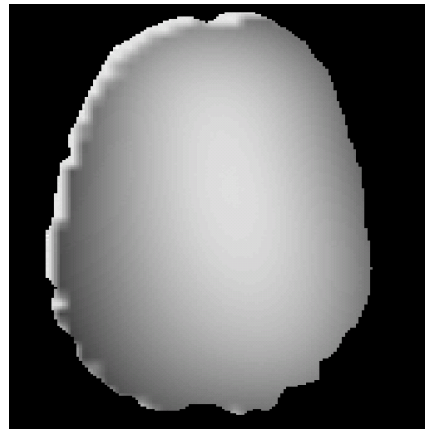
(c)
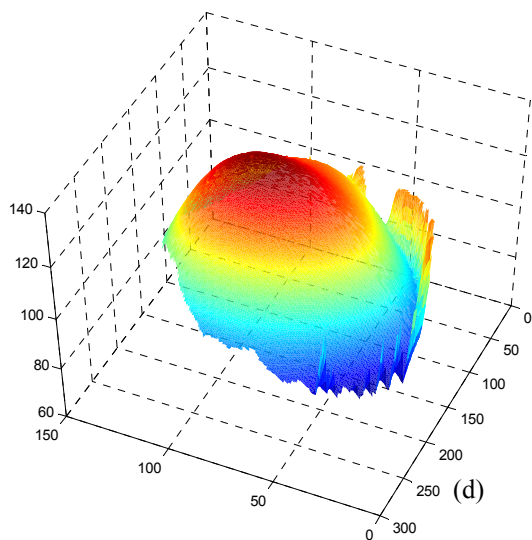
(d)

Figure 3.5 An illustration of bias correction using the N3 algorithm. (a) A T1w slice that exhibits the intensity inhomogeneity. (b) The slice after N3 correction. (c) The estimated bias field and its 3D rendering (d).

In the cortical reconstruction approaches by MacDonald et al. (2000) and Kim et al. (2005), the image inhomogeneity is corrected using a popular and robust bias correction algorithm, called N3 (Nonparametric Nonuniform intensity Normalization) proposed in Sled et al. (1998). This method neither relies on prior knowledge of tissue class distribution nor on any explicit image segmentation. It assumes the occurrence of bias field widens the intensity distribution of a tissue class. To correct the intensity inhomogeneity, the N3 method iteratively sharpens the image histogram by removing the spatial bias field from the image. As the method assumes that the observed image signal is obtained by multiplying the real image signal with the estimated bias field, a logarithmic transformation is first used to separate the real signal and bias field. The histogram of the log-transformed image is estimated and sharpened by de-convolution with a Gaussian kernel. The resulting intensity distribution is an estimate of real log-transformed image intensities. An intensity mapping can be estimated to match the original histogram to the sharpened one. After applying this intensity mapping, an estimate of bias field can be computed by dividing the sharpened image by the original. The bias field is then smoothed using B-spline. This whole process is performed iteratively until the change of estimated bias field is smaller than a preset threshold. Two parameters are required for the N3 algorithm: the initial probability distribution of the bias field and the smoothness ratio controlling the precision of B-spline representation. Sled et al. (1998) shows that the performance of the bias correction is robust to different initial parameters. Figure 3.5 shows an example of intensity inhomogeneity correction using N3.

The bias correction in the BrainSuite (Shattuck and Leahy, 2002) is based on the estimation of local intensity changes throughout the image domain. The probabilities of tissue intensity are modelled by a Gaussian mixture model. First, a global estimate of the tissue means and variances is obtained by automatic analysis of the histogram of the skull-stripped brain. The centroids of particular peaks of the histogram are computed as the means for WM, GM and CSF. The image domain is uniformly divided by defining a lattice of control points. For every control point,

its local histogram is computed. Similar to the N3 method, a tri-cubic B-spline is used to interpolate the intensity inhomogeneity coefficient at every control point and provide an estimated value for any point in the image. A drawback of this method is that intra-tissue intensity variation is ignored. Also, because B-spline only provides local support, a dense control point lattice has to be used to maintain the sufficient precision for interpolating the bias coefficients.

Unlike the explicit bias correction mentioned above, a compound strategy is used in Xu et al. (1999) and further in Han et al. (2004) and Tosun et al. (2006). These authors propose an algorithm called the adaptive fuzzy C-means (AFCM) brain segmentation combining the tissue classification with the estimation and removal of smooth bias fields, which eases the pre-processing from adding an extra inhomogeneity correction step. More details will be given in the next section.

While there has been intensive used in the cortical reconstruction application, the intensity inhomogeneity correction itself has been actively investigated and a number of different methods have been proposed in the literature. Some of them are based on the specialized image acquisition protocols (Narayana et al., 1988; Thulborn et al., 1993; Stollberger and Wach, 1996; Samson et al., 2006). Other methods estimate the bias field based on the images acquired for a homogenous phantom (Axel et al., 1987; Tincher et al., 1993; Wicks et al., 1993). The main disadvantage of these two approaches is the extra requirement of specific image acquisitions or phantoms, which limits their applicability in routine clinical setting. The methods based on the homogeneity of phantoms may also have difficulty in removing the intensity bias caused by electromagnetic properties of the subjects in the scanner (Sled and Pike, 1998a; Sled and Pike, 1998b).

The methods more suitable for the image analysis applications estimate the inhomogeneity fields directly from the image data (e.g. the N3 method). In addition to those used in the cortical reconstruction, some others use the spatial or harmonic filtering to remove the bias field (Haselgrove and Prammer, 1986; Axel et al., 1987;

Brey and Narayana, 1988; Narayana and Borthakur, 1995). Approaches in this category try to estimate and suppress the frequency spectrum of smooth bias field. The disadvantage of harmonic filtering is the assumption that the frequency spectrum of the bias field can be separable from image signal, which does not hold when there are extended regions of uniform tissue such as WM. Approaches relying on user interaction also have been developed for bias correction. Dawant et al. (1993) proposes to estimate the bias field from intensity values at a set of manually selected WM locations. The whole bias field is obtained using thin-plate spline interpolation. The manual initialization of this method can be avoided if a roughly accurate pre-segmentation is provided. Meyer et al. (1995) present another method that requires initial segmentation. This approach uses polynomials to approximate the bias fields and the coefficients of polynomials are estimated from the segmented WM.

Several other methods combine bias correction and brain segmentation: One example is the adaptive fuzzy C-means (AFCM) brain segmentation (Xu et al., 1999; Tosun et al., 2004a; Han et al., 2004). Other examples include the Expectation-Maximation (EM) segmentation developed by Wells et al. (1996), and its enhanced version proposed by Van Leemput et al. (1998, 1999a). Wells et al. (1996) models the distribution of bias field as a M-dimensional (M is the number of voxels) zero-mean Gaussian probability density function. A residual image is obtained and updated during the EM iteration by computing the differences between local voxel intensity and global mean. The classification errors are assumed to be caused by the bias fields. The bias field is computed using a low-pass filter which is convolved with the residual image. In the later paper (Van Leemput et al., 1999a), however, a parameter model is used to describe the smooth bias field. The inhomogeneity coefficients are modelled by a linear combination of polynomial basis functions. The polynomial functions are fitted to the same residual images using a weighted least-square approximation. The parameter model and EM parameters (means and variances) are iteratively updated until the parameter changes are less than a preset threshold or the maximal number of

iterations is reached. In general, these data-driven methods are easier to implement and offer more flexibility. Their performances on MR T1w or T2w images are often satisfied given the higher SNR provided by modern 1.5T or 3T MR scanners.

3.3 Cortex segmentation and surface reconstruction

Most cortical reconstruction pipelines have an explicit segmentation step to generate a detailed gray matter map before applying a parametric or implicit surface evolution scheme (Davatzikos and Bryan, 1996; Dale et al., 1999; Xu et al., 1999; Zeng et al., 1999; Joshi et al., 1999; Fischl et al., 1999a; MacDonald et al., 2000; Goldenberg et al., 2002; Han et al., 2004; Kim et al., 2005). Other techniques (Zeng et al., 1999; Goldenberg et al., 2002; Xu et al., 2006) combine the cortical segmentation with the surface reconstruction as a single image processing step. Although both strategies can generate faithful representations of cortical surfaces (at least for the inner cortex), they differ in the way the surface evolution is performed. For the methods separating the segmentation and reconstruction, the outputs of cortical segmentation are used to define external forces which drive the deformation of parametric or implicit surfaces. On the other hand, the coupled approaches define the external forces by enhancing the cortical boundary features. Edge detectors or other filters are normally applied to the MR brain images before the surface evolution.

3.3.1. Explicit cortex segmentation and reconstruction

The method presented in Davatzikos and Bryan (1996) is one of the first attempts to employ an explicit segmentation before surface reconstruction. Their brain segmentation algorithm is semiautomatic. A human operator is required to manually place seed points throughout the WM and cortical GM to guide a region growing process. Due to the intra-tissue intensity variation and image noise, a significant amount of manual editing is necessary to optimize the binary cortex

labels obtained from the region growing. The segmentation output is transformed to a mass function, which is defined within the cortex binary volume and represents the confidence that a point belongs to the cortex. An external force is defined as a centre-of-mass force which drives the surface towards the geometric centre of the cortical volume and vanishes when the mass function reaches its local maxima near the central cortex. The deformable surface is initialized as a sphere surrounding the cortical volume and it shrinks towards the centre-of-mass. The drawback of this method is the lack of ability to go deep into the sulci as the initial surface is too far from the correct cortical surface. Thus the segmentation often does not preserve the shapes of sulci. This method was applied to 80 T1w adult MR datasets, but no numerical validation was provided to quantify the surface reconstruction errors.

Joshi et al. (1999) aims to reconstruct the cortex from the macaque cryosectional images. The WM/GM segmentation is achieved using a maximum likelihood classifier. Two different approaches are proposed in Joshi et al. (1999) to approximate the histogram of 3D macaque brains. The first employs the Gaussian mixture model to match the histogram. The means and variances of multiple Gaussian functions are computed using the standard EM algorithm. To cope with the local image noise and intensity variation, the histograms are estimated locally within the neighbourhood of each voxel. As the initial means and variances can be reliably obtained from the global histogram (only GM and WM are presented in their images), the Gaussian mixture model can be solved automatically. The authors however point out the parametric Gaussian functions may not give the best segmentation and the results can be improved by replacing the Gaussian functions with general histograms directly measured from the image. To obtain these empirical histograms, two sets of voxels are manually selected for both GM and WM. The histograms estimated from these points cannot be described in a closed form, so their amplitudes, shifts and scales are numerically solved in the M-step during the EM iteration. Although the later approach clearly improves the segmentation according to the validation, it still is a semiautomatic solution. However, compared to Davatzikos and Bryan (1996), less user interaction is

required. Once the WM segmentation is generated, an isosurface generation algorithm proposed in Gueziec and Hummel (1995) is used. Compared to the standard method like marching cubes (Lorensen and Cline, 1987), this isosurface generation approach is based on the tetrahedral decomposition and avoids generating surfaces with holes on them. The inner cortical surface is then decimated by removing some edges and vertexes while preserving the overall shape. The authors propose to remove the vertices in the low curvature region and edges which are relatively small in length. The surface is finally smoothed by locally fitting quadratic patches. Besides its semiautomatic segmentation, the authors point out that a time-consuming manual editing is required to correct the small imperfections on the reconstructed surfaces, which can be due to the lack of smoothing constraints during the surface generation. The method is applied to macaque cryosectional images as well as to the Visible Human dataset, but no quantitative validation is reported.

In the work published by Dale et al. (1999), the cortical local geometric information is combined into the tissue segmentation process. The approach aims to develop an accurate WM segmentation and exploits the observation that cortical surfaces are smooth with finite curvature everywhere. This means that the local shape has the laminar structure. The segmentation makes use of this information by detecting a local plane with the least in-plane intensity variance. The intensity information in this plane is used to optimize the classification on the tissue boundary. The segmentation process first labels all voxels as WM if their intensities fall in the preset range. For every WM voxel labelled in this step, its neighbourhood is checked and those with inconsistent labels are selected as ambiguous voxels. For every ambiguous voxel, the authors propose to compute the plane-of-least-variance by calculating the intensity variances within different planes distributed uniformly over the unit sphere. An order statistic filtering is performed to decide the plane-of-least-variance. The previous tissue classification is changed if more than 60% of the in-plane voxels are labelled differently. After segmentation, the largest connected component is selected as the WM volume and

small holes are filled using a morphological operator. The advantage of this segmentation method is the combination of local cortical geometrical information with the intensity based tissue classification. A disadvantage of the proposed approach is the fact that the WM thresholds have to be manually adjusted for images with different noise levels and intensity variation. To obtain the inner cortical surface, an isosurface algorithm is used on the region labelled as WM. Unlike the approach in Joshi et al. (1999), an explicit surface smoothing is applied to regularize the initial tessellation. The smoothing is achieved using a parametric deformable model. The internal energy is defined by integrating the surface deformation along the normal and tangential directions. The image-based external force is defined as $\frac{1}{2V}\sum_{i=1}^{V}\left(T(i)-I(x_i)\right)^2$ where the V is the number of vertices and $T(i)$ is the target intensity value for the ith vertex. This value is estimated locally for all WM boundary voxels. To reconstruct the pial surface, the authors propose to set a global threshold T which is sufficiently low compared to mean intensity of GM. Any self-intersections during the surface deformation are detected and removed. The proposed method is applied to 24 subjects, but only visual inspection is used to verify the accuracy of reconstructed surfaces. The proposed method is now implemented as a part of the freely available cortical analysis software package FreeSurfer (http://surfer.nmr.mgh.harvard.edu/).

The semiautomatic segmentation and parameter selection was quickly replaced by the fully automatic fuzzy segmentation. The latter is more powerful as it retains more information compared to hard segmentation by estimating the possibility that two or more tissue classes occur within a single voxel (this possibility is also called as membership function). For cortical reconstruction, fuzzy segmentation improves the precision of reconstructed surface by allowing segmentation with sub-voxel accuracy. In addition it is more robust towards image noise, as small intensity changes only change the segmentation by some fractional degree, but not alter the entire classification of a voxel.

Xu et al. (1999) achieves the fully automated fuzzy cortical segmentation using a technique called adaptive fuzzy C-means (AFCM) algorithm (Pham and Prince, 1996). The AFCM algorithm is based on the simultaneous estimation of membership functions for each tissue class, the mean intensity of each class and the intensity inhomogeneity field. No explicit bias correction is therefore required in this framework. Let $y(x)$ be the image intensity at a voxel x, M be the total number of image voxels, $u_k(x)$ be the membership function at x for the tissue class k, c_k be the global intensity centroid of class k, and $g(x)$ be the bias field. The input of this fuzzy segmentation is a set of initial centroids c_k, $k = 1, \cdots, N$ where N is the total number of tissue classes. The initial bias field $g(x)$ is set to identity over the image domain. To maintain the smoothness of the bias field, the following cost function is minimized during the segmentation:

$$J_{AFCM} = \sum_{i=1}^{M} \sum_{k=1}^{N} u_k(x_i) \| y(x_i) - g(x_i) c_k \|^2 + \sum_{i=1}^{M} \left(\lambda_1 (g(x_i) * D_1(x_i))^2 + \lambda_2 (g(x_i) * D_2(x_i))^2 \right)$$

where D_1 and D_2 are first and second-order finite difference operators and the symbol $*$ denotes a discrete convolution. The first term in the above equation minimizes the differences between the estimated tissue intensity $g(x_i) c_k$ and observed values $y(x_i)$. The differences are weighted by the membership function and integrated over the whole image domain. The second term serves as a regularizer to constrain the bias field to be spatially smooth and slowly varying. This cost function can be minimized by computing the derivative with respect to the bias field. In each iteration, the membership function $u_k(x)$ and class centroid c_k are updated using the Bayes rule and the new bias field is updated by minimizing J_{AFCM}. A clear advantage of this segmentation method is its unsupervised nature. Neither training data nor the manual seeding or editing is required.

Based on the cortical segmentation, the GM/WM boundary is reconstructed by applying an isosurface algorithm to the WM membership function. The obtained surfaces are smoothed using a median filter. The smoothed WM surface is used as the starting point for a parametric deformation model. The internal force is defined as the weighted sum of first and second-order difference for all surface vertices, which constrains the surface to be smooth. The external force driving the surface towards the central cortical surface is derived from the GM membership function. The gradient vector flow (GVF) proposed in Xu and Prince (1998) is used to generate an external force field pushing the surface towards the central layer of GM. To speedup the convergence of the surface deformation, another constrained pressure force is added to the external force. It is defined as $C(\boldsymbol{x}) = 2u_{WM}(\boldsymbol{x}) + u_{GM}(\boldsymbol{x}) - 1$. This force diminishes within the cortex, but is positive in WM and negative in CSF. The positive force will push the surface outward from WM to cortex while the negative force will push the surface back from CSF toward the cortex. The method was applied to six subjects as well as the simulated brain data. A landmark validation was performed to test the precision of the surface reconstruction. The average reconstruction errors are within 1-2mm. The main advantage of this method is its capability of recovering the central cortical surface and good performances in capturing deep sulci. This is partly due to the use of the GVF external force field during the surface deformation. Also, its cortical reconstruction process is fully automated and does not require any manual interaction.

 MacDonald et al. (2000) presents a multiple parametric surface deformation technique, called anatomical segmentation using proximities (ASP). This method recovers both the inner and outer surfaces simultaneously while explicitly preventing self-intersections. The deformation starts from two concentric ellipsoids which are simultaneously deformed to approximate the outer and inner cortical surfaces. The external force is defined as the distance of a vertex on the deforming surface to the nearest cortex boundary in the direction of the local surface normal. The regularization forces, similar to the internal forces in Dale et al. (1999), consist

of two terms: One imposes constraints on the minimal distance between two adjacent vertexes. The other term imposes constraints on the surface bending. The authors propose two new ideas to explicitly prohibit self-intersections which can occur within deformed single surface or between inner and outer surfaces. The self-proximity term is added to enforce a minimal distance between two nonadjacent polygons in a surface. Similarly, a vertex-vertex minimal distance is used to impose the minimal distance constraint between inner and outer surfaces. A conjugate gradient approach (Press et al., 1992) is used to minimize the cost function. To avoid local optima, a multi-scale mesh deformation technique is used. The technique has been tested on 150 normal subjects. For every subject, the T1w, T2w and PD images were acquired. The multi-channel brain images are segmented using a neural network based classification algorithm (Zijdenbos et al., 1993). As all cortical surfaces are created from the same initial ellipsoid, vertex-to-vertex correspondences are maintained across subjects. This simultaneously establishes the cortical correspondences across different brains, although the authors acknowledge that the resulting correspondences may not be realistic. No validation is performed to quantify the reconstruction errors, but all datasets are visually reviewed to judge the success of the proposed technique. A drawback of this technique is the minimal cortical thickness constraint has to be specified explicitly.

Kim et al. (2005) avoid the minimal thickness constraint in MacDonald et al. (2000). They first generate the inner cortical surface using the ASP technique and expand it to recover the pial surface. The neural network based brain segmentation in MacDonald et al. (2000) is replaced by a k-nearest neighbour (k-NN) segmentation technique. This method automatically labels the brain volume to four tissue classes (background, CSF, WM and GM). An intensity homogeneity spatial prior is combined into the k-NN classifier to reduce the influences of random noise (Cocosco et al., 2003). The key improvement of this algorithm, compared to the ASP, is the introduction of a skeletonization of the CSF membership image. All voxels classified to include the CSF tissue are binarized to 1 and all others are 0. The obtained CSF volume are skeletonized and added to the external force to refine

the reconstruction of outer surface. The authors report the geometry of deep sulci is much better recovered. The algorithm is applied to 70 paediatric brains with tight gyri. No manual ground-truth is used for evaluation.

The BrainSuite system proposed in Shattuck and Leahy (2002) performs brain segmentation with a Gibbs prior. The prior probability favors continuous tissue classification while penalizes dissimilar tissue types. A Gaussian mixture model is used to compute the data likelihood for all tissue classes. The means and variances of each Gaussian are updated using the iterated conditional modes (ICM) algorithm. Unlike most cerebral tissue classification methods, the BrainSuite uses six tissue classes, i.e. WM, GM, CSF, CSF/GM, GM/WM and CSF/background. After segmentation, the WM is binarized. The Marching Cubes isosurface algorithm (Lorensen and Cline, 1987) is applied to the WM volume to generate a geometrical representation of the inner cortical surface. Similar to Joshi et al. (1999), no smoothness constraints are imposed during the surface generation; but, the BrainSuite uses a Topological Constraint Algorithm (TCA) (Shattuck and Leahy, 2001) to correct the topological errors on the WM volume before surface extraction using Marching Cubes. The TCA is an iterative approach which decomposes the WM region into a graph representation and removes all handles until the WM surface is topologically equivalent to a sphere. This system is validated using the BrainWeb phantom (Cocosco et al., 1997; Collins et al., 1998) and 20 real images. The main drawback of BrainSuite is the lack of smoothness constraints during the surface generation; thus, the generated surface is often not smooth.

An implicit surface evolution based cortical reconstruction framework is proposed in Han et al. (2004). Unlike in parametric deformable models where the surface geometry is explicitly represented as polygon meshes, the implicit surface is defined by the zero level-set of a higher dimensional spatial scalar function. In Han et al. (2004), automated cortical segmentation is achieved by improving the adaptive fuzzy C-means (AFCM) algorithm used in Pham and Prince (1996) and Xu et al. (1999). A new term with the similar effects to the Gibbs prior in Shattuck

et al. (2001) is added to the AFCM equation. The tolerance of the cortical segmentation to image noise is improved (Pham and Prince, 1999). A novel step called anatomically consistent GM enhancement (ACE) is developed in Han et al. (2004) to enable the deformed cortical surface to capture deep sulci. The effect of this ACE step is similar to the CSF skeletonization in Kim et al. (2005). The evolution of the implicit surfaces is driven by the signed pressure forces derived from the membership functions. A nested surface deformation process is applied to reconstruct the inner, outer and central surfaces. This method is further validated in Tosun et al. (2006), where about 300 T1 volumes are processed and 60 landmarks are picked for central cortex with the average error being 0.51mm. A total of 420 landmarks are selected from inner and outer surfaces. The average error is reported to be 0.46mm. The reported processing time on a regular desktop is less than 25 minutes, while the reconstruction step takes ~10 minutes. More technical details about this approach will be described in Chapter 5, where we adopt it to reconstruct cortical surfaces for neonatal MRI and present a detailed quantitative validation.

3.3.2. Compound approaches

Although the majority of cortical reconstruction methods rely on an explicit segmentation step to obtain a detailed GM segmentation, some authors (Zeng et al., 1999; Goldenberg et al., 2002; Xu et al., 2006) propose to directly reconstruct cortical surfaces from the original MR images. No segmentation is required in these approaches, while the tissue boundaries are often enhanced and serve as the image-based force to drive a surface evolution.

Zeng et al. (1999) present a cortical reconstruction method based on a coupled-surfaces propagation algorithm. The authors propose not to segment the cortical gray matter before surface reconstruction, but instead compute a tissue boundary likelihood as the pressure force for surface evolution. The tissue boundary likelihood measures the probability of a voxel lying on the boundary between two tissue classes. For a voxel x, given a possible boundary with the normal direction

$\vec{\theta}$, its neighbourhood is divided into parts $R1$ and $R2$, the tissue boundary likelihood is defined as $p_{AB}(\vec{\theta}) = p(R1 \in TissueA) \cdot p(R2 \in TissueB)$. The probability distributions of GM and WM are modelled as Gaussian functions and the optimal mean and variance and normal direction are computed to maximize $p_{AB}(\vec{\theta})$. The proposed surface reconstruction is based on the assumption that the cortical layer has a nearly constant thickness. This assumption and the idea of coupling inner and outer cortical evolution are also employed in MacDonald et al. (2000), where two polygon meshes are deformed simultaneously to approximate the inner and outer surfaces. Zeng et al. (1999) however makes use of two coupled implicit surfaces which are deformed by solving a level-set equation. Both surfaces are initialized as concentric spherical surfaces; afterwards each surface propagates along its outward normal direction and stops at the desired tissue boundary. The evolution of each surface is only driven by image-based information if the distance between inner and outer cortex lies in a preset range (1.5–5.5mm). Unlike MacDonald et al. (2000) where only a minimal thickness constraint is applied, Zeng et al. (1999) explicitly set both minimal and maximal thicknesses. To speedup the level-set evolution, the authors implement a level-set algorithm using the narrow-band technique (Adalsteinsson and Sethian, 1995) which only updates the level-set function near the current propagating fronts. The proposed method is tested on both simulated brain datasets and 20 normal T1w images. Although the authors report a mean overlap ratio between automatically generated cortex volume and manual segmentation being 0.657 for all 20 images, no validation is performed to directly quantify the precision of reconstructed inner and outer surfaces.

The coupled-surface propagation principle proposed in Zeng et al. (1999) is further formalized as an energy minimization problem using a variational geometric framework by Goldenberg et al. (2002), where the ordinary Euler scheme to solve the level-set equation is replaced by a fast geodesic active contours approach (Weickert et al., 1998; Goldenberg et al., 2001). Again, the narrow-band algorithm is exploited to speedup the surface deformation and the same tissue boundary

likelihood functions are used as the pressure forces. Note that both methods require a minimal amount of user interaction for the initialization of the cortical surfaces as concentric spheres within the WM area of the brain.

Xu et al. (2006) propose a cortical reconstruction method which is not based on a parametric deformation model or implicit surface evolution. A particle system is employed to achieve a mesh-free cortical reconstruction. In this framework, the continuous cortical surface is represented by an unstructured point cloud uniformly sampled from an initial geometric mesh. Adaptive refinement is used to insert new nodes in the high curvature regions. Self-intersections are avoided by tracing the movement of every particle point. To transform the point cloud to a geometric mesh, the authors propose to construct a geodesic Voronoi diagram from the particle system. An image-based force to drive the particle system to approach the GM boundaries is defined using the gradient vector flow (GVF) field. Unlike in Xu et al. (1999), where the cortical membership function is used, the authors simply use the image gradient to derive the GVF field. This algorithm is applied to 21 normal subjects with the available manual segmentation. The ground-truth surfaces are obtained by applying the Marching Cubes algorithm to manual segmentation of the cortex. The mean distance between the cortical surfaces generated from the particle system and manual segmentation is 0.96 to 0.99mm for the outer surface and 1.24 to 1.29mm for the inner surface. As a huge amount of particles (~70,000 or more) are required to approximate the highly folded cortical surfaces, the proposed method is quite time-consuming (~1.5 hours), compared to the implicit surface evolution in Han et al. (2004) (~10 minutes). Another limitation of this method is its inability to reconstruct the central cortical surface, as the image-based forces are derived from image gradient and gray matter threshold.

So far we have presented a comprehensive review of cortical reconstruction algorithms in the literature. As a whole, both parametric and geometric deformable models have been used for this purpose. Parametric deformable models (Dale et al., 1999; MacDonald et al., 2000; Xu et al., 1999) transform the segmentation results

into a surface tessellation and deform the mesh with a self-intersection check and surface regularization. Geometric deformable models (or Implicit surface evolution) (Zeng et al., 1999; Goldenberg et al., 2002; Han et al., 2004) use an implicit representation of the cortex and deform the cortical surface by solving a level-set equation. An explicit triangulation of cortical surfaces can be obtained using isosurface algorithms (Lorensen et al., 1987; Han et al., 2003). It should be noted that both strategies can generate appropriate cortical surfaces if the segmentation of cortical gray matter is satisfactory.

3.4   Cortical surface registration

Cortical surface registration is an important step beyond the segmentation and reconstruction which aims to estimate an accurate spatial transformation to establish the anatomical and/or functional correspondence across multiple cortical surfaces. An effective cortical registration can have many different applications, including automatic sulci/gyri labelling and quantification (Le et al., 1999; Tosun et al., 2004b), enhanced visualization of specific cortical regions (Huppertz et al., 2007; Van and Dierker, 2007), quantitative structural and functional comparison of human cerebral cortex (Van and Drury, 1997; Joshi et al., 1999), brain mapping (Toga and Mazziotta, 2000) and neurosurgical planning (Nakajima et al., 1997; Murphy et al., 2001b; Miga et al., 2003). For many of these applications the generation of average cortical maps or atlases in a standardized coordinate system in such a way that stable anatomical features, i.e. the major sulci and gyri, are mapped to the same coordinates is very important (Fischl et al., 1999a; Fischl et al., 1999b; Van et al., 2001b; Tosun et al., 2004b; Van and Dierker, 2007). These standardized cortical surfaces can be derived for different populations, e.g. normal subjects in terms of age, gender, handedness or life style (e.g. smokers or non-smokers). A cortical map can also be built for patients with diseases such as Alzheimer's (Thompson et al., 1998; Lerch et al., 2006), schizophrenia (Staal et al., 2000; Gogtay et al., 2003), dyslexia (Schultz et al., 1994) and panic disorder

(Vythilingam et al., 2000). Another interest is the ability to quantify cortical evolution in neonates whose cortical folding patterns change dramatically within the third trimester (Huppi et al., 1998; O'Shea et al., 2005; Kapellou et al., 2006). Cortical morphometric information, e.g. thickness, curvature, surface types (gyri or sulci) and sulcal depth can be averaged and presented using average maps, which will enable the comparisons across different subjects, different population and different ages.

In general, intensity-based image registration methods can be used to align the cerebral cortex. These approaches try to find the best deformation so that a voxel based similarity measure such as cross correlation or mutual information is optimized (Hajnal, 2001). An early attempt to normalize the cerebral brain as well as cortical gray matter has been proposed by Talairach and Tournoux (1988) and Collins and Neelin (1994). Here all brains are transformed into a standardized Talairach coordinate system. However, its ability to align the main anatomical features of the cortex is very limited because the simple transformation model is used and misalignment errors are on the order of several centimetres (Thompson et al., 1997; Van and Drury, 1997). To achieve a better brain alignment, more complex transformation models are usually required. Most non-rigid registration approaches (Bajcsy and Kovacic, 1989; Christensen et al., 1996; Thirion, 1998; Rueckert et al., 1999) model the image transformation with a large number of degrees of freedom (DOF), allowing high-dimensional volumetric deformations to accommodate complex anatomical variations. Unfortunately, these methods often fail to align the cortical structures sufficiently well or lead to an unrealistic transformation such that a point on the cortical surface in one brain may not lie on the cortex of another brain (Fischl et al., 1999a) due to the lack of an explicit representation to constrain the deformation of cortical surfaces, as only image intensity information is used.

To tackle this problem, several improvements have been proposed. The basic idea of these approaches is to make explicit use of the extracted cortical surfaces to constrain the registration process. Most approaches employ the cortical surface within a surface registration framework (Davatzikos and Bryan, 1996; Van and Drury, 1997; Fischl et al., 1999a; Fischl et al., 1999b; MacDonald et al., 2000; Van et al., 2001a; Van et al., 2001b; Liu et al., 2004a; Tosun et al., 2004b; Tosun and Prince, 2005). Moreover, some of them (Van and Drury, 1997; Fischl et al., 1999a; Fischl et al., 1999b; Van et al., 2001a; Van et al., 2001b; Tosun et al., 2004b; Tosun and Prince, 2005) require mapping the cortex into an intermediate space such as sphere or hemisphere.

Specifically, Davatzikos (1997) extracts the outer cortical surface using a parametric surface model and proposes a two-step approach to compute a 3D elastic transformation that anatomically aligns corresponding regions. To improve the robustness and extend the capture range for large cortical variations, the authors first propose to simplify the pial surface to exclude small sulci and gyri. A uniform stretching or shrinking is computed to match the overall shapes of two cortical surfaces. Second, to match the small sulci and gyri, a curvature map is used to quantify the distribution of maximum, minimum and Gaussian curvatures. An external force which deforms one cortical surface to match the other minimizes the squared difference between the two curvature maps. Although this multi-scale approach offers better alignment of detailed sulci and gyri, the authors fail to provide any quantitative results to validate the accuracy of sulci mapping. Liu et al. (2004b) further enhances the surface registration in Davatzikos (1997) by performing a volumetric registration before the surface registration. The extracted cortical surface is used in the volumetric registration to help alignment of gyri. For every vertex on the cortical surface, the authors extract an attribute vector consisting of local edge information and geometric invariant moments. This attribute vector is used as an extra constraint besides image intensity.

Fischl et al. (1999a, 1999b) aims to develop a surface coordinate system to achieve the inter-subject averaging and comparison. They first inflate the cortical surface to determine its large-scale folding pattern and map the surface onto a sphere by minimizing the metric distortion of the cortical surface. The metric distortion, designed to preserve the local areas and lengths, is a linear combination of two statistics: the differences of spatial distance between vertices and the differences of triangle area before and after inflation. Once the inflated representation is obtained, the alignment is carried out by minimizing the mean squared difference of surface convexity between the average and individual flattened cortical surfaces. The convexity measure reflects the large-scale geometry of the surface and is more robust to noise than the mean curvature. The main drawback of employing a sphere as the intermediate coordinate for cortical registration is that the inflation process tends to smooth out the detailed folding patterns and the mapping from the original surface to a sphere may lead to some geometrical distortion.

The idea of combining cortical inflation and registration is also adopted in Tosun et al. (2004b) and Tosun and Prince (2005). They apply a conformal mapping (Angenent et al., 1999; Gu et al., 2003; Gu et al., 2004) to establish the spherical coordinates on a cortical surface. Compared to the parametric surface inflation approaches (Sereno et al., 1996; Fischl et al., 1999a; Timsari and Leahy, 2000), the conformal mapping is more computationally efficient and can preserve relative angles, local shape and connectivity of the adjacent triangles. The authors suggest it can provide a spherical mapping with less geometrical distortions. As the conformal mapping is sensitive to the details of cortical surface triangulation, the authors propose to partially inflate the cortical surfaces before mapping them onto a sphere. The alignment of corresponding main sulci is achieved by rigidly registering the partially inflated cortex. A modified iterated closest point (ICP) algorithm is used for this purpose, where the closet point of a vertex is computed as its closet projection point on the triangle mesh, not from the triangle vertices. Once two cortical surfaces are rigidly registered, they are mapped to the spherical

representations where the main anatomical features are largely aligned. This technique is used to build an atlas of sulci from 35 subjects. For each subject, four sulcal regions (central sulcus, superior frontal sulcus, cingulated sulcus and parieto-occipital sulcus) are manually labelled. As a rigid transformation is not sufficient to capture the large variation of local cortical folding patterns, the registration is improved by adding an additional optical flow based non-rigid registration (Tosun and Prince, 2005). The feature maps used for registration are the shape index and a curvedness measure. The shape index is positive for gyri and negative for sulci, specifying the local geometry of the cortical folding. The curvedness measure quantifies the local curvature of cortical shape. The optical flow based registration is defined on the spherical coordinate and aims to find a dense transformation to align the two feature maps. The optical flow field is estimated by iteratively solving an Euler-Lagrange equation. This method is used to build an atlas of sulci from 32 subjects. The authors show that with the combination of optical flow based non-rigid registration, an improved atlas can be generated. Similar to Fischl et al. (1999a, 1999b), this method can still lead to geometrical distortions of cortical features. As the optical-flow based registration is performed on the spherical representation, it may not be able to achieve detailed cortical correspondence of the secondary sulci, as all fine-grained details have been smoothed out before the mapping.

The cortical surface visualization and analysis software, SureFit and Caret (http://brainvis.wustl.edu/SureFit/), developed and validated in Van Essen and Drury (1997) and Van et al. (2001a, 2001b), also performs the cortical alignment. This system is able to perform surface based analysis and cortex normalization by mapping the cortex to a sphere or flat plane. The approach requires a user-defined north point to determine a polar coordinate. The spherical map or flat map is generated and the polar coordinates are used to localize every 3D point on the cortical surface. The software allows the source map (sphere or flat plane) to be deformed to the atlas map while constrained by explicitly designated landmarks.

The alignment of sphere representation is achieved using an algorithm based on landmark-constrained smoothing and morphing and the flat plane registration is performed by estimating a 2D diffeomorphic transformation.

Compared to surface-based approaches, several researchers propose to use specific anatomical features to guide the registration process. For example, Thompson and Toga (1996) models the cortical alignment as an elastic warping process. This approach first extracts the cortical surface using an active surface method, but only parts of the cortical surface are used for surface warping. For each hemisphere, 6 main sulci surfaces are selected to represent the internal cortex. In parallel, 4 meshes jointly representing the lateral ventricles are also used. The sulci or ventricular correspondences between two subjects are manually established. A deformation map is computed based on this information and interpolated to cover the whole brain area. In Thompson et al. (2000), the same feature based surface registration approach is used to align 36 major external fissures and sulci. The deformation fields obtained for multiple sulci are averaged and combined to build the probability atlas for these 36 anatomical features. The authors estimate the anatomical variability for a specific sulcus by computing the root mean square (r.m.s.) magnitude of 3D displacement vectors. As only part of the cortical surface is used to constrain the deformation computation, this method tends to misalign gyrification features that were not included in the alignment process. Chui et al., (1999) presents an interactive approach. In this work, spatial points near the main sulci are manually selected. A robust point matching algorithm is then used to register the point sets and estimate an affine transformation between the cortical surfaces. Wang et al. (2003) develops an automated scheme using the mesh-refinement technique. The density of a point cloud is gradually increased and more details are aligned. They propose to select points with higher curvature throughout the whole cortex surface. The point correspondence between the template and a new cortical surface is established by combining the information about vertex distance, local surface orientation and folding pattern. More recently, Miga et al.

(2003) uses the manually extracted main sulci for image-guided neurosurgery. The sulci features from the pre-operative MR images are identified and aligned to the optical brain surface images acquired during the surgery.

These feature-based methods are computationally more efficient and are able to correct the global deformation between two cortical surfaces. However, as they fail to provide correspondences for the whole cortex, it can be difficult to only use them to analyze whole cortical variability or to build population specific cortical atlases; instead, they can serve as a preliminary step for more detailed surface registration.

Despite the variant approaches published in the literature, they mainly focus on the cross-sectional studies for adults and have not been applied to tracking the fast development of neonatal cortical surfaces. To address this deficit, in Chapter 5 we develop a surface based cortical registration approach and apply it to exploring this intact topic.

3.5 Summary

In this chapter we have reviewed the state-of-the-art cortical reconstruction and registration with emphasis on cortical segmentation and surface reconstruction. The latest reconstruction approaches, e.g. the implicit evolution proposed in Han et al. (2004), are able to build a detailed representation for inner, central and outer cortical surfaces. These geometrically accurate surfaces serve as the basis for surface-based cortex registration. Different cortical registration algorithms have been developed and population specific cortical atlases have been successfully built.

Despite the success of reconstructing and normalizing cortical surfaces in MR images obtained from adults, none of these approaches, to the best of our

knowledge, have been applied to neonatal cerebral MR images. Therefore, within the next two chapters, we will present a complete cortical segmentation, reconstruction and registration approach and validate its effectiveness on the large group of neonates from very preterm to term-equivalent age.

Chapter 4

Automatic Cortical Segmentation of Neonatal MRI

4.1 Introduction

Neonatal brain development proceeds rapidly in the 3rd trimester of pregnancy. Infants born preterm appear to be vulnerable to disruption of these developmental processes, and are at high risk of cognitive and behavioral impairment during childhood and adolescence (McCormick et al., 1992; McCormick et al., 1996; Hack et al., 2002; Marlow et al., 2005). Abnormal development of the cerebral cortex and cortical connectivity has been suggested as a major neurological correlate of neurodevelopmental abnormalities following preterm birth (Peterson et al., 2000; Isaacs et al., 2001; Peterson et al., 2003). Clinical studies have shown reduced cortical growth, decreased thalamic volume and diffuse white matter (WM) abnormalities in preterm infants at term equivalent age (Woodward et al., 2006; Boardman et al., 2006; Counsell et al., 2006; Kapellou et al., 2006). The detailed morphometric analysis of brain growth is an active research area which seeks to understand the nature of these neurodevelopmental abnormalities.

Ajayi-Obe et al. (2000) and Kapellou et al. (2006) have manually traced the cortex to measure its surface area and volume from multiple 2D slices. However, the manual segmentation is tedious and time consuming. The reproducibility is even more problematic if the human operator is less experienced or if the image contrast between WM and GM is deteriorated by artifacts. As a result, a robust,

accurate and automatic 3D segmentation of the developing cortex is an essential prerequisite for quantitative cortical analysis.

4.2   Challenges of automatic cortical segmentation in neonatal MRI

The reliable automatic segmentation and reconstruction of cortex would facilitate the quantification of neonatal brain development; however, several specific characteristics of the brain during this period of development have hindered automated morphometric analysis. A key difference between the neonatal and adult brain is that the WM/GM contrast on both T1 weighted and T2 weighted MR images is usually reversed. This is caused by the increased water content of the cerebral structures and the presence of largely unmyelinated WM. In the neonatal T2w images (Figure 4.1(a-c)), most of the white matter in brains of new-borns is not myelinated and appears brighter than gray matter (in adult T2w, the gray matter is brighter). In T1w images (Figure 4.1(d)), neonatal white matter is darker and gray matter is brighter. For the very premature infants (Figure 4.1(a)), almost all white matter is not myelinated. As the brain of infants matures more white matter is becoming myelinated thus producing a similar contrast to the adult brain (as shown in Figure 4.1(b-c)). During the first two years of life the WM/GM contrast keeps changing as various processes such as cortical organization and myelination of the WM tracts cause progressive changes in the T1 and T2 relaxation times. By the age of ca. 2 years, the myelination process is nearly complete and the contrast on MR images is similar to that of adult brains (see Rutherford (2002)). For the sake of simplicity and since the majority of WM in neonatal brains is non-myelinated, we refer to non-myelinated WM in the remainder of the chapters as WM.

The inverted GM/WM contrast will lead to mislabeled voxels at the interface between the cerebrospinal fluid (CSF) and GM. Because CSF has the highest

(a)

(b)

(c)

(d)
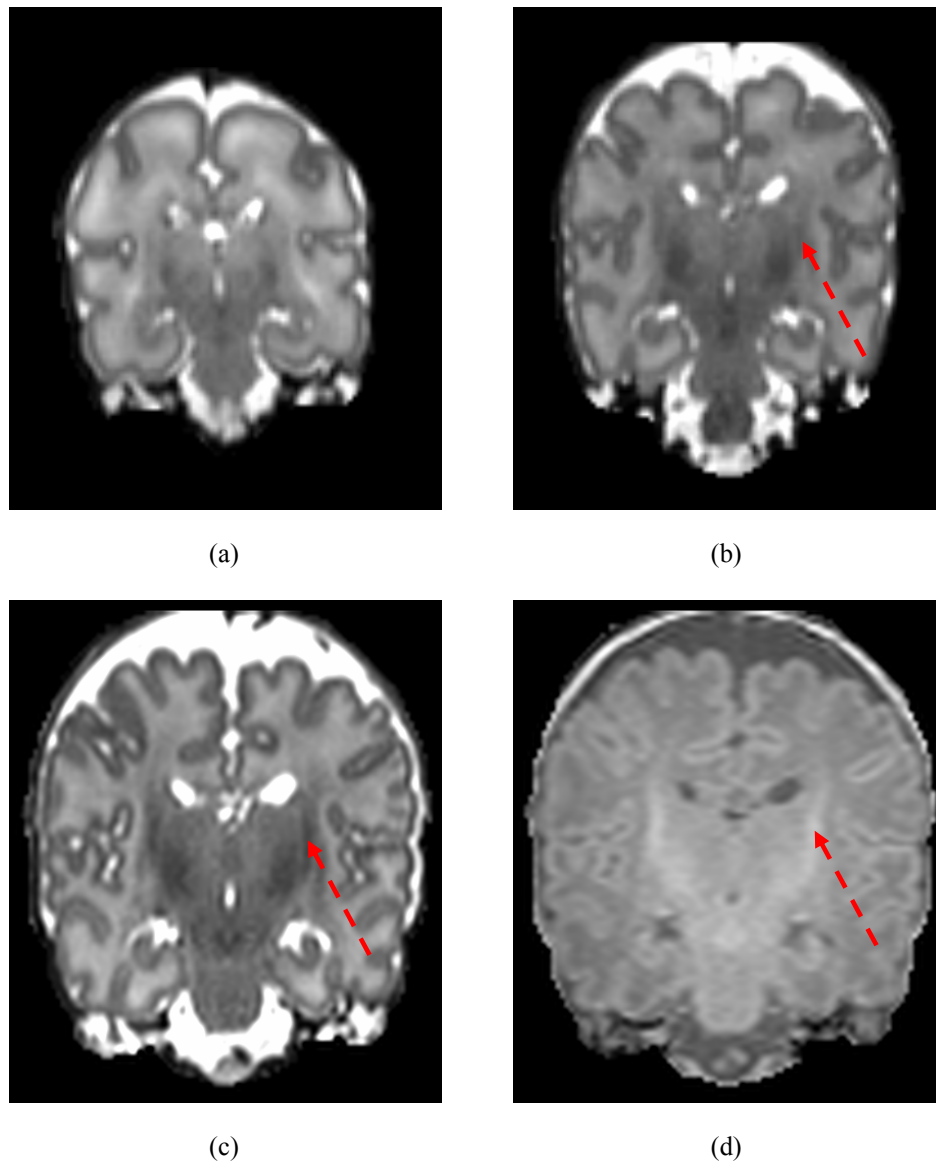
Figure 4.1. The same neonate (GA at birth: 27.86w) was scanned at three times with the GA being (a) 29.86, (b) 34.29 and (c-d) 39.86 weeks. (a-c) are T2w images and (d) is the corresponding T1w image to (c). It can be seen that most white matter in neonatal brains are not myelinated and the gray-white matter contrast is inverted. The dashed arrow points to the myelinated white matter. When the infant is very premature, no white matter is myelinated. As the baby becomes mature, more white matter is becoming myelinated.

intensity in neonatal T2w images and the image resolution of neonatal MRI is limited, many voxels between CSF and GM will be subject to partial volume effects and thus have similar intensities to WM (Figure 4.2(a)). These voxels are brighter than GM and darker than CSF and can be incorrectly classified as WM by conventional intensity-based segmentation approaches which ignore partial volume effects. The same problem occurs in neonatal T1w images. In this case, CSF is the darkest and GM is the brightest; thus voxels at the interface between CSF and GM will have intensities similar to those of WM (Figure 4.2(b)). In the following we refer to these voxels as *mislabeled partial volume voxels* (MLPV) since the mislabeling is primarily a consequence of the mixing of tissues in a voxel (partial volume). In T1w/T2w images of adult brains, partial volume effects also occur but these do not lead to similar MLPV because the WM is fully myelinated and has the highest/lowest intensity respectively.

As mentioned previously the brain segmentation is usually preceded by a brain extraction step which aims to exclude non-brain tissue. If the brain extraction does not exclude all non-brain tissues, there will be another source of MLPV at the CSF-non-brain tissue boundary. Because CSF has high signal intensity in T2w images and non-brain tissues generally have low signal intensity, there are voxels on the intermediate boundary having similar intensities to both GM and WM. In T1w images, CSF has low signal intensity and scalp has high signal intensity, so that similar MLPV can appear. This latter type of MLPV can also occur in adult brain MR images.

(a)

(b)

(c)

(d)
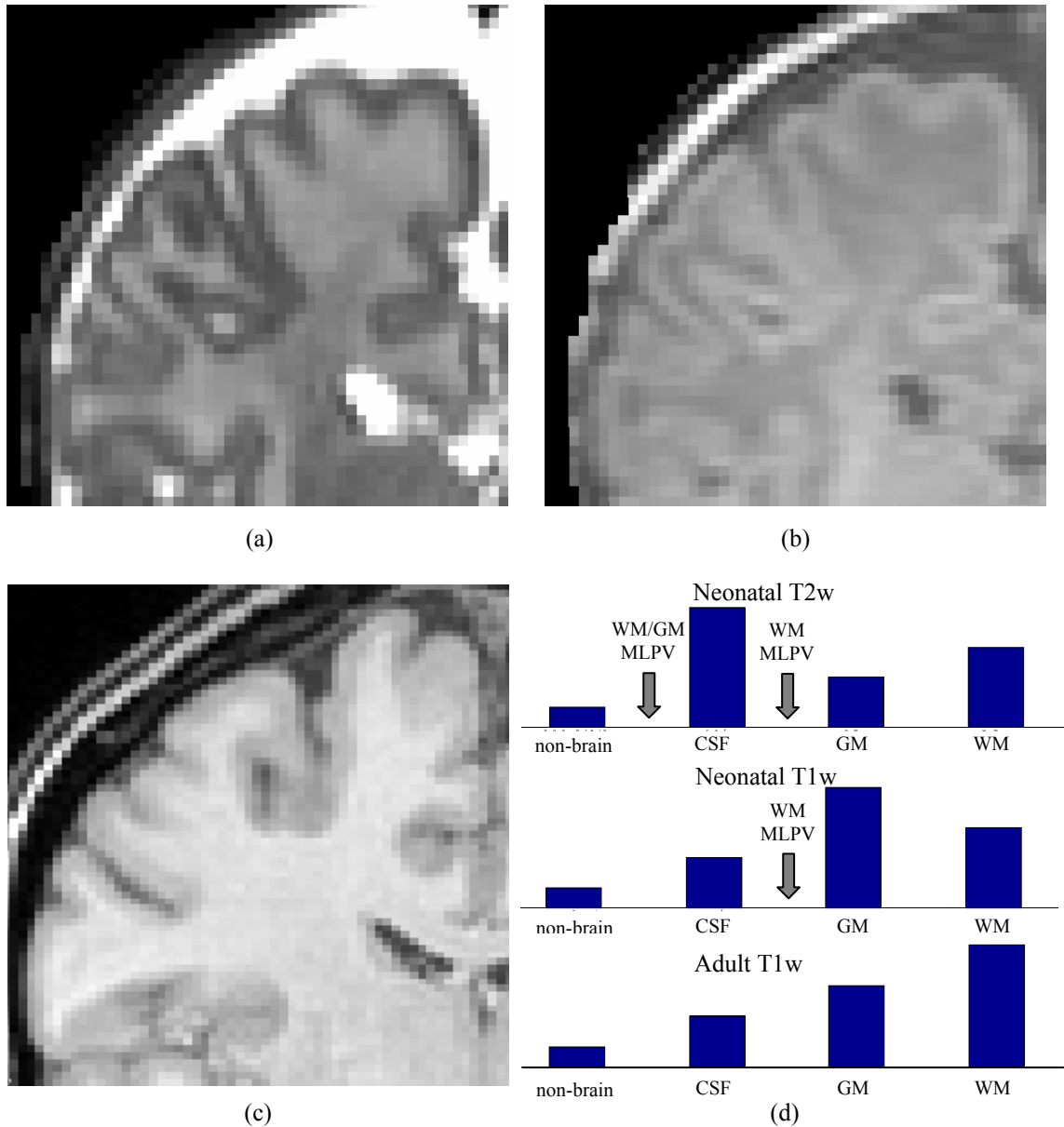
Figure 4.2. Representative coronal MRI slices of neonates and adults showing the different contrast patterns. (a) T2w and (b) T1w images for a neonate (GA at scan 39.86 weeks). Due to the inverted GM-WM contrast, many voxels on the CSF-GM boundary have the similar intensities to WM. If the brain is not properly extracted, partial volume voxels will also appear between the non-brain tissues and CSF. For the purpose of comparison, an enlarged coronal T1w slice of an adult (male, 40 years) is shown in (c). (d) From top to bottom, the relative intensity levels of non-brain tissue, CSF, GM and WM for neonatal T1w, T2w and adult T1w MRI are demonstrated as bar charts. Note that the intensity levels of partial volumes in adult T1w do not overlap the characteristic intensity of any pure tissue classes, which is not true for neonates.
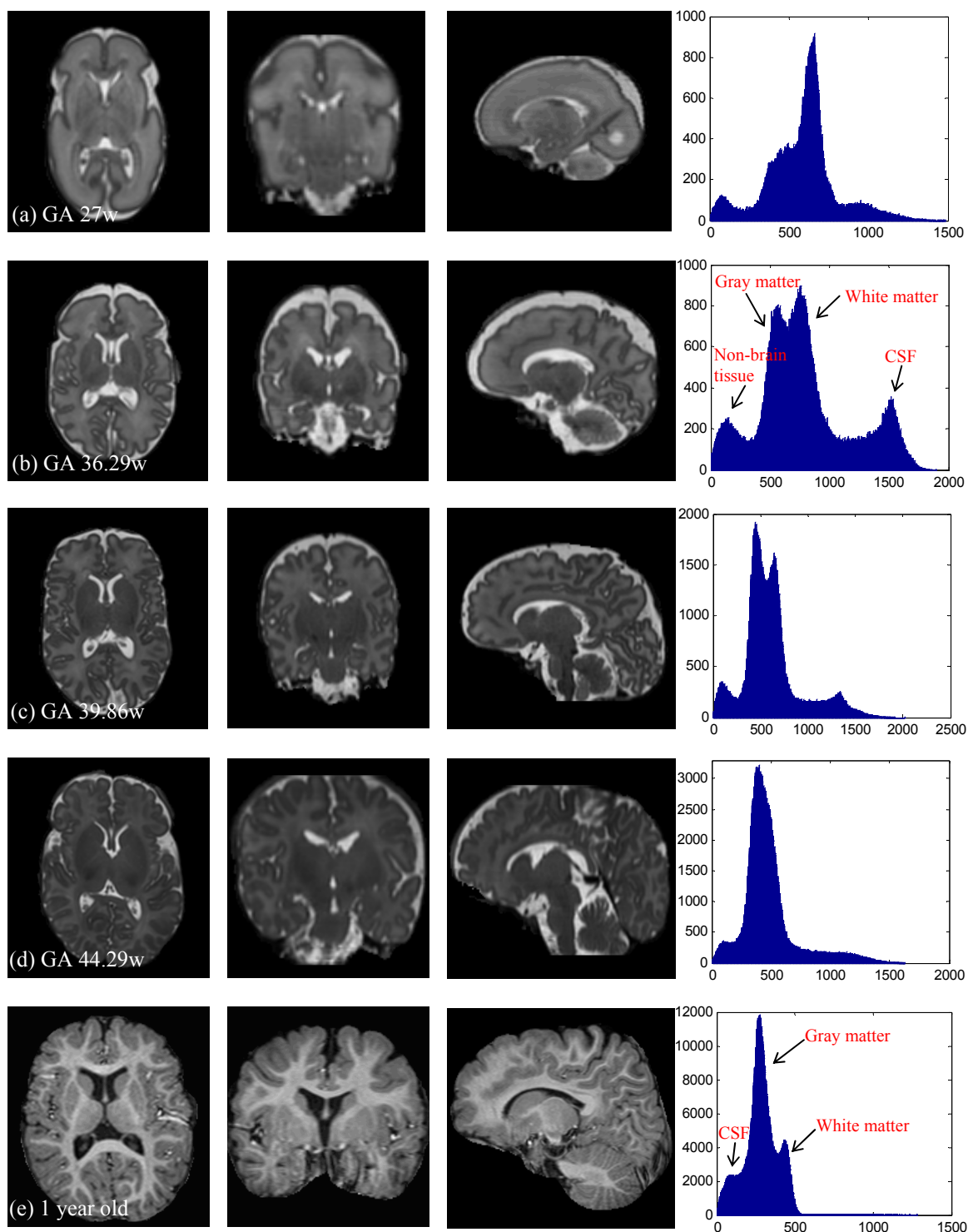
Figure 4.3. (a-d) MR T2w images of developing neonates from very premature to term equivalent age. The relative gray-white matter contrast presented in T2w images can keep decreasing, as neonates become more mature. (e) A T1w image of a 1-year old infant. The gray-white matter contrast is now adult-like.
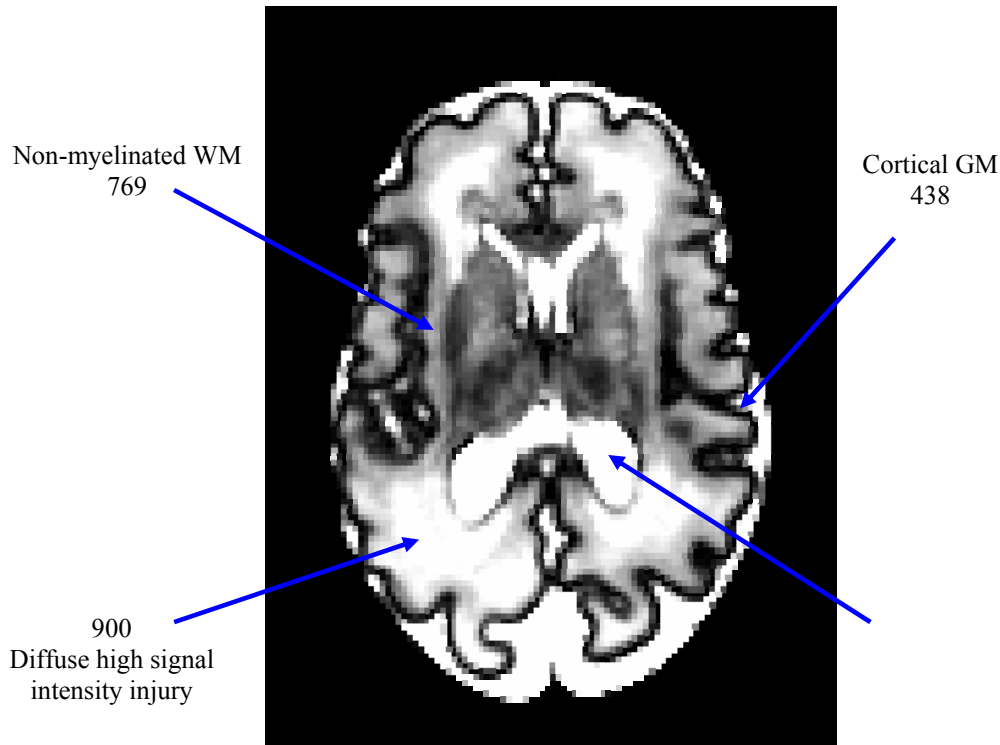
Figure 4.4. A transverse T2w image of a premature neonate (GA at birth: 27w; GA at scan: 34w). Intensity variability in the WM caused by there being a mixture of myelinated and unmyelinated tissue is compounded by the effects of diffuse WM injury (excessively bright areas in WM) which is a common in infants born pre-term.

Besides the problem of MLPV at the CSF/GM interface which is unique to neonatal MRI, there are some other problems which make the task of neonatal cortical segmentation challenging:

- Lower contrast-to-noise ratio (CNR) in neonatal MRI: Due to the insufficient T1 differences between neonatal GM and WM neonatal T1 images have typically less GM/WM contrast than in adult T1 images (Jones et al., 2004). Moreover, the scanning time is frequently limited by the fact that infants move periodically when in natural sleep or even when sedated, which reduces the CNR and produces artifacts. Thus even though neonatal T2w images usually show sharper cortical surfaces, the CNR can be as low as the half of an adult brain (Prastawa et al., 2005).

- Age dependent gray-white contrast: As the neonatal brain matures the GM/WM contrast in T2w images changes. WM gradually becomes darker and finally has lower intensity than the GM (in T1w images, WM finally becomes brighter than GM). At some time-point of this myelination process (approx. GA of 45-50 weeks GA), GM and WM can have similar intensities. Figure 4.3 illustrates this process with examples of neonatal MR images from very preterm to term equivalent age and beyond.

- Tissue signal heterogeneity: Especially WM in neonatal MRI shows significant intra-class intensity variability. This is caused by the combined effects of RF inhomogeneity when using higher field strength scanners (e.g. 3T) and biological properties of brain tissues. For the preterm neonates, there are often diffuse high signal intensities in WM which are recognized as a common form of brain damage (Maalouf et al., 1999; Counsell et al., 2006). An example of this is shown in Figure 4.4.

- Rapid evolution of cortical geometry: Besides the special intensity and contrast characteristics, the shape of the neonatal cortex is rapidly developing and folding. It can pose problems for segmentation methods which rely on a-priori information in form of probabilistic atlases or shape models since the precise non-rigid registration of cortical surfaces is becoming more challenging and large deformations are required for good matching. Also, a single atlas or shape model may not be sufficient to characterise the variability of the cortical geometry at different stages of development.

4.3   Neonatal cortex segmentation in the literature

The automatic segmentation of the adult brain in MRI based on tissue classification has been intensively studied. Several segmentation algorithms have been developed and applied to both normal subjects and subjects with pathology. Most methods developed for this purpose are based on analyzing voxel intensities using statistical techniques. Specifically, methods based on the Expectation-Maximization (EM)

algorithm (Wells et al., 1996; Van Leemput et al., 1998; Van Leemput et al., 1999a; Van Leemput et al., 1999b; Ashburner, 2000), fuzzy C-means (Pham and Prince, 1996; Pham and Prince, 1999), k-nearest neighbor and template matching (Warfield, 1996; Warfield et al., 2000), support vector machines (Karp and Vigário, 2004), neural networks (Powell et al., 2006) and the graph cuts algorithm (Zhuang et al., 2007) have been proposed by different researchers.

Unfortunately, compared to the comprehensive literature for adults, there are fewer studies on segmentation of neonatal brain MRI. As the first example, semi-automated methods have been proposed by Peterson et al. (2000) and Nishida et al. (2007). In these schemes, voxels throughout the cerebral area are manually sampled and the typical intensity value for every tissue class is estimated. The image segmentation is achieved by thresholding. Manual editing is often required to complete the segmentation and correct all errors. Clearly, these semi-automated approaches require extensive human interventions. Also, the thresholding assumes the less noticeable inter-tissue intensity variability, which generally is not true for neonates.

Another approach which requires some manual interaction is proposed by Weisenfeld et al. (2006), where a probabilistic atlas is generated using the affine registration of 20 neonates all scanned at approximate GA of ~42 weeks. A human operator is required to select a set of voxels which represent the intensity of every tissue class. The prior probability is obtained by registering a new image to the atlas. The segmentation is achieved using a k-nearest neighbour classifier (k-NN) originally proposed in Warfield (1996) and Warfield et al. (2000). A Markov Random Field (MRF) extension is developed and combined with the k-NN classifier to improve the robustness to image noise. In this scheme, the neonatal brain is classified into 6 classes (cortical GM, myelinated and non-myelinated WM, CSF, basal ganglia and extra-cerebral tissue). The algorithm has been tested on a total of 5 subjects. A manual segmentation is used to evaluate the method. The

mean Dice similarity ratio (Dice, 1945; Warfield, 1996) between manual and automated segmentation is 0.75 for cortical GM and 0.69 for non-myelinated WM.

This k-NN based segmentation method has been used to study the abnormal cerebral structures related to preterm birth (Inder et al., 2003; Inder et al., 2005) and to quantify the diffuse WM injury (Murphy et al., 2001a). The authors also use this technique to investigate the relationship between regional cerebral changes and various perinatal risk facts (Thompson et al., 2007).

Prastawa et al. (Prastawa et al., 2005) proposed another atlas-based approach for neonatal brain segmentation. They generate a probabilistic atlas by manually segmenting the MR images of three subjects. A tissue classification is achieved using the expectation-maximization (EM) scheme proposed by Van Leemput et al. (1998, 1999a), where the bias field is explicitly parameterized as a linear combination of polynomial basis functions. Both polynomial functions and EM parameters (means and variances) are iteratively updated. Again, affine registration is used to register the atlas to each subject. A robust graph clustering method (Cocosco et al., 2003) which is able to prune data outliers, is integrated into this scheme, providing better initial parameter estimates for every tissue class. In the final step the EM segmentation is refined with the non-parametric kernel density estimation. A Parzen window method (Parzen, 1962) is used after applying the EM algorithm, producing the final segmentation. This method has been tested on 4 neonates. The neonatal brain is segmented into four classes (Myelinated WM, non-myelinated WM, GM and CSF). The reported overlapping ratio against the ground truth (Dice similarity ratio) is between 0.63-0.81 depending on the structure and subjects. Gilmore et al. (2007) from the same group has recently reported the segmentation results of 70 term born neonates to show regional growth patterns, sexual dimorphism and cerebral asymmetry.
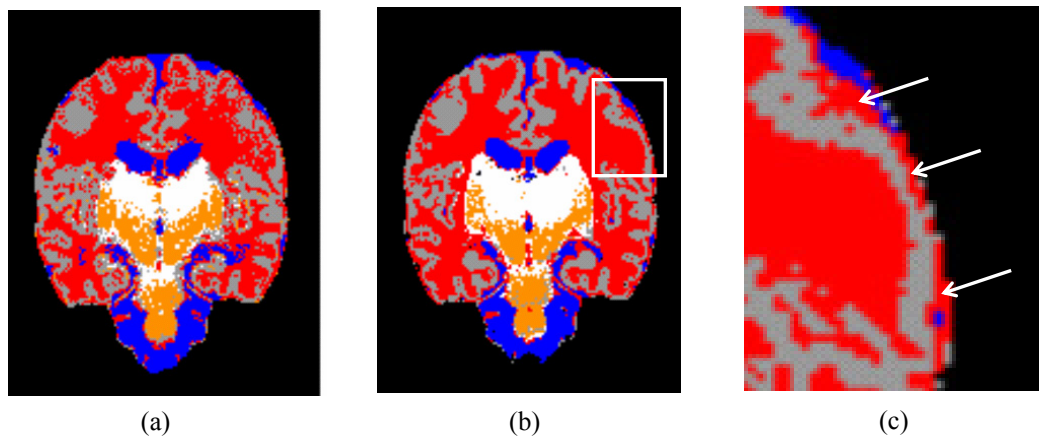
Figure 4.5. Neonatal segmentation from Weisenfeld et al. (2006). (a) The initial k-NN segmentation; (b) The segmentation is improved by combining the probabilistic atlas and MRF extension; (c) As highlighted by the arrows, MLPV are clearly visible where the CSF and GM voxels are misclassified as WM due to the inverted GM/WM contrast (colour code: WM = Red, GM = Grey, CSF = blue).

As previously published methods are essentially derived from related algorithms for adults, they are generally not optimal for the segmentation of the neonatal cortex. First, the MLPV problem on the CSF-GM boundary is not explicitly tackled in any of the previously published methods. Although the use of a probabilistic atlas can provide prior knowledge, the registration between the atlas and new subjects may not be perfect, especially when only affine transformations are used. Although previous methods are able to consistently segment most of the cerebral structures, there are noticeable MLPV visible in the segmentation results, as shown in Figure 4.5. Clearly, the MLPV problem in neonatal segmentation has not been solved by these methods. Secondly, the previous methods are essentially global schemes, meaning that the probability density estimators (either parametric or non-parametric) are used to estimate the distribution of tissue classes throughout the whole brain. However, if the intra-class intensity variability, especially in WM is significant, we have observed that the local segmentation of the cortical GM-WM boundary may be suboptimal. Thirdly, the evaluation of previously published methods is rather limited. To the best of our knowledge none of these methods has been tested on datasets ranging from very premature neonates to neonates at term equivalent age. However, applicability to a wide range of ages is essential if these

approaches are to be used to measure brain development and to quantify any abnormalities related to premature birth. Finally, the construction of a neonatal brain atlas usually requires the segmentation of a large set of representative datasets. However, due to the rapid brain development between 25 weeks GA and 45 weeks GA, many different atlases are required to capture the anatomical changes during the whole period of neonatal cerebral development. As a result, it is a highly challenging task to build brain atlases for developing neonates.

4.4 Neonatal cortex segmentation with MLPV removal

The focus of this work is the segmentation and reconstruction of the neonatal cortex in subjects over a wide age range from very premature (e.g. GA ~ 27 weeks) to beyond term using information from MR images. T2w images have been selected as the source data as they have superior CNR compared to T1w images in this GA group; however the methods developed are not essentially limited to T2w images. An EM-MRF scheme is adopted to perform the tissue classification. The key contribution is a modification of the EM-MRF scheme which allows the detection and removal of MLPV. We introduce a knowledge-based approach to identify and reduce MLPV after every iteration of the EM algorithm. To deal with the WM intensity variability, we split the brain into several regions after the global segmentation. This segmentation algorithm has been quantitatively evaluated on 25 subjects with GA ranging from 27 weeks to 45 weeks.

As the focus of this work is the cerebral cortex, we decided not to explicitly segment subcortical GM, myelinated WM, the corpus callosum and cerebellum. While the contrast between myelinated WM and adjacent deep GM (thalamus and basal ganglia) is relatively small, our experiments show that for the GA range from ~27 to 45 weeks the intensities of T2w MRI alone can consistently provide sufficient gray-white contrast for differentiating cortical GM from WM.

In conclusion, the proposed method aims to segment of cortical GM, non-myelinated WM, CSF and non-brain tissues. Subcortical GM, myelinated WM, corpus callosum and cerebellum are masked off before performing the segmentation.

An overview of the proposed algorithm is shown in Figure 4.6. The following sections describe the algorithm in detail.

4.4.1 Brain extraction and removal of central deep tissues

As the first step of the segmentation process, we use label propagation via image registration to achieve brain extraction and removal of central deep tissues, as these tissues are not relevant for the segmentation of the cortex and their signal intensities are similar to those of cortical GM. The label propagation is implemented as an atlas-based segmentation process. To deal with the fact that neonatal brains are rapidly developing, multiple atlases are used to facilitate the registration and thus the atlas-based segmentation (see Section 4.6 for more details). Briefly, the subjects used for evaluation were separated into three groups according to their gestational age and one subject was randomly selected as the atlas for each group. The brain stem, cerebellum, deep GM (including basal ganglia and thalamus) and corpus callosum were manually labeled in these three subjects. For every testing image, the brain extraction and skull-stripping was achieved using the Brain Extraction Tool (Smith, 2002). These three atlas images are then non-rigidly aligned to each subject and the labels of central deep tissues are propagated into this subject's coordinate system. A binary mask of the cerebral tissues of the atlas brain is also non-rigidly warped to the subject's coordinate system to achieve the skull-stripping. The non-rigid registration algorithm used here is based on the multi-level free-form deformations (FFD) (Rueckert et al., 1999; Schnabel et al., 2001), where the deformations are represented by a 3D tensor product B-Spline

and the non-rigid transformation is computed by moving the control points of the FFD to maximize the normalized mutual information between the images.

Raw T2w MR images

Atlas based brain extraction
and deep GM removal

EM initialization

Three-step
EM iteration

E-step: Compute posterior

$$p(j|\mathbf{x}) = \frac{p(\mathbf{x}|j)p(j)}{p(\mathbf{x})}$$

MRF prior

$$p_{mrf}(k|x_i) = \frac{exp(-U_{mrf}(k|x_i,\boldsymbol{\Phi}))}{\sum\limits_{j=1}^{K} exp(-U_{mrf}(j|x_i,\boldsymbol{\Phi}))}$$

M-step: Compute PDF

MLPV removal

For every voronoi region

Local segmentation

Segmentation results

Cortex reconstruction using
implicit surface evolution

Cortical surfaces

Figure 4.6. Flow diagram of the overall system for neonatal cortical segmentation and reconstruction. The cortical reconstruction will be discussed in the next chapter.

4.4.2 Expectation-Maximization (EM) algorithm for tissue classification

The EM algorithm is a general statistical technique to estimate missing information based on observed data. It was originally presented in a general form by Dempster et al. (1977). In the context of brain segmentation, the observations are the image intensities, the missing data are the class labels for every voxel and the parameters of the class likelihood probabilities. The intensity inhomogeneity or bias fields which can cause noticeable misclassification are often modelled and estimated by extending the standard EM method. Wells et al. (1996) proposed an EM algorithm in which the probability density function (PDF) of every tissue class is modelled by a Gaussian distribution and the bias field is modelled by a zero mean Gaussian prior probability density. Van Leemput et al. (1999a) suggested integrating a probabilistic atlas into this framework to provide spatially varying prior probabilities at every voxel. The bias field in this work is represented as a linear combination of smooth basis functions.

The EM algorithm consists of an expectation step (E-step) which performs the classification and a maximization step (M-step) which updates the parameter estimation. Assuming a Gaussian distribution and given the initial parameters $\mu_k^{(0)}$ and $\sigma_k^{(0)}$, the algorithm iteratively maximizes the data likelihood and updates the tissue classification.

$$\text{E-step:} \qquad p(k|x_i) = \frac{p(x_i|k)prior(k)}{p(x_i)} \qquad\qquad (4.1)$$

$$\text{M-step:} \qquad \mu_k^{(m+1)} = \frac{\sum_{i=1}^{N} p^{(m)}(k|x_i)x_i}{\sum_{i=1}^{N} p^{(m)}(k|x_i)} \qquad\qquad (4.2)$$

Data probability

$$p(\boldsymbol{x}) = \sum_{k=1}^{M} p(k)p(\boldsymbol{x}|k)$$

Class likelihood probability

$$p(\boldsymbol{x}|k) = Gaussian\_distribution$$

Posterior probability

$$p(k|\boldsymbol{x}) = \frac{p(\boldsymbol{x}|k)p(k)}{p(\boldsymbol{x})}$$
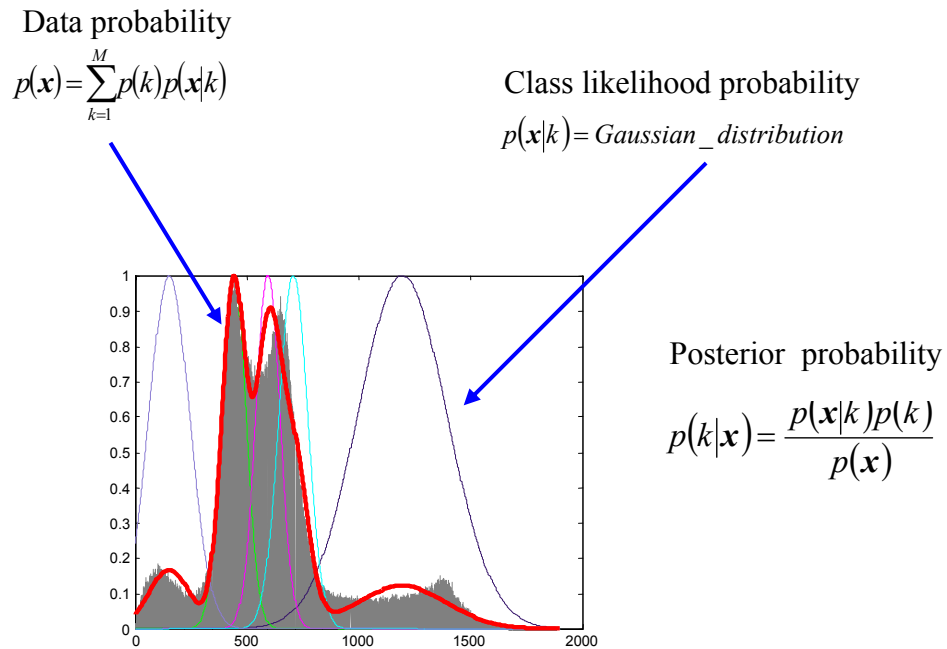
(a) An illustration of data probability and class likelihood probability

Initialize the Gaussian distribution

$$p(\boldsymbol{x}|k) = Gaussian\_distribution$$

E-step
compute posterior
probability

$$p(k|\boldsymbol{x}) = \frac{p(\boldsymbol{x}|k)p(k)}{p(\boldsymbol{x})}$$

M-step
adjust the Gaussian
parameters
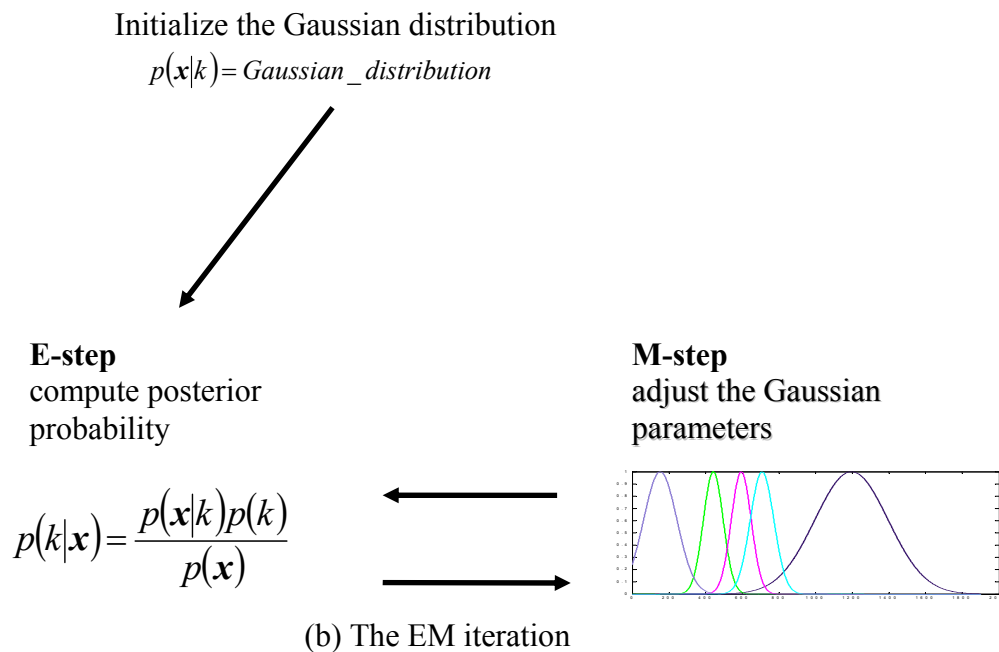
(b) The EM iteration

Figure 4.7. An illustration of Expectation-Maximization (EM) algorithm. (a) The data probability is the weighted summation of prior probability and class likelihood probability. Posterior probability is computed from data probability, class likelihood probability and prior knowledge. (b) The EM iteration consists of an E-step where the posterior probability is computed and a M-step where the parameters of Gaussian distribution are optimized.

$$\left(\sigma_k^{(m+1)}\right)^2 = \frac{\sum_{i=1}^{N} p^{(m)}\left(k|x_i\right)\left(x_i - \mu_k\right)^2}{\sum_{i=1}^{N} p^{(m)}\left(k|x_i\right)} \tag{4.3}$$

Here x_i is the intensity of a voxel i and $prior(k)$ is the prior probability for tissue class k. $p(x_i|k)$ is the class likelihood probability which is a Gaussian distribution. The corresponding class posterior probabilities $p(k|x_i)$ are computed in the E-step. An illustration of the EM algorithm is shown in Figure 4.7.

The EM algorithm requires an initial estimate of tissue class parameters which can be computed from the prior probabilities. Probabilistic atlases are often used for this purpose. They act as the prior $p(k|x_i)$ to predict the probability of a voxel x_i belonging to the tissue class k and combine spatial information about different tissues into the EM algorithm. However, the large anatomical changes that occur in the neonatal period preclude the use of a single standard atlas, especially in the cortical regions, for the full age range in this study. We initialized the EM algorithm by performing a k-means clustering to generate an initial segmentation for each subject that is then slightly blurred by a Gaussian kernel
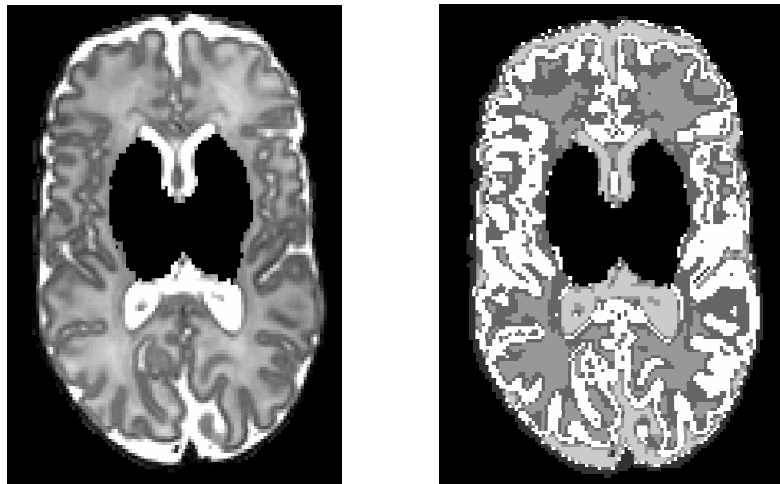
Figure 4.8. An illustration to show the performance of k-means segmentation. This intensity-based classifier causes lots of mislabeled partial volume voxels on the WM/GM and WM/CSF boundaries.

($\sigma = 1.5 \times voxelsize$) and normalized to simulate an atlas. Figure 4.8 shows the performance of k-means segmentation. Note the MLPV are noticeable on the GM/WM and WM/CSF boundaries. Our experience has shown that there is sufficient contrast between cortical GM and WM in T2w images of neonates to successfully achieve GM-WM segmentation.

4.4.3 MLPV detection and removal

The EM algorithm in its original form will wrongly classify partial volume voxels on the CSF-GM boundary in neonatal MR Images. An example illustrating this problem in the case of a T2w image is given in Figure 4.9(a-b): Many voxels on the CSF-GM boundary are incorrectly classified as WM. A similar problem occurs at the CSF-nonbrain tissue boundary because CSF is the brightest and non-brain tissue is darkest.

These errors are partly caused by the voxel-wise tissue classification used in the EM scheme, since the posterior probability of a voxel only depends on the signal intensity and prior probability. Thus, no information about spatial homogeneity is used in this segmentation scheme. Markov Random Fields (MRFs) are commonly used to constrain the spatial homogeneity of the tissue labelling. Elfadel and Picard (1994) has exploited the MRF to impose a spatial homogeneity constraint on image segmentation. The exact calculation of the MRF posterior is not practically feasible (Van Leemput et al., 1999a) and mean field theory (Langan et al., 1992; Zhang, 1992) is often used to provide an approximation as it is a minimum variance Bayes estimator of the true MRF (Li, 1995). A widely used algorithm for brain MRI segmentation proposed by Van Leemput et al. (1999a) uses MRF with constraints to avoid over smoothing effects in fine brain structures.

Specifically, the tissue class k is assumed to be a realization of a random process and the Hammersley-Clifford theorem states that this random field can be

described as a Gibbs Random Field (Li, 1995). Its configuration obeys the Gibbs distribution:

$$f(k|\boldsymbol{\Phi}) = \frac{\exp(-U_{mrf}(k|\boldsymbol{\Phi}))}{\sum\limits_{k}\exp(-U_{mrf}(k|\boldsymbol{\Phi}))} \tag{4.4}$$

where $U_{mrf}(k|\boldsymbol{\Phi})$ is an energy function and $\boldsymbol{\Phi}$ represent the MRF parameters. The prior probability that a voxel belongs to a tissue type depends on the tissue type of its neighbors.

We exploit a first-order neighborhood system, i.e., the six nearest neighbors on the 3D image grid are used. Given a voxel i, its neighborhood is defined by $N_i = \{i^n, i^s, i^w, i^e, i^t, i^b\}$ where i^n, i^s, i^w and i^e are four neighbors in the imaging plane and i^t and i^b are the nearest voxels out of the imaging plane. Following the Potts model (Ising, 1925), the MRF energy function at voxel i is:

$$U_{mrf}(k|x_i, \boldsymbol{\Phi}) = \boldsymbol{z}_i^t \boldsymbol{G} \boldsymbol{g}_i \tag{4.5}$$

$$\boldsymbol{z}_i = \boldsymbol{e}_k$$

$$\boldsymbol{g}_i = \boldsymbol{z}_{i^n} + \boldsymbol{z}_{i^s} + \boldsymbol{z}_{i^w} + \boldsymbol{z}_{i^e} + \boldsymbol{z}_{i^t} + \boldsymbol{z}_{i^b}$$

where $\boldsymbol{z}_i = \boldsymbol{e}_k$ is a unit vector with the kth component being one and $\boldsymbol{g}_i$ counts for every tissue class k the number of neighbouring voxels belonging to k. The matrix $\boldsymbol{G}$ is the so-called tissue class compatibility matrix. The (m, n) element in $\boldsymbol{G}$ denotes the contribution of a neighbor voxel belonging to class n to the energy function $U_{mrf}(m|x_i, \boldsymbol{\Phi})$. The tissue class compatibility matrix $\boldsymbol{G}$ is estimated using a least square fitting procedure (Li, 1995; Van Leemput et al., 1999a).
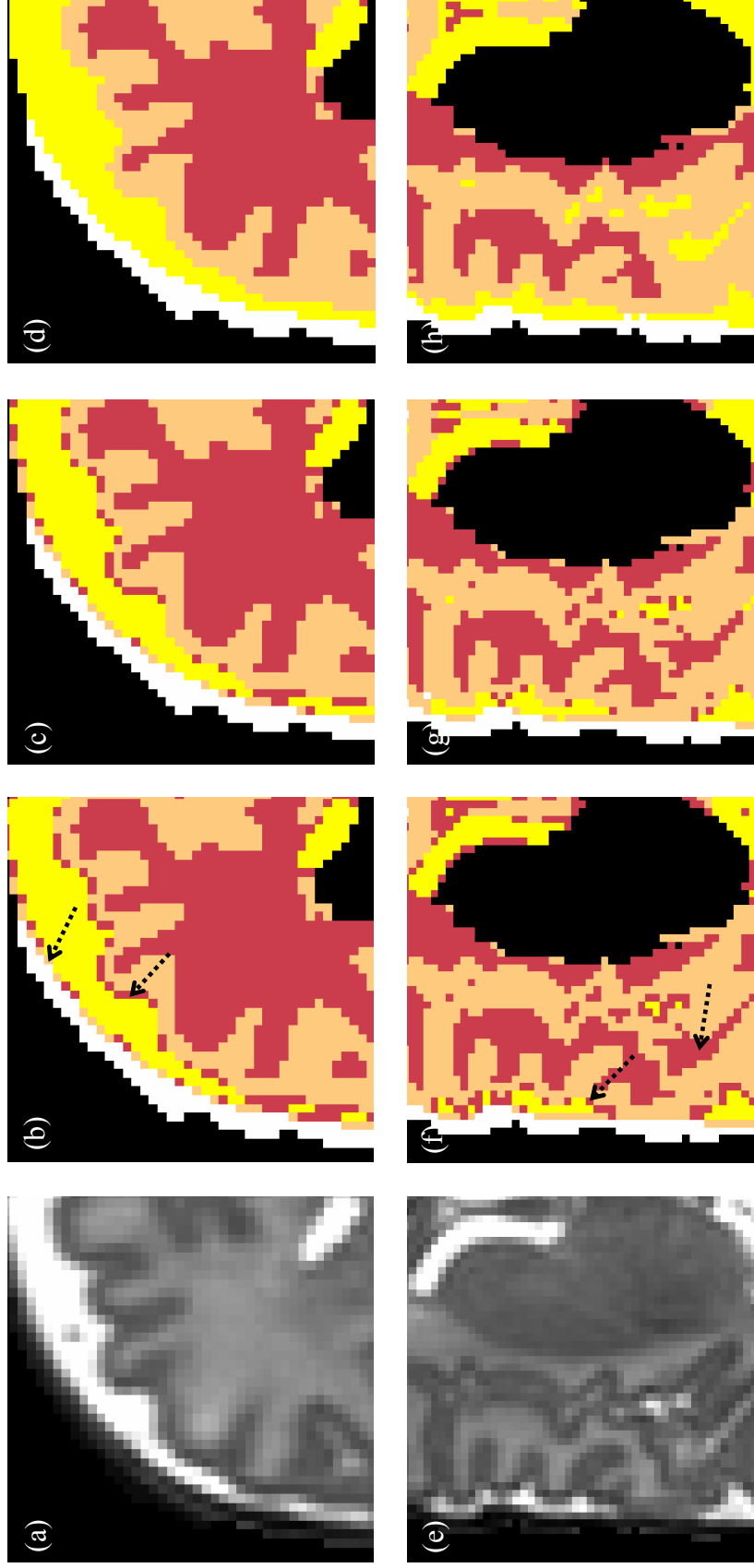
Figure 4.9. An illustration of the three-step EM scheme with PV removal. (a) An enlarged neonatal T2w image; (b) Partial volume voxels on the CSF-GM and CSF-non-brain boundaries are incorrectly classified by the original EM method (e.g. at locations marked by arrows); (c) Segmentation results after the 4-th iteration of three-step EM method; (d) The final results after 14 iterations. Similarly, (e-f) shows CSF voxels in the sulci that are originally classified as WM due to partial volumes from adjacent GM are finally segmented properly. (g) Results after 8-th iteration; (h) Final classification after 14-th iteration. The colour-coding scheme is defined as follows: ▮-WM, ▮-GM, ▮-CSF, ☐-nonbrain tissue.

It is worthwhile to discuss the performance of the EM-MRF scheme on MLPV removal. Note that the matrix G is estimated globally and determines the computation of the MRF energy function (equation 4.5) for a specific voxel by combining the tissue class information of its first-order neighbors. The introduction of the MRF energy function and tissue class compatibility matrix enhances the classic EM scheme by removing the isolated partial volumes; however, the EM-MRF scheme alone is not sufficient to remove the MLPV in neonatal brain MRI. The reason for this is the fact that there are a large number of voxels on the CSF/GM boundary which can be misclassified. If two MLPV are neighboring each other, one can prohibit the other from being corrected by contributing to its energy function via the tissue class compatibility matrix. Therefore, to allow the removal of MLPV we have developed a knowledge based approach to improve the EM-MRF scheme. For this purpose we use the knowledge that WM MLPV typically appear on the CSF-GM boundary for neonatal T1w and T2w images. If a voxel is classified as WM and within its first order neighbourhood there are CSF and GM voxels simultaneously, this voxel is likely to be a partial volume voxel. The same detection rule can be used for WM and GM MLPV on the CSF-nonbrain tissue boundary in neonatal T2w images.

Mean field theory is used to compute the optimal parameters. The update equation 4.1 is kept unchanged while the prior probability is now computed from both atlas prior $p_{atlas}(k|x_i)$ and MRF prior $p_{mrf}(k|x_i)$.

$$p(k|x_i) = \frac{p(x_i|k) \cdot prior(k|x_i)}{p(x_i)} \tag{4.6}$$

$$prior(k|x_i) = \frac{p_{atlas}(k|x_i) \cdot p_{mrf}(k|x_i)}{\sum_{j=1}^{K}\left(p_{atlas}(j|x_i) \cdot p_{mrf}(j|x_i)\right)}$$

$$p_{mrf}(k|x_i) = \frac{\exp\left(-U_{mrf}(k|x_i, \boldsymbol{\Phi})\right)}{\sum_{j=1}^{K}\exp\left(-U_{mrf}(j|x_i, \boldsymbol{\Phi})\right)}$$

The voxels which are labelled as MLPV after each EM step can be relabelled by adjusting the prior probabilities to favor more appropriate tissue classes. If a voxel x_i is likely to be incorrectly classified as WM on the CSF-GM boundary, the prior probability $p_{atlas}(wm|x_i)$ should be decreased. Because the sum of prior probability of all tissue classes should always be one, the expected tissue classes can be favoured by increasing their prior probabilities. Specifically, the following rules are used to adjust $p_{atlas}(wm|x_i)$:

$$p_{atlas}^{(m+1)}(wm|x_i) = \lambda p_{atlas}^{(m)}(wm|x_i), \ 0 < \lambda < 1 \qquad (4.7)$$

$$p_{atlas}^{(m+1)}(CSF|x_i) = p_{atlas}^{(m)}(CSF|x_i) \left(1 + (1-\lambda) \frac{p_{atlas}^{(m)}(wm|x_i)}{p_{atlas}^{(m)}(CSF|x_i) + p_{atlas}^{(m)}(gm|x_i)} \right)$$

$$p_{atlas}^{(m+1)}(gm|x_i) = p_{atlas}^{(m)}(gm|x_i) \left(1 + (1-\lambda) \frac{p_{atlas}^{(m)}(wm|x_i)}{p_{atlas}^{(m)}(CSF|x_i) + p_{atlas}^{(m)}(gm|x_i)} \right)$$

The final classification of x_i will be determined by both the priors for CSF and GM and the signal intensity (influencing the class likelihood $p(x|k)$). As a result, the original two-step classification (EM-MRF) is transformed into a three-step (EM-MRF-MLPV) process. Figure 4.9(c-d) indicates the segmentation results after the MLPV removal step is integrated into the EM algorithm. As more iterations are preformed, fewer misclassifications are observed in the resulting segmentation. The algorithm is stopped either when the parameters converge (the relative changes of mean and variance between two consecutive iterations are smaller than 1%) or a maximum number of iterations is reached (35 iterations in our experiments). The parameter λ in equation 4.7 influences the speed of convergence, but we have found that the final segmentation results are relatively insensitive to its value. As a result we set λ to be 0.5 for all experiments.

The MLPV removal strategy can be extended to refine the classification of CSF voxels in sulci. Because of the limited image resolution, the CSF voxels in some sulci may be mislabeled as WM (Figure 4.9(e-f)). These mislabeled CSF voxels are detected by performing a connected component labeling on the WM volume after

each iteration. Small unconnected WM components are identified if they are much smaller in volume than the largest component. The first-order neighborhood of every small component is checked. If the component is included within CSF and/or GM, it is suspected to be CSF and the prior probabilities are then adjusted. Figure 4.9(g-h) shows the detection and classification of CSF voxels in sulci. The misclassification is gradually corrected and the CSF voxels are properly segmented.

4.4.4 Local segmentation by brain splitting

Neonatal brain MR images typically exhibit higher intra-tissue intensity variability mainly due to the immaturity of developing brain tissues. The effects of intensity variability cannot be totally eliminated by inhomogeneity (bias field) correction and so its influences on tissue classification cannot be ignored.

On the other hand, the EM algorithm described in the previous section is essentially a global scheme, which means that a tissue class throughout the image is modelled by as a single Gaussian distribution. Global schemes often show limited performance if the intensity variability is significant. Figure 4.10 gives an example to illustrate this imperfection. The coronal slice in Figure 4.10(a) shows substantial intensity variability in both GM and WM, although boundaries between these tissues are clearly visible to human observers. The intensity variability, although not very noticeable to the naked eye, can be highlighted if different thresholds are used to extract cortical GM. In the case shown, the global segmentation oversegments the inferior-left area and undersegments the anterior-left area.

Since the tissue boundaries are visible, a local segmentation technique should be able to improve the results. This can be achieved if the brain is parcellated into multiple regions and a separate set of Gaussians is used to estimate the tissue class parameters in each region; that is, only voxels within in one region are used to estimate Gaussian parameters for that region. We have not found it necessary to

use overlapping regions or blending regional parameters, to ensure reliable segmentation at region boundaries although this is an option.

A reasonable parcellation of the brain should balance the ability of PDF estimation to tackle local intensity variability and the segmentation stability to noise. If the brain is parcellated into too few regions and each one contains a large number of voxels, the local PDF estimation will be more robust, but the resulting segmentation tends to miss small details. The use of a larger number of smaller regions strengthens the ability to capture local intensity differences, but may suffer from lack of robustness.

To perform the brain parcellation, we assemble a 4D vector $\vec{d} = (x, y, z, I)$ of all GM and WM voxels which have been labelled by the global segmentation step, as these two tissues have the most intensity variability. (x, y, z) is the 3D coordinate of a voxel and I is its intensity. A k-means clustering is performed on the 4D vectors and the coordinates of clustering centres are used to define a Voronoi tessellation on the brain space. The motivation for adding intensity I to the feature vector is to prevent the regions with consistent local intensity from being split. The k-means algorithm is initialized by the centroids of large voxel groups. To avoid the convergence to local minima, the clustering process is repeated 10 times with random perturbations added to the initial centres. The maximal magnitude of perturbation along each axis is set to be 10% of the length of bounding box enclosing the initial centres. The maximal perturbation for intensities is 10% of mean WM intensity. Figure 4.10f-g shows the Voronoi regions obtained for one subject. The number of Voronoi regions is empirically determined, with 7 regions providing good performance in our experiments.

The segmentation step is finally performed independently on every Voronoi region, initialized by the output of a global segmentation. As a result, the over-segmentation of cortical GM is corrected (Figure 4.10(e)). In our experience the

intensity-spatial clustering usually generates a nearly uniform splitting for a brain mainly due to the spherical shape of the brain.

(a)

(b)

(c)

(d)

(e)

(f)

(g)
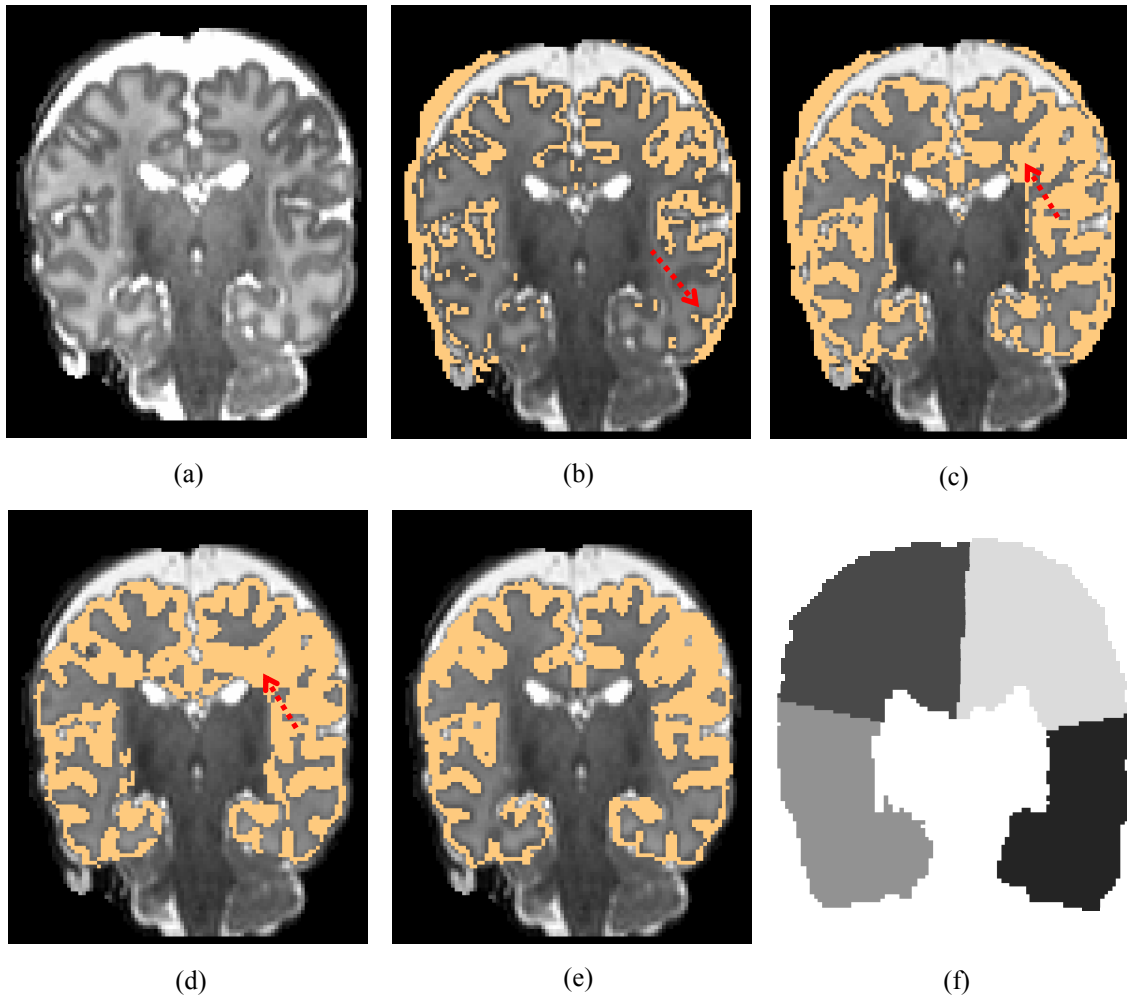
Figure 4.10. (a) A typical T2w image has substantial intensity variability in WM, which degrades the segmentation. (b) A threshold of 450 is sufficient to segment cortical GM in the top-left part, but results in clear under-segmentation in the bottom-left area. (c) Increasing the threshold to 510 causes over-segmentation in the top-left area. (d) This intra-class intensity variability leads to segmentation errors if a global EM scheme is used (arrows indicate imperfections of segmentation). (f) The segmentation is improved by performing a regional segmentation to refine the output of the global method. The computed Voronoi regions that were used in (e) are shown in (f) and (g).
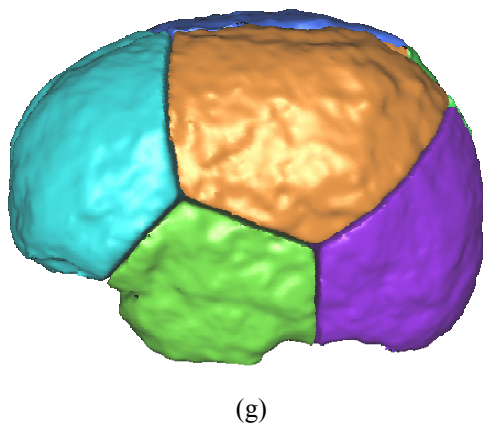
4.5 Experimental approaches

4.5.1 Selection of subjects

We applied our method to 25 pre-term subjects selected from a large longitudinal MR study of cerebral development of pre-term and term-born neonates. The pre-term infants were recruited from the Neonatal Intensive Care Unit at Hammersmith Hospital, and term-born control infants were recruited from the postnatal wards. Infants with congenital anomalies, metabolic disease or congenital infections were excluded and there were no focal lesions in the brains studied. The median GA at birth for these neonates was 28.86 (range 24–40) week and the median GA at scan was 34.86 (range 27–44) week. The median birth weight was 871g (range 370–1,606 g). All studies were conducted with approval from Hammersmith Hospital Research Ethics Committee and the infants were scanned following written parental consent. Preterm infants born at <32 weeks gestation were scanned from within the first week of life to term equivalent age at varying gestations.

4.5.2 Image acquisition

MR images were acquired on a 3T Philips Intera system (Best, Holland) using a standard 6 head channel array coil. Preterm infants were sedated with chloral hydrate and a trained neonatologist was present throughout scanning. Term born controls were fed, swaddled and the examination was carried out in natural sleep. All infants were monitored with pulse oximetry and electrocardiography. Ear protection, consisting of silicon-based dental putty individually moulded and fitted into the external ear and mini-muffs (Natus Medical, San Carlos, CA) was used to achieve approximately 30 dB sound attenuation. The infant's position was stabilized using a suction-evacuated pillow.

The MR sequence parameters were as follows: Multi-slice T2-weighted fast spin echo images composed into 3D pseudo volumes by prescribing an overlapping slice geometry were acquired with TR=1712/TE=160ms, FOV=220mm, matrix 224×224, flip angle 90°, slice thickness 2mm with 50% slice overlap and SENSE factor 1 with intensity normalized to a body coil image. All T2 weighted images were acquired in the transverse plane. The acquisition produces voxels at approximately 1mm spacing in all 3 orthogonal directions and the resulting T2 images were interpolated to isotropic $0.86mm^3$ voxels using cubic B-spline interpolation. T1-weighted images were also acquired using a MPRAGE sequence for all neonates. However, the contrast between cortical GM and WM/CSF is less pronounced on T1w images. Therefore, we have only used T2w images in this study. As RF inhomogeneity is more pronounce in high field MR scanners, a bias correction procedure is performed for all images using the N3 software (Sled et al., 1998) prior to the application of segmentation algorithm.

4.5.3 Comparison with manual segmentations

To quantitatively evaluate the segmentation results, the author first manually segmented three orthogonal slices for every subject. A radiologist then checked all manual segmenation and corrected any errors. A manual segmentation of the whole cortex in 3D was not attempted due to the complexity of the structure and the large number of partial volume voxels. The overlap ratio between the automatic and manual segmentation is quantified by the Dice similarity coefficient (DSC) (Dice, 1945). For two segmented regions A and B , the DSC is defined as: $DSC = \frac{2 \times |A \cap B|}{|A| + |B|}$. A DSC of zero means complete dissimilarity and a value of one means perfect overlap. DSC measures above 0.7 are usually regarded as a satisfactory level of agreement between two independent segmentations (Zijdenbos et al., 1994).

To further evaluate the performance of EM-MRF-MLPV scheme, the number of false positives (FP) and false negatives (FN) between the automatic and manual segmentation are also computed. FP is defined as the percentage area of automatic segmentation that is not labeled manually and FN is defined as the percentage area of manual segmentation that is not labeled by the automatic approach. We also estimate the segmentation errors along the tissue boundary by calculating the boundary segmentation errors which is defined as the mean minimal distances between two contours extracted from automated and manual segmentation.

4.6 Results and evaluation

Label propagation is used to segment deep structures and exclude them from further analysis. As there are noticeable developments in the neonatal brains during the GA range from ~27 to 45 weeks, to aid the initial non-rigid registration used for label propagation, we empirically divided the 25 neonates into three groups according to their gestational age: ~27 – 34 weeks (simple brains, 9 subjects), 34 – 39 weeks (medium brains, 6 subjects) and 39 – 45 weeks (complex brains, 10 subjects), as the GA is positively correlated with increasing cortical complexity. One image was selected as an atlas for each group and the subcortical GM, myelinated WM, corpus callosum and cerebellum were manually segmented. The atlas image was registered to all other images in its group using the multi-level FFDs based non-rigid registration algorithm (Rueckert et al., 1999; Schnabel et al., 2001). Parameters for the non-rigid registration were as follows: 4 levels of FFDs, control point spacing: 20mm, 10mm, 5mm and 2.5mm for each level, gradient descent optimization and normalized mutual information as the similarity measure.

The atlas images were only used for the purpose of label propagation, and still segmented for performance evaluation. Figure 4.11 shows typical results of label propagation to exclude tissues in four infants spanning the age range. The contours of the propagated masks are overlaid on transverse and sagittal views. All subjects

were visually assessed for label accuracy and the label propagation strategy shows good performance in all three GA groups.
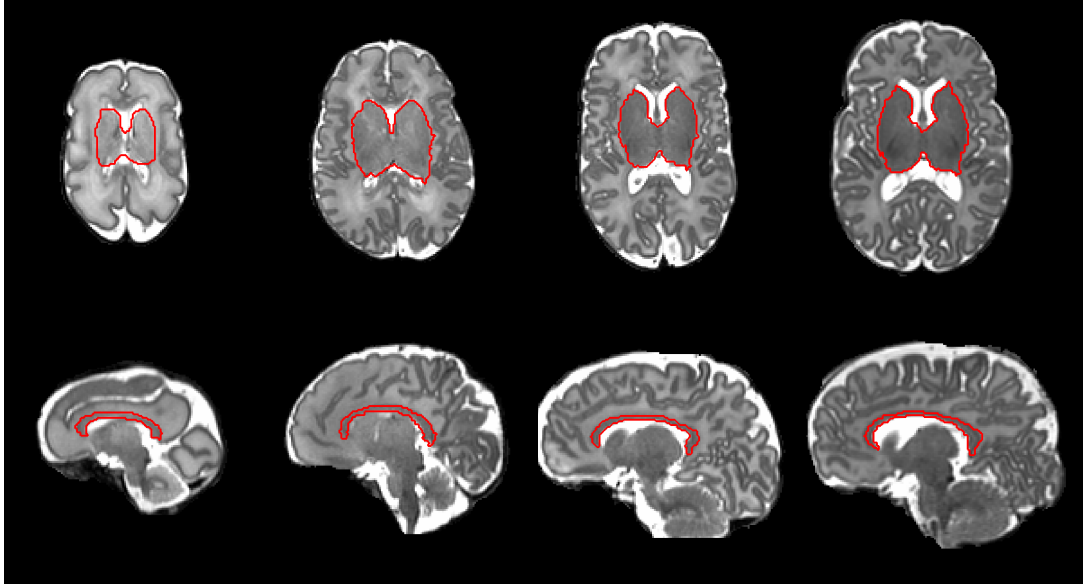
Figure 4.11. Results of label propagation to exclude the deep GM and corpus callosum. From left to right, the gestational ages at scan are 29.86, 34.14, 39.86 and 44 weeks.

Figure 4.12 illustrates the improvements produced by the MLPV removal step and local segmentation for a typical subject. A T2w coronal view of a preterm infant at term equivalent age whose images display significant WM intensity variability is shown in Figure 4.12(a). When only the global Gaussian mixture model and two-step EM method is used, a substantial number of MLPV voxels can be seen on the CSF-GM and CSF-non brain tissue boundaries (Figure 4.12(b)). These voxels are assigned to the correct tissue class labels after the MLPV removal step is integrated into the EM iteration (Figure 4.12(c)). The segmentation of the inner cortical surface is improved when the brain splitting strategy is used, as shown in Figure 4.12(d).

Results of the automatic segmentation of a number of neonates at different gestational ages are presented in Figure 4.13. Visual inspection of these results shows that cortical GM is reasonably well segmented. Partial volume voxels on the CSF-GM and CSF-non-brain boundaries are successfully removed. The majority of

CSF voxels in sulci are correctly classified. Table 4.1 summarizes the results of the comparison with the manual segmentation. The mean DSC values for cortical GM and WM for each GA group are presented, for the case where four classes are used: GM, WM, CSF and non-brain background. The WM results exclude the corpus callosum and any WM within the region of deep GM removed by the initial label propagation step. The EM-MRF-MLPV scheme significantly improves the DSC measures of cortical GM and WM compared to the EM-MRF method when no

(a)   (b)

(c)   (d)
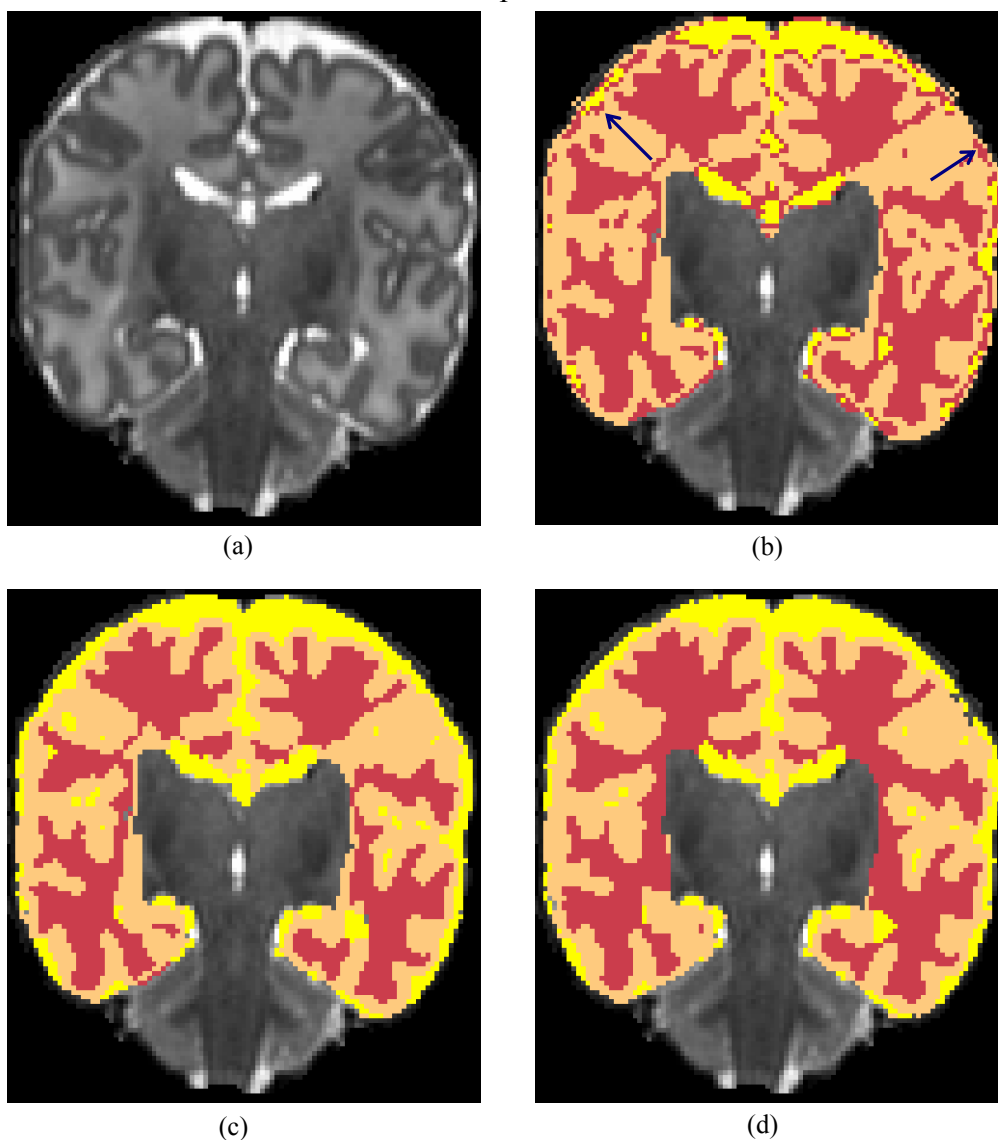
Figure 4.12. An illustration to show the effects of refining the segmentation. (a) A coronal slice from a neonate scanned at 44 weeks. (b) When only the two-step EM method is used, voxels at the CSF-GM and CSF-nonbrain boundaries are classified as WM – i.e. they are mislabeled (MLPV effect, arrows). (c) This is successfully corrected if the MLPV removal step is integrated. (d) Refining the result using regional segmentation further improves the GM-WM delineation (e.g. at arrow).
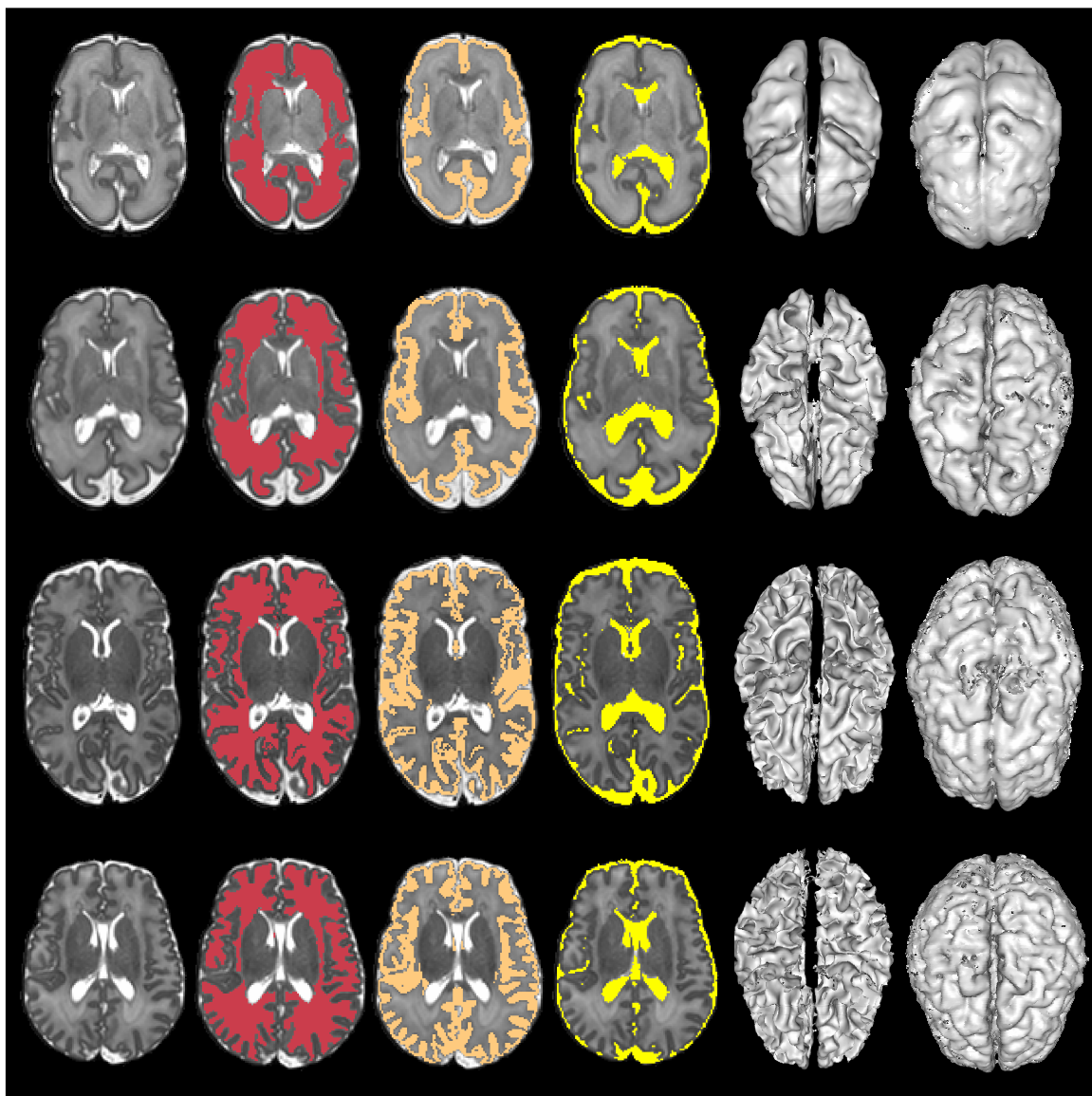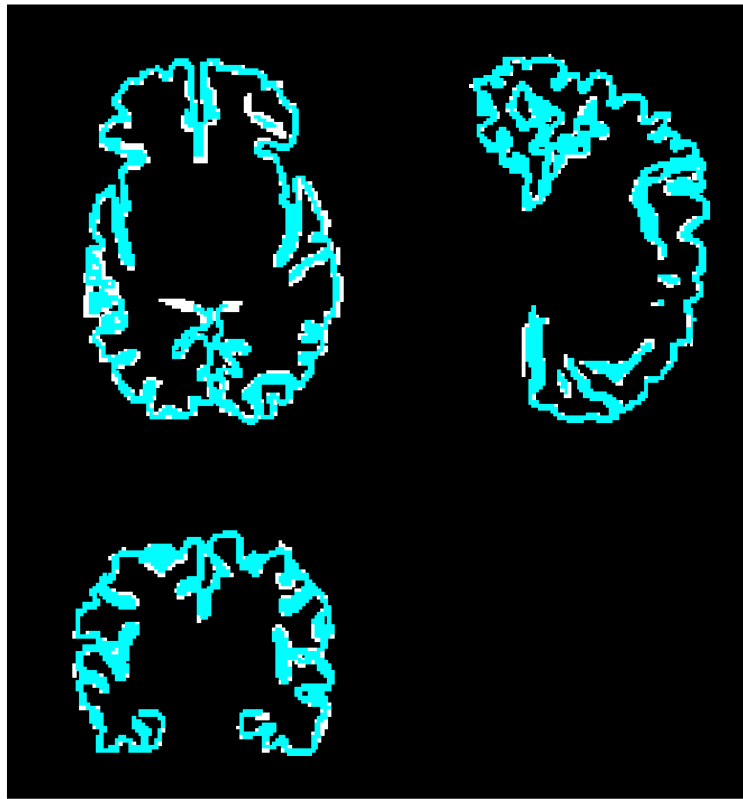
Figure 4.14. An example of intra-rater reproducibility test. The same subject is manually segmented twice by the same human operator. Good reproducibility is observed.

MLPV removal step is performed (for GM: $t=13.43$, $P<0.0001$; for WM: $t=4.90$, $P<0.0001$; paired t-test). The performance of the EM-MRF-MLPV scheme is further improved by the proposed local segmentation scheme (for GM: $t=7.07, P<0.0001$; for WM: $t=5.35$, $P<0.0001$). This improvement is more noticeable in preterm infants with non cystic WM disease who have diffuse excessive high signal intensity injury (DEHSI) on T2W images. Furthermore, for the simple brain group, the intra-tissue class intensity variability is even more pronounced and we found that dividing the WM of these very premature infants into two tissue classes can improve the segmentation. A total of five classes (WM modeled by two Gaussian distributions) were therefore used. The second row in Table 4.1 summarizes the corresponding DSC values. Compared to the results with four tissue classes (the first row in Table 4.1), the improvement for GM are significant (for GM: $t=5.65$, $P=0.0005$; for WM: $t=2.34$, $P=0.0472$). The

mean DSC of all 25 subjects is 0.758 ± 0.037 for GM and 0.794 ± 0.078 for WM. The overall performance is good to excellent compared to the manual labeling as neonates become more mature. This supports the statement that neonatal T2w MRI can consistently provide sufficient GM/WM contrast for intensity based segmentation in neonates from a very premature age to term-equivalent age.

Table 4.2 reports the false positive and false negative errors using the three step EM scheme. Both FP and FN are low, showing a good agreement between automatic and manual segmentation. The boundary segmentation errors of cortical GM are reported in Table 4.3. The overall boundary errors are smaller than 1 voxel. Less than 10% of the GM boundaries show errors greater than 2 voxel, which indicates that large errors are not common.

Reasonable intra- and inter-rater reproducibility is important for assessing the results of the automatic segmentation. For the estimation of the intra-rater variability, the same rater was asked to redo the segmentation of cortical GM on the same three orthogonal slices in 6 selected neonates. The time interval between two manual segmentations was four weeks. Table 4.4 lists the DSC values for these 6 neonates. An example of this intra-rater reproducibility test is given in Figure 4.14. The mean DSC is 0.874 ± 0.034, which suggests that the differences between two manual segmentations are relatively small and the intra-rater reliability is high.

As for the inter-rater reproducibility, two independent observers had interactively marked the cortical and thalamic areas on every slice of 10 preterm infants in two of our previous studies. The variation between measured cortical surface area, volume and thalamic volume assessed by the different raters was less than 3% (Srinivasan et al., 2006; Kapellou et al., 2006). Prastawa et al. (2005) also reported good inter-rater reproducibility where the mean DSC values between two operators were 0.755 for GM and 0.758 for non-myelinated WM respectively.

Table 4.1
Dice similarity values of cortical GM and WM for each GA group.

GA	GM			WM		
	Global	Global+PVs	Global+Local +PVs	Global	Global+PVs	Global+Local +PVs
27w − 34w	0.67 ± 0.04	0.70 ± 0.04	0.71 ± 0.04	0.77 ± 0.02	0.81 ± 0.02	0.82 ± 0.02
27w − 34w Five tissue classes	0.69 ± 0.03	0.72 ± 0.04	0.73 ± 0.03	0.77 ± 0.02	0.82 ± 0.01	0.82 ± 0.01
34w − 39w	0.74 ± 0.03	0.76 ± 0.03	0.77 ± 0.02	0.75 ± 0.03	0.81 ± 0.02	0.81 ± 0.02
39w − 45w	0.76 ± 0.03	0.78 ± 0.02	0.79 ± 0.02	0.71 ± 0.05	0.75 ± 0.11	0.76 ± 0.12

Table 4.2
False positive and false negative errors of EM-MRF-MLPV scheme.

GA	GM		WM	
	False positive	False negative	False positive	False negative
27w − 34w	0.14 ± 0.04	0.05 ± 0.01	0.04 ± 0.01	0.13 ± 0.03
27w − 34w Five tissue classes	0.10 ± 0.06	0.07 ± 0.02	0.07 ± 0.02	0.09 ± 0.02
34w − 39w	0.08 ± 0.06	0.06 ± 0.02	0.07 ± 0.02	0.11 ± 0.02
39w − 45w	0.06 ± 0.05	0.06 ± 0.02	0.09 ± 0.02	0.12 ± 0.05

Table 4.3
Boundary segmentation errors (in mm) of EM-MRF-MLPV scheme.

GA	GM				WM			
	Mean	Std	> 1 voxel	> 2 voxel	Mean	Std	> 1 voxel	> 2 voxel
27w – 34w	0.47	1.84	11.2%	7.9%	0.31	1.23	14.7%	7.8%
27w – 34w Five tissue classes	0.41	1.68	9.9%	6.7%	0.28	1.27	15.9%	9.0%
34w – 39w	0.30	1.46	8.6%	6.0%	0.22	1.01	11.1%	6.1%
39w – 45w	0.11	0.81	6.2%	3.4%	0.29	1.37	15.0%	9.0%

Table 4.4
The Dice similarity values between two manual segmentations.

GA	27	29.86	33.86	36.57	39.86	43.86
DSC	0.836	0.833	0.890	0.878	0.890	0.919

4.7 Discussion

We have presented a fully automatic segmentation algorithm for neonatal brain MRI with emphasis on the classification of cortical GM. After studying the intensity characteristics of both T1w and T2w MRI of developing brains from early premature to term equivalent age we identified the phenomenon of mislabelled partial volumes (MLPV) at CSF-GM interfaces, caused by the inverted GM-WM contrast, as a key source of errors in cortical segmentation. To address this problem we extended the classical EM-MRF scheme with a MLPV removal step. Our experiments show that this extension plays an important role in achieving accurate segmentation of cortical surfaces in neonates. Initial spatial priors for tissue class were obtained directly from the MR images of each infant using a k-means clustering. This method was adopted as there are no suitable probabilistic atlases available for neonatal brains and the rapid pace of development during this period of life undermines the use of a single atlas for the whole age range. The intensity variability in WM in neonates can also be a challenge for global intensity-based segmentation methods. We therefore adopted an approach in which the brain is subdivided into a few Voronoi regions, each of which is segmented using the EM-MRF-MLPV approach. Our method has been evaluated on T2w images from 25 neonates with a wide range of gestational age (from GA ~27w to 45w), and the contribution of each algorithmic step has been demonstrated. The segmentation results have been validated against manual segmentation of selected orthogonal slices using the DSC similarity measure and verified by visual inspection. DSC scores of 0.758 ± 0.037 for GM and 0.794 ± 0.078 for WM confirm reliable and accurate segmentation for both preterm and term-born subjects.

It is worth mentioning that even if an atlas were available, relying solely on the atlas may not be sufficient to eliminate all MLPV. There are a couple of reasons for this. First, the non-rigid registration between atlas and images may not be perfect

(a)

(b)

(c)
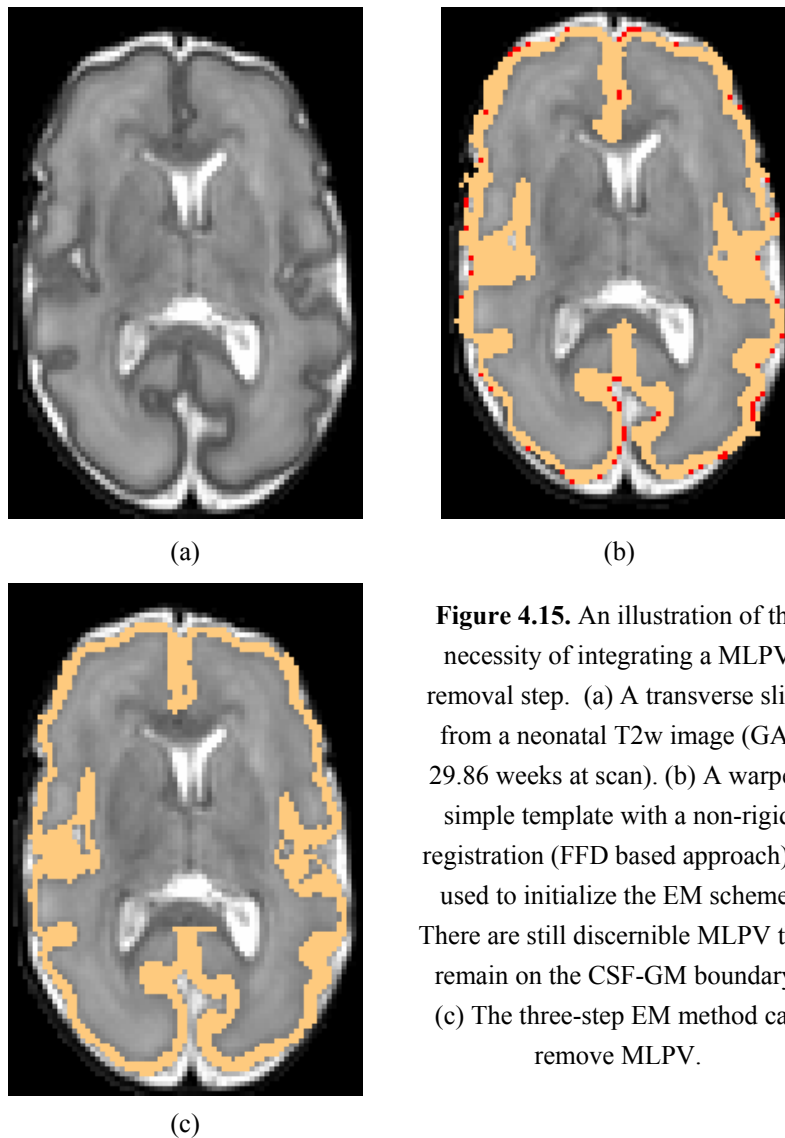
Figure 4.15. An illustration of the necessity of integrating a MLPV removal step. (a) A transverse slice from a neonatal T2w image (GA: 29.86 weeks at scan). (b) A warped simple template with a non-rigid registration (FFD based approach) is used to initialize the EM scheme. There are still discernible MLPV that remain on the CSF-GM boundary. (c) The three-step EM method can remove MLPV.

throughout the images, especially in the cortical regions. Second, the final posterior is determined by the combination of prior and class likelihood. The former is derived from the atlas while the latter is evaluated from the voxel intensity. As the MLPV voxels on the GM-CSF boundary can have exactly the same intensity levels as the WM, even a prior from an atlas may not be sufficient to guarantee the correct classification. Thus, the explicit MLPV removal step is necessary. This statement is supported by the illustration in Figure 4.15. Here the simple template is non-rigidly registered to a T2w image of a very premature baby using the FFD based approach (Rueckert et al., 1999) and usually the non-rigid registration will give even worse performance for more complex brains.

Several algorithms have been proposed to address the problem of partial volume effects in the segmentation of images. These approaches are focused on the adult brain. The first approach was proposed by Santago P. and Gage (1993), who assumes a uniform prior probability for non-pure tissues and derives the intensity distribution of partial volumes by minimizing the distance between an image histogram and a model. Other approaches (e.g. Choi et al. (1991), Nocera L. and Gee (1997)) employ Markov Random Fields (MRF) to impose spatial smooth variations of tissue mixing proportions and a maximum a posterior (MAP) estimation is commonly computed for PV segmentation. A recent work by Van Leemput et al. (2003) presents a uniform framework for PV segmentation. This method assumes that an additional downsampling step is performed to cause partial volumes and estimates the mixing proportions to maximize the data likelihood. There is no heuristic assumption for the prior distribution of mix proportions. Very promising results have been reported for these PV segmentation algorithms applied to adult T1w MRI. However, they implicitly rely on the fact that the intensity levels of partial volumes in adult T1w images do not predominantly overlap the characteristic intensity of any pure tissue class (Figure 4.1(d)), which is not true for neonatal MRI due to the inverted gray-white matter contrast. Having corrected MLPV explicitly, these and more conventionally appearing PV (for example at the GM-WM boundary) could be further dissected using methods similar to the established PV segmentation for adult MRI. However, pilot experiments with our data showed that given the spatial resolution of our T2w imaging protocol this refinement did not appear to enhance the segmentation and so we decided not to explicitly estimate the mixing proportions.

The current implementation exploits a label propagation strategy to automatically identify deep GM and myelinated WM. This process enables the segmentation of cortical GM and non-myelinated WM. The detailed delineation of deep central tissues, such as the thalamus and basal ganglia, may not be possible with current methods because of insufficient intensity contrast in these regions. Since these

structures show less variability between subjects than the cortex, a solution may be to use registration based label propagation methods possibly with the aid of additional spatial prior information from a probability atlas to refine the segmentation. Automated segmentation of deep brain structures in the neonatal brain remains a significant challenge, but if it can be achieved reliably, its use in combination with the current cortical approach could provide fully automated segmentation of the complete brain, so facilitating studies of complete cerebral circuits.

There is no established gold standard for the evaluation of neonatal brain segmentations. In this chapter, we performed a limited evaluation using three orthogonal slices, which were intended to be representative for each subject. For adults a reliable gold standard for segmentation evaluation has been established based on simulated brain datasets (Cocosco et al., 1997; Collins et al., 1998). Development of analogous models or the use of standard datasets and manual segmentation of neonatal brains would be required to achieve a similar level of comprehensive evaluation of segmentation algorithms for neonatal MRI.

4.8 Summary

This chapter has presented an automatic cortex segmentation algorithm which detects and corrects mislabelled partial volume voxels. The inverted GM/WM contrast in neonatal MR images has been investigated to highlight the occurrence of mislabelled partial volume voxels, which is unique for developing neonates. The MLPV makes intensity-based tissue classification more difficult as a large amount of voxels on the WM/CSF boundary will be misclassified. To avoid these errors, the classic EM algorithm is modified and a knowledge-based partial volume removal step is added. The new three-step EM method is able to correct errors in the segmentation of both GM and WM compared to the classic EM scheme. Quantitative validation against manual segmentation demonstrates good

performance (the mean Dice value: 0.758 ± 0.037 for GM and 0.794 ± 0.078 for WM). The segmentation has been tested on 25 neonates with the gestational ages ranging from ~27 to 45 weeks.

In conclusion, by identifying the MLPV phenomenon associated with the specific signal properties of MR images of the brain in neonates of varying gestational ages, we have developed and evaluated segmentation methods designed specifically to extract the cortical GM. The resulting methods are effective for segmentation of cortical GM over a wide range of GA. This serves as a starting point for effective cortical reconstruction, which will be the theme of the next chapter.

Chapter 5

Cortical Reconstruction and Registration of neonatal MRI

5.1 Introduction

Cortical surface reconstruction is a step which immediately follows the segmentation technique described in the previous chapter and aims to accurately localize and represent the three cortical surfaces (inner, central and outer). As discussed in chapter 3, the reconstruction of cortical surfaces from MR images is a challenging task, due to the thin curved shape of cortical surface, the intensity inhomogeneity, limited image resolution and partial volume effects. Furthermore, the occurrence of noise in the MR images often causes errors in the cortical GM segmentation. This in turn leads to imperfections on the geometric mesh of cortex, as shown in Figure 3.3. As a result, an explicit surface reconstruction step is required which suppresses the influence of image noise and removes the imperfections in the cortical surface geometry. This will enable the morphometric quantification of the cortical geometry and allow tasks like human brain normalization and functional mapping to be carried out.

In chapter 3, the state-of-art of cortical surface reconstruction for adults has been reviewed. Several authors have proposed algorithms to reconstruct the cortical surfaces from the results of a segmentation step. Both parametric and geometric deformable models have been used for this purpose. Parametric deformable models (Dale et al., 1999; Xu et al., 1999; MacDonald et al., 2000) transform the

segmentation results into surface tessellation and deform the surface with self-intersection check and smooth regularization. On the other hand geometric deformable models (Zeng et al., 1999; Goldenberg et al., 2002; Han et al., 2004) use the implicit representation of cortex and deform the cortical surface by solving the level-set equation. An explicit triangulation of cortical surfaces can be obtained using isosurface algorithms such as the marching cubes algorithm (Lorensen and Cline, 1987; Han et al., 2003). In the end both parametric and geometric strategies can generate accurate and topologically correct cortical surfaces if the segmentation of cortical gray matter is satisfactory.

To the best of our knowledge none of these techniques previously reported have been applied to neonates ranging from very premature to term equivalent age, which is partly due to the difficulties encountered in segmenting neonatal brain MRI. In last chapter, we have developed an adaptive knowledge-based cortical GM segmentation algorithm for neonatal MRI. We have shown that this algorithm achieves good-to-excellent GM segmentation results by explicitly removing the mislabelled partial volume voxels, which opens up the opportunity to achieve the good cortical surface reconstruction for neonates.

In this chapter, we adopt an implicit surface evolution technique originally developed for adults (Han et al., 2004) to neonatal cortex reconstruction. Its performance is quantitatively evaluated by performing a detailed landmark study. In addition we develop a cortical surface registration technique that establishes direct correspondence between cortical surfaces across different gestational ages and subjects. The performance of this technique is evaluated by quantifying the established correspondences of main cortical features across multiple time-points in single individuals as well as between different subjects.

To further evaluate the cortical segmentation-reconstruction pipeline for neonates (shown in Figure 4.6), we have collected a large number of MR brain images of neonates at different gestational ages (99 preterm infants with GA from 27 to 49

weeks). The proposed segmentation-reconstruction pipeline has been applied to these images and cortical surfaces have been successfully reconstructed for all subjects. Automated cortical morphometric quantification is achieved based on successful reconstruction and a number of different geometrical quantities are computed and analyzed to characterize the development and growth of the cortex.

The remainder of this chapter is organized as follows: In section 5.2, the cortical reconstruction algorithm based on implicit surface evolution is presented. The cortical surface registration algorithm is the topic of section 5.3. Section 5.4 describes the experimental setup for the evaluation of these techniques. The automated quantification of cortical morphology for the large number of preterm infants is reported in section 5.5. The final two sections 5.6 and 5.7 discuss the methodology and validation protocol and summarize the chapter.

5.2   Cortex reconstruction using implicit surface evolution

To reconstruct the cortex from the probabilistic tissue classification, an implicit surface evolution based cortical reconstruction framework is employed, which is originally developed in Han et al. (2004). Compared to other approaches for the reconstruction of the cerebral cortex, this implicit surface evolution approach has several advantages: First, it has the ability to reconstruct the inner, central and outer surfaces, while most other methods cannot easily recover the central cortical surface. Secondly, the approach explicitly includes a step which aims to improve the recovery of deep sulci. This step modifies the initial GM segmentation to create a thin, digital separation between sulcal banks. This is especially useful for MR of more mature neonates, since in general younger brains tend to have more tightly packed sulci compared to adults, which makes the recovery of deep sulci more difficult for neonates. Moreover, this method has been carefully validated in Tosun

et al. (2006). Finally, the computation time for the surface reconstruction is ~10mins, which is acceptable for routine use.

The level-set framework (Osher and Fedkiw, 2003; Sethian, 2007) is the key technique of this cortex reconstruction approach. The main feature of the level-set based surface representation is that the surface is defined by the zero level-set of a higher dimensional spatial scalar function $\phi(\vec{x}, t)$ (Figure 5.1). This avoids the need to represent the surface using a triangle or polygon mesh as is common in parametric surface representations. The embedded surface will be propagated with the temporal evolution of level set function $\phi(\vec{x}, t)$. To maintain the precision of numerical solution, ϕ is chosen to be the signed distance function of the surface, which means the value at a spatial point equals the closest distance from this point to the surface with the negative value inside and positive outside (Osher and Fedkiw, 2003; Sethian, 2007).

In general, the level set function can be evaluated by solving a set of time-dependent Hamilton-Jacobi partial differential equations (HJ-PDE) (Osher and Fedkiw, 2003; Ian Mitchell, 2005; Sethian, 2007). Actually, as a strategy to simulate the dynamic implicit surfaces in image processing and computer vision, this HJ-PDE has been used in many other fields, such as fluid and combustion simulation, control, robotics, dynamic programming, mesh generation and financial mathematics (Adalsteinsson et al., 1997; Kimmel and Sethian, 1998; Adalsteinsson and Sethian, 2002; Sethian and Smereka, 2003; Wilkening et al., 2004; Hogea et al., 2005; Sethian, 2007).

A general time-dependent Hamilton-Jacobi equation, defined on fixed and structured lattice (image grid), has the following form:

$$\phi_t(\vec{x}, t) + H(\vec{x}, t, \phi, \nabla\phi, \phi_{xx}) = 0 \qquad (5.1)$$

subject to the initial condition $\phi(\vec{x}, t) = \phi_0(\vec{x})$ when $t = 0$

Here $\phi_t(\vec{x}, t)$ is the partial derivative of ϕ with respect to the time variable t. $\nabla \phi$ is the gradient of ϕ with respect to the spatial coordinate $\vec{x}$. ϕ_{xx} is the second order derivative of ϕ with respect to $\vec{x}$. If the dimension is higher than 1D, ϕ_{xx} is the Hessian matrix. The general Hamilton-Jacobi term is defined as $H(\vec{x}, t, \phi, \nabla \phi, \phi_{xx})$. As suggested by its form, a fully general function H can be a function of spatial coordinate $\vec{x}$, time t or function value ϕ. It can even be nonlinear and can depend on the gradient and Hessian matrix of ϕ.
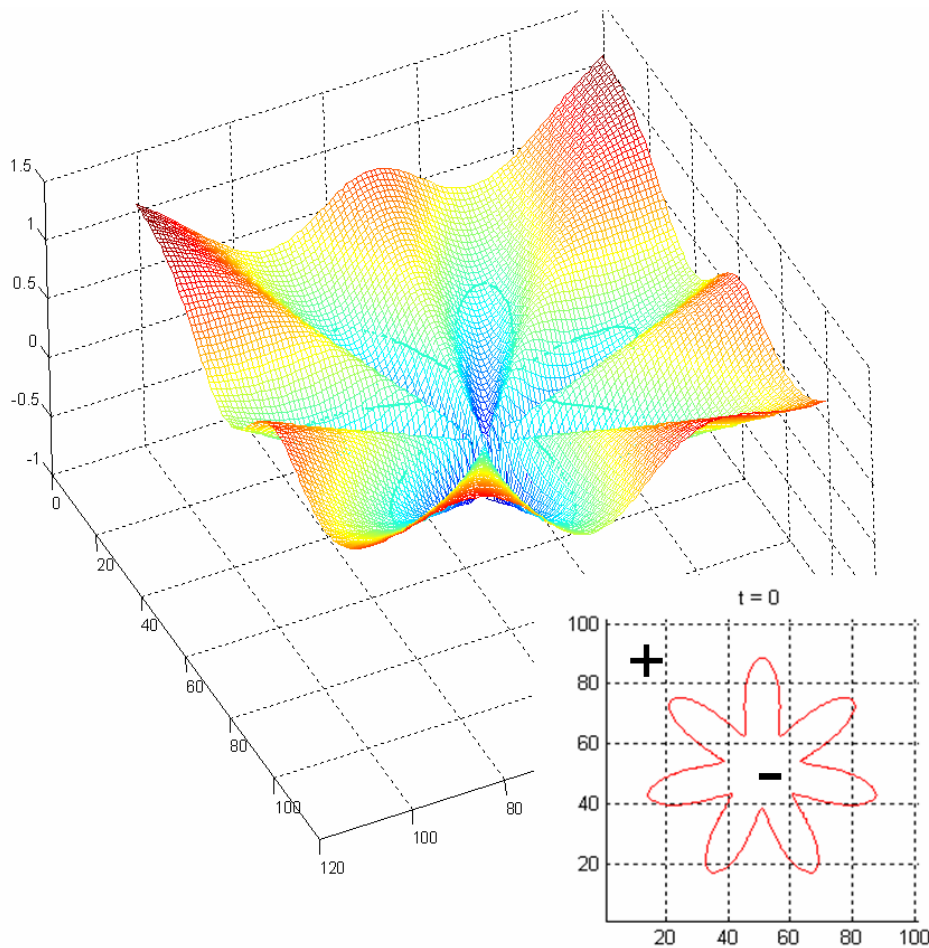
Figure 5.1. An example of implicit surface representation. The star shape is represented by the zero-isocontour of a level-set function which is negative inside and positive outside.

The numerical approximation to the general function H can be difficult. Fortunately, in the context of image processing and surface evolution, several

special cases of H are frequently sufficient, as shown in equation 5.2. As a result, the general form of level-set equation (5.1) can be simplified as:

$$
\begin{aligned}
0 = {}& \phi_t(\vec{x},t) \\
& + a(\vec{x},t)\|\nabla\phi(\vec{x},t)\| \\
& - b(\vec{x},t)\kappa(\vec{x},t)\|\nabla\phi(\vec{x},t)\| \\
& + \vec{v}(\vec{x},t)\cdot\nabla\phi(\vec{x},t) \\
& + sign(\phi(\vec{x},0))(\|\nabla\phi(\vec{x},t)\|-1)
\end{aligned}
\tag{5.2}
$$

A HJ-PDE for surface evolution usually has the time derivative and at least one of the other four terms.

The key step to implement the level-set equation (5.2) is to compute a numerical approximation to the time derivative and spatial derivatives (the last four items). As suggested in Osher and Fedkiw (2003) and Sethian (2007), a simple central difference scheme often fails to provide the sufficient numerical stability, which forces a tiny time step to be used and causes very slow convergence. As a result, approximation techniques with high-order precision have been proposed to improve the computation of time and spatial derivative of $\phi(\vec{x},t)$ (Shu and Osher, 1988; Shu and Osher, 1989; Osher and Fedkiw, 2003).

The time derivative $\phi_t(\vec{x},t)$ is usually approximated with a general Euler forward time difference, which provides first order of accuracy, as Osher and Fedkiw (2003) has suggested that the level-set equation is more sensitive to the precision of spatial terms, while the temporal truncation errors produce less deterioration of the final solution. However, more precision can still be achieved using the explicit total variation diminishing Runge-Kutta integration scheme (TVD-RK) (Shu and Osher, 1988; Shu and Osher, 1989). The second-order accurate TVD-RK scheme is most frequently used as a replacement for the simple Euler forward time difference if necessary. In this scheme, an Euler step is first taken to advance the solution to time $t + \Delta t$ to compute $\phi(\vec{x}, t+\Delta t)$:

$$\frac{\phi(\vec{x}, t+\Delta t) - \phi(\vec{x}, t)}{\Delta t} + H(t) = 0 \qquad\qquad (5.3)$$

Then a second Euler step is performed to compute $\phi(\vec{x}, t+2\Delta t)$:

$$\frac{\phi(\vec{x}, t+2\Delta t) - \phi(\vec{x}, t+\Delta t)}{\Delta t} + H(t+\Delta t) = 0 \qquad\qquad (5.4)$$

An averaging step leads to the improved estimation of $\phi(\vec{x}, t+\Delta t)$:

$$\phi(\vec{x}, t+\Delta t) = \frac{1}{2}\phi(\vec{x}, t) + \frac{1}{2}\phi(\vec{x}, t+2\Delta t) \qquad\qquad (5.5)$$

This TVD-RK scheme guarantees no oscillations are produced as a side-effect of high-order temporal discretization (Osher and Fedkiw, 2003).

The spatial term $a(\vec{x}, t)\|\nabla\phi(\vec{x}, t)\|$ provides the surface motion along the normal direction $\|\nabla\phi(\vec{x}, t)\|$. $a(\vec{x}, t)$ is the external force field which is application specific. For cortical reconstruction, $a(\vec{x}, t)$ is defined from the output of segmentation (see section 5.2.1 for details). The approximation of $\nabla\phi(\vec{x}, t)$ can be achieved using the upwind finite difference scheme (Chen et al., 1997; Osher and Fedkiw, 2003) or essentially nonoscillatory scheme (ENO) (Shu and Osher, 1988; Osher and Sethian, 1988; Shu and Osher, 1989; Osher and Shu, 1991). The former analyzes the directions of the external force and propagation of truncation errors and simply picks the forward or backward difference to minimize the error propagation. The extra computational costs from the upwind finite difference scheme are less significant, but the analysis of error propagation can be complicated. The latter improves the precision by replacing the simple linear interpolant with smoothing polynomials, which is straightforward to implement but computationally more expensive. More details of the numerical solution and the theory of level set can be found in Osher and Fedkiw (2003). As an example, Figure 5.2 illustrates the motion along the normal direction.

The term $-b(\vec{x},t)\kappa(\vec{x},t)\|\nabla\phi(\vec{x},t)\|$ works as a smoothing term in the surface evolution. With the positive speed $b(\vec{x},t)$, the direction of evolution will be opposite to the outer surface normal, which means the surface is gradually smoothed (Figure 5.3). The curvature item $\kappa(\vec{x},t)$ can be approximated by the central difference while the approximation of $\nabla\phi(\vec{x},t)$ can be achieved using the upwind finite difference scheme or ENO.
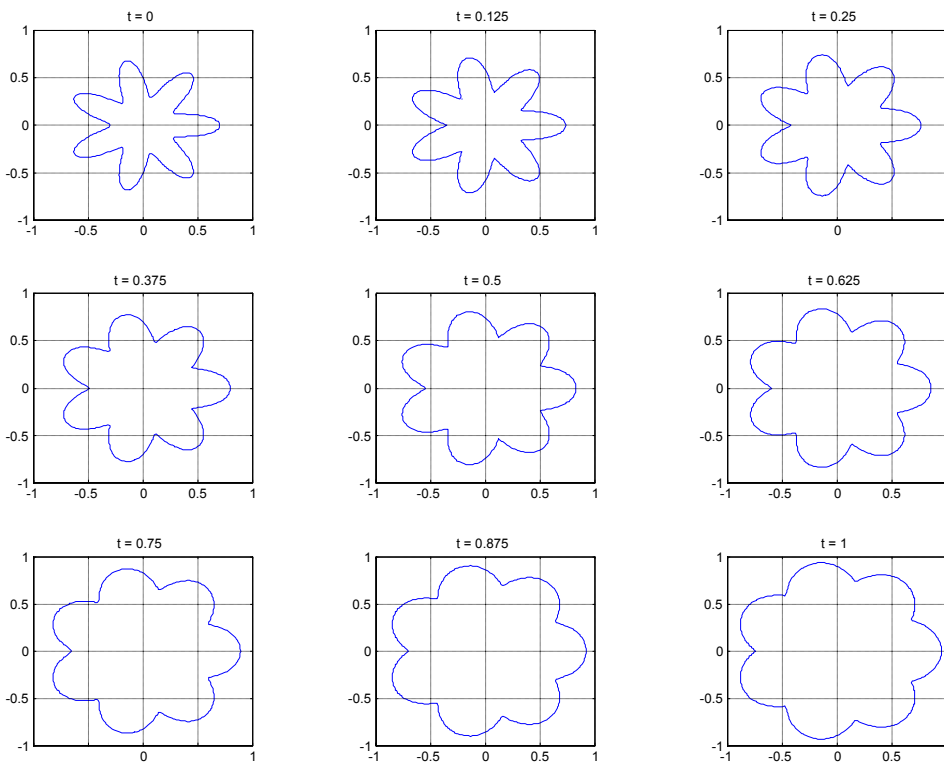
Figure 5.2. An illustration to show the surface motion along the normal direction.
As more iteration is performed, the curve gradually expanded.

The term $\vec{v}(\vec{x},t)\cdot\nabla\phi(\vec{x},t)$ denotes the motion along a external force field (actually $a(\vec{x},t)\|\nabla\phi(\vec{x},t)\|$ is a special case of $\vec{v}(\vec{x},t)\cdot\nabla\phi(\vec{x},t)$). Again, the upwind finite difference scheme or ENO is used to compute $\nabla\phi(\vec{x},t)$.

The last term $sign(\phi(\vec{x},0))(\|\nabla\phi(\vec{x},t)\|-1)$ is used to reinitialize the level set function to be a signed distance function, which is necessary to maintain the numerical precision and ease the distance computation. The corresponding equation is also called the "reinitialization equation":

$$0 = \phi_t(\vec{x},t) + sign(\phi(\vec{x},0))(\|\nabla\phi(\vec{x},t)\|-1) \tag{5.6}$$

As the $\phi(\vec{x},t)$ can gradually deviate from its original nature of a signed distance function during the surface evolution, the reinitialization is generally performed as a helper step after a couple of level set iteration to transform the $\phi(\vec{x},t)$ back to a signed distance function.
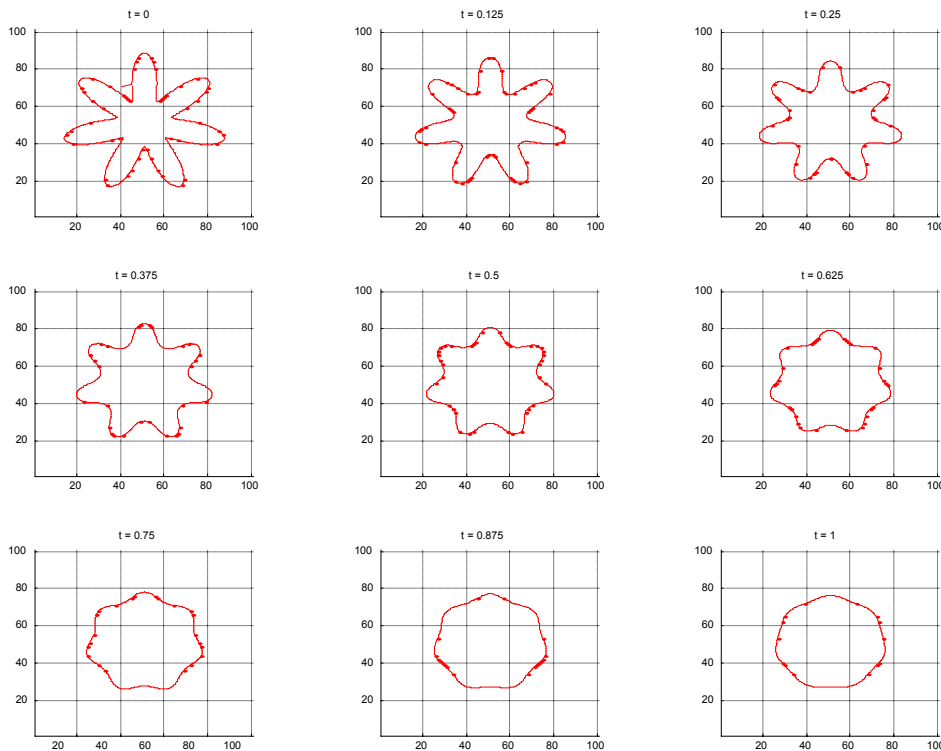
Figure 5.3. An illustration to show the curve motion driven by mean curvature. Compared to the previous example, there is progressive decrease in the mean curvature without expansion of the total area enclosed.

Some geometric measures are easy to evaluate using the implicit surface representation. For example, the unit normal of embedded surface can be computed as:

$$\vec{N} = \frac{\nabla \phi}{\|\nabla \phi\|} \tag{5.7}$$

The curvature is defined as the divergence of the normal:

$$\kappa(\vec{x},t) = \nabla \cdot \vec{N} = \nabla \cdot \left(\frac{\nabla \phi}{\|\nabla \phi\|} \right) \tag{5.8}$$

which can be estimated using the second-order finite difference scheme.

In the applications to deform the 3D surfaces, every lattice point in the image domain needs to update in every time step. Therefore, the related computational complexity is $O(n^3)$, which may prohibit the effective surface propagation in the large images. The so-called "narrow-band" speedup strategy (Adalsteinsson and Sethian, 1995; Sethian, 1996) has been developed to decrease the computational costs. The key idea in this method is to build an adaptive strip around the zero-level set fronts. The update is only performed in this thin band of neighboring points, not in the whole image domain. Although the programming complexity is increased, Adalsteinsson and Sethian (1995) has shown the speedup is significant (~10 times, depending on the nature of problem) and the precision lost is generally acceptable for many applications.

5.2.1 Cortex reconstruction using level-set evolution

Starting from the probabilistic tissue classification obtained via the automated segmentation algorithm, the inner, central and outer cortical surfaces are reconstructed, thus enabling quantification of cortical changes during the early phases of brain development.

The movement of the cortical surface can be determined by motion in the normal direction and the curvature and the equation (5.2) can be rewritten as

$$0 = \phi_t + \omega_a \cdot a(\vec{x},t)\|\nabla \phi(\vec{x},t)\| - \omega_\kappa \cdot \kappa(\vec{x},t)\|\nabla \phi(\vec{x},t)\| \tag{5.9}$$
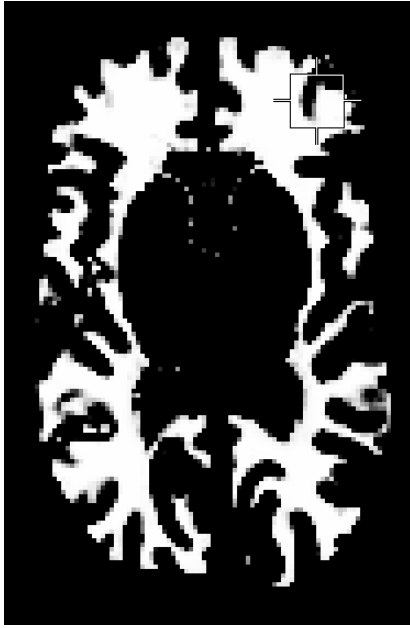
1.00	1.00	1.00	0.91	-0.94	-0.99	-0.86	-0.80	-0.87	-0.11	-1.00	-1.00
1.00	1.00	1.00	0.58	-0.99	-0.98	0.13	0.26	-0.97	-0.97	-0.95	-0.06
1.00	1.00	0.99	-0.55	-0.99	-0.94	0.75	0.84	-0.69	-0.95	-0.87	-1.00
1.00	1.00	0.91	-0.94	-0.94	-0.76	0.87	0.99	0.99	0.99	0.96	0.86
1.00	1.00	0.66	-0.96	-0.95	-0.46	0.94	1.00	1.00	0.99	0.99	0.98
1.00	1.00	0.46	-0.96	-0.90	0.18	0.97	1.00	1.00	1.00	1.00	1.00
1.00	1.00	0.73	-0.84	-0.67	0.53	0.98	1.00	1.00	1.00	1.00	1.00
1.00	1.00	0.97	-0.30	-0.64	0.55	0.99	1.00	1.00	1.00	1.00	1.00
1.00	1.00	0.99	0.07	-0.43	0.53	0.97	1.00	1.00	1.00	0.99	1.00
1.00	1.00	1.00	0.89	0.53	0.68	0.93	0.99	1.00	1.00	0.97	0.98
1.00	1.00	1.00	1.00	0.96	0.90	0.96	0.99	1.00	1.00	1.00	1.00
1.00	1.00	1.00	1.00	1.00	0.99	0.99	1.00	1.00	1.00	1.00	1.00

Figure 5.4. Surface evolution force for the inner cortex. The force is positive inside the WM, expanding the cortical surface while negative outside, shrinking the surface. The evolution will stop around the 0.5-isosurface.

The weights ω_a and ω_κ are empirically selected to differentially emphasize the motion along the normal direction and surface smoothness caused by the curvature term.

The numerical solution of equation (5.9) can be obtained using the numerically stable finite difference method, either upwind scheme or ENO. Specifically, if the first-order forward time derivative is used, the above equation is resolved by computing the level set function for next time step $t + \Delta t$:

$$\phi_{t+\Delta t} = \phi_t + \Delta t \cdot \left(\omega_a \cdot a(\vec{x},t) \left\| \nabla \phi(\vec{x},t) \right\| - \omega_\kappa \cdot \kappa(\vec{x},t) \left\| \nabla \phi(\vec{x},t) \right\| \right) \quad (5.10)$$

The level set function for the inner surface is initialized by the signed distance function corresponding to the binary segmentation of WM and its evolution stops when the probability of white matter voxels reaches ~0.5. This is achieved by defining the signed pressure $a_{inner}(\vec{x})$ for the inner surface to be as follows (Figure 5.4):

$$a_{inner}(\vec{x}) = 2P_{WM}(\vec{x}) - 1 \quad\quad\quad (5.11)$$

When the WM posterior probability is less than 0.5, the $a_{inner}(\vec{x})$ is negative, pushing the surface to move inwards. When the surface is within the WM, the $P_{WM}(\vec{x})$ is ~1. The $a_{inner}(\vec{x})$ is positive and moves the surface outward. A small curvature force is required to constrain the smoothness of the surface. Han et al. (2004) found the weights ω_a and ω_κ for determining the motion of the signed pressure curves by normal direction and mean curvature to be 1 and 0.02 respectively. The same values are found to be appropriate for the reconstruction of the neonatal cortex.

The outer cortical surface is obtained by evolving the level-set function initialized from the inner cortical surface with the signed pressure function defined as

$$a_{outer}(\vec{x}) = 2(P_{WM}(\vec{x}) + P_{GM}(\vec{x})) - 1 \qquad (5.12)$$

This definition removes the ambiguity with the inner 0.5-isosurface of $P_{GM}(\vec{x})$, as the desired surface is also given by the isosurface of $P_{WM}(\vec{x}) + P_{GM}(\vec{x})$. This force will cause the surface to expand if inside the GM or WM and to contract if in the CSF. The same curvature force is also used to maintain the smoothness. An example of the signed pressure function for outer cortex is shown in Figure 5.5(b).

Unlike the method in Han et al. (2004), we exploit a simple approach to compute the level-set function corresponding to the central surface: given that the obtained level-set functions ϕ_{inner} and ϕ_{outer} for the inner and outer surfaces are signed distance functions, the central surface is defined to be equidistant from the inner and outer surfaces; thus, the level set function for central surface $\phi_{central}$ can be computed by $\phi_{central} = \phi_{inner} + \phi_{outer}$ because the level-set functions used are negative inside and positive outside. The central surface can be explicitly generated as the zero-level isosurface of $\phi_{central}$. As ϕ_{inner} and ϕ_{outer} may deviate from signed distance functions during the level-set evolution, either the reinitialization equation or fast marching algorithm (Tsitsiklis, 1994; Tsitsiklis, 1995; Sethian, 1996; Sethian, 1999;

Sethian and Vladimirsky, 2000) needs to be used before computing the central surface.

Figure 5.5. An illustration of topology preserving level-set to enhance the shape recovery of deep sulci. The first row: Original level-set scheme allows the topology change of embedded shape, which can cause the incorrect merging of two sulcal banks. Second row: With the topology preserving constraint, two sulcal banks will not merge as this will change the essential topology. Third row: During the surface evolution of the topology preserving level-set, the non-simple points are detected (colored in red). The sign of these points are kept unchanged to preserve the topology. Points with their sign changed during this iteration are marked in green. Note the sign inversion of a spatial point means the level-set front passes this position.

Because the level-set evolution may not conserve the surface topology, a topology preserving level-set approach (Han et al., 2003) is used for both inner and outer surfaces. This approach preserves the change of digital topology of initial surfaces during the evolution by detecting the so-called "non-simple points". A "non-simple point" is prevented from inverting its sign if this change will modify the local topology, as the level-set function is negative inside and positive outside. The topology preserving level-set algorithm prevents two sulcal banks from merging into each other and thus maintains sulci and reclassifies the probability of GM at

the sulcal regions, as illustrated in Figure 5.5, which favors the reconstruction of very thin sulci.

The proper surface nesting is achieved by constraining $\phi_{inner} > \phi_{outer}$. As the level set function is negative inside and positive outside, the lower value of ϕ_{outer} means the outer cortex always include the inner cortex.

Cortical reconstruction algorithms for adults often assume that the topology of the cortical surface is equivalent to a sphere, and an explicit topology correction step may be used during the reconstruction (Goldenberg et al., 2002; Shattuck and Leahy, 2002; Han et al., 2004). However, since to the best of our knowledge the topology of the cortical surfaces at different gestational ages in developing neonates is not well documented, we have only preserved the topology of the input binary segmentation without imposing any prior assumptions. If a spherical topology is required, existing topology correction methods (Han et al., 2001; Shattuck and Leahy, 2001; Fischl et al., 2001; Kriegeskorte and Goebel, 2001; Han et al., 2002; Ségonne et al., 2005; Chen and Wagenknecht, 2006) can be applied in a straightforward way.

5.2.2 Automatic sulcus enhancement

As shown in Figure 5.6(a-b), the segmentation often fails to identify CSF correctly within tight sulci in neonatal brain. The most common cause for this is the insufficient image resolution compared to the small size of neonatal brain and partial volume averaging at voxels in the deep sulci. On the other hand, the CSF layer within a sulcus which is often thin in neonatal brains may not even be present in the "back-to-back" sulcal regions. As a result, the external force for outer cortex defined in equation 5.12 can cause large inaccuracies for both outer and central cortical reconstruction (as the inner cortex is defined by the WM boundary, its reconstruction is less error-prone).

(a)

(b)

(c)
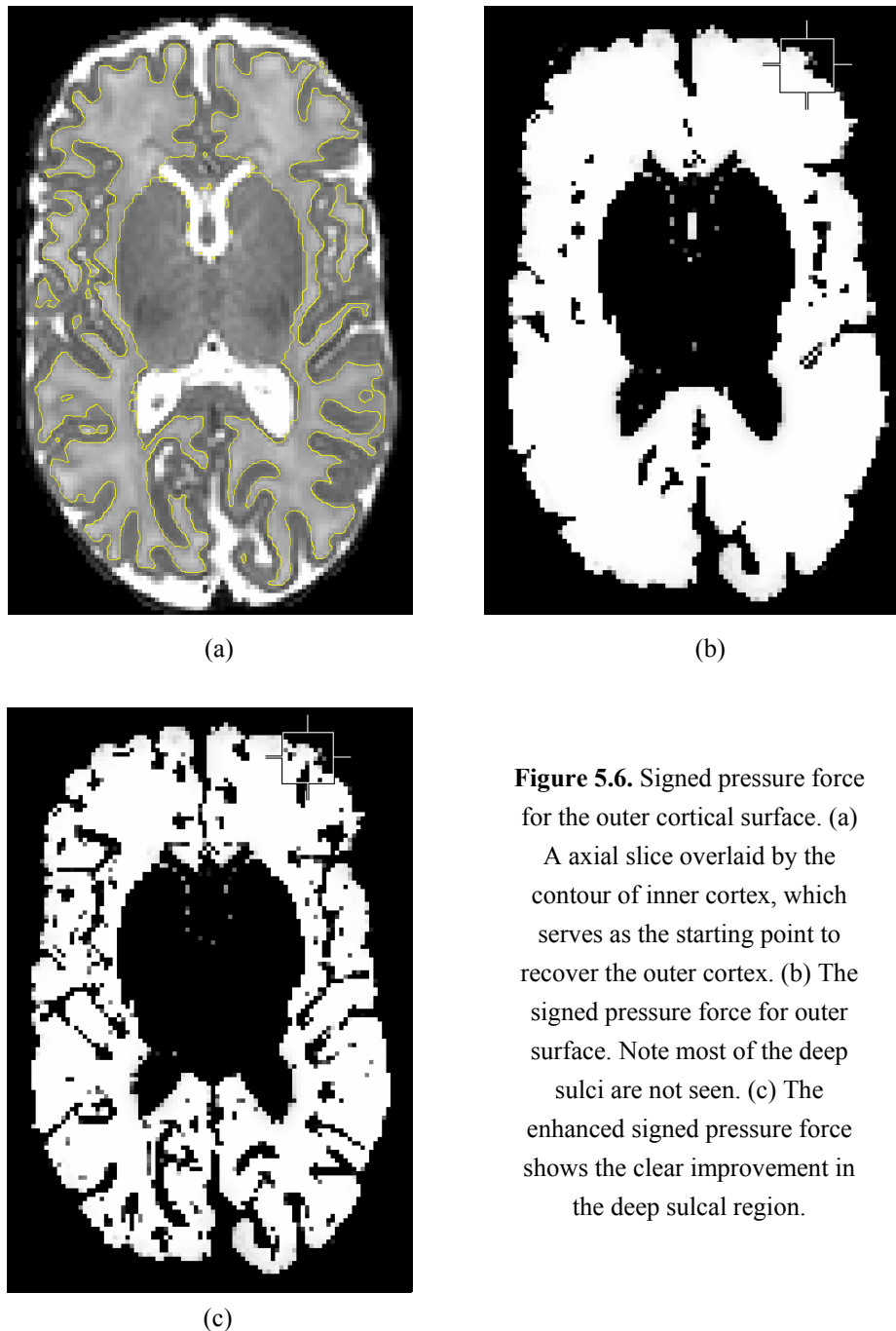
Figure 5.6. Signed pressure force for the outer cortical surface. (a) A axial slice overlaid by the contour of inner cortex, which serves as the starting point to recover the outer cortex. (b) The signed pressure force for outer surface. Note most of the deep sulci are not seen. (c) The enhanced signed pressure force shows the clear improvement in the deep sulcal region.

To address these difficulties, Han et al. (2004) has proposed to add an automatic sulcus enhancement step into the reconstruction pipeline. The idea is to modify the initial cortical GM segmentation to create a thin strip of CSF between two sulcal banks. This thin strip can be defined by the exterior skeleton of the inner cortical surface. Once the skeleton is identified, the fuzzy GM membership of voxels belonging to the skeleton can be reduced. This leads to the relabelling of the

corresponding voxels as CSF. Note this method is essentially based on a-prior relating to the geometrical shape of sulci.

The level-set framework is used to evaluate the exterior distance function $D(\vec{x})$ to the inner cortex. The level set function remains a signed distance function as it is evolved for each time step and the following equation is solved to compute the $D(\vec{x})$:

$$0 = D_t(\vec{x},t) + F(\vec{x})\|\nabla D(\vec{x},t)\| \qquad (5.13)$$

where $D(\vec{x}) = \phi_{inner}$ at $t = 0$ and $F(\vec{x})$ is a spatially varying speed function. This equation causes the inner cortex to expand along its normal under the force of $F(\vec{x})$. If $F(\vec{x})$ is unity at every point in the image domain, then $D(\vec{x})$ is guaranteed to be the Euclidean distance.

In the sulci where there is evidence for CSF, the evolution of $D(\vec{x})$ should stop within the CSF and this can be achieved by defining the force so it is reduced in these regions:

$$F(\vec{x}) = 1 - 0.9 P_{CSF}(\vec{x}) \qquad (5.14)$$

Using this force definition, the moving front will slow down within the CSF and the skeleton estimated will be shifted towards the CSF. When there is no CSF, $F(\vec{x})$ will be unity and the gyral banks will be equally split along their skeleton.

The localization of skeletal points from the distance $D(\vec{x})$ equals to the detection the so-called "shocks" point of equation 5.13. At those shock points, the surfaces from two sulcal banks will merge and the gradient of $D(\vec{x})$ will be small (as the $D(\vec{x})$ is the distance to the nearest sulcal bank). As a result, the value of $F(\vec{x})\|\nabla D(\vec{x},t)\|$ will be much smaller than unity on the shocks. To maximize the numerical feature of shock points, $\|\nabla D(\vec{x},t)\|$ needs to be estimated using the

central finite difference operator. As proposed in Han et al. (2004), the following criteria are used to identify the set of skeleton points S :

$$S = \left\{ \vec{x} \middle| F(\vec{x}) \middle\| D(\vec{x}) \middle\| \leq T \right\}$$

$$\phi_{inner}(\vec{x}) > 0 \qquad\qquad (5.15)$$

where the threshold T is empirically set to be 0.8. The second equation constrains the skeleton points to lie outside of the inner cortex.

With the identification of potential sulcal skeleton, related GM membership can be modified:

$$P_{GM}(\vec{x}) = F(\vec{x}) \middle\| D(\vec{x}) \middle\| P_{GM}(\vec{x}) \text{ if } \vec{x} \in skeleton \qquad (5.16)$$

For all other points, the $P_{GM}(\vec{x})$ remains unchanged.

Figure 5.6(c) shows the performance of this sulcal enhancement process. In the cases where no CSF is present in the initial segmentation, the distance estimation and shock detection identify the skeleton. The corresponding GM membership function is modified to favor the shape recovery.

5.3   Cortical registration for developing neonates

Clinical studies have shown delayed cortical folding and white matter (WM) related macro- and micro-structural changes in preterm infants at term equivalent age (Counsell and Boardman, 2005; Kapellou et al., 2006). By analyzing changes in the neonatal cortex during the early phases of brain development, it may be possible to detect precursors of cerebral abnormalities prior to term equivalent age, which would allow treatment options to be tested during the neonatal period. Also, the rapid anatomical and functional evolution of the neonatal cortex itself is poorly understood by evolutionary biologists and neuroscientists. Cortical development during the third trimester of pregnancy is extensive with noticeable increase in cortical folding. In addition there is significant cortical variability across infants.

Thus, the precise localization and tracking of principal anatomical features, i.e. central sulcus and sylvian fissure, is difficult.

As reviewed in Chapter 3, several researchers have presented algorithms to unfold and align the cerebral cortex in cross-sectional studies in adulthood (Carman et al., 1995; Fischl et al., 1999a; Fischl et al., 1999b; Tosun et al., 2004b; Tosun and Prince, 2005). Methods based on cortex unfolding aim to inflate the highly folded surfaces and map the whole cortex (or hemisphere) to some standard representations like a flat surface or a sphere. The inflation process is normally regularized by ensuring that several constraints, like rigidity between neighbouring points, or the minimum distortion of local area and angle during the unfolding procedure. The alignment of corresponding anatomical features is partly achieved by identifying these features manually and then normalizing the spherical representation into a standard coordinate space. This requirement of maintaining strict point correspondences was relaxed by Tosun et al. (2004b). They applied a rigid surface registration to remove global misalignment between two cortical surfaces before applying a conformal mapping to transform them to a spherical representation. Although some measurements, such as surface area and distance can be computed with the spherical coordinate normalized by a rigid body transformation, this representation tends to smooth out fine-grain details of the complex cortical anatomy. However, in the developing brain, specific sulci can experience significant morphometric changes during the third trimester of pregnancy. Also, a global rigid body transformation clearly is not able to capture local non-rigid deformations occurring as a result of growth. Instead a non-rigid registration procedure is required to follow the growth of specific sulci across gestational ages (GAs).

The aim of cortical surface registration in the developing brain is to develop a methodology which is able to track and quantify cortical development in neonates across different gestational ages and subjects. To enable the tracking of cortical development we have developed a cortical registration algorithm, which consists of

two stages: In the first stage the cortical surfaces are smoothed. For longitudinal surface registration the more complex cortical surface is progressively smoothed until it is maximally similar to the less complex cortex. For cross-sectional surface registration, both surfaces are smoothed until they are similar to each other. In the second stage any residual misalignment of the cortex is corrected by performing a non-rigid surface registration using free-form deformations (FFDs) (Rueckert, 2007). We have performed a quantitative evaluation of the cortical registration by propagating sulci across multiple gestational ages and computing the overlap ratios with a manually established ground-truth labelling of cortical sulci.

5.3.1   Adaptive surface relaxation

Surface relaxation has been originally designed to smooth reconstructed polygon surfaces and to reduce artifacts which often appear as abrupt or stair-step artefacts in meshes. The relaxation process is also helpful for improving visualization (Drury et al., 1996; MacDonald et al., 2000). To facilitate any non-rigid surface registration, we here employ surface relaxation prior to the surface registration to inflate the more complex cortex.

One iteration step of this relaxation process is defined as follows (Drury et al., 1996; Timsari and Leahy, 2000; Tosun et al., 2004b):

$$v_{t+1}^i = (1-\lambda) \cdot v_t^i + \lambda \cdot \bar{v}_t^i \qquad (5.17)$$

Here v_t^i is the position of vertex i at the iteration t. $\lambda \in [0,1]$ is a pre-defined smoothing factor. $\bar{v}_t^i$ is the average vertex position of all polygons sharing vertex i:

$$\bar{v}_t^i = \frac{1}{\sum\limits_{j \in N_i} A_j} \sum\limits_{j \in N_i} A_j \cdot C_j \qquad (5.18)$$

where N_j is the set of polygons using the vertex i. A_j and C_j are the surface area and centre of polygon j. Note this surface relaxation process maintains point-to-

point correspondences, which makes the propagation of labelled cortical features from the original surface to its smoothed version possible.

It is necessary to define a stopping criterion for the surface relaxation, so that the cortical folding complexity of the more complex surface is comparable to the folding complexity seen at the earlier gestational age. We have tested various cortical folding measures. In this thesis we have decided to use a criterion that is based on the computation of the intrinsic curvature index (ICI) and mean curvature L2 norm (MLN). Both measures are dimensionless and measure different aspects of cortical folding complexity. The former is originally defined in Van Essen and Drury (1997), measuring the local intrinsic convexity of surface. The MLN is the L2 norm of the mean curvature of cortical surfaces which takes a minimum value for a sphere and is called bending energy (Batchelor et al., 2002).

$$ICI = \int_S \|K\|_+ \, dA$$

$$MLN = \sqrt{\int_S H^2 \, dA} \tag{5.19}$$

Here S is the whole cortical surface. K and H are Gaussian and mean curvature. $\|K\|_+$ equals K if $K > 0$ and otherwise it is zero. Both measures are computed and integrated over the whole cortical surface S. The surface relaxation will stop when both ICI and MLN of inflated surface fall below the corresponding values for the less mature cortex. An illustration of this surface relaxation is given in Figure 5.7.

5.3.2   Non-rigid surface registration based on free-form deformations (FFDs)

After smoothing of the cortical surfaces any residual misalignment is corrected using a non-rigid surface registration algorithm. We use an algorithm based on free-form deformations (FFDs) which is a powerful tool for modelling 3-D deformable objects (Lee et al., 1996). The basic idea of this scheme is to deform an object by manipulating an underlying mesh of control points. The resulting

deformation controls the shape of the 3-D object and remains as a C^2 continuous transformation, which smoothly deforms the cortical surfaces.

To define a FFD for a cortical surface S, we define the spatial domain occupied by this surface as follows: $\Omega_S = \{(x, y, z) | 0 \le x \le X, 0 \le y \le Y, 0 \le z \le Z\}$ and ϕ_s denotes a $n_x \times n_y \times n_z$ grid of control points $\varphi_{i,j,k}$. The spacing between adjacent control points is uniform in all coordinate directions. The deformation of a vertex $v_i = (x, y, z)$ is represented as the 3D tensor of the 1-D cubic B-spline (Lee et al., 1996; Rueckert et al., 1999):

$$T_{local}(v_i) = \sum_{l=0}^{3} \sum_{m=0}^{3} \sum_{n=0}^{3} B_l(u) B_m(v) B_n(w) \varphi_{i+l, j+m, k+n} \qquad (5.20)$$

where $i = \lfloor x / n_x \rfloor - 1$, $j = \lfloor y / n_y \rfloor - 1$, $k = \lfloor z / n_z \rfloor - 1$, $u = x / n_x - \lfloor x / n_x \rfloor$, $v = y / n_y - \lfloor y / n_y \rfloor$ and $w = z / n_z - \lfloor z / n_z \rfloor$. B_l represents the l-th basis function of the B-spline. The basis functions of cubic B-spline have limited support. Therefore changing a control point in the grid affects only a 4×4×4 region around that control point. Surface registration is achieved by specifically moving the control points to minimize a cost function. The cost function which we try to minimize is the average symmetric spatial distance f:

$$f(S, W, T_{local}) = \frac{1}{N_S} \sum_{i=1}^{N_S} \|v_i - \ell(v_i, T_{local}(W))\|_2 + \frac{1}{N_W} \sum_{j=1}^{N_W} \|w_j - \ell(w_j, S)\|_2 \qquad (5.21)$$

where S and W are two cortical surfaces which are being registered. N_S is the number of vertexes in surface S. N_W is the number of vertexes in surface W. For every vertex $v_i \in S$, $\ell(v_i, T_{local}(W))$ defines the closest vertex of v_i on the transformed surface $T_{local}(W)$. Similarly, for every vertex $w_j \in T_{local}(W)$, $\ell(w_j, S)$ defines the closest vertex of w_j on the surface S. The purpose of adding the second term is to force the registration of deep sulci. To ensure that the spatial transformation defined by the FFD is smooth, the standard second order

regularization penalty should be minimized (Wahba, 1990). This penalty is added to the surface similarity to produce the final cost function.
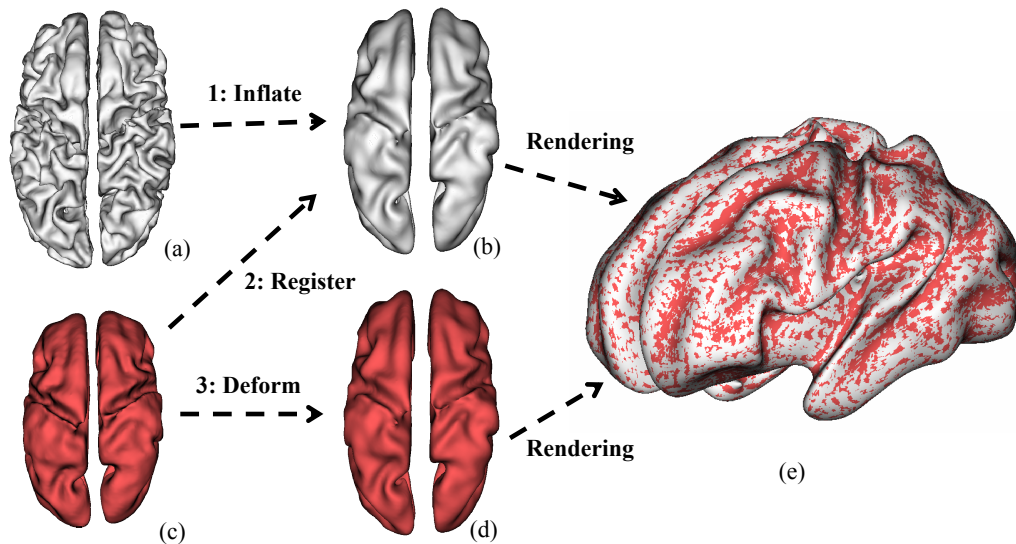
Figure 5.7. An illustration of cortex surface relaxation and non-rigid registration for a longitudinal study. A neonate was scanned three times. The inner cortical surface of the first scan (GA: 29.86 weeks) is shown in (c). The cerebral cortex has undergone noticeable development by the scan at term equivalent age (GA: 39.86 weeks), as shown in (a). The inflated surface after adaptive relaxation is shown in (b), where the cortical folding complexity is substantially decreased. Non-rigid surface registration is performed to align the less mature cortex (c) and inflated surface (b). The deformed surface of (c) is shown in (d). (e) renders (b) and (d) together. The zigzag pattern shows these two surfaces are spatially very close.

5.4   Experimental approaches

5.4.1   Landmark validation for cortical surface reconstruction

The quantitative measurement of cortical reconstruction accuracy is difficult in neonatal MRI because of the lack of a ground-truth cortical surface. In the case of adults, simulated MRI images and datasets with manual segmentation have been used to validate cortex reconstructions (Zeng et al., 1999; Goldenberg et al., 2002; Kim et al., 2005). As no segmentation is available, landmark studies are often

performed. In these studies an experienced operator delineates landmark points on the inner/central/outer surfaces (Han et al., 2004; Tosun et al., 2006). We have adopted this approach using 10 subjects selected randomly, including infants from very premature to term equivalent ages. For each subject a neurologist marked 80 landmark points located on the inner interface and 80 on the outer. These landmarks were placed directly in the source grey scale images and spatially distributed to cover the whole cortical area, with 20 points on each surface in each cortical lobe (frontal, temporal, occipital and parietal lobe). Surface reconstruction errors (SRE) were defined as the minimum distance between a given landmark and the corresponding reconstructed surface. The distance is negative if the landmark is inside the surface and positive if outside.

5.4.2   Sulcus mapping and cortical lobe labeling

To quantitatively evaluate the accuracy of the proposed cortical registration method, the main anatomical features on the cortical surfaces are manually marked by an experienced neonatologist. The manual labelling of one cortex can then be mapped to a second cortical surface and generate an automatic sulcus mapping via the non-rigid deformation. The overlap between automatic labelling and the manually established ground-truth were computed as a quantitative measurement of registration performance. Both true positive (TP) and false positive (FP) errors are computed. TP is computed as the percentage area of the manual labelling that is accurately labelled by the automatic mapping. FP is defined as the percentage area of the automatic labelling that is not labelled manually.

The central sulcus is selected and manually labelled for further validation. This sulcal region, defined as the buried cortex surrounding the sulcal spaces, is identified in both hemispheres. For the longitudinal studies, these sulci can be reliably tracked throughout the different gestational ages, which makes them good candidates to track the development of neonatal cortices.

For the inter-subject cortical registration, establishing the correspondence between corresponding main sulci is difficult due to the large inter-cortical variability. We therefore decided to perform some preliminary testing to validate the global applicability of the proposed registration approach by automatic propagation of the four cortical lobes from a template cortex to new subjects. Specially, the four lobes (frontal, parietal, occipital and temporal) were manually labelled in each template brain of the three neonatal groups (simple, medium and complex, as suggested in section 4.6). The Bayer and Altman atlas was used in the construction of the templates (Bayer and Altman, 2004; Bayer and Altman, 2005). All manual segmentations were initially performed in the sagittal plane and then checked in the other two orthogonal orientations (coronal and axial). For the frontal lobe, the anterior edge of the central sulcus is identified as the posterior-superior border. The parietal lobe is bounded by the body and splenium of the corpus collosum and the lateral ventricles inferior-medially. The parieto-occipital fissure is identified as the posterior border and separates this lobe from the occipital lobe. After the other three lobes are identified, the temporal lobe was constructed by subtracting these templates from the rest of the cerebral hemispheres where already the basal ganglia and brainstem had masked out by label propagation. The insular cortex is included as part of the temporal lobe.
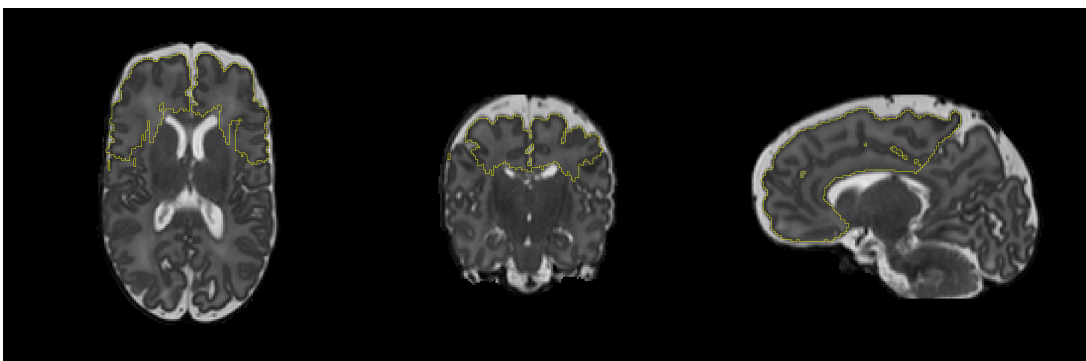
Figure 5.8. The manually labeled temporal lobe area for the *complex* template. For the template of every GA group, all four lobes are manually segmented and the cerebral tissues are split into four regions accordingly.

As an example, Figure 5.8 shows the manually labelled temporal lobe for the complex template (GA: 40 weeks), where the whole hemisphere is split into four lobes accordingly and so is the cortical surface. The 3D renderings of the four lobes partition for all three templates are shown in Figure 5.9. For all following inter-subject cortical registration, these three templates are used.

Given the manually labelled sulci or cortical lobes on a template cortex and the result of the cortical surface registration, a simple thresholding strategy is used to propagate these cortical labels to a new cortex. We define a distance threshold T to be the spatial size of a voxel in the image (e.g. 0.86mm in all tests). For a triangle vertex $\vec{p}_1$ on one surface S_1, a point $\vec{p}_2$ on surface S_2 corresponding to $\vec{p}_1$ should satisfy the following criterion:

$$\left\| \vec{p}_1^{\,s} - \vec{p}_2^{\,s} \right\| < T \tag{5.22}$$

where $\vec{p}_i^{\,s}$ is the corresponding point to $\vec{p}_i$ on the smoothed S_i, $i = 1,2$. After mapping all vertices belonging to a template ROI to the new surface, the propagated ROI can be obtained by excluding all other triangles having no intersections with mapped vertices.
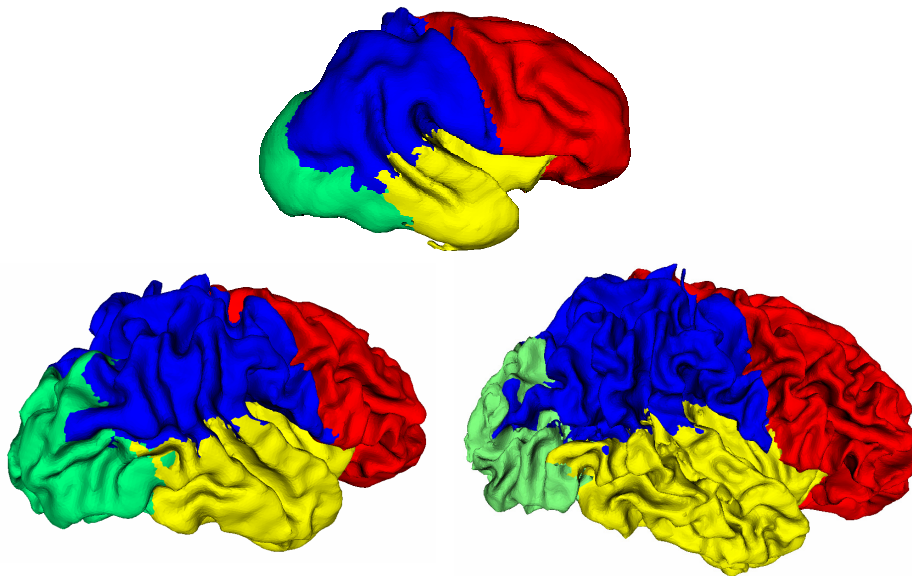
Figure 5.9. The 3D renderings of the four lobes partition for all three templates.

5.5   Results and evaluation

5.5.1   Cortex surface reconstruction

 After automatic segmentation of the cortical GM and WM, an implicit cortical surface reconstruction was performed for all 25 subjects (these are the same subjects used in Chapter 4). To evaluate the performance of the method we visually inspected the reconstructed surfaces and examined contours of intersection between the reconstructed cortical surfaces and 2D anatomical slices. The inner,
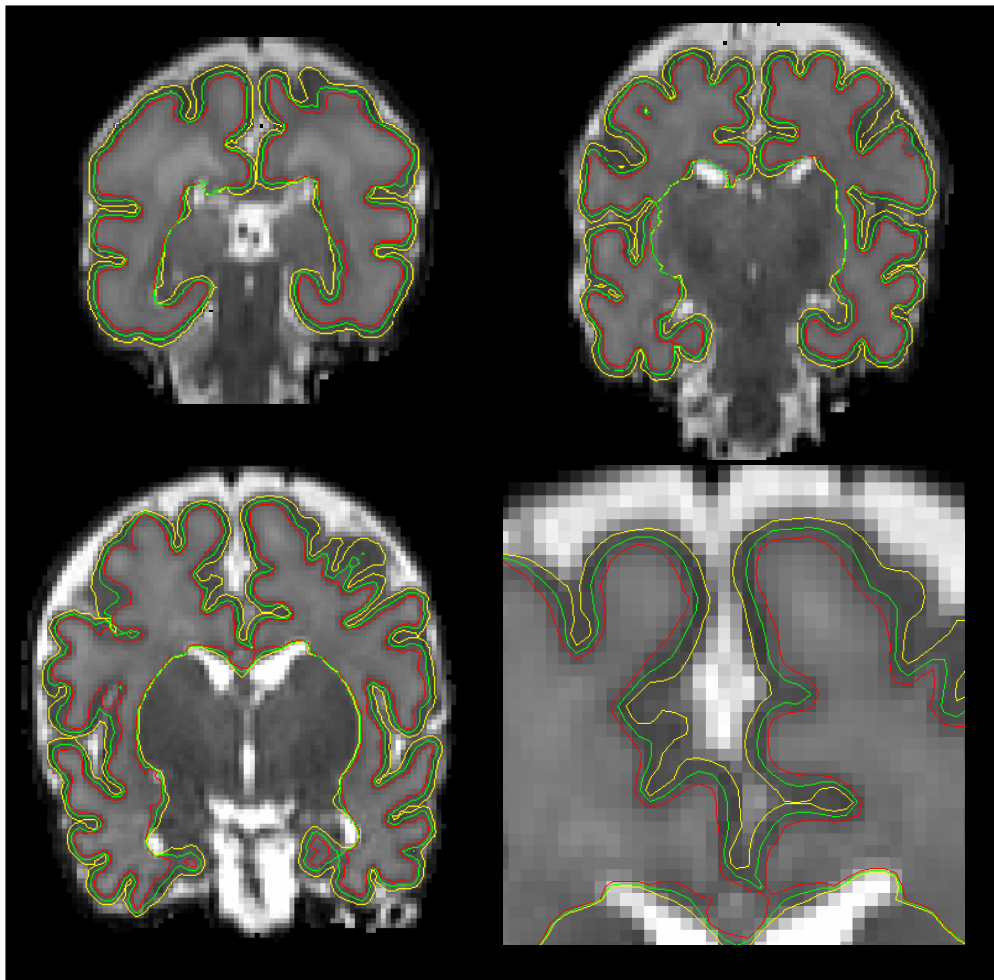
Figure 5.10. Three reconstructed surfaces displayed on coronal slices of T2w MRIs of neonates of varying GA. Top left 29.86w, top right 34.39 w, bottom left 39.86w, bottom right detail of 39.86w.

central and outer cortical surfaces were successfully reconstructed for all subjects. As an example, Figure 5.10 shows the 2D intersection contours of the inner, central and outer cortical surfaces for neonates over a representative range of GA. The corresponding 3D surfaces are presented in Figure 5.11. The colours on the surfaces indicate the mean curvature of the surfaces.

The results of landmark validation are reported in Table 5.1. For both the inner and outer cortical surfaces, the mean absolute distance errors are less than 1 voxel (<0.86mm), with less than 5% of all landmark points having an error of more than 2 voxels. This illustrates that the overall reconstruction has sub-voxel accuracy for both the inner and outer surfaces. No systematic patterns were observed in the anatomical distribution of these errors, which may indicate that reconstruction errors are fairly uniformly distributed in the cerebral space. More detailed studies are ongoing to quantify reconstruction errors in specific cortical regions.
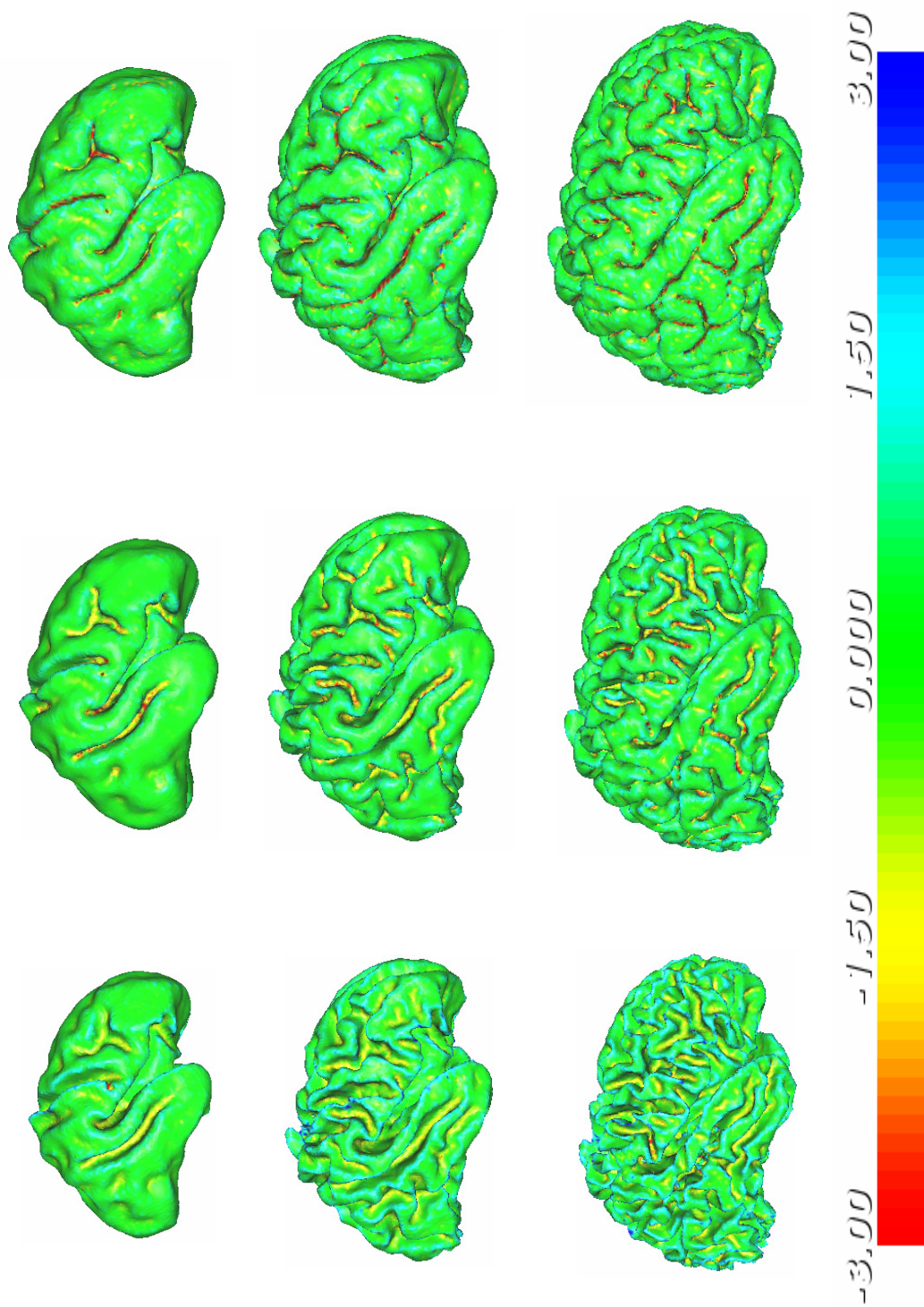
Figure 5.11. 3D rendering of reconstructed central cortex surfaces for three neonates in Figure 5.10 color coded by mean curvature as indicated by the color bar. From left to right, the inner, central and outer surfaces are shown.

Table 5.1

Surface reconstruction errors (mm) measured in the landmark study.

	Inner surface					Outer surface				
	Frontal	Temporal	Occipital	Parietal	**Total**	Frontal	Temporal	Occipital	Parietal	**Total**
Mean	0.39	0.003	0.14	0.60	0.28	-0.05	-0.41	-0.13	0.25	-0.08
Std	0.77	1.10	0.73	1.18	0.99	0.88	0.81	0.72	0.75	0.82
Mean (AD)	0.70	0.81	0.62	0.80	0.73	0.68	0.67	0.61	0.57	0.63
Std (AD)	0.50	0.75	0.41	1.05	0.73	0.55	0.60	0.41	0.55	0.53
> 1 voxel	28.0%	28.0%	25.0%	24.5%	26.4%	26.4%	22.9%	19.5%	13.0%	20.4%
> 2 voxel	5.5%	8.5%	0.5%	6.0%	5.1%	4.5%	3.6%	2.0%	5.0%	3.8%

AD: absolute distance.

5.5.2   Longitudinal cortex registration and sulcus mapping

We applied the cortical registration method to 15 images acquired from 5 neonates. These infants are selected from a longitudinal MR study of cerebral development of premature neonates. Every subject has had three longitudinal MR scans. The initial scans were performed between 27 weeks and 33 weeks gestational age. The second scans were performed at a mean GA of 35 weeks and the final images were acquired at the term equivalent age (mean of 41 weeks).

(a)   (b)

(c)   (d)
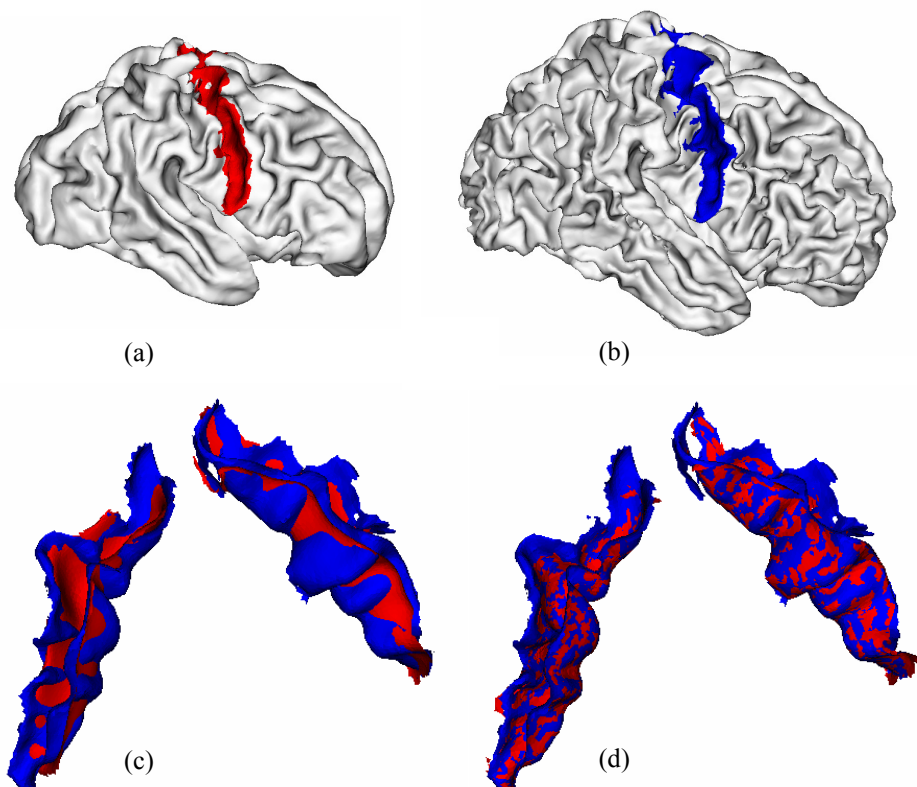
Figure 5.12. Automatic sulcus labelling via non-rigid cortical registration for a neonate scanned three times. (a) The inner cortex of the second scan (GA: 33.86 weeks); (b) the cortex at term equivalent age (GA: 39.86 weeks). Their central sulci have been manually labelled. (c) Global affine transformation does not transform the central sulcus between the time points, while (d) non-rigid surface registration captures the local evolution.

MR images were acquired on a 3T Philips Intera system (Best, Holland) with the same MR sequence parameters as described in section 4.5. After acquisition, the T2 images were segmented using the algorithm described in section 4.5 and the inner cortical surfaces were reconstructed and used for registration.

Figure 5.7 shows an example of the surface relaxation and cortical registration results between longitudinal scans. The more mature cortex is smoothed until its folding complexity is comparable to the less mature cortex. When working with the registration between two later scans (scans of 35 weeks and 41 weeks) where folding patterns are becoming more complex, we found that inflating ~35 weeks surfaces can improve the registration. Those cortical surfaces were therefore smoothed until their ICI and MLN decreased by 15%. The cortical surfaces at ~41 weeks were then inflated to match folding measurements from previous time points.

We have performed cortical registration between consecutive time points for all subjects. Also, we have registered the cortical surface at the first time point directly to the cortical surface at the last time point (term-equivalent age) which is more challenging due to the significant cortical development taking place during this time interval.

To quantify the ability of the proposed registration method to localize and track the main anatomical features of the cortex, an experienced neonatologist was asked to manually label the central sulci on all 15 cortical surfaces. Following cortical registration, the native manual segmentations can be compared to those propagated from other cortical reconstructions. Figure 5.12 gives an illustration of this automatic sulcus labelling. Note that a significant amount of non-rigid deformation is required to map the sulcus extracted from less mature cortices to later scans. This deformation itself can be used to describe the local evolution of the cortex over time, which may not be explicitly represented using spherical mapping.

The overlap between automated results and manually established ground-truth were computed and both true positive (TP) and false positive (FP) errors are estimated. Table 5.2 summarizes the results. In all cases, the cortical registration with surface inflation shows the best performance. It is also clear that performing just global affine transformation is not sufficient for automated sulcus mapping.

Table 5.2
Mean overlap ratios of central sulcus mapping for intra-subject studies.

	1st to 2nd				2nd to 3rd				1st to 3rd			
	Affine	IM	NR	NR+I	Affine	IM	NR	NR+I	Affine	IM	NR	NR+I
TP	0.16	0.81	0.73	0.97	0.20	0.77	0.71	0.91	0.07	0.31	0.41	0.72
FP	0.76	0.15	0.14	0.12	0.71	0.25	0.08	0.11	0.87	0.71	0.41	0.27

- 1st to 2nd: mapping central sulcus from the first scan to the second scan; 2nd to 3rd and 1st to 3rd are similarly defined;
- Affine: global affine transformation; IM: intensity based non-rigid registration; NR: only non-rigid surface registration; NR+I: non-rigid surface registration with adaptive surface inflation.

Direct non-rigid surface registration shows higher error rates possibly because the more folds a cortical surface presents, the more local optima the surface similarity can have.

Once we have obtained a cortical registration, we can simulate the cortical development process using the resulting transformation. Figure 5.13 shows an example in which a less mature cortex (GA: 27 weeks) gradually morphs into a mature one (GA: 35 weeks). As the proposed registration method is able to establish the direct surface correspondence, sulcal development can be described by interpolating the spatial trajectory between corresponding vertices on the cortical surface meshes. For every triangle vertex on the less mature cortex, its deformation vector is computed via the FFD estimated during the registration. A simple linear interpolation is then used to obtain the intermediate surface at multiple time steps. Although no guarantee can be made that this interpolation process agrees with the true brain development, a visually plausible evolution is obtained, which suggests the established cortical surface correspondence is reasonable and consistent with multiple cortical features.

Figure 5.13. A simulation of cortical development. A neonate was scanned at GA 27 and 35 weeks (top left and bottom right images). After cortical registration, intermediate cortical phases have been estimated by linearly interpolating the deformation field and warping the less mature cortex accordingly. Although no guarantee can be given that this procedure will recover the real evolution, the simulated development appears plausible.

5.5.3   Inter-subject testing

Using the same data as for section 5.5.2, each cortex is registered to its corresponding template (simple 27 weeks, medium 35 weeks and complex 40 weeks). The labels of central sulcus are propagated from the template and compared to the manual segmentation. The true positive (TP) and false positive (FP) errors are computed. Table 5.3 lists the results. As with the intra-subject cases, the cortical registration with surface inflation shows the best performance. In both inter- and intra-subject experiments the intensity based non-rigid registration shows limited performance to align the cortical surfaces. The reason for the poor performance of the intensity-based registration compare to the surface-based registration is the intensity-based registration uses no explicit knowledge about the cortical surface. Figure 5.14 illustrates this phenomenon. Although the intensity-based registration has largely matched the image intensities, the resulting deformation field shows unrealistic deformation on the cortical surfaces, which supports the idea that the surface based approaches are necessary in this scenario.

Table 5.3
Mean overlap ratios of central sulcus mapping for inter-subject studies.

	Simple				Medium				Complex			
	Affine	IM	NR	NR+I	Affine	IM	NR	NR+I	Affine	IM	NR	NR+I
TP	0.26	0.73	0.67	0.97	0.09	0.65	0.59	0.80	0.05	0.36	0.32	0.59
FP	0.65	0.21	0.27	0.13	0.84	0.21	0.24	0.15	0.89	0.46	0.48	0.34

- 1st to 2nd: mapping central sulcus from the first scan to the second scan; 2nd to 3rd and 1st to 3rd are similarly defined;
- Affine: global affine transformation; IM: intensity based non-rigid registration; NR: only non-rigid surface registration; NR+I: non-rigid surface registration with adaptive surface inflation.

The four lobe mapping has been performed between the manually labelled templates and target subjects. As mentioned in section 4.6, a total of three templates are used to divide the subjects into three groups that together span the full gestational range. Each subject is registered to its template designated according to gestational age and complexity of cortical folding. In this way an

automated cortical parcellation is achieved for each subject. Figure 5.15 shows the four lobe labelling results for neonates with different gestational ages. The performance of the cortical parcellation has been visually reviewed by an experienced neonatologist to prove its success in all tested cases. No substantial errors in parcellation were found (i.e. there were no cases where the cortical lobe boundaries were located in incorrect cortical areas).   The labels of central sulcus are also propagated to each cortical surface. The central sulcus is also shown in Figure 5.15.
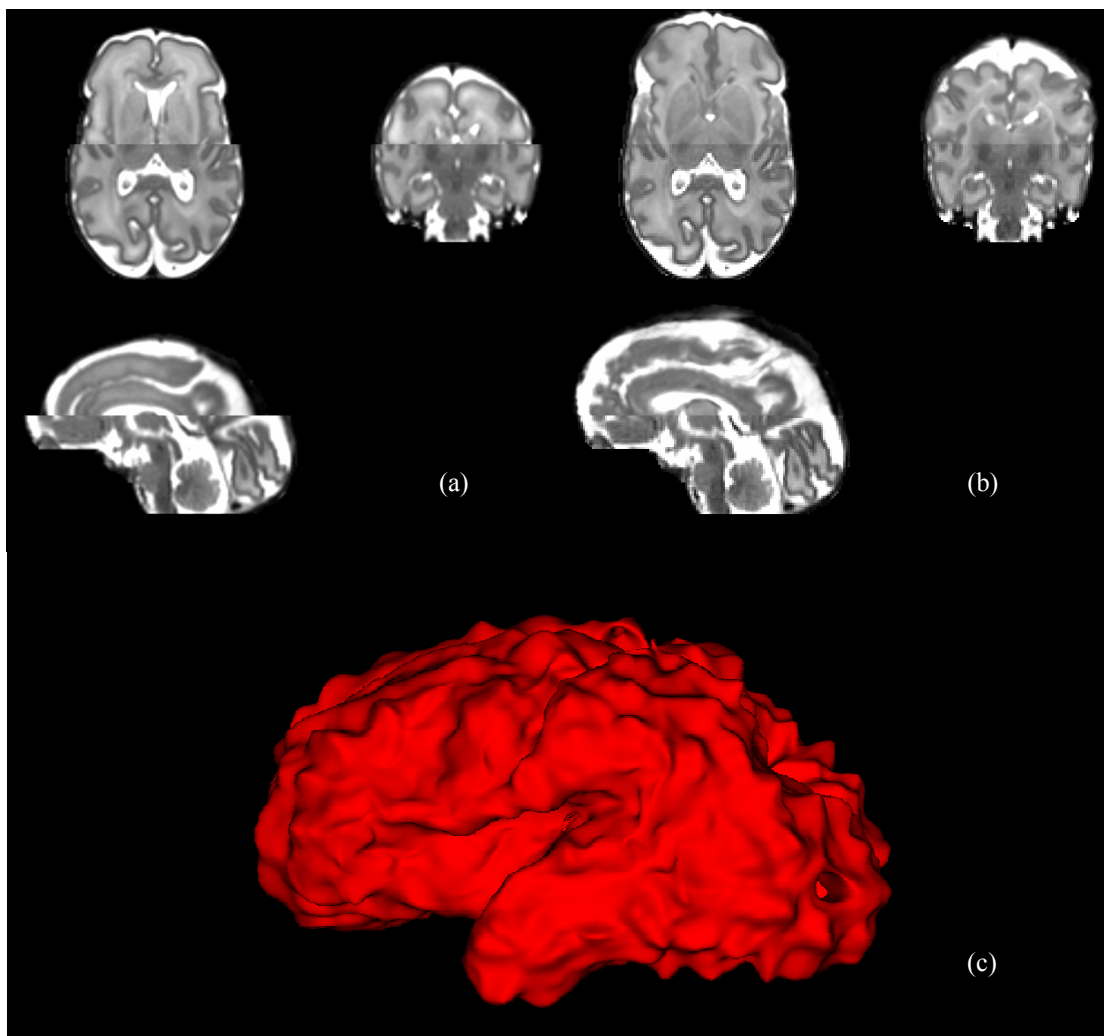
Figure 5.14. An illustration to show the limited performance of intensity based non-rigid registration to align the cortical surfaces. Compared to the situation without registration (a), the intensity based approach has largely registered two brains (b); however, the warped cortical surface can show clear unrealistic deformation (c).
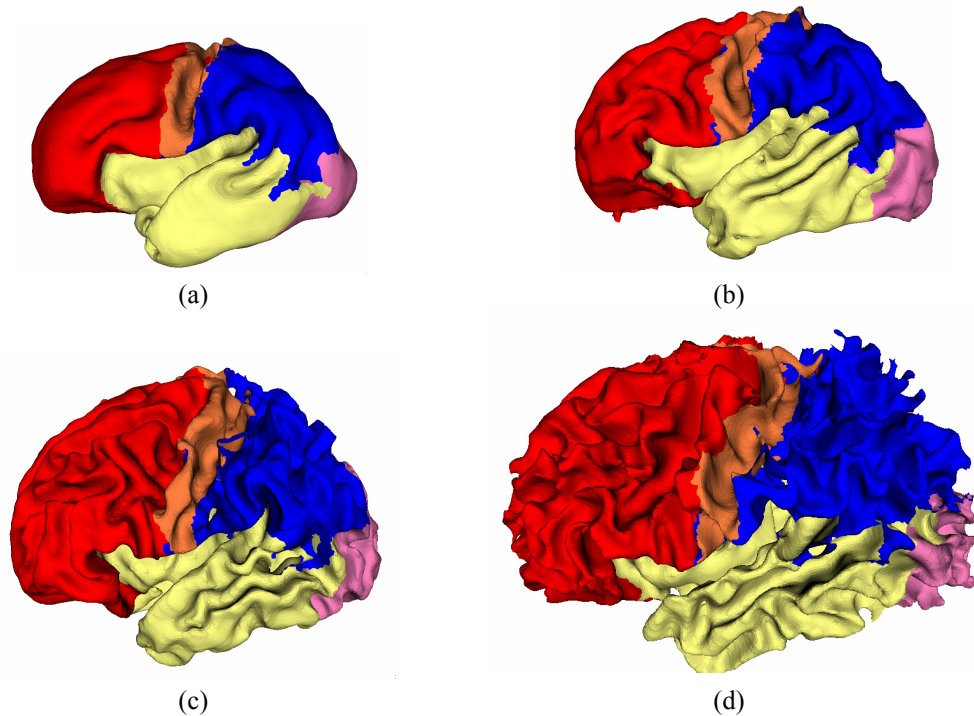
Figure 5.15. Cortical parcellation and labeling of the central sulcus mapping. The gestational ages at scan for these neonates are (a) 29 weeks, (b) 32.29 weeks, (c) 38.29 weeks and (d) 42.71 weeks. All parcellation and labelling results are automatically generated by propagating the manual labelling in variant templates.

5.5.4   Cortical morphological quantification for developing neonates

To further evaluate the proposed approach, we have collected a large number of MR brain images from neonates at different ages. The proposed segmentation-reconstruction framework was applied to this large group and cortical surfaces were generated. Results for all subjects are visually reviewed to ensure the success.

5.5.4.1 Data acquisition

Preterm infants were recruited from the Neonatal Intensive Care Unit at Hammersmith Hospital. None of the infants had congenital anomalies, metabolic disease or congenital infections or other pathological brain lesions, which is confirmed by our radiologists. The cohort consisted of 99 T2w images acquired

from 82 preterm infants born before ~34 weeks gestation. Preterm infants who weigh less than 1 kg were not sedated during the scan. Preterm infants, who weigh above 1 kg, were sedated with chloral hydrate 30-50mg/kg. All infants were stabilized using suction-evacuated pillows to reduce motion. The median gestational age at birth of these preterm infants was 28.44 weeks (range: 23.43 - 34.29 weeks). They had a median birth weight of 1.075 kg (range: 0.55 - 2.12 kg) and a median head circumference at birth of 25.5 cm (range: 23.5 - 27.1 cm). These infants were scanned between 27.14 weeks and 49.86 weeks post menstrual age (the distribution of GA at scan is shown in Figure 5.16). The median weight and head circumference at scan were 1.65 kg (range: 0.54 - 5.3 kg) and 29.7 cm (range 22.1 - 39.1 cm) respectively.
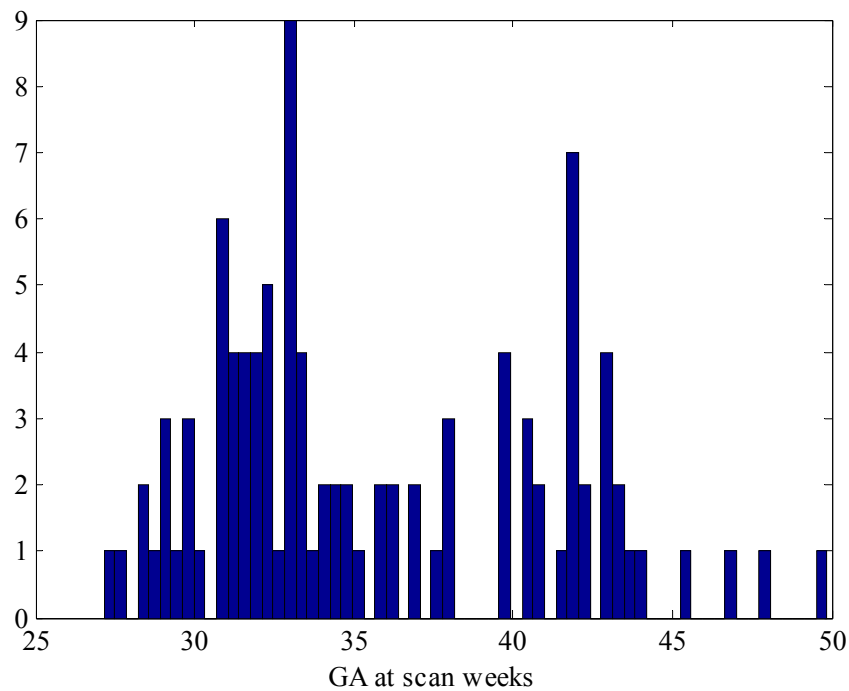
Figure 5.16. The distribution of GA at scan for all images in the cohort.

Automated cortical surface reconstruction was achieved using the proposed segmentation and reconstruction approach. Although no quantitative validation has been attempted due to the lack of ground-truth and time limitations, an experienced neonatologist has reviewed all segmentation and reconstruction results.

5.5.4.2 Cortical morphometric statistics

A number of different statistics have been computed and analyzed to explore the essential evolution patterns of developing cortex (Note some of these statistics have been applied to quantifying the cortex in Batchelor et al. (2002)).

Cortical thickness (TH): The thickness of the cortex is evaluated as the sum of signed distance functions of the inner and outer surfaces. The reinitialization equation (equation 5.6) is applied to both inner and outer level set function before computing the thickness measure.

Cortical surface area (SA): The cortical surface is represented as a triangular mesh. The surface area of this triangular mesh is computed to estimate the cortical surface area. The inner cortical surface is used since it preserves the shape of deep sulci well.

Cerebral volume (BV): The cerebral volume is calculated from the total brain mask after excluding CSF (including ventricles) and non-brain voxels.

Cortical volume (CV): The cortical volume is quantified as the spatial volume occupied by voxels between inner and outer surfaces. It is computed by counting the number of voxels which are positive in inner level set function and negative in outer level set function.

Mean curvature (MC): The mean of two principle curvatures k_{min} and k_{max} are computed at each vertex. The principle curvatures are computed from the embedded implicit function, which is an advantage of the level set method (Osher and Fedkiw, 2003; Sethian, 2007).

Convexity ratio (CR): The convexity ratio is defined as the ratio between the cortical surface area and the surface area of its convex hull. This measure is

dimensionless and invariant to surface orientation and scale. The convexity ratio is minimal for convex shapes.

Isoperimetric ratio (IPR): The isoperimetric ratio is another scale-invariant measure, calculated by division of the cortical surface area by cortical volume to the power of 2/3. It is a dimensionless measure, reaching the minimum for a sphere.

CR and IPR are zero-order measures of folding complexity of cortical surface. Both measures increase for more complex surfaces.

5.5.4.3 Cortical thickness

The mean cortical thickness is 1.64 mm with a range of 1.27-2.02 mm for all subjects, which agrees with the reported regular range of cortical thickness (1-5mm). The thickness is slowly increasing with the gestational age at scan (averaging ~0.01 mm per week). This tendency is found to be statistically related to gestational age ($r = 0.4214$, $P < 0.0001$).
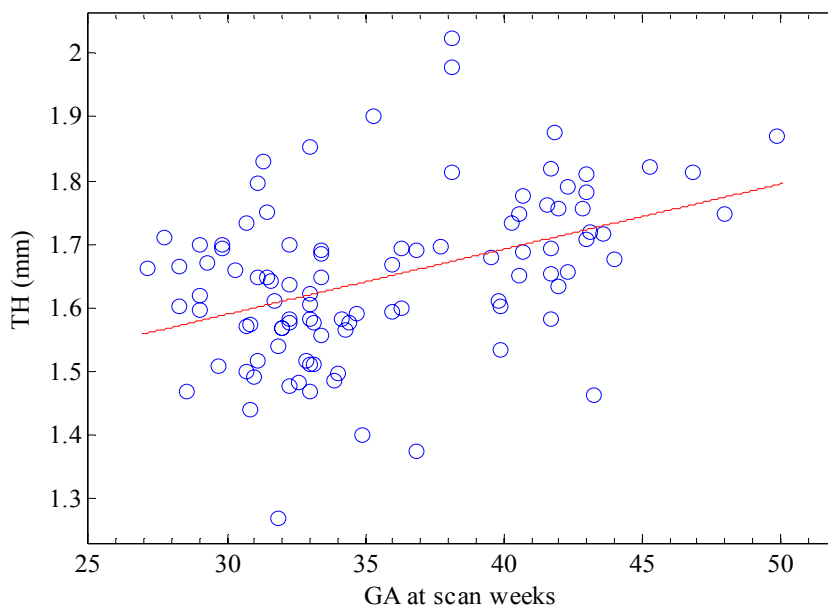
Figure 5.17. Mean cortical thickness during development of the whole cohort.

5.5.4.4 Cerebral volume, surface area and cortical volume

The cerebral volume (BV), surface area (SA) and cortical volume (CV) are plotted against the gestational age at scan in Figure 5.16. The absolute increase of these measures with GA can be observed. The mean cerebral volume is 229 cm^3, increasing from 82 cm^3 to 452 cm^3 for the whole cohort. The surface area ranges from 144 cm^2 to 933 cm^2 (mean SA: 455 cm^2) and the cortical volume from 27 ml to 204 ml (mean CV: 86 ml) (Figure 5.18). All three measures are found to significantly increase with the gestational age (linear regression, BV: $r = 0.9261$, $P < 0.0001$; SA: $r = 0.9302$, $P < 0.0001$; and CV: $r = 0.9363$, $P < 0.0001$).

5.5.4.5 Scaling relationship

The relationship between cortical surface area and volume can be expressed as a scaling relationship. Ideally, for a sphere the surface area s and volume v follow a scaling relation with the form of $s = kv^a$ where $\alpha = 2/3$ is a scaling exponent and k is a constant. Transforming to log coordinates, we obtain $\log s = \alpha \log v + c$ where $c = \log k$.

In the case of developing brain, the surface area becomes relatively larger as the brain grows. It might be expected to find a scaling relationship between SA and CV, but with a larger value of α compared to that of a sphere. The value α can be estimated by plotting a scatter graph of log s against log v and determining whether the data lie approximately on a straight line.

Indeed the log-log plot of surface area versus cerebral volume is quite linear (Figure 5.19). The scaling exponent for the SA to BV is 1.14 (95% CI: 1.10 to 1.18) and for the SA to CV, the exponent is 0.89 (95% CI: 0.85 to 0.93).
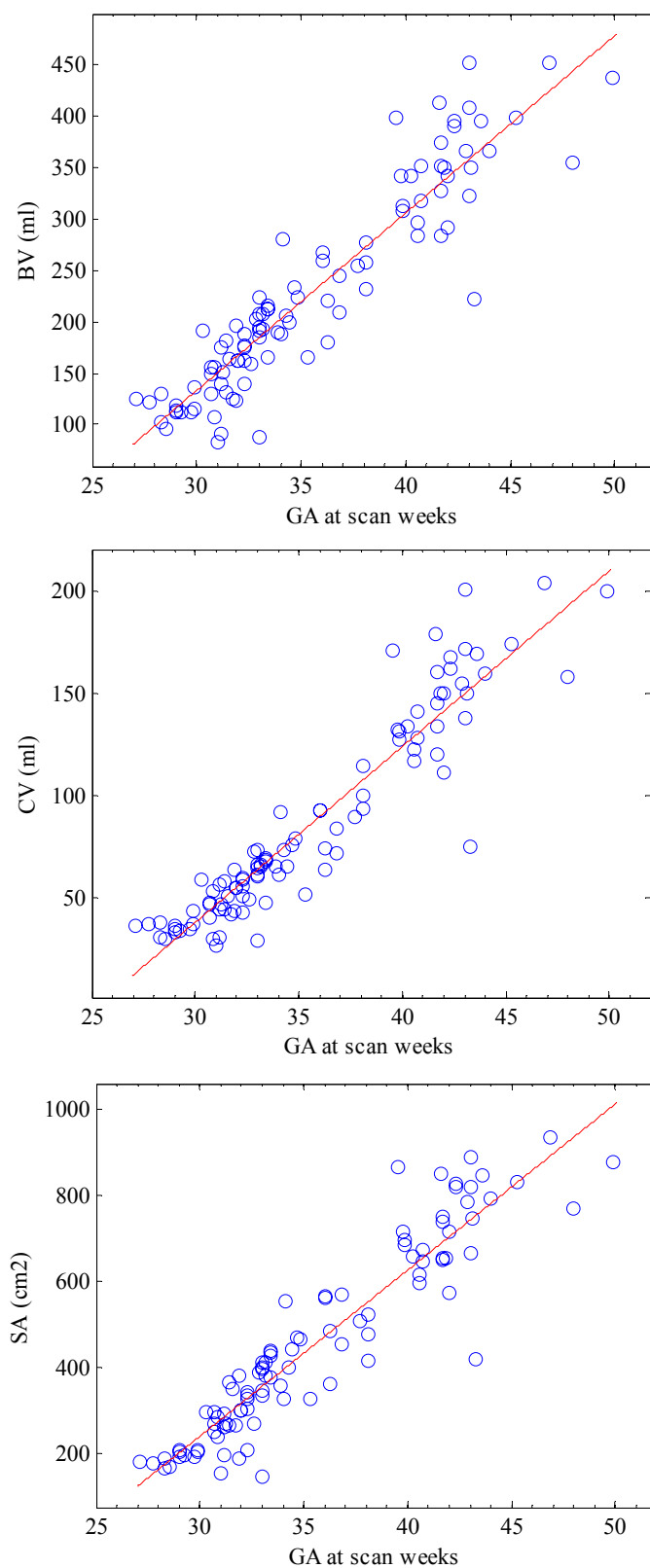
Figure 5.18. Cerebral volume, surface area and cortical volume in preterm infants
with and without lesions during development.
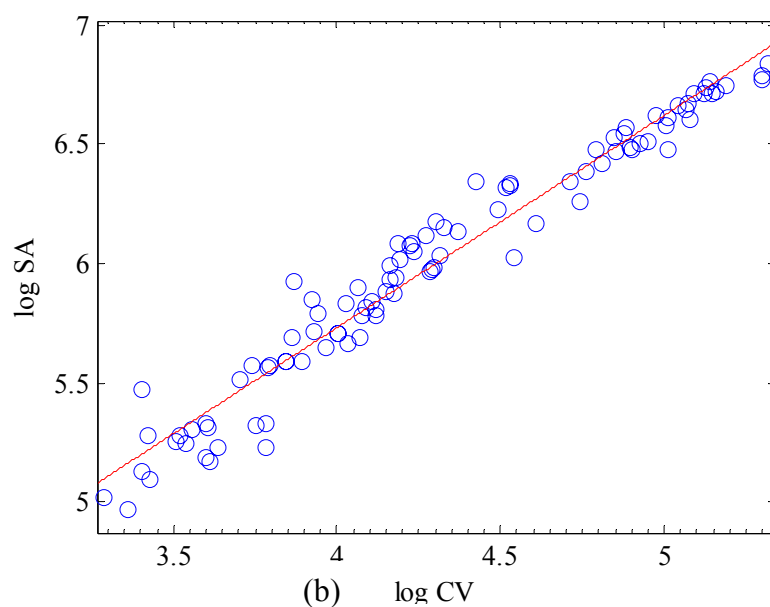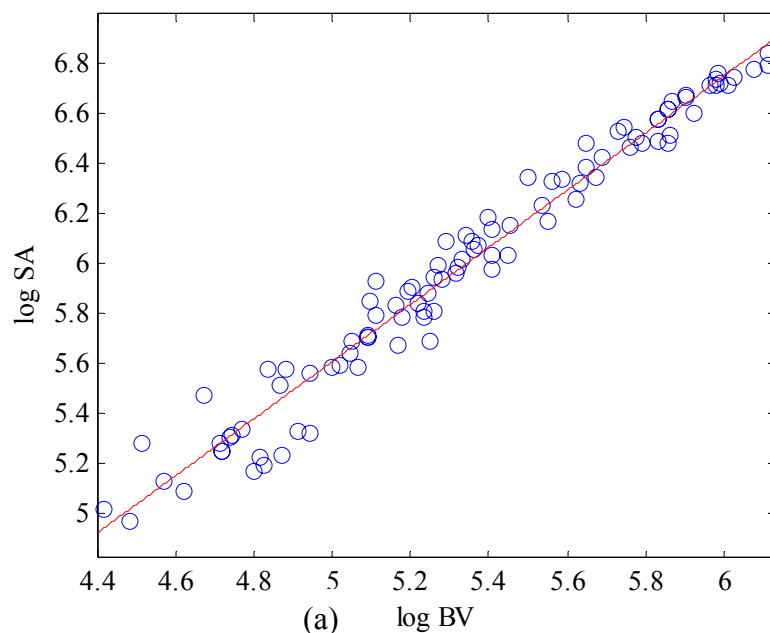
Figure 5.19. Scaling relationships in preterm infants including subjects with and without lesions during development. (a) Log-log plot of the cortical surface area (SA) against the total brain volume (BV). The regression equation is $\ln(SA) = 1.143 \times \ln(BV) - 0.1085$. (b) Similar plot of the SA to CV. The linear regression equation is $\ln(SA) = 0.8896 \times \ln(CV) + 2.172$.

5.5.4.6 Mean curvature, Convexity ratio and Isoperimetric ratio

These three measures (MC, CR and IPR) quantify the complexity of cortical folding pattern. As expected, the mean curvature increases with the gestational age at scan (Figure 5.20). The mean curvature rises from 0.33-1.2 mm^{-1}. The overall increase is significantly related to the GA ($r = 0.9189$, $P < 0.0001$), while the tendency starts to slow down after ~40 weeks.
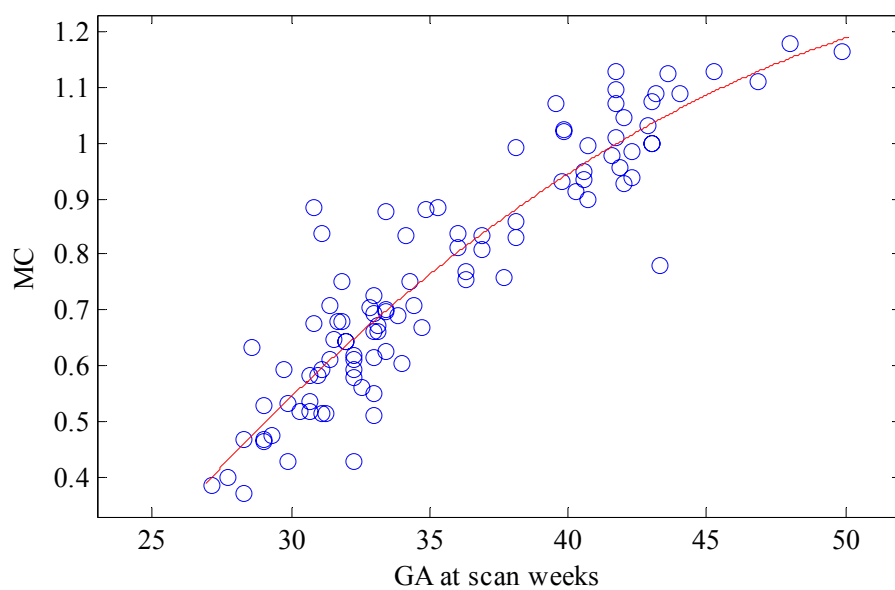
Figure 5.20. Mean curvature during development of the whole cohort. The mean curvature of the whole cohort of preterm infants increases with the gestation age.

The convexity ratio is given by the ratio of the cortical surface area and convex hull surface area. We have also observed a significant increase in CR with GA at scan as shown in Figure 5.21 ($r = 0.9072$, $P < 0.0001$).

The CR also tails off by ~40 weeks which agrees with the finding of mean curvature. This may suggest the increase of surface area begins to slow down at that stage.

The isoperimetric ratio ranges from 13-29 for all subjects. The isoperimetric ratio is rising until approx. 36 to 40 weeks (Figure 5.22), suggesting that at the early stage the increase in cortical area is much faster compared to the volume increase

and while the infants are more mature, the cortex tends to become thicker, not to develop more folds.
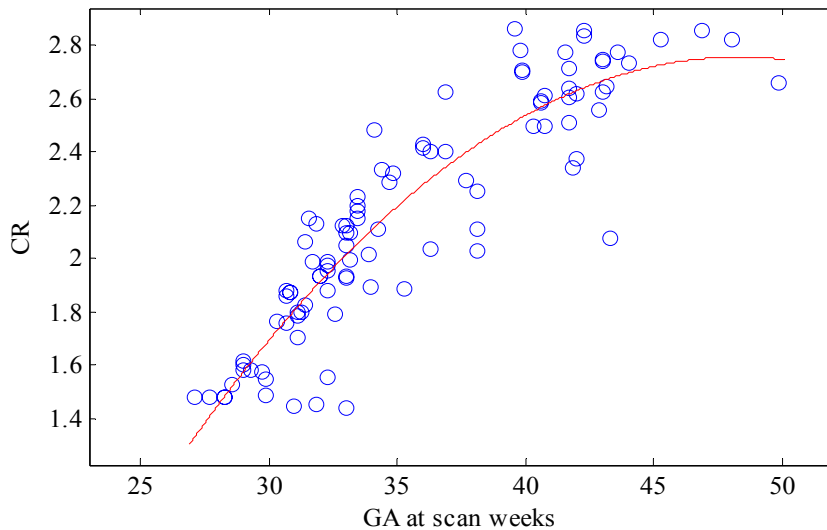
Figure 5.21. Convexity ratio during development of the whole cohort. Clear increase in convexity ratio of the whole cohort of preterm infants with gestational age at scan till 40 weeks is depicted.
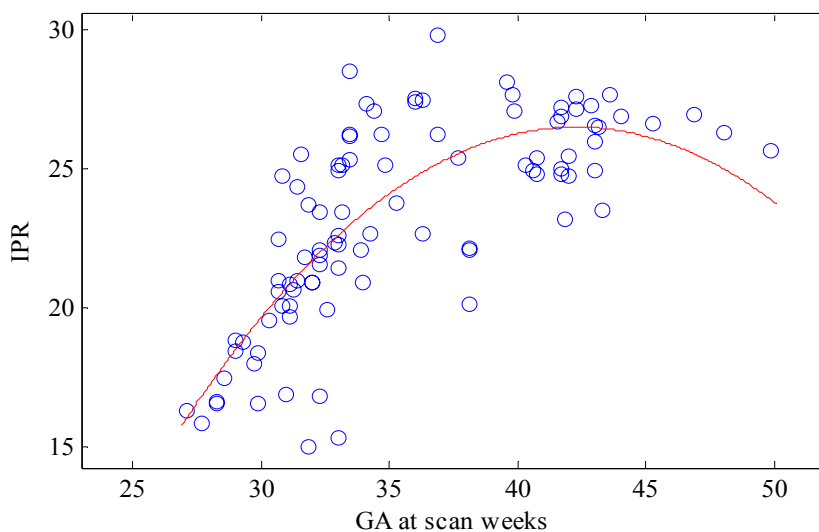
Figure 5.22. Isoperimetric ratio during development of the whole cohort. The rapid increase in IPR with gestational age at scan occurs until ~36 weeks.

5.5.4.7 Regional variations in cortical morphology

We have applied cortical parcellation to all subjects and the regional cortical volume, surface area are calculated. As expected, all four regions increase in

volume and area with GA, while the differences during the development of these cortical regions can be viewed in Figure 5.23.
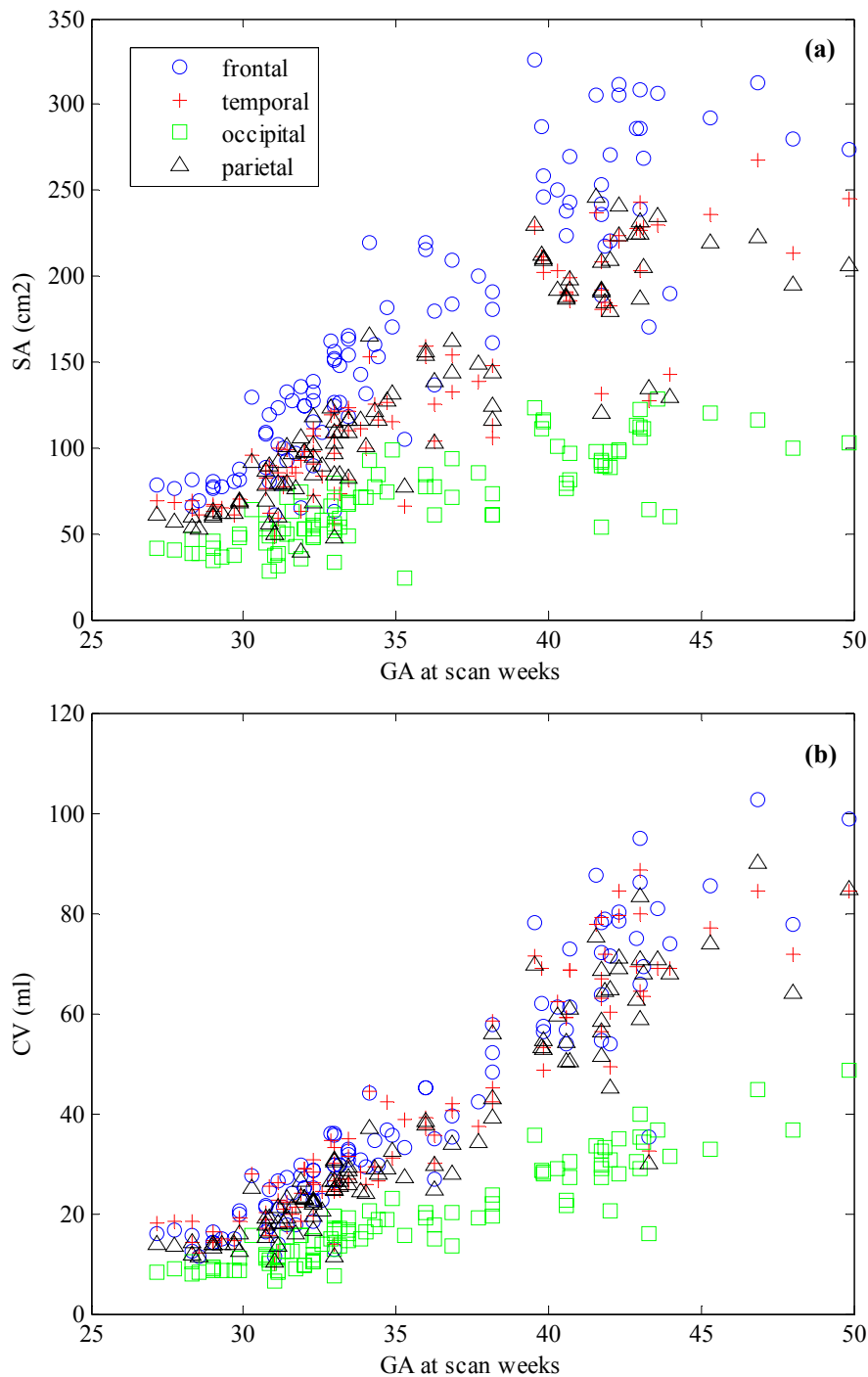
Figure 5.23. Regional cortical morphology of the whole cohort during development. (a) The frontal lobe shows increased SA compared to all other regions and the occipital is significantly reduced compared to the other lobes. (b) Cortical volumes show similar pattern although the temporal and parietal lobes are not significantly reduced compared to frontal lobe volume.

5.6 Discussion

In this chapter we have developed a method for cortical surface reconstruction using implicit surface evolution. This level-set based framework is able to generate a complete cortical surface representation, including the inner, central and outer surfaces of the cortex. The precision of the resulting extracted surfaces has been verified by direct comparison with manually positioned landmark points and found to be in agreement to within ~1 voxel for each of the inner and outer cortical boundaries. The cortical reconstruction has been applied to perform a preliminary quantitative study of different cortical morphological parameters on a large group of preterm infants with different gestational ages. The results of this preliminary analysis show systematic trends, which in themselves provide a form of validation of the method. The scaling laws found relating cortical surface to brain volume are in accord with previous work showing that surface area/volume growth in the brain during this period of development obeys an allometric scaling law of approximately 1.29 (Kapellou et al., 2006), while there is only marginal increase in cortical thickness.

Although the overall performance of the method is good, the precision of reconstructed outer cortex can be problematic in deep sulci. This is mainly due to the insufficient image resolution and tight sulci in the immature brains. The current solution integrated into the reconstruction pipeline is based on the detection of exterior inner cortical skeleton. If there are no clues of CSF, this method tends to split the gyral banks equally. Although this is a reasonable assumption without other image clues, the equidistant skeleton may not in fact agree with the real anatomical configuration of deep sulci. On the other hand, as the numerical scheme used to solve the level-set equation can only capture the features which are not smaller than 2 or 3 voxels, the very thin sulci generated by the skeleton enhancement may not be sufficient to stop the level-set front. This problem can be

partially solved by over-sampling the images; however this leads to higher computational costs. Due to the essential ambiguity for the outer cortical surface in the deep sulci from neonatal brain MR images, the inner cortical surface is used for further surface registration and cortex morphometry quantification.

The less than perfect recovery of deep sulci is related to thickness measures which are always affected by the CNR and spatial resolution. This might explain the limited increase of measured cortical thickness (TH) with increasing GA. It is worth mentioning that any validation of the TH measures requires careful post-mortem and 3D normal neonatal correlations. In the current study, we have emphasised global thickness measurements. However, regional variations in thickness within individual gyri and sulci may be more biologically interesting as they may give insight into the different cortical layers and in turn their functional significance when coupled with functional MR imaging (fMRI) data, which is one of the topics for our further exploration.

On the other hand, we have shown that with the effective cortical segmentation-reconstruction workflow developed, it is possible to perform automated neonatal cortical morphometry. Indeed these computerized techniques ease the workload for the human operator and even outperform the experts as many statistics can not be measured from manually labelled 2D slices, e.g. mean curvature and more complicated second-order statistics, i.e. MLN and ICI.

In this chapter we have also developed a cortical registration approach, which has the ability to track neonatal cortical development. This is of great importance in studying brain evolution in the early phase of human life. Unlike the methods based on spherical mapping or other intermediate coordinate transformation, the proposed algorithm aims to establish a direct point-to-point correspondence across different cortical surfaces. An adaptive surface inflation step is introduced to smooth out the less significant sulci and gyri. A quantitative validation of cortical registration is achieved by computing the overlap ratio between the automatically

labelled main sulci and manually established ground-truth. The direct nature of the proposed surface registration method allows the recovery of the cortical development trajectory.

The evaluation results in this chapter show that the non-rigid registration achieves better performance if the cortical surfaces are partially inflated. We hypothesize that partial inflation reduces the likelihood of the algorithm stopping in local optima of the surface similarity measure. This aids the registration performance. However, the inflation may smooth out the secondary sulci and other smaller features, which can limit the non-rigid surface deformation to only capture significant remaining features. This might be reduced by designing a knowledge-based surface similarity measure based on sulcus shape. Improving the surface initialization method may also reduce the degree of inflation needed for effective non-rigid registration. In the future we would like to apply this type of registration technique to both fetal and neonatal brains at different gestational ages in order to develop atlases of normal cortical growth patterns so that temporal events in altered cortical development of preterm infants can be identified.

5.7   Summary

In this chapter we developed a technique for neonatal cortical reconstruction by integrating the implicit surface evolution technique. A comprehensive landmark study is performed to evaluate the surface reconstruction. Isotropic reconstruction errors are less than 1 voxel. A cortical registration technique is also developed. We have shown the proposed strategy has the potentials to map the main sulcal features and cortical lobe labelling across multiple cerebral coordinate systems, which will favor the automated cortical tracking during the early phase of life.

This framework, to the best of our knowledge, is the first to successfully reconstruct cortical surface models from neonatal MRI. This serves as a starting

point for both longitudinal and cross-sectional studies of cortical morphology in the developing brain.

Chapter 6

Conclusion and Outlook

6.1 General conclusion

The main objective of this dissertation has been the development and validation of computerized techniques to model the cerebral anatomies in neonates. Specifically, we have focused on the following two challenges:

- Cortical segmentation and reconstruction of neonatal MRI. A complete cortex reconstruction framework has been developed to reconstruct the inner, central and outer cortical surfaces for neonates over a large range of gestational ages. This neonatal cortical reconstruction framework, to the best of our knowledge, is the first to successfully reconstruct cortical surface models from neonatal MRI. The key part of this framework is the automatic cortex segmentation algorithm which detects and corrects for mislabelled partial volume voxels that are a specific feature of neonatal MRI data because of the different contrast between GM and WM as compared to the adult pattern. An implicit surface evolution technique is employed to reconstruct the cortical surface based on the improved cortical GM segmentation. A comprehensive landmark study is performed to evaluate its accuracy. In addition a cortical registration technique is developed. The proposed strategy is capable of mapping main sulcal and cortical lobe labels across multiple cerebral coordinates, which makes the automated cortex tracking during the early phase of life feasible.

- Cerebral vasculature extraction and modelling of neonatal MRI. A methodology is presented for automatically extracting and matching cerebral vasculatures from MRA-TOF images. Its performance has been tested in neonates at various gestational ages. The extraction step consists of automatic seed generation, optimal scale estimation and a ridge transversal algorithm. Even when the SNR is low the proposed method is able to provide seeds covering the whole vessel tree allowing extraction of most visible vessels. The consistency of the vessel extraction in the presence of noise has been demonstrated by computing the averaged spatial distance between extracted vessel trees for different levels of noise. A vessel tree matching algorithm is developed for use in longitudinal studies. This allows the vasculatures of neonates at different ages to be compared in the presence of growth and development. The resulting tree matching algorithm is able to recover branch-by-branch correspondences and can highlight newly-developed vessel segments. With the computerized vasculature modelling in hand, 3D vessel morphology quantification can be performed. In the preliminary experiment, reduced tortuosity of middle cerebral artery (MCA) in pre-term infants has been demonstrated. This finding agrees with a previous clinical study, supporting the clinical applicability of proposed techniques.

The most difficulty of effectively validating proposed algorithms is related to the lack of ground-truth. In this dissertation, both quantitative and qualitative validations are performed. The former relies on the manually established ground-truth and the later is mainly based on visual inspection. Since the proposed techniques appear to generate good results in the initial experiments, they have been made accessible to all clinicians in our institute. It is hoped that routine use of proposed algorithms will help to enhance their clinical applicability and finally lead to a highly effective solution.

6.2   Future work

There are a number of interesting questions raised by the work presented in this dissertation, involving both the methodology development and clinical applications.

As for the methodology development, an unsolved challenge is to develop a spatio-temporal model of the human cerebral cortex during the early phase of brain development. The resulting spatio-temporal model will allow the proper parameterization of the cortical shape and patterns in terms of space and time. Once such a model is constructed, it is possible to compare the cortical surface of an individual subject with a population average, to predict the cortical development and to correlate cortical development with neuro-cognitive abilities. The construction of this model requires the accurate segmentation and reconstruction of the cortical surfaces for neonates with a range of gestational ages. It also requires effective cortical registration across subjects and gestational ages. Both of these challenges have been addressed in this dissertation. The next step is to apply the proposed technique to a representative large dataset and study the proper biological or mathematical models to combine the inter-subject variability of cortical development. The output will be a 4D cortical growth-map for neonates. A proper cortical growth interpolation scheme needs to be developed and validated to generate the growth between those time points at which the growth map is defined.

The idea to build the spatio-temporal cortical model can be extended to cover the whole cerebral area, which requires the effective delineation of central deep structures, e.g. thalamus and basal ganglia. As no published attempts to segment those tissues exist, more studies are required. The main difficulty in achieving a good segmentation of central deep tissues is the presence of partially myelinated WM. Although no mislabelled partial volume voxels appear, the contrast between myelinated WM and thalamus is far from satisfactory. This may prohibit intensity-based segmentation methods from being effective. However, as has been shown in chapter 4, non-rigid registration can perform well in these tissues because of less

curved geometrical shape and lower inter-subject variability. We propose to segment the subcortical regions using the label propagation based techniques which rely on the registration between the target image and a group of templates. For every template, the different tissue classes have been manually segmented and the labels are propagated into the new subject using the non-rigid registration. Normally a voting strategy is required to combine the information from multiple templates.

The work presented in this dissertation also enables clinical applications to study the neonatal brain development and quantify the influences of different pathologies. Among them is the subject of automated cortical morphometry. Although we have shown the automated cortical morphometric analysis is possible given the proposed segmentation-reconstruction workflow, no detailed studies have been performed to track the global or regional morphometric changes across different GA or pathological groups. With the help of cortical registration and mapping approaches, the morphometric quantification can be extended to track the changes for a specific cortical lobe or sulcal region, which present a clear improvement compared to the global measurement.

Both cerebral cortical surfaces and vasculatures can be extracted for a specific subject, which offers the unique opportunity to relate both anatomies. Although existing clinical studies have shown the preterm birth can delay the development of cortical surface and cause the less curved cerebral arteries, it is still unclear which phenomenon dominates the brain development. Also, it is expected that less curved arteries are correlated with delayed cortical development. This suspicion will need to be further examined as well.

The interactive stimulation between methodology development and clinical investigation will make benefits for both sides. We believe that the work presented in this dissertation will open new opportunities for researches of both developing

human brain and computational anatomy modelling, and will serve as a starting point for more novel studies.

Bibliography

Adalsteinsson, D., Rey, J., Sethian, J.A., 1997. Void Development in Plasma Enhanced CVD Models. Proceedings Third International Dielectrics for VLSI/ULCI Multilevel Interconnection Conference, Santa Clara, California.

Adalsteinsson, D., Sethian, J.A., 1995. A fast level set method for propagating interfaces. Journal of Computational Physics 118, 269-277.

Adalsteinsson, D., Sethian, J.A., 2002. Transport and Diffusion of Material Quantities on Propagating Interfaces via Level Set Methods. J.Comp.Phys. 185, 271-288.

Adamsbaum, C., 2007. Neonatal MRI and neurodevelopmental outcomes in preterm infants. J.Radiol. 88, 601-603.

Ajayi-Obe, M., Saeed, N., Cowan, F.M., Rutherford, M.A., Edwards, A.D., 2000. Reduced development of cerebral cortex in extremely preterm infants. Lancet 356, 1162-1163.

Angenent, S., Haker, S., Tannenbaum, A., Kikinis, R., 1999. On the Laplace-Beltrami operator and brain surface flattening. IEEE Trans Med Imaging 18, 700-711.

Anstrom, J.A., Brown, W.R., Moody, D.M., Thore, C.R., Challa, V.R., Block, S.M., 2002. Anatomical analysis of the developing cerebral vasculature in premature neonates: absence of precapillary arteriole-to-venous shunts. Pediatr.Res. 52, 554-560.

Arnaud, C., Vincent, A., Grégoire, M., Stéphane, N., Mohamed, T., Luc, S., 2005. Design of Robust Vascular Tree Matching: Validation on Liver. Proc.Information Processing in Medical Imaging, 443-455.

Ashburner, J., 2000. Computational Neuroanatomy. PhD Thesis, University College London.

Ashburner, J., Friston, K.J., 2000. Voxel-based morphometry--the methods. Neuroimage. 11, 805-821.

Axel, L., Costantini, J., Listerud, J., 1987. Intensity correction in surface-coil MR imaging. AJR Am.J.Roentgenol. 148, 418-420.

Aylward, S.R., Bullitt, E., 2002. Initialization, noise, singularities, and scale in height ridge traversal for tubular object centerline extraction. IEEE Trans.Med.Imaging 21, 61-75.

Aylward, S.R., Bullitt, E., Pizer, S.M., 1996. Intensity ridge and widths for tubular object segmentation and registration. IEEE Workshop on Mathematical Methods in Biomedical Image Analysis, 131-138.

Bajcsy, R., Kovacic, S., 1989. Multiresolution elastic matching. Comp Vision Graphics Image Processing 46, 1-21.

Barkovich, A.J., Simon, E.M., Clegg, N.J., Kinsman, S.L., Hahn, J.S., 2002. Analysis of the cerebral cortex in holoprosencephaly with attention to the sylvian fissures. AJNR Am.J.Neuroradiol. 23, 143-150.

Batchelor, P.G., Castellano Smith, A.D., Hill, D.L., Hawkes, D.J., Cox, T.C., Dean, A.F., 2002. Measures of folding applied to the development of the human fetal brain. IEEE Trans.Med.Imaging 21, 953-965.

Bayer, S.A., Altman, J., 2004. The Human Brain During the Third Trimester. CSC press.

Bayer, S.A., Altman, J., 2005. The Human Brain During The Second Trimester. CSC press.

Beatty, J., 2001. The Human Brain: Essentials of Behavioral Neuroscience. Sage Publications Inc., California.

Besl, P., Mckay, N., 1992. A Method for Registration of 3-D Shapes. IEEE Trans.Pattern Analysis and Machine Intelligence 14, 239-256.

Boardman, J.P., Counsell, S.J., Rueckert, D., Kapellou, O., Bhatia, K.K., Aljabar, P., Hajnal, J., Allsop, J.M., Rutherford, M.A., Edwards, A.D., 2006. Abnormal deep grey matter development following preterm birth detected using deformation-based morphometry. Neuroimage. 32, 70-78.

Boardman, J.P., Dyet, L.E., 2007. Recent advances in imaging preterm brain injury. Minerva Pediatr. 59, 349-368.

Boesen K, Rehm K, Schaper K, Stoltzner S, Woods R, Luders E, Rottenberg, D., 2004. Quantitative Comparison of Four Brain Extraction Algorithms. Neuroimage 22, 1255-1261.

Brey, W.W., Narayana, P.A., 1988. Correction for intensity falloff in surface coil MRI. Medical Physics 15, 245.

Bullitt, E., Aylward, S., Smith, K., Mukherji, S., Jiroutek, M., Muller, K., 2001. Symbolic description of intracerebral vessels segmented from magnetic resonance angiograms and evaluation by comparison with X-ray angiograms. Med.Image Anal. 5, 157-169.

Bullitt, E., Ewend, M.G., Aylward, S., Lin, W., Gerig, G., Joshi, S., Jung, I., Muller, K., Smith, J.K., 2004. Abnormal vessel tortuosity as a marker of treatment response of malignant gliomas: preliminary report. Technol.Cancer Res.Treat. 3, 577-584.

Bullitt, E., Gerig, G., Aylward, S., 2003a. Vascular Attributes and Malignant Brain Tumors. MICCAI, 671-679.

Bullitt, E., Gerig, G., Pizer, S.M., Lin, W., Aylward, S.R., 2003b. Measuring tortuosity of the intracerebral vasculature from MRA images. IEEE Trans.Med.Imaging 22, 1163-1171.

Bullitt, E., Muller, K.E., Jung, I., Lin, W., Aylward, S., 2005a. Analyzing attributes of vessel populations. Med.Image Anal. 9, 39-49.

Bullitt, E., Zeng, D., Gerig, G., Aylward, S., Joshi, S., Smith, J.K., Lin, W., Ewend, M.G., 2005b. Vessel tortuosity and brain tumor malignancy: a blinded study. Acad.Radiol. 12, 1232-1240.

Canny, J.F., 1986. A computational approach to edge detection. IEEE Trans Pattern Analysis and Machine Intelligence 8, 679-698.

Carman, G.J., Drury, H.A., Van, E., 1995. Computational methods for reconstructing and unfolding the cerebral cortex. Cereb.Cortex 5, 506-517.

Chapman, B.E., Parker, D.L., 2005. 3D multi-scale vessel enhancement filtering based on curvature measurements: application to time-of-flight MRA. Medical Image Analysis 9, 191-208.

Chen, L., Wagenknecht, G., 2006. Automated topology correction for human brain segmentation. Med.Image Comput.Comput.Assist.Interv.Int.Conf.Med.Image Comput.Comput.Assist.Interv. 9, 316-323.

Chen, S., Merriman, B., Osher, S., Smereka, P., 1997. A Simple Level Set Method For Solving Stefan Problems. Journal of Computational Physics 135, 8-29.

Choi, H.S., Haynor, D.R., Kim, Y., 1991. Partial volume tissue classification of multichannel magnetic resonance images—A mixed model. IEEE Trans.Med.Imaging 10, 395-407.

Christensen, G.E., Rabbitt, R.D., Miller, M.I., 1996. Deformable templates using large deformation kinematics. IEEE Transactions on Image Processing 5, 1435-1447.

Chui, H., Rambo, J., Duncan, J.S., Schultz, R.T., Rangarajan, A., 1999. Registration of Cortical Anatomical Structures via Robust 3D Point Matching. Proc.of Image Processing in Medical Imaging, 168-181.

Cocosco, C.A., Kollokian, V., Kwan, R.K.S., Evans, A.C., 1997. BrainWeb: online interface to a 3D MRI simulated brain database. Neuroimage. 5, 425.

Cocosco, C.A., Zijdenbos, A.P., Evans, A.C., 2003. A fully automatic and robust brain MRI tissue classification method. Med Image Anal. 7, 513-527.

Collins, D.L., Neelin, P., 1994. Data in Standardized Talairach Space. J.Comput.Assist.Tomogr. 18, 292-205.

Collins, D.L., Zijdenbos, A.P., Kollokian, V., Sled, J.G., Kabani, N.J., Holmes, C.J., Evans, A.C., 1998. Design and construction of a realistic digital brain phantom. IEEE Trans.Med.Imaging 17, 463-468.

Cootes, T.F., Edwards, G.J., Taylor, C.J., 2001. Active Appearance Models. IEEE Transactions on Pattern Analysis and Machine Intelligence 23, 681-685.

Cootes, T.F., Taylor, C.J., 1992. Active shape models. Springer-Verlag, 266-275.

Cootes, T.F., Taylor, C.J., 2004. Anatomical statistical models and their role in feature extraction. Br.J.Radiol. 77 Spec No 2, S133-S139.

Counsell, S.J., Boardman, J.P., 2005. Differential brain growth in the infant born preterm: current knowledge and future developments from brain imaging. Semin.Fetal Neonatal Med. 10, 403-410.

Counsell, S.J., Dyet, L.E., Larkman, D.J., Nunes, R.G., Boardman, J.P., Allsop, J.M., Fitzpatrick, J., Srinivasan, L., Cowan, F.M., Hajnal, J.V., Rutherford, M.A., Edwards, A.D., 2007. Thalamo-cortical connectivity in children born preterm mapped using probabilistic magnetic resonance tractography. Neuroimage. 34, 896-904.

Counsell, S.J., Rutherford, M.A., Cowan, F.M., Edwards, A.D., 2003. Magnetic resonance imaging of preterm brain injury. Arch.Dis.Child Fetal Neonatal Ed 88, F269-F274.

Counsell, S.J., Shen, Y., Boardman, J.P., Larkman, D.J., Kapellou, O., Ward, P., Allsop, J.M., Cowan, F.M., Hajnal, J.V., Edwards, A.D., Rutherford, M.A., 2006. Axial and radial diffusivity in preterm infants who have diffuse white matter changes on magnetic resonance imaging at term-equivalent age. Pediatrics 117, 376-386.

Cox R., 1999. AFNI software. http://afni.nimh.nih.gov.

d'Orey, C., Mateus, M., Guimaraes, H., Ramos, I., Melo, M.J., Silva, J., Ramos, E., Montenegro, N., Barros, H., Santos, N., 1999. Neonatal cerebral Doppler: arterial and venous flow velocity measurements using color and pulsed Doppler system. J.Perinat.Med. 27, 352-361.

Dale, A.M., Fischl, B., Sereno, M.I., 1999. Cortical surface-based analysis. I. Segmentation and surface reconstruction. Neuroimage 9, 179-194.

Davatzikos, C., 1997. Spatial Transformation and Registration of Brain Images Using Elastically Deformable Models. Computer Vision and Image Understanding 66, 207-222.

Davatzikos, C., Bryan, R.N., 1996. Using a deformable surface model to obtain a shape representation of the cortex. IEEE Trans Med Imaging 15, 785-795.

Dawant, B.M., Zijdenbos, A.P., Margolin, R.A., 1993. Correction of intensity variations in MR images for computer-aided tissue classification. IEEE Trans Med.Imaging 12, 781.

Dempster, A.P., Laird, N.M., Rubin, D.B., 1977. Maximum likelihood from incomplete data via the EM algorithm. Journal of the Royal Statistical Society 39, 1-38.

Dice, L.R., 1945. Measures of the amount of ecologic association between species. Ecology 26, 297-302.

Drury, H.A., Van, E., Anderson, C.H., Lee, C.W., Coogan, T.A., Lewis, J.W., 1996. Computerized mappings of the cerebral cortex: a multiresolution flattening method and a surface-based coordinate system. J.Cogn Neurosci. 8, 1-28.

Eberly, D., 1996. Ridges in Image and Data Analysis. Dordrecht, The Netherlands: Kluwer Academic.

Edwards, W.T., Zheng, Y., Ferrara, L.A., Yuan, H.A., 2001. Structural features and thickness of the vertebral cortex in the thoracolumbar spine. Spine 26, 218-225.

Elfadel, I.M., Picard, R.W., 1994. Gibbs Random Fields, Cooccurrences, and Texture Modeling. IEEE Transactions on Pattern Analysis and Machine Intelligence 16, 24-37.

Evans, A.C., Marrett, S., Neelin, P., Gum, T., Dai, W., Milot, S., Meyer, E., Bub, D., 1992. Anatomical mapping of functional activation in stereotactic coordinate space. Neuroimage 1, 43-53.

Farkas, E., Luiten, P.G., 2001. Cerebral microvascular pathology in aging and Alzheimer's disease. Prog.Neurobiol. 64, 575-611.

Fischl, B., Dale, A.M., 2000. Measuring the thickness of the human cerebral cortex from magnetic resonance images. Proc.Natl.Acad.Sci.U.S.A 97, 11050-11055.

Fischl, B., Liu, A., Dale, A.M., 2001. Automated manifold surgery: constructing geometrically accurate and topologically correct models of the human cerebral cortex. IEEE Trans.Med.Imaging 20, 70-80.

Fischl, B., Sereno, M.I., Dale, A.M., 1999a. Cortical surface-based analysis. II: Inflation, flattening, and a surface-based coordinate system. Neuroimage 9, 195-207.

Fischl, B., Sereno, M.I., Tootell, R.B., Dale, A.M., 1999b. High-resolution intersubject averaging and a coordinate system for the cortical surface. Hum.Brain Mapp. 8, 272-284.

Fornito, A., Wood, S.J., Whittle, S., Fuller, J., Adamson, C., Saling, M.M., Velakoulis, D., Pantelis, C., Yucel, M., 2007. Variability of the paracingulate sulcus and morphometry of the medial frontal cortex: Associations with cortical thickness, surface area, volume, and sulcal depth. Hum.Brain Mapp.

Fox, N.C., Schott, J.M., 2004. Imaging cerebral atrophy: normal ageing to Alzheimer's disease. Lancet 363, 392-394.

Frangi, A.F., Niessen, W.J., Hoogeveen, R.M., van, W.T., Viergever, M.A., 1999. Model-based quantitation of 3-D magnetic resonance angiographic images. IEEE Trans.Med.Imaging 18, 946-956.

Frangi, A.F., Niessen, W.J., Nederkoorn, P.J., Bakker, J., Mali, W.P., Viergever, M.A., 2001. Quantitative analysis of vascular morphology from 3D MR angiograms: In vitro and in vivo results. Magn Reson.Med. 45, 311-322.

Frangi, A.F., Niessen, W.J., Vincken, L., Viergever, M.A., 1998. Muliscale Vessel Enhancement Filtering. Proc. MICCAI, 130-137.

Gerig, G., Koller, T., Szekely, G., Brechbuhler, C., Kubler, O., 1993. Symbolic description of 3-d structures applied to cerebral vessel tree obtained from MR angiography volume data. Lecture Notes in Computer Science 687, 94-111.

Gerig, G., Kubler, O., Kikinis, R., Jolesz, F., 1992. Nonlinear anisotropic filtering of MRI data. IEEE Trans Med.Imaging 11, 221-232.

Gilmore, J.H., Lin, W., Prastawa, M.W., Looney, C.B., Vetsa, Y.S., Knickmeyer, R.C., Evans, D.D., Smith, J.K., Hamer, R.M., Lieberman, J.A., Gerig, G., 2007. Regional gray matter growth, sexual dimorphism, and cerebral asymmetry in the neonatal brain. J Neurosci. 27, 1255-1260.

Gogtay, N., Sporn, A., Clasen, L.S., Greenstein, D., Giedd, J.N., Lenane, M., Gochman, P.A., Zijdenbos, A., Rapoport, J.L., 2003. Structural brain MRI abnormalities in healthy siblings of patients with childhood-onset schizophrenia. Am.J.Psychiatry 160, 569-571.

Goldenberg, R., Kimmel, R., Rivlin, E., 2001. Fast geodesic active contours. IEEE Trans.Image Processing 10, 1467-1475.

Goldenberg, R., Kimmel, R., Rivlin, E., Rudzsky, M., 2002. Cortex segmentation: a fast variational geometric approach. IEEE Trans.Med.Imaging 21, 1544-1551.

Goldszal, A.F., Davatzikos, C., Pham, D.L., Yan, M., Bryan, R.N., Resnick, S.M., 1998. An image processing protocol for the analysis of MR images from an elderly population. J.Computer-Assisted Tomogr. 22, 827-837.

Griffin, L.D., 1994. The intrinsic geometry of the cerebral cortex. J.Theor.Biol. 166, 261-273.

Griffin, L.D., Colchester, A.C.F., 1995. Superficial and deep structure in linear diffusion scale space: isophotes, critical points and separatrices. Image and Vision Computing 13, 543-557.

Gu, X., Wang, Y., Chan, T.F., Thompson, P.M., Yau, S.T., 2003. Genus zero surface conformal mapping and its application to brain surface mapping. Inf.Process Med Imaging 18, 172-184.

Gu, X., Wang, Y., Chan, T.F., Thompson, P.M., Yau, S.T., 2004. Genus zero surface conformal mapping and its application to brain surface mapping. IEEE Trans Med Imaging 23, 949-958.

Gueziec, A., Hummel, R., 1995. Exploiting triangulated surface extraction using tetrahedral decomposition. IEEE Trans.Vis.Comput.Graph. 1, 328-334.

Guillemaud, R., Brady, M., 1997. Estimating bias field of MR images. IEEE Trans Med.Imaging 16, 238-251.

Haacke, E.M., Brown, R.W., Thompson, M.R., 1999. Magnetic Resonance Imaging: Physical Principles and Sequence Design. Wiley and Sons.

Hack, M., Flannery, D.J., Schluchter, M., Cartar, L., Borawski, E., Klein, N., 2002. Outcomes in young adulthood for very-low-birth-weight infants. N.Engl.J.Med. 346, 149-157.

Hajnal, J.V., 2001. Medical Image Registration. CRC Press.

Han, X., Jovicich, J., Salat, D., van der, K.A., Quinn, B., Czanner, S., Busa, E., Pacheco, J., Albert, M., Killiany, R., Maguire, P., Rosas, D., Makris, N., Dale, A., Dickerson, B., Fischl, B., 2006. Reliability of MRI-derived measurements of human cerebral cortical thickness: the effects of field strength, scanner upgrade and manufacturer. Neuroimage 32, 180-194.

Han, X., Pham, D.L., Tosun, D., Rettmann, M.E., Xu, C., Prince, J.L., 2004. CRUISE: cortical reconstruction using implicit surface evolution. Neuroimage. 23, 997-1012.

Han, X., Xu, C., Braga-Neto, U., Prince, J.L., 2002. Topology correction in brain cortex segmentation using a multiscale, graph-based algorithm. IEEE Trans.Med.Imaging 21, 109-121.

Han, X., Xu, C., Braga-Neto, U., Prince, J.L., 2001. Graph-Based Topology Correction for Brain Cortex Segmentation. Proc.of Image Processing in Medical Imaging, 395-401.

Han, X., Xu, C.Y., Prince, J.L., 2003. A topology preserving level set method for geometric deformable models. IEEE Transactions on Pattern Analysis and Machine Intelligence 25, 755-768.

Haralick, R.M., 1983. Ridges and valleys in digital images. Computer Vision & Graphic Image Processing 22, 25-38.

Haselgrove, C., Prammer, M., 1986. An algorithm for compensation of surface-coil images for sensitivity of the surface coil. Magn Reson Imaging 4, 469-472.

Hogea, C.S., Murray, B.T., Sethian, J.A., 2005. Computational Modeling of Solid Tumor Evolution via a General Cartesian Mesh/level set method. 1 ed.

Hohne, K., Hanson, W., 1992. Interactive 3D segmentation of MRI and CT volumes using morphological operations. J.Comput.Assist.Tomogr. 16, 185-294.

Huppertz, H.J., Kassubek, J., Altenmuller, D.M., Breyer, T., Fauser, S., 2007. Automatic curvilinear reformatting of three-dimensional MRI data of the cerebral cortex. Neuroimage.

Huppi, P.S., Inder, T.E., 2001. Magnetic resonance techniques in the evaluation of the perinatal brain: recent advances and future directions. Semin.Neonatol. 6, 195-210.

Huppi, P.S., Warfield, S., Kikinis, R., Barnes, P.D., Zientara, G.P., Jolesz, F.A., Tsuji, M.K., Volpe, J.J., 1998. Quantitative magnetic resonance imaging of brain development in premature and mature newborns. Ann.Neurol. 43, 224-235.

Husain, A.M., Smergel, E., Legido, A., Faerber, E.N., Foley, C.M., Miles, D.K., Grover, W.D., 2000. Comparison of MRI and MRA findings in children with a variety of neurologic conditions. Pediatr.Neurol. 23, 307-311.

Ian Mitchell, 2005. A Toolbox of Level Set Methods, 1,1 ed. www.cs.ubc.ca/~mitchell/ToolboxLS/index.html.

Inder, T.E., Huppi, P.S., 2000. In vivo studies of brain development by magnetic resonance techniques. Ment.Retard.Dev.Disabil.Res.Rev. 6, 59-67.

Inder, T.E., Warfield, S.K., Wang, H., Huppi, P.S., Volpe, J.J., 2005. Abnormal cerebral structure is present at term in premature infants. Pediatrics 115, 286-294.

Inder, T.E., Wells, S.J., Mogridge, N.B., Spencer, C., Volpe, J.J., 2003. Defining the nature of the cerebral abnormalities in the premature infant: a qualitative magnetic resonance imaging study. J.Pediatr. 143, 171-179.

Isaacs, E.B., Edmonds, C.J., Lucas, A., Gadian, D.G., 2001. Calculation difficulties in children of very low birthweight: a neural correlate. Brain 124, 1701-1707.

Ising, E., 1925. Beitrag zur Theorie des Ferromagnetismus. Zeitschrift fˇur Physik 31, 258.

Jiang, S., Xue, H., Glover, A., Rutherford, M., Rueckert, D., Hajnal, J.V., 2007. MRI of moving subjects using multislice snapshot images with volume reconstruction (SVR): application to fetal, neonatal, and adult brain studies. IEEE Trans.Med.Imaging 26, 967-980.

Jones, R.A., Palasis, S., Grattan-Smith, J.D., 2004. MRI of the neonatal brain: optimization of spin-echo parameters. AJR Am.J.Roentgenol. 182, 367-372.

Joshi, M., Cui, J., Doolittle, K., Joshi, S., Essen, D., Wang, L., Miller, M.I., 1999. Brain segmentation and the generation of cortical surfaces. Neuroimage 9, 461-476.

Kapellou, O., Counsell, S.J., Kennea, N., Dyet, L., Saeed, N., Stark, J., Maalouf, E., Duggan, P., jayi-Obe, M., Hajnal, J., Allsop, J.M., Boardman, J., Rutherford, M.A., Cowan, F., Edwards, A.D., 2006. Abnormal cortical development after premature birth shown by altered allometric scaling of brain growth. PLoS.Med. 3, e265.

Karp, E., Vigário, R., 2004. Unsupervised MRI Tissue Classification by Support Vector Machines.

Kim, J., Crespo-Facorro, B., Andreasen, N.C., O'Leary, D.S., Zhang, B., Harris, G., Magnotta, V.A., 2000. An MRI-based parcellation method for the temporal lobe. Neuroimage 11, 271-288.

Kim, J.S., Singh, V., Lee, J.K., Lerch, J., Ad-Dab'bagh, Y., MacDonald, D., Lee, J.M., Kim, S.I., Evans, A.C., 2005. Automated 3-D extraction and evaluation of the inner and outer cortical surfaces using a Laplacian map and partial volume effect classification. Neuroimage 27, 210-221.

Kimmel, R., Sethian, J.A., 1998. Fast Marching Methods on Triangulated Domains. Proceedings of the National Academy of Sciences, 8341-8435.

Kirbas, C., Quek, F., 2004. A Review of Vessel Extraction Techniques and Algorithms. ACM Computing Surveys 36, 81-121.

Kochunov, P., Mangin, J.F., Coyle, T., Lancaster, J., Thompson, P., Riviere, D., Cointepas, Y., Regis, J., Schlosser, A., Royall, D.R., Zilles, K., Mazziotta, J., Toga, A., Fox, P.T., 2005. Age-related morphology trends of cortical sulci. Hum.Brain Mapp. 26, 210-220.

Kostovic, I., Judas, M., 2006. Prolonged coexistence of transient and permanent circuitry elements in the developing cerebral cortex of fetuses and preterm infants. Dev.Med.Child Neurol. 48, 388-393.

Kriegeskorte, R., Goebel, R., 2001. An Efficient Algorithm for Topologically Correct Segmentation of the Cortical Sheet in Anatomical MR Volumes. Neuroimage 14, 329-346.

Krissian, K., Malandain, G., Ayache, N., Vaillant, R., Trousset, Y., 1998. Model-Based Detection of Tubular Structures in 3D Images. Proc. CVPR, 722-727.

Krissian, K., Malandain, G., Ayache, N., Vaillant, R., Trousset, Y., 2000. Model-Based Detection of Tubular Structures in 3D Images. Computer Vision and Image Understanding 80, 130-171.

Kruggel, F., Bruckner, M.K., Arendt, T., Wiggins, C.J., von Cramon, D.Y., 2003. Analyzing the neocortical fine-structure. Med.Image Anal. 7, 251-264.

Langan, D.A., Molnar, K.J., Modestino, J.W., Zhang, J., 1992. Use of the mean-field approximation in an EM-based approach to unsupervised stochastic model-based image segmentation. Proceedings on ICASSP, 57-60.

Le, G.G., Procyk, E., Collins, D.L., Venugopal, R., Barillot, C., Evans, A.C., 1999. Automated extraction and variability analysis of sulcal neuroanatomy. IEEE Trans Med Imaging 18, 206-217.

Lee, S., Wolberg, G., Chwa, K.-Y., Shin, S.Y., 1996. Image metamorphosis with scattered feature constraints. IEEE Trans.Visualization Comput.Graph. 2, 337-354.

Lemieux, L., Hagemann, G., Krakow, K., Woermann, F.G., 1999. Fast, accurate, and reproducible automatic segmentation of the brain in T1-weighted volume MRI data. Magn Reson Med 42, 127-135.

Lerch, J.P., Pruessner, J., Zijdenbos, A.P., Collins, D.L., Teipel, S.J., Hampel, H., Evans, A.C., 2006. Automated cortical thickness measurements from MRI can accurately separate Alzheimer's patients from normal elderly controls. Neurobiol.Aging. 29, 23-30.

Li, S.Z., 1995. Markov Random Field Modeling in Computer Vision. Springer-Verlag.

Lindeberg, T., 1998. Feature detection with automatic scale selection. International Journal of Computer Vision 30, 77-116.

Liu, T., Shen, D., Davatzikos, C., 2004a. Deformable registration of cortical structures via hybrid volumetric and surface warping. NeuroImage 22, 1790-1801.

Liu, T., Shen, D., Davatzikos, C., 2004b. Deformable registration of cortical structures via hybrid volumetric and surface warping. NeuroImage 22, 1790-1801.

Lorensen, W.E., Cline, H.E., 1987. Marching Cubes: A High-Resolution 3D Surface Construction Algorithm. ACM Computer Graphics 21, 163-170.

Lorenz, C., Carlsen, I.C., Buzug, T.M., Fassnacht, C., Weese, J., 1997. Multi-scale line segmentation with automatic estimation of width, contrast and tangential direction in 2D and 3D medical images. Proc.CVRMed-MRCAS. 233-242.

Lorigo, L.M., Grimson, W., Eric, L., Faugeras, O., Keriven, R., Kikinis, R., Nabavi, A., Westin, C.F., 1999. Co-dimension 2 geodesic active contours for MRA segmentation. Proc. 16th Infom.Processing Med.Imaging. 126-139.

Lorigo, L.M., Grimson, W., Eric, L., Faugeras, O., Keriven, R., Kikinis, R., Nabavi, A., Westin, C.F., 2000. Two geodesic active contours for the segmentation of tubular structures. Proc. CVPR. 444-451.

Luo, L.M., Hamitouche, C., Dillenseger, J.L., Coatrieux, J.L., 1993. A moment based 3D edge operator. IEEE Trans Med Imaging 40, 693-703.

Maalouf, E.F., Duggan, P.J., Rutherford, M.A., Counsell, S.J., Fletcher, A.M., Battin, M., Cowan, F., Edwards, A.D., 1999. Magnetic resonance imaging of the brain in a cohort of extremely preterm infants. J.Pediatr. 135, 351-357.

MacDonald, D., Kabani, N., Avis, D., Evans, A.C., 2000. Automated 3-D extraction of inner and outer surfaces of cerebral cortex from MRI. Neuroimage 12, 340-356.

Magnotta, V.A., Andreasen, N.C., Schultz, S.K., Harris, G., Cizadlo, T., Heckel, D., Nopoulos, P., Flaum, M., 1999. Quantitative in vivo measurement of gyrification in the human brain: changes associated with aging. Cereb.Cortex 9, 151-160.

Malamateniou, C., Counsell, S.J., Allsop, J.M., 2005. Optimized Magnetic Resonance Angiography at 3 Tesla for neonates. Proceedings of International Society of Magnetic Resonance in Medicine. Miami, USA.

Malamateniou, C., Counsell, S.J., Allsop, J.M., Fitzpatrick, J.A., Srinivasan, L., Cowan, F.M., Hajnal, J.V., Rutherford, M.A., 2006. The effect of preterm birth on neonatal cerebral vasculature studied with magnetic resonance angiography at 3 Tesla. Neuroimage. 32, 1050-1059.

Manceaux-Demiau, A., Bryan, R.N., Davatzikos, C., 1998. A probabilistic ribbon model for shape analysis of the cerebral sulci: application to the central sulcus. J.Comput.Assist.Tomogr. 22, 962-971.

Manniesing, R., Niessen, W.J., 2005. Multiscale Vessel Enhancing Diffusion in CT Angiography Noise Filtering. Proc. IPMI, 138-149.

Marlow, N., Wolke, D., Bracewell, M.A., Samara, M., 2005. Neurologic and developmental disability at six years of age after extremely preterm birth. N.Engl.J.Med. 352, 9-19.

Marr, D., Hildreth, E., 1980. Theory of edge detection. Proceedings of the Royal Society London 207, 187-217.

Martinussen, M., Fischl, B., Larsson, H.B., Skranes, J., Kulseng, S., Vangberg, T.R., Vik, T., Brubakk, A.M., Haraldseth, O., Dale, A.M., 2005. Cerebral cortex thickness in 15-year-old adolescents with low birth weight measured by an automated MRI-based method. Brain 128, 2588-2596.

Masutani, Y., Kurihara, T., Suzuki, M., 1995. Quantitative vascular shape analysis for 3D MR-angiography using mathematical morphology. Proc.Int.Conf.Computer Vision, Virtual Reality and Robotics, 449-454.

McCormick, M.C., Brooks-Gunn, J., Workman-Daniels, K., Turner, J., Peckham, G.J., 1992. The health and developmental status of very low-birth-weight children at school age. JAMA 267, 2204-2208.

McCormick, M.C., Workman-Daniels, K., Brooks-Gunn, J., 1996. The behavioral and emotional well-being of school-age children with different birth weights. Pediatrics 97, 18-25.

Meyer, C.R., Bland, P.H., Pipe, J., 1995. Retrospective correction of intensity inhomogeneities in MRI. IEEE Trans Med.Imaging 14, 36-41.

Miga, M.I., Sinha, T.K., Cash, D.M., Galloway, R.L., Weil, R.J., 2003. Cortical surface registration for image-guided neurosurgery using laser-range scanning. IEEE Trans Med Imaging 22, 973-985.

Murphy, B.P., Inder, T.E., Huppi, P.S., Warfield, S., Zientara, G.P., Kikinis, R., Jolesz, F.A., Volpe, J.J., 2001a. Impaired cerebral cortical gray matter growth after treatment with dexamethasone for neonatal chronic lung disease. Pediatrics 107, 217-221.

Murphy, M., O'Brien, T.J., Morris, K., Cook, M.J., 2001b. Multimodality image-guided epilepsy surgery. J.Clin.Neurosci. 8, 534-538.

Nakajima, S., Atsumi, H., Kikinis, R., Moriarty, T.M., Metcalf, D.C., Jolesz, F.A., Black, P.M., 1997. Use of cortical surface vessel registration for image-guided neurosurgery. Neurosurgery 40, 1201-1208.

Narayana, P.A., Borthakur, A., 1995. Effect of radio frequency inhomogeneity correction on the reproducibility of intra-cranial volumes using MR image data. Magn Reson Imaging 33, 400.

Narayana, P.A., Brey, W.W., Kulkarni, M.V., Sievenpiper, C.L., 1988. Compensation for surface coil sensitivity variation in magnetic resonance imaging. Magn Reson Imaging 6, 271-274.

Neil, J.J., Inder, T.E., 2004. Imaging perinatal brain injury in premature infants. Semin.Perinatol. 28, 433-443.

Niessen, W.J., Montauban, A.D., Swijndregt, V., Elsman, B., Wink, O., Mali, W., Viergever, M.A., 1999. Artery Visualization in Blood Pool MRA: Results in the Peripheral Vasculature. Proc. of IPMI, 340-345.

Nishida, M., Nikolaos Makris, David N.Kennedy, Mark Vangel, Bruce Fischl, Kalpathy S.Krishnamoorthy, Verne S.Caviness, P.Ellen Grant, 2007. Detailed semiautomated MRI based morphometry of the neonatal brain: Preliminary results. Neuroimage 32, 1041-1049.

Nocera L., Gee, J.C., 1997. Robust partial volume tissue classification of cerebral MRI scans. SPIE Medical Imaging, 312-322.

O'Shea, T.M., Counsell, S.J., Bartels, D.B., Dammann, O., 2005. Magnetic resonance and ultrasound brain imaging in preterm infants. Early Hum.Dev. 81, 263-271.

Okahara, M., Kiyosue, H., Mori, H., Tanoue, S., Sainou, M., Nagatomi, H., 2002. Anatomic variations of the cerebral arteries and their embryology: a pictorial review. Eur.Radiol. 12, 2548-2561.

Osher, S., Sethian, J.A., 1988. Fronts propagating with curvature dependent speed. Algorithms based on Hamilton-Jacobi formulations. Journal of Computational Physics 79, 49.

Osher, S., Shu, C.W., 1991. High-order essentially nonoscillatory schemes for Hamilton-Jacobi equations. SIAM J.Numer.Anal. 28, 907-922.

Osher, S.J., Fedkiw, R.P., 2003. Level Set Methods and Dynamic Implicit Surfaces. Springer-Verlag.

Pajdla, T., Gool, L.V., 1995. Matching of 3-D Curves using Semi-differential Invariants. ICCV, 390-395.

Parker, D.L., Chapman, B.E., Roberts, J.A., 2007. Enhanced Image Detail Using Continuity in the MIP Z-Buffer: Applications to Magnetic Resonance Angiography. Journal of Magnetic Resonance Imaging 11, 378-388.

Parzen, E., 1962. On the estimation of a probability density function and the mode. Annals of Math.Stats. 33, 1065-1076.

Peterson, B.S., Anderson, A.W., Ehrenkranz, R., Staib, L.H., Tageldin, M., Colson, E., Gore, J.C., Duncan, C.C., Makuch, R., Ment, L.R., 2003. Regional brain volumes and their later neurodevelopmental correlates in term and preterm infants. Pediatrics 111, 939-948.

Peterson, B.S., Vohr, B., Staib, L.H., Cannistraci, C.J., Dolberg, A., Schneider, K.C., Katz, K.H., Westerveld, M., Sparrow, S., Anderson, A.W., Duncan, C.C., Makuch, R.W., Gore, J.C., Ment, L.R., 2000. Regional brain volume abnormalities and long-term cognitive outcome in preterm infants. JAMA 284, 1939-1947.

Pezzati, M., Dani, C., Biadaioli, R., Filippi, L., Biagiotti, R., Giani, T., Rubaltelli, F.F., 2002. Early postnatal doppler assessment of cerebral blood flow velocity in healthy preterm and term infants. Dev.Med.Child Neurol. 44, 745-752.

Pham, D.L., Prince, J.L., 1999. Adaptive fuzzy segmentation of magnetic resonance images. IEEE Trans.Med.Imaging 18, 737-752.

Pham, D.L., Prince, J.L., 1996. An Adaptive Fuzzy C-Means Algorithm for Image Segmentation in the Presence of Intensity Inhomogeneities. Pattern Recognition Letters 20, 57-68.

Pisupati, C., Wolff.L., Mitzner, W., Zerhouni, E., 1996. Tracking 3-d pulmonary tree structures. Workshop on Mathematical Methods in Biomedical Image Analysis., 160-169.

Powell, S., Magnotta, V., Johnson, H., Andreasen, N., 2006. Automated brain segmentation using neural networks. SPIE Conference of Medical Imaging, 1188-1198.

Prastawa, M., Gilmore, J.H., Lin, W., Gerig, G., 2005. Automatic segmentation of MR images of the developing newborn brain. Med Image Anal. 9, 457-466.

Press, W.H., Teukolsky, S.A., Vetterling, W.T., Flannery, B.P., 1992. Numerical Recipes in C, 2 ed. Cambridge University Press.

Reith, W., Shamdeen, M.G., 2003. Vascular malformations in newborn infants, infants and children. Radiologe 43, 934-947.

Rettmann, M.E., Kraut, M.A., Prince, J.L., Resnick, S.M., 2006. Cross-sectional and longitudinal analyses of anatomical sulcal changes associated with aging. Cereb.Cortex 16, 1584-1594.

Richard, A., 2000. Biomedical Imaging, Visualization, and Analysis. Wiley, New York.

Robel-Tillig, E., Huckel, D., Vogtmann, C., 2000. Value of brain ultrasound studies of newborn infants for prediction of neurological development in the 1st year of life. Klin.Padiatr. 212, 312-317.

Robel-Tillig, E., Mockel, A., Vogtmann, C., 1999. Normal Doppler ultrasound values of the anterior cerebral artery of premature and newborn infants with reference to cardiac function parameters and intestinal blood flow profile. Z.Geburtshilfe Neonatol. 203, 234-240.

Rousseau, F., Glenn, O.A., Iordanova, B., Rodriguez-Carranza, C., Vigneron, D.B., Barkovich, J.A., Studholme, C., 2006. Registration-based approach for reconstruction of high-resolution in utero fetal MR brain images. Acad.Radiol. 13, 1072-1081.

Rueckert, D., 2007. Image Registration Toolkit www.doc.ic.ac.uk/~dr/software/.

Rueckert, D., Sonoda, L.I., Hayes, C., Hill, D.L., Leach, M.O., Hawkes, D.J., 1999. Nonrigid registration using free-form deformations: application to breast MR images. IEEE Trans Med Imaging 18, 712-721.

Rutherford, M., Srinivasan, L., Dyet, L., Ward, P., Allsop, J., Counsell, S., Cowan, F., 2006. Magnetic resonance imaging in perinatal brain injury: clinical presentation, lesions and outcome. Pediatr.Radiol. 36, 582-592.

Rutherford, M.A., 2002. MRI of the Neonatal Brain. W.B.Saunders.

Rutherford, M.A., Ward, P., Malamatentiou, C., 2005. Advanced MR techniques in the term-born neonate with perinatal brain injury. Semin.Fetal Neonatal Med. 10, 445-460.

Saha, P.K., Udupa, J.K., Odhner, D., 2000. Scale-Based Fuzzy Connected Image Segmentation: Theory, Algorithms, and Validation. Computer Vision and Image Understanding 77, 145-174.

Samson, R.S., Wheeler-Kingshott, C.A., Symms, M.R., Tozer, D.J., Tofts, P.S., 2006. A simple correction for B1 field errors in magnetization transfer ratio measurements. Magn Reson Imaging 24, 255-263.

Sandor, S., Leahy, R., 1997. Surface-based labeling of cortical anatomy using a deformable database. IEEE Trans Med.Imaging 16, 41-54.

Santago P., Gage, H.D., 1993. Quantification of MR brain images by mixture density and partial volume modeling. IEEE Transactions on Medical Imaging 12, 566-574.

Schnabel, J.A., Rueckert, D., Quist, M., Blackall, J.M., Castellano Smith, A.D., Hartkens, T., Penney, G.P., Hall, W.A., Liu, H., Truwit, C.L., Gerritsen, F.A., Hill, D.L.G., Hawkes, D.J., 2001. A generic framework for non-rigid registration based on non-uniform multi-level free-form deformations. Fourth Int. Conf. on Medical Image Computing and Computer-Assisted Intervention, 573-581.

Schultz, R.T., Cho, N.K., Staib, L.H., Kier, L.E., Fletcher, J.M., Shaywitz, S.E., Shankweiler, D.P., Katz, L., Gore, J.C., Duncan, J.S., ., 1994. Brain morphology in normal and dyslexic children: the influence of sex and age. Ann.Neurol. 35, 732-742.

Ségonne, F., im, n, E., Fischl, B., 2005. A Genetic Algorithm for the Topology Correction of Cortical Surfaces. Proc. of Image Processing in Medical Imaging, 393-405.

Sereno, J.I., Dale, A.M., Liu, A., Tootell, R.B.H., 1996. A surfacebased coordinate system for a canonical cortex. Neuroimage 3, 252.

Sethian, J.A., 1996. A Marching Level Set Method for Monotonically Advancing Fronts. Proc.Nat.Acad.Sci. 93.

Sethian, J.A., 1999. Fast Marching Methods. SIAM Review 41, 199-235.

Sethian, J.A., 2007. Level Set Methods and Fast Marching Methods, 2nd ed. Cambridge Univ. Press.

Sethian, J.A., Smereka, P., 2003. Level Set Methods for Fluid Interfaces. Annual Review of Fluid Mechanics 35, 341-372.

Sethian, J.A., Vladimirsky, A., 2000. Fast methods for the eikonal and related hamilton- jacobi equations on unstructured meshes. Proc.Natl.Acad.Sci.U.S.A 97, 5699-5703.

Seydel, C., 2001. Developmental biology. Organs await blood vessels' go signal. Science 28.

Shah, D.K., Daley, A.J., Hunt, R.W., Volpe, J.J., Inder, T.E., 2005. Cerebral white matter injury in the newborn following Escherichia coli meningitis. Eur.J.Paediatr.Neurol. 9, 13-17.

Shattuck, D.W., Leahy, R.M., 2001. Automated graph-based analysis and correction of cortical volume topology. IEEE Trans.Med.Imaging 20, 1167-1177.

Shattuck, D.W., Leahy, R.M., 2002. BrainSuite: an automated cortical surface identification tool. Med.Image Anal. 6, 129-142.

Shattuck, D.W., Sandor-Leahy, S.R., Schaper, K.A., Rottenberg, D.A., Leahy, R.M., 2001. Magnetic resonance image tissue classification using a partial volume model. Neuroimage 13, 856-876.

Shaw, P., Lerch, J., Greenstein, D., Sharp, W., Clasen, L., Evans, A., Giedd, J., Castellanos, F.X., Rapoport, J., 2006. Longitudinal mapping of cortical thickness and clinical outcome in children and adolescents with attention-deficit/hyperactivity disorder. Arch.Gen.Psychiatry 63, 540-549.

Shechter, G., Devernay, F., Coste-Maniere, E., Quyyumi, A., McVeigh, E.R., 2003. Three-dimensional motion tracking of coronary arteries in biplane cineangiograms. IEEE Trans.Med.Imaging 22, 493-503.

Shechter, G., Resar, J.R., McVeigh, E.R., 2006. Displacement and velocity of the coronary arteries: cardiac and respiratory motion. IEEE Trans.Med.Imaging 25, 369-375.

Shu, C.W., Osher, S., 1988. Efficient Implementation of Essentially Non-Oscillatory Shock Capturing Schemes. Journal of Computational Physics 77, 439-471.

Shu, C.W., Osher, S., 1989. Efficient implementation of essentially non-oscillatory shock-capturing schemes,II. Journal of Computational Physics 83, 32-78.

Sled, J.G., Pike, G.B., 1998a. Standing-Wave and RF Penetration Artifacts. Caused by Elliptic Geometry: An Electrodynamic Analysis of MRI. IEEE Trans Med.Imaging 17, 662.

Sled, J.G., Pike, G.B., 1998b. Understanding intensity non-uniformity in MRI. Proc. Of 1st MICCAI.,614-622.

Sled, J.G., Zijdenbos, A.P., Evans, A.C., 1998. A nonparametric method for automatic correction of intensity nonuniformity in MRI data. IEEE Trans.Med.Imaging 17, 87-97.

Smith, H.W., De Smet, A.A., Levine, E., 1982. Measurement of cortical thickness in a human cadaver femur. Conventional roentgenography versus computed tomography. Clin.Orthop.Relat Res., 269-274.

Smith, S.M., 2002. Fast robust automated brain extraction. Hum.Brain Mapp. 17, 143-155.

Srinivasan, L., Allsop, J., Counsell, S.J., Boardman, J.P., Edwards, A.D., Rutherford, M., 2006. Smaller cerebellar volumes in very preterm infants at term-equivalent age are associated with the presence of supratentorial lesions. AJNR Am.J.Neuroradiol. 27, 573-579.

Srinivasan, L., Dutta, R., Counsell, S.J., Allsop, J.M., Boardman, J.P., Rutherford, M.A., Edwards, A.D., 2007. Quantification of deep gray matter in preterm infants at term-equivalent age using manual volumetry of 3-tesla magnetic resonance images. Pediatrics 119, 759-765.

Staal, W.G., Hulshoff Pol, H.E., Schnack, H.G., Hoogendoorn, M.L., Jellema, K., Kahn, R.S., 2000. Structural brain abnormalities in patients with schizophrenia and their healthy siblings. Am.J.Psychiatry 157, 416-421.

Stollberger, R., Wach, P., 1996. Imaging of the active B1 field in vivo. Magn Reson Med 35, 246-251.

Suri, J.S., Liu, K., Reden, L., Laxminarayan, S., 2002a. A review on MR vascular image processing algorithms: acquisition and prefiltering: part I. IEEE Trans.Inf.Technol.Biomed. 6, 324-337.

Suri, J.S., Liu, K., Reden, L., Laxminarayan, S., 2002b. A review on MR vascular image processing: skeleton versus nonskeleton approaches: part II. IEEE Trans.Inf.Technol.Biomed. 6, 338-350.

Talairach, J., Tournoux, P., 1988. Co-Planar Stereotaxic Atlas of the Human Brain. Thieme Medical Publishers, New York.

Tarby, T.J., Volpe, J.J., 1982. Intraventricular hemorrhage in the premature infant. Pediatr.Clin.North Am. 29, 1077-1104.

Thirion, J.-P., 1998. Image matching as a diffusion process: an analogy with Maxwell's demons. Med Image Anal. 2, 243-260.

Thompson, D.K., Warfield, S.K., Carlin, J.B., Pavlovic, M., Wang, H.X., Bear, M., Kean, M.J., Doyle, L.W., Egan, G.F., Inder, T.E., 2007. Perinatal risk factors altering regional brain structure in the preterm infant. Brain 130, 667-677.

Thompson, P.M., MacDonald, D., Mega, M.S., Holmes, C.J., Evans, A.C., Toga, A.W., 1997. Detection and mapping of abnormal brain structure with a probabilistic atlas of cortical surfaces. J.Comput.Assist.Tomogr. 21, 567-581.

Thompson, P.M., Moussai, J., Zohoori, S., Goldkorn, A., Khan, A.A., Mega, M.S., Small, G.W., Cummings, J.L., Toga, A.W., 1998. Cortical variability and asymmetry in normal aging and Alzheimer's disease. Cereb.Cortex 8, 492-509.

Thompson, P.M., Toga, A.W., 1996. A Surface-Based Technique for Warping Three-Dimensional Images of the Brain. IEEE Trans Med Imaging 15, 402-417.

Thompson, P.M., Woods, R.P., Mega, M.S., Toga, A.W., 2000. Mathematical/computational challenges in creating deformable and probabilistic atlases of the human brain. Hum.Brain Mapp. 9, 81-92.

Thulborn, K.R., Boada, F.E., Christensen, J.D., Haung-Hellinger, F.R., Reese, T.G., Kosewski, J.M., 1993. B1 correction maps and apparent water density maps as tools for quantitative functional MRI. Proc. of 12th ISMRM, 347.

Timsari, B., Leahy, R., 2000. Optimization method for creating semiisometric flat maps of the cerebral cortex. Proceedings of the SPIE Conference on Medical Imaging: Image Processing, 698-708.

Tincher, M., Meyer, C.R., Gupta, R., Williams, D.M., 1993. Polynomial modeling and reduction of RF body coil spatial inhomogeneity in MRI. IEEE Trans Med.Imaging 12, 361-365.

Toga, A.W., Mazziotta, J.C., 2000. Brain Mapping: The Systems. Academic Press, San Diego.

Tosun, D., Prince, J.L., 2005. Cortical surface alignment using geometry driven multispectral optical flow. Inf. Process Med.Imaging 19, 480-492.

Tosun, D., Rettmann, M.E., Han, X., Tao, X., Xu, C., Resnick, S.M., Pham, D.L., Prince, J.L., 2004a. Cortical surface segmentation and mapping. Neuroimage 23 Suppl 1, S108-S118.

Tosun, D., Rettmann, M.E., Naiman, D.Q., Resnick, S.M., Kraut, M.A., Prince, J.L., 2006. Cortical reconstruction using implicit surface evolution: accuracy and precision analysis. Neuroimage 29, 838-852.

Tosun, D., Rettmann, M.E., Prince, J.L., 2004b. Mapping techniques for aligning sulci across multiple brains. Med.Image Anal. 8, 295-309.

Tschirren, J., Hoffman, E.A., McLennan, G., Sonka, M., 2005. Matching and Anatomical Labeling of Human Airway Tree. IEEE Trans.Med.Imaging 24(12), 1540-1547.

Tschirren, J., Pal, K., Reinhardt, J.M., Hoffman, E.A., Sonka, M., 2002. Segmentation, Skeletonization, and Branchpoint Matching - A Fully Automated Quantitative Evaluation of Human Intrathoracic Airway Trees. Lecture Notes in Computer Science 2489, 12-19.

Tsitsiklis, J.N., 1994. Efficient algorithms for globally optimal trajectories. Proc. of the 33rd Conference on Decision and Control, 1368-1373.

Tsitsiklis, J.N., 1995. Efficient algorithms for globally optimal trajectories. IEEE Transactions on Automatic Control 40, 1528-1538.

Van Essen, D.C., Drury, H.A., 1997. Structural and Functional Analyses of Human Cerebral Cortex Using a Surface-Based Atlas. The Journal of Neuroscience 17, 7079-7102.

Van Leemput, K., Maes, F., Vandermeulen, D., Suetens, P., 2003. A unifying framework for partial volume segmentation of brain MR images. IEEE Trans.Med.Imaging 22, 105-119.

Van Leemput, K., Maes, F., Vandermeulen, D., Suetens, P., 1999a. Automated model-based tissue classification of MR images of the brain. IEEE Trans.Med.Imaging 18, 897-908.

Van Leemput, K., Maes, F., Vandermeulen, D., Suetens, P., 1998. Automatic segmentation of brain tissues and MR bias field correction using a digital brain atlas. Medical Image Computing and Computer-Assisted Intervention - Miccai'98 1496, 1222-1229.

Van Leemput, K., Maes, F., Vandermeulen, D., Suetens, P., 1999b. Automated model-based bias field correction of MR images of the brain. IEEE Trans.Med.Imaging 18, 885-896.

Van, E., Dierker, D.L., 2007. Surface-based and probabilistic atlases of primate cerebral cortex. Neuron 56, 209-225.

Van, E., Drury, H.A., 1997. Structural and functional analyses of human cerebral cortex using a surface-based atlas. J.Neurosci. 17, 7079-7102.

Van, E., Drury, H.A., Dickson, J., Harwell, J., Hanlon, D., Anderson, C.H., 2001a. An integrated software suite for surface-based analyses of cerebral cortex. J Am.Med Inform.Assoc. 8, 443-459.

Van, E., Lewis, J.W., Drury, H.A., Hadjikhani, N., Tootell, R.B., Bakircioglu, M., Miller, M.I., 2001b. Mapping visual cortex in monkeys and humans using surface-based atlases. Vision Res. 41, 1359-1378.

von Economo, C., 1929. The Cytoarchitectonics of the Human Cerebral Cortex. Oxford Univ. Press, London.

Vythilingam, M., Anderson, E.R., Goddard, A., Woods, S.W., Staib, L.H., Charney, D.S., Bremner, J.D., 2000. Temporal lobe volume in panic disorder--a quantitative magnetic resonance imaging study. Psychiatry Res. 99, 75-82.

Wahba, G., 1990. Spline models for observational data. Soc.Industr.Applied Math.

Wang, Y., Peterson, B.S., Staib, L.H., 2003. 3D Brain surface matching based on geodesics and local geometry. Computer Vision and Image Understanding 89, 252-271.

Ward, B., 1999. Intracranial segmentation. Medical College of Wisconsin.

Warfield, S., 1996. Fast k-NN classification for multichannel image data. Pattern Recognition Letters 17, 713-721.

Warfield, S.K., Kaus, M., Jolesz, F.A., Kikinis, R., 2000. Adaptive, template moderated, spatially varying statistical classification. Med Image Anal. 4, 43-55.

Weickert, J., ter Haar Romeny, B.M., Viergever, M.A., 1998. Efficient and reliable scheme for nonlinear diffusion filtering. IEEE Trans.Image Processing 7, 398-410.

Weisenfeld, N.I., Mewes, A.U.J., Warfield, S.K., 2006. Segmentation of newborn brain MRI. Proceedings of the 3rd IEEE International Symposium on Biomedical Imaging: Macro to Nano, 766-769.

Wells, W.M., Kikinis, R., Grimson, W.E.L., Jolesz, F., 1996. Adaptive segmentation of MRI data. IEEE Transactions of the Medical Imaging 15, 429-442.

Wicks, D.A., Barker, G.J., Tofts, P.S., 1993. Correction of intensity nonuniformity in MR images of any orientation. Magn Reson Imaging 11, 183-196.

Wilkening, J., Borucki, L., Sethian, J.A., 2004. Analysis of Stress Driven Grain Boundary Diffusion, Part I. SIAM J.Appl.Math. 64, 1839-1863.

Wilson, D.L., Nobel, A.J., 1999. An adaptive segmentation algorithm for extracting arteries and aneurysms from time-of-Flight MRA data. IEEE Trans.Med.Imaging 18, 938-945.

Wilson, D.L., Nobel, A.J., 1997. Segmentation of cerebral vessels and aneurysms for MR angiography. Proc.Information Processing in Medical Imaging, 423-428.

Wilson, T.T., Waters, L., Patterson, C.C., McCusker, C.G., Rooney, N.M., Marlow, N., Halliday, H.L., 2006. Neurodevelopmental and respiratory follow-up results at 7 years for children from the United Kingdom and Ireland enrolled in a randomized trial of early and late postnatal corticosteroid treatment, systemic and inhaled (the Open Study of Early Corticosteroid Treatment). Pediatrics 117, 2196-2205.

Wink, O., Niessen, W.J., Viergever, M.A., 2000. Fast delineation and visualization of vessels in 3-D angiographic images. IEEE Trans Med Imaging 19, 337-346.

Woodward, L.J., Anderson, P.J., Austin, N.C., Howard, K., Inder, T.E., 2006. Neonatal MRI to predict neurodevelopmental outcomes in preterm infants. N.Engl.J.Med. 355, 685-694.

Xu, C., Pham, D.L., Rettmann, M.E., Yu, D.N., Prince, J.L., 1999. Reconstruction of the human cerebral cortex from magnetic resonance images. IEEE Trans.Med.Imaging 18, 467-480.

Xu, C., Prince, J.L., 1998. Snakes, Shapes, and Gradient Vector Flow. IEEE Transactions on Image Processing 7, 359-369.

Xu, M., Thompson, P.M., Toga, A.W., 2006. Adaptive reproducing kernel particle method for extraction of the cortical surface. IEEE Trans.Med.Imaging 25, 755-767.

Yezzi, A.J., Jr., Prince, J.L., 2003. An Eulerian PDE approach for computing tissue thickness. IEEE Trans Med.Imaging 22, 1332-1339.

Yoon, U.C., Kim, J.S., Kim, I.Y., Kim, S.I., 2001. Adaptable fuzzy c-means for improved classification as a preprocessing procedure of brain parcellation. J.Digit.Imaging 14, 238-240.

Zeng, X., Staib, L.H., Schultz, R.T., Duncan, J.S., 1999. Segmentation and measurement of the cortex from 3-D MR images using coupled-surfaces propagation. IEEE Trans.Med.Imaging 18, 927-937.

Zhang, J., 1992. The mean-field theory in EM procedures for markov random fields. IEEE Transactions on Signal Processing 40, 2570-2583.

Zhuang, S., Tustison, N., Avants, B., Gee, J., 2007. Adaptive graph cuts with tissue priors for brain MRI segmentation. Proceedings of the 3rd IEEE International Symposium on Biomedical Imaging: Macro to Nano, 762-765.

Zijdenbos, A.P., Dawant, B.M., Margolin, R.A., 1993. Measurement reliability and reproducibility in manual and semi-automatic mri segmentation. Proc.Annu.Conf.Eng.Med.Biol., 162-163.

Zijdenbos, A.P., Dawant, B.M., Margolin, R.A., Palmer, A.C., 1994. Morphometric analysis of white matter lesions in MR images: Method and validation. IEEE Transactions on Medical Imaging 13, 716-724.

Zilles, K., 1990. Cortex in the Human Nervous System. Academic Press, San Diego, CA.